

# PROCEEDINGS OF THE DINEST 2021

2<sup>nd</sup> Conference on Structural Dynamics 2021

Gijón, 22 -23 July



# **2<sup>nd</sup> Conference on Structural Dynamics (DinEst 2021)**

---

## **Editors**

Aenlle López, Manuel  
Fernández Fernández, Pelayo  
Muñiz Calvente, Miguel  
López Gallego, Mario  
Álvarez Vázquez, Adrián  
García Diéguez, Marta  
Lamela Rey, María Jesús

# Sponsors of the Conference

---



## **Organization**

---

### **Scientific committee**

Alberto Fraile de Lerma, ETSII-UPM, España  
Alejandro E. Martínez-Castro, Universidad de Granada, España  
Amadeo Benavent Climent, ETSII - UPM, España  
Antolín Lorenzana, EII- UVA, España  
Carlos Zanuy Sánchez, ETSICCP - UPM, España  
Daniel Cantero, NTNU, Noruega  
Daniel García Vallejo, ETSI - US, España  
M. Dolores G. Pulido, IETCC-CSIC, ETSICCP-UPM, España  
Felipe Gabaldón Castillo, ETSICCP - UPM, España  
Francisco López Almansa, UPC, España  
Francisco Martínez Cutillas, ETSICCP - UPM, España  
Gia Khanh Nguyen, ETSIAE - UPM, España  
Guillermo Rus, Universidad de Granada, España  
Ignacio Romero Olleros, ETSII - UPM, España  
Iván M Díaz, ETSICCP - UPM, España  
Jaime Domínguez, ETSI - US, España  
Jaime H. García-Palacios, ETSICCP - UPM, España  
Javier Cara Cañas, ETSII - UPM, España  
Joaquín Martí Rodríguez, ETSIME - UPM, España  
Jose Maria Goicolea, ETSICCP UPM, España  
Juan Carlos García Orden, ETSICCP - UPM, España  
Juana Mayo, ETSI - US, España  
M<sup>a</sup> Dolores Martínez Rodrigo, UJI, España  
Manuel Aenlle López, UNIOVI, España  
María Jesús Elejabarrieta, Universidad de Deusto, España  
Mario López Gallego, UNIOVI, España  
Miguel Muñiz-Calvente, UNIOVI, España  
Orlando Maeso, ULPGC, España  
Pedro Galvín, ETSI - US, España  
Pedro Museros Romero, UPV, España  
Pelayo Fernández Fernández, UNIOVI, España  
Ricardo Perera Velamazán, ETSII - UPM, España  
Salvador Ivorra-Chorro, UA, España

### **Organizing committee**

Manuel Aenlle López, EPI Gijón-UNIOVI, España  
Pelayo Fernández Fernández, EPI Gijón-UNIOVI, España  
Miguel Muñiz Calvente, EPI Gijón-UNIOVI, España  
Mario López Gallego, EPM-UNIOVI, España  
Adrián Álvarez Vázquez, EPI Gijón-UNIOVI, España  
Marta García Dieguez, EPM-UNIOVI, España  
María Jesús Lamela Rey, EPI Gijón-UNIOVI, España

## Preface

---

Gijón, 21<sup>st</sup> July 2021

Welcome to the 2nd Conference on Structural dynamics, Gijón, Spain, July 22-23 (Thursday-Friday), 2021. This Conference was planned to be organized in June 2020, but it was postponed to July 2021 due to the COVID-19 pandemic. This conference is the continuation of the successful 1st Conference on Structural Dynamics organized by the Polytechnic University of Madrid (ETSICCP) in June 2018. Structural dynamics is a type of structural analysis which covers the behavior of a structure subjected to dynamic loadings (people, wind, waves, traffic, earthquakes, machinery, explosions, impacts, etc.). Civil, Mechanical, Aerospace, and Ocean Engineers, face every day with topics related to structural dynamics with analytical, numerical, and experimental approaches.

This Conference covers all major aspects of Structural Dynamics with focus on the following topics: Analytical Techniques, Numerical Techniques, Experimental Techniques, Aeroelasticity, Damping, Dynamic Loadings, Vibration Control, Model Correlation, Model Updating, Dynamic Behavior of Materials, Dynamics of Bridges, Earthquake Engineering, Structural Health Monitoring, etc. A pre-conference course is also organized on Wednesday 21st from Sunday to Monday.

Beyond a good number of interesting papers on these topics, presented by researchers, technical specialists and students, the Conference comprehends two Keynote Lectures by Professor Alvaro Cunha and Professor Salvador Ivorra.

As the previous Conference, held in Madrid in 2018, scientists, applicants, and students have the occasion to share their knowledge in this rather fascinating field and to improve their specific skills.

We warmly thank all the contributors, authors, speakers, and sponsors of the event and wish this conference offering you fruitful discussion and a pleasant time in Gijón.



Prof. Manuel Aenlle López  
Dept. of Construction and Manufacturing Eng.  
University of Oviedo

## Plenary keynote lectures

---

### “COMPORTAMIENTO DINÁMICO DE CHIMENEAS INDUSTRIALES DE OBRA DE FÁBRICA REFORZADAS DE TRM”

by Prof. Salvador Ivorra Chorro

#### About keynote speaker

Salvador Ivorra Chorro is Full Professor of Continuum Mechanics and Structure Theory at the Department of Civil Engineering of the University of Alicante, where he is Vice-Rector for Infrastructure, Sustainability and Occupational Safety and head of the research group GRESMES. He holds a PhD in Industrial Engineering (Mechanical Engineering) from the Polytechnic University of Valencia and University Specialist in Occupational Risk Prevention by the same university. Since July 2018 he is the Coordinator of the Subarea of Civil Engineering and Architecture of the State Research Agency of Spain. His research activity has been focused on the dynamic behaviour of structures and structural reinforcement, and he has devoted an important part of his research to the structures belonging to the historical heritage.



He is author of 79 scientific articles (61 in JCR-indexed journals) and more than 120 conference papers and is co-inventor of two patents. He has also directed 17 doctoral theses. He has participated in 29 competitive research projects (as principal investigator in 17) and in more than 200 research and technical assistance contracts with public agencies and private companies. He coordinated a project financed with €2,000,000 from FEDER funds for the construction of Civil Engineering research laboratory of the University of Alicante. According to the Scopus bibliometric analysis, his h-index is 25, with more than 1737 citations to his works.

At the University of Alicante, he was deputy director of Civil Engineering from 2006 to 2013, being responsible for implementing the new Undergraduate and Master's degrees in Civil Engineering under this period. He was also Deputy Director of the Department of Civil Engineering from 2016 to 2019 and Director from 2019 to 2020. Between 2017 and 2018 he was the Manager of the State R&D Plan in the Construction area of the Ministry of Economy and Competitiveness (Spain).

He was awarded the Teaching Excellence Award by the University of Alicante Social Council in 2010. In 2015, the Kiss Bridge pedestrian footbridge in Pilar de la Horadada (Alicante), which he co-designed, was nominated by the FIB as one of the best concrete works in 2009-2014. In 2002 he co-designed the Polytechnic Tower in Valencia, the highest tower completely made of FRP in Europe until that moment. In 2019 he received the prize of the Association of Structural Consultants for the intervention project in the "La Paz" masonry chimney. In 2019 he received the Outstanding or Productive Young Researcher Award from Alconpat.

## VIBRATION-BASED SHM OF TRANSPORTATION AND ENERGY INFRASTRUCTURES

by Prof. Álvaro Cunha

### About keynote speaker

Alvaro Cunha is Full Professor at the Department of Civil Engineering of the Faculty of Engineering of the University of Porto, Scientific Coordinator of the Research Unit CONSTRUCT (Institute of R&D in Structures and Construction), Head of Laboratory of Vibrations and Monitoring (ViBest) of FEUP and Member of the Scientific Council of Exact Sciences and Engineering of FCT.



He is President of the European Association on Structural Dynamics (EASD) and he was Chair of SEM Civil Structures Testing Technical Division, Vice-Chair of IABSE Working Group 4 on Vibrations, Chair of the international conferences EVACES'07, SMART'09, CIAHP'2010, IOMAC 2013, EURODDYN 2014 and SHMII-10 and Co-Chair of FOOTBRIDGE'08.

His main fields of interest are Dynamics of Bridges and Special Structures, Measurement of Vibrations, Modal Identification, Structural Health Monitoring of Large Civil Structures and Control of Vibrations.

He has been responsible by the development and implementation of 12 vibration based SHM demonstrators in large Civil structures with different typologies (roadway and railway bridges, footbridges, stadium suspension roof, wind turbine tower and arch dam), active since 2007, and creation of a digital data repository stemming from all monitoring activity (<http://vibest.fe.up.pt/shm>).

He has been principal investigator of 12 national or European Research Projects, and researcher of other 9, focused on the themes: (1) Dynamic measurements with Laser sensors, (2) Modal Identification of Large Structures and Finite Element Updating, (3) Dynamics of Cable-Stayed Bridges, (4) Dynamic Effects of Traffic Loads on Bridges, (5) Wind and Structures, (6) Fatigue assessment in metallic Railway Bridges, (7) Vibrations in Footbridges, (8) Control of Vibrations in Civil Structures, (9) Structural Health Monitoring of Bridges and Wind Turbines, (10) Deterioration of Dams.

## Table of contents

---

<b>SECTION 1: ANALYTICAL AND COMPUTATIONAL DYNAMICS.....</b>	<b>1</b>
OBTAINING A FEM-LESS PHYSICAL MODEL OF A STRUCTURE. A CASE STUDY .....	2
APPLICATION OF SEMI-ANALYTICAL METHODS TO HYBRID SIMULATION OF BEAM-LIKE STRUCTURES WITH VIBRATION ABSORBERS UNDER MOVING INERTIAL LOADS .....	12
ANALYSIS OF DYNAMIC LOADS IN STRUCTURES WITH NEURONAL NETWORK .....	23
LOW-COST ARDUINO-BASED HORIZONTAL SENSOR AND DATA ACQUISITION SYSTEM FOR LOW- LEVEL AMBIENT VIBRATION MEASUREMENTS.....	32
MODAL MASS IN SYSTEMS WITH TWO PARTS OF DIFFERENT MASS-DENSITY .....	44
MODAL MASS IN CONSTANT MASS-DENSITY SYSTEMS.....	52
<b>SECTION 2: SEISMIC ENGINEERING .....</b>	<b>61</b>
MAGNETO RHEOLOGICAL FLUIDS IN CIVIL ENGINEERING .....	62
REINFORCEMENT OF ADOBE CONSTRUCTION DAMAGED BY SEISMIC LOADS .....	70
<b>SECTION 3: RAILWAY DYNAMICS.....</b>	<b>81</b>
RAILWAY INDUCED VERTICAL VIBRATIONS IN TWO-SPAN CONTINUOUS BRIDGES.....	82
TRACK-BRIDGE INTERACTION IN RAILWAY BRIDGES COMPOSED BY SINGLE-TRACK ADJACENT DECKS USING 3D FE MODELS.....	93
BALLAST TRACK-BRIDGE INTERACTION IN SINGLE-TRACK RAILWAY BRIDGES OF DIFFERENT TYPOLOGIES .....	104
DYNAMIC ANALYSIS OF A RAILWAY BRIDGE WITH TUNED VIBRATIONS ABSORBERS SUBJECTED TO HIGH SPEED TRAIN LOAD MODELS.....	116
EXPERIMENTAL MEASUREMENTS ON RAILWAY BRIDGES BELONGING TO SPANISH LINES .....	126
<b>SECTION 4: MARINE STRUCTURES .....</b>	<b>133</b>
DYNAMIC ANALYSIS OF FLOATING BREAKWATERS: A CASE STUDY .....	134
MOTION AND DYNAMIC RESPONSE APPROACH FOR FLOATING PHOTOVOLTAIC STRUCTURES UNDER MARINE LOADS .....	146
<b>SECTION 5: VIBRATION CONTROL .....</b>	<b>158</b>
COMPOSITE FLOOR BEAMS WITH CONSTRAINED LAYER DAMPING: EXPERIMENTAL TESTS ON REDUCED SCALE MODELS .....	159
SEMI-ACTIVE TUNED MASS DAMPER: MAGNETORHEOLOGICAL DAMPER IDENTIFICATION AND PERFORMANCE EVALUATION .....	172

<b>SECTION 5: VIBRATION CONTROL (CONT.) .....</b>	<b>183</b>
DESIGN, IMPLEMENTATION AND EXPERIMENTAL VALIDATION OF AN ACTIVE MASS DAMPER FOR VIBRATION MITIGATION IN SLENDER STRUCTURES USING A LOW-COST PROCESSOR.....	183
PARAMETRIZATION OF A TELESCOPE MOUNT WITH PYANSYS FOR INITIAL MODAL PERFORMANCE EXPLORATION .....	195
KALMAN-BASED VIRTUAL SENSING FOR STRUCTURAL HEALTH MONITORING.....	202
ANALYSIS AND CORRECTION OF VIBRATIONS GENERATED BY APLASTIC BAG PRODUCTION MACHINE .....	214
OPERATIONAL MODAL ANALYSIS FOR BUILDINGS EFFICIENT SEISMIC DAMAGE IDENTIFICATION.....	223
TOWARDS AUTONOMOUS VEHICLE COMFORT MODELLING FOR REAL WORLD ROAD VEHICLE SIMULATION.....	233
<b>SECTION 6: BRIDGE DYNAMICS.....</b>	<b>239</b>
NUMERICAL MODELLING AND MODAL ANALYSIS OF THE PEDESTRIAN FOOTBRIDGE AT THE MILAN'S CAMPUS.....	240
INFLUENCE OF PASSIVE AND ACTIVE PEDESTRIANS ON THE DYNAMIC PARAMETERS OF A LIGHTWEIGHT FRP FOOTBRIDGE .....	246

## **Section 1: Analytical and computational dynamics**

## OBTAINING A *FEM-LESS* PHYSICAL MODEL OF A STRUCTURE. A CASE STUDY

Álvaro Magdaleno\*, César Peláez† and Antolín Lorenzana‡

Escuela de Ingenierías Industriales,  
Universidad de Valladolid  
47011 Valladolid, Spain

e-mail: \*alvaro.magdaleno@uva.es, †cesar.pelaez@uva.es, ‡ali@eii.uva.es  
ORCID: \*0000-0002-5606-1545, †0000-0003-1260-8112, ‡0000-0003-2562-0532

**Abstract.** A direct method to estimate a set of physical matrices from a modal model is proposed. After assuming the validity of some hypothesis, like linear behavior, an inverse approach is formulated to obtain a set of mass, stiffness and damping matrices from a modal model that realistically reproduce the dynamics of a structure. The physical model, which is often incomplete due to the difference between the number of measured modes and monitored degrees of freedom, can be used to simulate the response of the structure subjected to any kind of load and, moreover, to simulate the effect of different types of structural modifications. The procedure is exemplified by applying it to a real structure. First, an EMA is performed to estimate its modal properties inside a certain frequency range from which a set of physical matrices is then calculated to reproduce the dynamics of those modes in the  $N$  monitored degrees of freedom. It can be shown that, despite not being unique, the model obtained in this work is perfectly useful to carry out simulations on it and to estimate the effect of several kinds of structural modifications.

**Key words:** Structural dynamics, Experimental Modal analysis, Singular Value Decomposition, Physical Model, Modal Model.

### 1 INTRODUCTION

The dynamic behaviour of a structure can be described by means of different types of models, such as physical models, which contain explicit information about its mass, stiffness and damping, or modal models, composed of natural frequencies, damping ratios and scaled mode shapes. Both types of models allow to perform simulations and test the dynamic behaviour of the structure in a wide variety of loading scenarios. Together with the loads themselves, the different scenarios may involve modifying one or more physical properties, like the structural mass or damping, or the addition of other kind of systems, such as tuned mass dampers (TMDs).

Although some workarounds exist, the physical properties of the structure that need to be modified are not explicitly represented in the modal models, which complicates performing such modifications or subsystem additions to that kind of models, and it is preferable having available a physical model for that type of tasks. Also, simulating the dynamic response of a structure subjected to the ground acceleration (to simulate a seismic action, for example) also requires having the structural mass explicitly modelled.

In some situations, for example after applying a complete experimental modal analysis procedure to a certain structure, only the modal model is available. On way to

overcome the aforementioned issues consists in applying a Model Updating technique. This family of procedures have been developed in parallel to the evolution of the Finite Element Method (FEM) and are aimed to adapt (or update) a previously conceived computational model to a set of measured properties of a real structure, typically its modal properties. As a result, the computational models behave similarly to the real structure and, indirectly, some of its physical properties can be estimated and eventually modified according to any simulation requirement. However, an appropriate application of a Model Updating technique often leads to an iterative and long process which usually rely on sophisticated and complex FEM models and powerful optimization algorithms to provide meaningful results. Moreover, if the computation model is not detailed enough and does not include all the required structural and non-structural elements, the properties of the updated model may not be realistic and, thus, may not trustworthily represent the effect of the required structural modifications.

As an alternative, direct methods exist to obtain physical models from experimentally estimated properties. These methods do not rely on the quality of a previously conceived model and directly provide a physical model of the structure from another kind of model, such as a modal model. In this work, a direct method is presented to estimate a linear model consisting of a set of physical matrices of a discretised structure from an experimentally estimated modal model, composed of a set of natural frequencies, damping ratios and scaled mode shapes. Note that the mode shapes need to be properly scaled in order to contain the full information required to perform simulations with it. The resulting structural model will be automatically discretized in the same degrees of freedom (DOFs) that have been monitored to estimate the modal model, which are the

same DOFs on which the mode shapes are estimated.

This kind of methods were first developed by Berman [1, 2], who warned about the solution of this problem not being unique if the number of identified modes,  $m$ , is fewer than the number of degrees of freedom,  $n$ , monitored to estimate them. Other authors have further explored this topic [3, 4] but restraining the applicability of their methods to proportional modal models, i.e., models with real-valued mode shapes. Very few authors have addressed the possibility of dealing with complex-valued mode shapes, like [5], but they tried to project them into the real axis rather than actually include the complex-valued vectors into a methodology which issued a damping matrix that truly represents them. Finally, many authors, like [6, 7, 8, 9, 10] have dealt with that issue alone, obtaining damping matrices that accurately provide complex-valued mode shapes, but assuming to know the mass and stiffness matrices beforehand.

The methodology proposed in this work is conceived to deal with both real and complex-valued mode shapes and simultaneously provides a complete set of physical matrices  $M$ ,  $C$  and  $K$ , that accurately reproduces the same dynamic behaviour than the modal model. To show its performance, the developed methodology is applied to a real structure consisting of a simple-supported timber beam.

## 2 THEORETICAL BACKGROUND

A linear model that represents the dynamic behaviour of a certain discretized structure can be described in terms of a set of three square and symmetric matrices: the mass matrix  $M$ , the damping matrix  $C$  and stiffness matrix  $K$  matrices, as shown in Eq. 1, where  $\mathbf{q}(t)$  and  $\mathbf{f}(t)$  are column vectors that represent the  $n$  displacements and the forces acting on them,

respectively. The dot operand ( $\dot{\cdot}$ ) represents a time derivative and  $t$  is the time variable.

$$\mathbf{M} \ddot{\mathbf{q}}(t) + \mathbf{C} \dot{\mathbf{q}}(t) + \mathbf{K} \mathbf{q}(t) = \mathbf{f}(t) \quad (1)$$

In the most general case, where non-proportional damping is assumed and the matrix  $\mathbf{C}$  cannot be expressed in terms of  $\mathbf{M}$  and  $\mathbf{K}$ , transforming the system of equations in Eq. 1 to the modal domain does not uncouple the equations [11]. One way to overcome this issue requires transforming Eq. 1 to its state space formulation, as shown in Eq. 2, where  $\mathbf{x}(t) = [\mathbf{q}^T(t) \ \dot{\mathbf{q}}^T(t)]^T$  is the state vector and  $\mathbf{u}(t) = [\mathbf{f}^T(t) \ \emptyset]^T$  is the input vector. The symbol  $\emptyset$  stands for a null matrix or vector of an appropriate dimension and the letter T indicates a matrix or vector transpose.

$$\begin{aligned} \mathbf{A} \dot{\mathbf{x}}(t) + \mathbf{B} \mathbf{x}(t) &= \mathbf{u}(t) \\ \mathbf{A} &= \begin{bmatrix} \mathbf{C} & \mathbf{M} \\ \mathbf{M} & \emptyset \end{bmatrix} \quad \mathbf{B} = \begin{bmatrix} \mathbf{K} & \emptyset \\ \emptyset & -\mathbf{M} \end{bmatrix} \end{aligned} \quad (2)$$

That system of equations can be uncoupled by means of the  $n$  pairs of eigenvectors ( $\tilde{\boldsymbol{\theta}}_r, \tilde{\boldsymbol{\theta}}_r^*$ ) that can be calculated together with their corresponding  $n$  pairs eigenvalues ( $s_r, s_r^*$ ) by solving the eigenproblem shown in Eq. 3. The symbol \* stands for the complex conjugate. The eigenvalues contain information about the natural frequency,  $\omega_r$ , and the damping ratio,  $\zeta_r$ , so  $s_r = -\omega_r \zeta_r + j \omega_r \sqrt{1 - \zeta_r^2}$ , where  $j$  is the imaginary unit.

$$(\mathbf{A} s_r + \mathbf{B}) \tilde{\boldsymbol{\theta}}_r = 0 \quad (3)$$

It is important to note that the eigenvectors  $\tilde{\boldsymbol{\theta}}_r$  obtained from Eq. 3 are composed of terms related to displacements and terms related to velocities, similarly to the state vector  $\mathbf{x}(t)$ . In fact, the displacement components and the velocity components are related through the eigenvalue  $s_r$ , so  $\tilde{\boldsymbol{\theta}}_r = [\boldsymbol{\theta}_r^T \ s_r \boldsymbol{\theta}_r^T]^T$ , where  $\boldsymbol{\theta}_r$  are the mode shapes. This relationship can be expressed in a more compact way as shown in Eq. 4, where the matrix  $\tilde{\boldsymbol{\Theta}}$  contains the

eigenvectors  $\tilde{\boldsymbol{\theta}}_r$  (column-wise),  $\boldsymbol{\Theta}$  is composed of the mode shapes  $\boldsymbol{\theta}_r$  and  $\mathbf{S}$  is a diagonal matrix containing the  $n$  eigenvalues. Note that the eigenvectors and mode shapes are ordered according to the eigenvalue order in  $\mathbf{S}$ .

$$\tilde{\boldsymbol{\Theta}} = \begin{bmatrix} \boldsymbol{\Theta} \\ \mathbf{S} \end{bmatrix} \quad (4)$$

Both matrices  $\mathbf{A}$  and  $\mathbf{B}$  can be diagonalised thanks to their orthogonality properties with respect to  $\tilde{\boldsymbol{\Theta}}$ , as shown in Eq. 5, where  $\tilde{\mathbf{A}}$  and  $\tilde{\mathbf{B}}$  are diagonal matrices satisfying  $\tilde{\mathbf{A}}^{-1} \tilde{\mathbf{B}} = -\mathbf{S}$ . It is also usual to scale the mode shapes so that matrix  $\tilde{\mathbf{A}}$  is an identity matrix and  $\tilde{\mathbf{B}} = -\mathbf{S}$ .

$$\begin{aligned} \tilde{\boldsymbol{\Theta}}^T \mathbf{A} \tilde{\boldsymbol{\Theta}} &= \tilde{\mathbf{A}} \\ \tilde{\boldsymbol{\Theta}}^T \mathbf{B} \tilde{\boldsymbol{\Theta}} &= \tilde{\mathbf{B}} \end{aligned} \quad (5)$$

Finally, by making use of Eqs. 2 and 4, Eq. 5 can be further developed obtaining another pair of orthogonality expressions, as shown in Eq. 6.

$$\begin{aligned} \boldsymbol{\Theta}^T \mathbf{C} \boldsymbol{\Theta} + \mathbf{S} \boldsymbol{\Theta}^T \mathbf{M} \boldsymbol{\Theta} + \boldsymbol{\Theta}^T \mathbf{M} \boldsymbol{\Theta} \mathbf{S} &= \tilde{\mathbf{A}} \\ \boldsymbol{\Theta}^T \mathbf{K} \boldsymbol{\Theta} - \mathbf{S} \boldsymbol{\Theta}^T \mathbf{M} \boldsymbol{\Theta} \mathbf{S} &= \tilde{\mathbf{B}} \end{aligned} \quad (6)$$

Eqs. 3 and 6 are the core of the methodology presented in the next section.

### 3 METHODOLOGY

As mentioned in the Introduction, the methodology presented in this work is aimed at estimating a set of physical matrices  $\mathbf{M}_e$ ,  $\mathbf{C}_e$  and  $\mathbf{K}_e$  that represents the same dynamic behaviour than a set of experimentally estimated set of modes. The subscript  $e$  stands for estimated to remark their nature, but they should be considered in the same one as the matrices  $\mathbf{M}$ ,  $\mathbf{C}$  and  $\mathbf{K}$  used in the previous section. The dimension of the resulting physical model,  $n$ , equals the number of DOFs monitored to obtain the modal model, which is composed by a total of  $m$  identified modes.

The procedure is divided into two stages. In the first stage, a system of linear equations is

built to account for the three main conditions that a physical model needs to meet in order to represent the same dynamic behaviour than a modal model. Due to an additional nonlinear inequality that need also to be imposed, the system of equations is solved in a second stage by carrying out an optimization procedure.

### 3.1 The system of equations

For an estimated physical model to be dynamically equivalent to a certain modal model, it needs to fulfil the following three conditions.

1. The three physical matrices must be symmetric. This is formulated as shown in Eq. 7, where the generic matrix  $\mathbf{P}$  can be substituted by  $\mathbf{M}_e$ ,  $\mathbf{C}_e$  and  $\mathbf{K}_e$  and the subscripts  $i$  and  $k$  are used to index the matrix elements.

$$P_{ik} - P_{ki} = 0 \quad \forall i \neq k, (i, k) \leq n \quad (7)$$

2. The physical model and the modal model must satisfy the eigenproblem in Eq. 3, which can be expressed in terms of the physical matrices, the complex eigenvalues  $\mathbf{s}_r$  and the complex mode shapes  $\boldsymbol{\theta}_r$  as shown in Eq. 8. Note that, since the matrices are symmetric (condition 1), it is not necessary to impose the eigenvalue condition to the complex conjugates of  $\boldsymbol{\theta}_r$  and  $\mathbf{s}_r$ , so Eq. 8 represents a total of  $m$  equations.

$$(\mathbf{M}_e \mathbf{s}_r^2 + \mathbf{C}_e \mathbf{s}_r + \mathbf{K}_e) \boldsymbol{\theta}_r = 0 \quad r = 1..m \quad (8)$$

3. If the two previous conditions are met, the resulting modal matrices  $\tilde{\mathbf{A}}$  and  $\tilde{\mathbf{B}}$  are diagonal and satisfy  $\tilde{\mathbf{A}}^{-1} \tilde{\mathbf{B}} = -\mathbf{S}$ . Only the mode shapes scaling is left to be accounted for through one of the orthogonality conditions in Eq. 6. As in the previous condition, the scaling condition needs not be imposed to the complex conjugates.

Note that the three conditions are linear with respect to the problem unknowns, which are the elements of the physical matrices. These elements can be wrapped in an unknown vector,  $\mathbf{x}_p$ , which has a length of  $3n^2$ . By using this vector, the three conditions can be rewritten in the form of a system of linear equations  $\mathbf{A}_p \mathbf{x}_p = \mathbf{b}_p$ , where  $\mathbf{A}_p$  and  $\mathbf{b}_p$  must be built according so that the chosen expression of Eq. 6, and Eqs. 7 and 8 are properly expressed. Once this is done, many terms in  $\mathbf{A}_p$  turn out to be complex due to conditions 2 and 3, which may lead to complex terms in  $\mathbf{x}_p$  if the system of equations is directly solved and complex physical matrices would be obtained. To avoid this, the subset of complex-valued equations  $\mathbf{A}_{pc} \mathbf{x}_p = \mathbf{b}_{pc}$ , where the subscript  $c$  stands for “complex”, must be reformulated by splitting it into its real and imaginary parts, leading to the final and real-valued system of equations in Eq. 9, where the subscript  $r$  stands for “real” and  $\mathbf{A}_q$  and  $\mathbf{b}_q$  are real-valued.

$$\begin{aligned} \mathbf{A}_q \mathbf{x}_p &= \mathbf{b}_q \\ \begin{bmatrix} A_{pr} \\ \text{Re}(A_{pc}) \\ \text{Im}(A_{pc}) \end{bmatrix} x_p &= \begin{bmatrix} b_{pr} \\ \text{Re}(b_{pc}) \\ \text{Im}(b_{pc}) \end{bmatrix} \end{aligned} \quad (9)$$

Any vector  $\mathbf{x}_p$  that satisfies Eq. 9 contains the elements of a set of physical matrices  $\mathbf{M}_e$ ,  $\mathbf{C}_e$  and  $\mathbf{K}_e$  that satisfies the three requirements described above and are, in principle, dynamically equivalent to the considered modal model.

### 3.2 The optimization strategy

In general terms, the number of equations in Eq. 9 is different from the number of unknowns. If the number of equations is greater, then a single solution can be obtained by pseudo-inverting the matrix  $\mathbf{A}_q$  and the resulting physical model only reproduces the

desired dynamic behaviour approximately. However, if the number of equations is lower than the number of unknowns, infinite solutions exist that exactly meet the three presented conditions, so they all reproduce the desired dynamics. When this happens, the difference among all the infinite solutions is found in the so-called exogenous modes, which are the modes that are mathematically computable from the  $n$ -dimensional estimated physical model, but that do not belong to the modal model used to obtain it. In such a scenario, controlling the properties of the exogenous modes is of extreme importance for the physical model to be useful.

If the properties of the exogenous modes are not constrained in any way, one major issue that may arise is that they may potentially have a negative damping ratio. This is equivalent to artificially increasing the energy in the structure over time, even if no acting force is applied on it, since the contribution of these modes would infinitely increase instead of decay to zero. To avoid this issue, a final condition must be imposed during the solution of the system of equations in Eq. 9, so that all the computable damping ratios (of the  $m$  used modes and specially those associated to the  $n - m$  exogenous modes) are strictly positive. This leads to a nonlinear inequality constraint which cannot be handled in a straightforward way. In this work, an optimization algorithm is proposed to be used in order to find an optimal  $\mathbf{x}_p$  according to a cost function (described below), subjected to the linear constraints expressed in Eq. 9 and the nonlinear one described above.

To perform the optimization procedure, different functions can be considered. In this work, the cost function shown in Eq. 10 is proposed, which is intended to simultaneously minimize the natural frequency of the exogenous modes, computed as  $|s_r|$ , and maximize their damping ratio, calculated as

$-|s_r|/\text{Re}(s_r)$ , where  $|\cdot|$  stands for the magnitude of the complex eigenvalue and  $\text{Re}(\cdot)$  represents the real part. The natural frequencies are minimised to make the exogenous dynamics as slow as possible. At the same time, their damping ratio is maximised to make the dynamic contribution less dominant even if the corresponding natural frequencies are not small enough.

$$J = \sum_{r=m+1}^n \frac{|s_r|^2}{-\text{Re}(s_r)} \quad (10)$$

To perform the minimization of Eq. 10, the `fmincon` function of MATLAB is used, which implements the Interior-Point optimization algorithm and allows to simultaneously consider linear and nonlinear constraints as well as boundaries for the variables (if required). After the algorithm has been successfully run, an optimum  $\mathbf{x}_p$  vector is obtained, which is later parsed to retrieve the sought physical matrices.

#### 4 CASE STUDY

To show its performance, the methodology is applied to a structural model consisting of a timber beam with a total length of approximately  $L = 13.5$  m (Figure 1a). It has a rectangular section with a height of 100 mm and a width of 140 mm. It is instrumented with 9 accelerometers (as the one shown in Figure 1b) placed at the locations depicted in the layout of Figure 2 and numbered from 1 to 9 (points 0 and 10 correspond to the support, which are assumed to be rigid enough). A force is applied by means of an instrumented hammer at point 8, which is  $L/6$  far from one end. All the sensors are connected to a data acquisition system that synchronously records the time domain signals. Then, the `tfestimate` MATLAB function helps to estimate the FRFs shown in Figure 3.



**Figure 1:** (a) Picture of the timber beam; (b) detail of an accelerometer

A complete modal identification procedure is performed to the FRFs by means of a curve fitting technique, by assuming a linear model as shown in Eq. 11, where  $a_r$  are the complex-valued residues that contain the mode shape information. The identification is carried out in the frequency range between 0.5 and 35 Hz, leading to the natural frequencies and damping ratios shown in Table 1, which correspond to

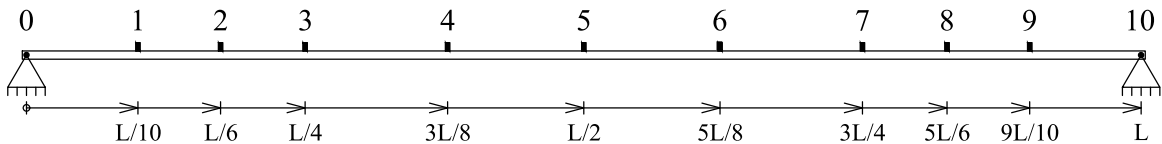


**Figure 2:** (a) Picture of the timber beam; (b) detail of an accelerometer

the mode shapes depicted in Figure 4 (note that, prior to generate the Figure, they have been projected on the real axis, but for further processing the original complex-valued mode shapes are kept).

$$h_{ik}(\omega) = \sum_{r=1}^m \left( \frac{a_{r,ik}}{j\omega - s_r} + \frac{a_{r,ik}^*}{j\omega - s_r^*} \right) \quad (11)$$

Mode	Natural frequency [Hz]	Damping ratio [%]
1	1.46	0.81
2	5.41	0.35
3	12.17	0.33
4	21.49	0.37
5	33.17	0.39

**Table 1:** Identified natural frequencies and damping ratios of the timber beam.

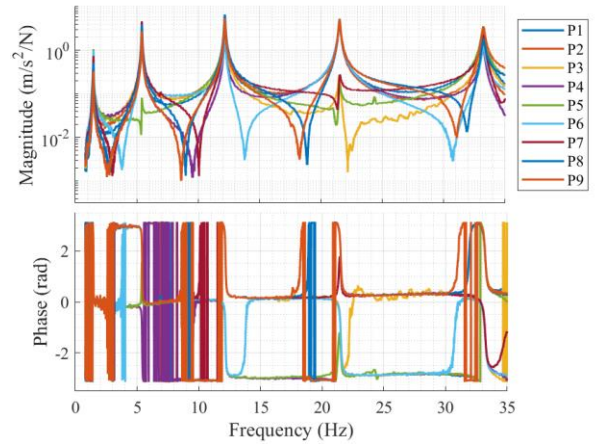


**Figure 3:** Experimental FRFs.

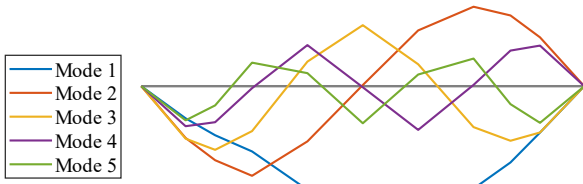


**Figure 4:** Identified mode shapes.

#### 4.1 Physical model estimation

The algorithm presented in Section 3 is applied to the identified modal model. As mentioned before, 9 DOFs have been monitored to obtain that model, so the estimated physical matrices are of dimension 9, and couple the dynamic behaviour only of those 9 DOFs of the structure. Since 5 modes are used to estimate the physical model, it is an incomplete model and the system of equations in Eq. 9 has infinite solutions. Moreover, after assembling it, a total of 208 equations are obtained to solve for the  $3 \cdot 9^2 = 243$  unknowns. Due to this, the optimization procedure needs also to be applied to minimise the objective function in Eq. 10.

After applying the whole procedure, a set of three physical matrices are obtained. They are not shown in this manuscript for brevity, and, *per se*, they lack interest because their terms do not have any meaning by themselves. Instead, the FRFs associated to the estimated physical model are compared with the experimental

ones used to identify the modal model in Figure 5, where only the point 7 is plotted for clarity, but similar conclusions can be drawn from the other 8 FRFs. As can be seen, there exist a high correspondence between both sets of FRFs, demonstrating that the estimated physical model accurately represents the desired dynamic behaviour in the range of interest. In addition, Table 2 summarises the natural frequencies and damping ratios of the nine computable modes of the estimated physical model compared to the original five identified ones. As mentioned above, there are other 4 exogenous modes that belong to the physical model but that do not have any impact on the dynamic response in the frequency range of interest, since they all have a damping ratio above 50%.

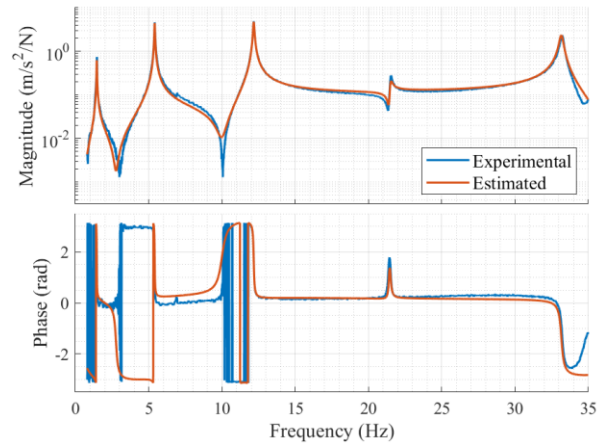


**Figure 5:** Experimental FRF vs. computed FRF by means of the estimated physical model (point 7)

Mode	Natural frequencies [Hz]			Damping Ratios [%]		
	Original	Estimated	Error [%]	Original	Estimated	Error [%]
1	1.46	1.46	$1.05 \cdot 10^{-4}$	0.81	0.81	$8.40 \cdot 10^{-2}$
2	5.41	5.41	$1.74 \cdot 10^{-6}$	0.35	0.35	$5.07 \cdot 10^{-3}$
3	12.17	12.17	$3.44 \cdot 10^{-7}$	0.33	0.33	$7.81 \cdot 10^{-4}$
4	21.49	21.49	$6.02 \cdot 10^{-8}$	0.37	0.37	$5.57 \cdot 10^{-4}$
5	33.17	33.17	$1.96 \cdot 10^{-8}$	0.39	0.93	$4.12 \cdot 10^{-5}$

**Table 2:** Comparison between the identified modes and the ones provided by the estimated physical model.

To show the usefulness of the estimated physical model, the next sections are devoted to applying some structural modifications to both the real structure and the estimated physical model.

## 4.2 Mass modification

First, a certain amount of mass is added on the real structure. To make sure that the modification can also be included in the estimated physical model, the point on which the mass is added must be one of the monitored DOFs. In this case, an additional mass of 5.97 kg is placed on point 5 (at  $L/2$ ) and the FRFs are experimentally estimated in this situation by applying the same procedure as before.

The same amount of mass is now added to the estimated physical model. To do so, the mass value is simply summed to the appropriate diagonal position of the mass matrix. In this case, the value 5.97 kg is summed to the fifth diagonal position of the mass matrix since the mass is placed on the fifth DOF. Then, the FRFs are computed by using the modified physical model compared with the experimental ones. Figure 6 shows the comparison of both modified FRFs (experimental and computational) together with the unmodified one.

As can be seen, in general, there is a high correspondence between the modified dynamics predicted by the estimated physical model and the actual behaviour. Some differences can be found in the surroundings of the first and third peaks, which may be due to the estimation errors committed during the modal identification procedure. Finally, it is worth noting that, since the mass is placed on  $L/2$ , which is a vibration node for modes 2 and 4 (see Figure 4), the second and fourth peaks are barely affected in both FRFs.

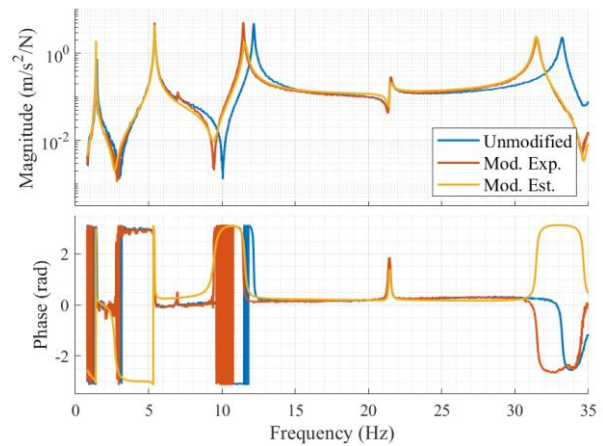


Figure 6: FRFs comparison of the model with modified mass (point 7)

## 4.3 SDOF addition

Finally, a single-degree-of-freedom system, composed by a 4.70 kg mass hanged from a 728 N/m spring is installed on the beam. Its properties confer it a natural frequency of 1.96 Hz (as an isolated system). The system could be interpreted as a tuned mass damped (TMD) if its natural frequency was closer to and under a natural frequency of the structure. It would also need to have a higher amount of damping to dissipate energy and reduce the overall response level. In this case, the only damping sources are the one associated to the spring deformation and the air friction, which are both very reduced. The ensemble is placed on the middle point of the beam (point 5), close to the maximum modal coordinate of the first mode, which is a proper location if a TMD would be installed on the beam to reduce the contribution of that mode to its dynamic response. Note that, again, due to being placed on the point at  $L/2$ , the second and fourth peaks of the FRFs should not be affected by this modification.

Similarly to the previous scenario, once the SDOF system is installed on the beam, the experimental FRFs are estimated by means of the same experimental modal analysis

procedure. A model of the same system is also applied to the estimated physical model and the corresponding FRFs are calculated to be compared with the experimental ones. The SDOF system is added by creating a new DOF in the physical model, which is equivalent to add a new row and column to the estimated physical matrices, leading to a total of 10 rows and columns. The moving mass is directly placed on the new diagonal position of the mass matrix. The stiffness is accounted for as the 2x2 matrix shown in Eq. 12, where  $\delta k$  stands for the spring stiffness. The elements of that matrix are added to the four positions of the stiffness matrix in the rows and columns 5 and 10, i.e., the positions  $(i, j)$  with  $i$  and  $j$  equalling 5 or 10. Finally, as mentioned before, no damping is to the model of this SDOF system for being very reduced in comparison to the structural damping, so the added column and row are full of zeroes.

$$\Delta K = \delta k \begin{bmatrix} 1 & -1 \\ -1 & 1 \end{bmatrix} \quad (12)$$

Once the FRFs are experimentally estimated and calculated by means of the modified physical model, they are plotted together in Figure 7, which shows the FRFs associated to point 7 in the three scenarios (experimental modified, modified estimated physical model and experimental unmodified). The frequency axis has been zoomed to emphasize the effect the SDOF system has around its natural frequency. As can be seen, there is again a high correspondence between the dynamic behaviour of the real structure and the prediction made by the estimated physical model, except for slight errors in some peaks, mainly caused by modal identification errors prior to estimating the physical model. Finally, the second peak is barely affected by this addition, as expected.

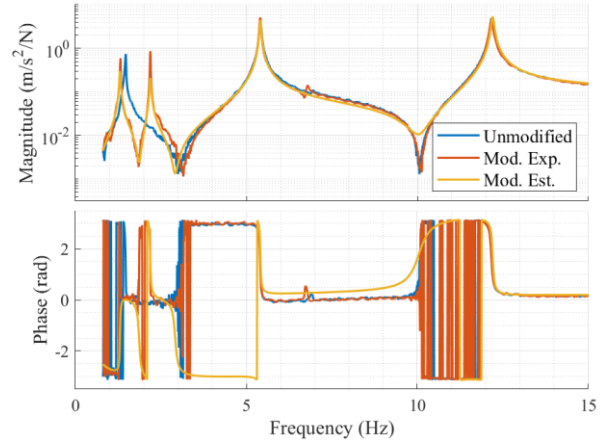


**Figure 7:** FRFs comparison of the model with the added SDOF system (point 7)

## 5 CONCLUSIONS

A method has been developed to obtain a physical model composed of three matrices (mass, stiffness and damping) that reproduces the same dynamic behaviour than an experimentally estimated modal model of a certain structure. The modal model must be composed of the natural frequencies and damping ratios of the structure, as well as the scaled mode shapes in order to apply the methodology.

The estimated physical matrices, which have the same dimension as the number of DOFs monitored to identify the modal model, can be used to simulate the response of the structure to a variety of loads and to perform different types of structural modifications, as shown. Mass modifications can be performed by adding a certain amount of mass to the corresponding diagonal element of the mass matrix, whereas a SDOF system can be included by also assembling its stiffness and damping 2x2 matrices to the unmodified matrices, making them increase by one DOF. In all cases, the predictions made by the estimated physical model are accurate enough for the engineering purposes intended for the physical model.

## ACKNOWLEDGEMENTS

This research was partially founded by the Ministerio de Economía y Competitividad, Spanish Government, through the research project number RTI2018-098425 and by the Ministerio de Educación, Cultura y Deporte, Spanish Government, through the predoctoral grant number FPU16/01339.

## REFERENCES

- [1] A. Berman, W. G. Flannelly, *Theory of incomplete models of dynamic structures*, AIAA Journal 9 (8) (1971) 1481-1487. DOI: [10.2514/3.49950](https://doi.org/10.2514/3.49950)
- [2] A. Berman, *System identification of structural dynamic models. Theoretical and practical bounds*, in: 25<sup>th</sup> Structures, Structural Dynamics and Materials Conference, American Institute of Aeronautics and Astronautics, Reston, Virginia, 1984. DOI: [10.2514/6.1984-929](https://doi.org/10.2514/6.1984-929)
- [3] M. Link, *Theory of a method for identifying incomplete system matrices from vibration test data*, Z. Flugwiss. Weltraumforsch. 9 (2) (1985) 76-82.
- [4] H.-P. Chen, N. Bicanic, *Assessment of damage in continuum structures based on incomplete modal information*, Computers & Structures 74 (5) (2000) 559-570. DOI: [10.1016/S0045-7949\(99\)00062-0](https://doi.org/10.1016/S0045-7949(99)00062-0)
- [5] S. R. Ibrahim, *Dynamic modeling of structures from measured complex modes*. AIAA Journal 21 (6) (1982) 898-901. DOI: [10.2514/3.8168](https://doi.org/10.2514/3.8168)
- [6] T. Kasai, M. Link, *Identification of non-proportional modal damping matrix and real normal modes*. Mechanical Systems and Signal Processing 16 (6) (2002) 921-934. DOI: [10.1006/mssp.2001.1478](https://doi.org/10.1006/mssp.2001.1478)
- [7] A. Srikantha Phani, J. Woodhouse, *Viscous damping identification in linear vibration*. Journal of Sound and Vibration 303 (3-5) (2007) 475-500. DOI: [10.1016/j.jsv.2006.12.031](https://doi.org/10.1016/j.jsv.2006.12.031)
- [8] S. Adhikari, A. Srikantha Phani, *Experimental identification of generalized proportional viscous damping matrix*, Journal of Vibration and Acoustics 131 (1) (2009) 011008. DOI: [10.1115/1.2980400](https://doi.org/10.1115/1.2980400)
- [9] M. Prandina, J. E. Mottershead, E. Bonisoli, *An assessment of damping identification methods*, Journal of Sound and Vibration 323 (3-5) (2009) 662-676. DOI: [10.1016/j.jsv.2009.01.022](https://doi.org/10.1016/j.jsv.2009.01.022)
- [10] A. Bakric, J. Hogsberg, *Identification of damping and complex modes in structural vibrations*, Journal of Sound and Vibration 431 (2018) 367-389. DOI: [10.1016/j.jsv.2018.05.048](https://doi.org/10.1016/j.jsv.2018.05.048)
- [11] D. J. Ewins, *Modal testing: Theory, practices and applications*, 2<sup>nd</sup> Edition, Research Studies Press (Hertfordshire, United Kingdom), 2000

# APPLICATION OF SEMI-ANALYTICAL METHODS TO HYBRID SIMULATION OF BEAM-LIKE STRUCTURES WITH VIBRATION ABSORBERS UNDER MOVING INERTIAL LOADS

José Ramírez-Senent\*, Jaime H. García-Palacios†, Iván M. Díaz† and Carlos Zanuy†

\* Escuela Técnica Superior de Ingenieros de Caminos, Canales y Puertos  
Universidad Politécnica de Madrid  
28040 Madrid, Spain  
e-mail: [jose.ramirez.senent@alumnos.upm.es](mailto:jose.ramirez.senent@alumnos.upm.es)  
ORCID: 0000-0002-1332-8182

† Escuela Técnica Superior de Ingenieros de Caminos, Canales y Puertos  
Universidad Politécnica de Madrid  
28040 Madrid, Spain

**Abstract.** In real-time hybrid simulation of structural systems, the parts of the structure under test whose behavior is not sufficiently well understood are actually tested, while the remainder of the structure is numerically simulated, very frequently via finite element models. Hybrid test proceeds as both domains, physical and numerical, exchange information in terms of kinematic and dynamic magnitudes. Consequently, the reliability of the hybrid solution strongly depends on the accuracy of the numerical model. In this paper, the use of semi-analytical methods in hybrid simulation or purely numerical simulation of beam-like structures subjected to inertial moving loads, equipped with vibration control devices, is studied and its effectiveness is assessed by means of numerical simulations. These solution methods yield better results than the classical approach involving proportional mass lumping in the load neighbor nodes. Simulation results indicate that the implementation of the suggested technique is feasible with common, widely available testing equipment. The proposed approach might be of interest to obtain quick and accurate qualitative estimates of the behavior of civil engineering structures, with passive, semi-active or active vibration control devices, subjected to moving loads such as automobiles, trains or humans.

**Key words:** Real-time Hybrid Simulation, Vibration Control Devices, Inertial Moving Load, Semi-analytical Methods, Active Vibration Control.

## 1 INTRODUCTION

Hybrid simulation (HS) has proven to be an effective approach to obtain reliable estimates of the behavior of complex structural systems [1]. In HS tests set-up the parts of the structure whose behavior is well understood are simulated numerically whereas the remainder of the system is tested experimentally. An example of a typical HS test set-up is shown in Figure 1, in which the test subject is a vibration

control device (VCD). The time evolution of the numerical subsystem is estimated by means of a numerical integration scheme, very frequently based on a finite element model, which makes use of the outputs of the experimental subsystem (for example forces). The outputs of the numerical scheme (for example displacements) are then often imposed on the physical structure by means

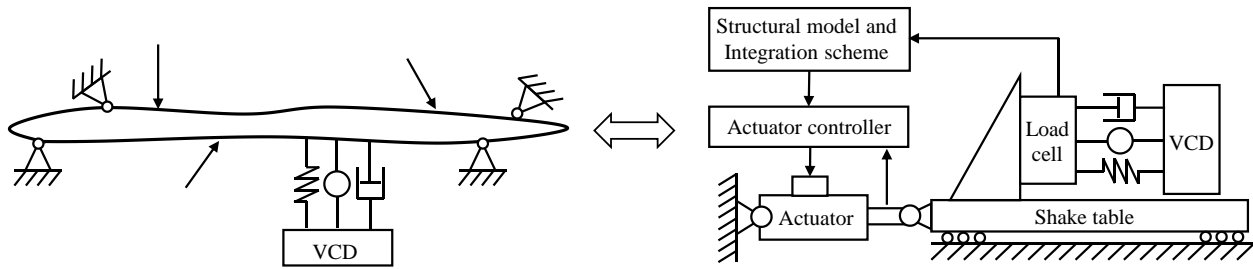


**Figure 1:** Scheme of hybrid simulation set-up for an active VCD.

of hydraulic servoactuators, governed by a sophisticated control system, at each time step. The hybrid test proceeds with this exchange of information between domains at each time step. Therefore, the goodness of the results of the HS strongly depends on the one hand, on the accuracy of the employed numerical integration scheme and on the accuracy of the kinematic magnitudes achieved by the servoactuator control system on the other.

When dealing with moving inertial loads problems, such as those found in railways or automobile traffic, the classical procedure of dividing and lumping the moving mass between the adjacent nodes may not yield accurate results for moderate to high load velocities, unless special methods are used [2,3]. The semi-analytical procedure may represent an appropriate technique to obtain accurate solutions for simple structural problems.

In this paper, the methodology for the application of semi-analytical integration techniques to the purely numerical simulation of beam-like structures, equipped with VCDs, subjected to inertial moving loads is studied. In addition, the feasibility of the realization of real-time hybrid tests employing the semi-analytical approach is assessed by means of numerical simulations. The HS approach allows to obtain accurate, qualitative results, which reflect the true dynamic behavior of the VCD. These results may assist the researchers in determining which vibration control strategy

should be applied to a particular moving load problem, even for multiple-input-multiple-output vibration control schemes.

The remainder of this paper is organized as follows. Section 2 provides a detailed description of the employed model of the system: subsection 2.1 deals with the semi-analytical integration procedure employed to estimate the response of the structure, subsection 2.2 explains the model implemented for the hydraulic servoactuation system used to simulate the hybrid test, subsection 2.3 covers the actuator control system and subsection 2.4 describes the active VCD employed in the simulations. Simulation results and their discussion, for both the uncontrolled and the controlled structure, are addressed in section 3. Finally, section 4 outlines the conclusions and the issues to consider for a successful implementation of the proposed procedure.

## 2 SYSTEM MODELING

In this section the model implemented to assess the application of semi-analytical techniques to beam-like structures with VCDs under the action of moving inertial loads is fully described.

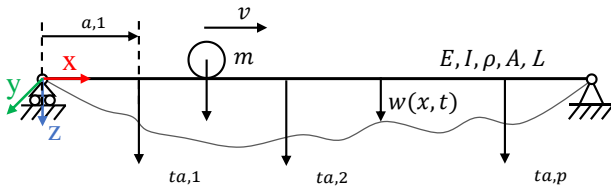
### 2.1 Semi-analytical model for the moving inertial load

Figure 2 depicts the scheme of a simply supported beam structure subjected to a moving inertial load and equipped with several

VCDs. The corresponding equation of motion is:

$$EI \frac{\partial^4 w(x, t)}{\partial x^4} + \rho A \frac{\partial}{\partial t} \frac{\partial w(x, t)}{\partial t} + cA \frac{\partial w(x, t)}{\partial t} = \delta(x - vt) \left[ P - m \frac{w(vt, t)}{dt^2} \right] + \sum_{p=1}^{N_a} \delta(x - x_{a,p}) F_{ta,p}, \quad (1)$$

where  $w$  is the beam deflection,  $L$  is beam length,  $E, I, \rho$  and  $A$  are, respectively, the elastic modulus, the area moment of inertia, the mass density and the cross section area of the beam,  $c$  is the damping per unit volume,  $P$  represents the moving load, and  $m$  and  $v$  are the moving mass and its velocity. Moreover,  $\delta$  stands for Dirac's delta,  $p = 1, \dots, N_a$  where  $N_a$  is the number of vibration absorption devices,  $x_{a,p}$  are the axial coordinates of VCD locations and  $F_{ta,p}(t)$  is the force transmitted by each VCD to the beam structure.



**Figure 2:** Simply supported beam subjected to a moving inertial load.

Equation (1) must be completed with the boundary conditions corresponding to a simply supported beam:

$$w(0, t) = w(L, t) = \frac{\partial^2 w(x, t)}{\partial x^2} \Big|_{x=0} = \frac{\partial^2 w(x, t)}{\partial x^2} \Big|_{x=L} = 0, \quad (2)$$

and the zero initial conditions:

$$w(x, 0) = \frac{\partial w(x, t)}{\partial t} \Big|_{t=0} = 0. \quad (3)$$

Below, the procedure explained in [2] will be followed. By expanding the beam deflection as a sine Fourier series the next relationship is obtained:

$$w(x, t) = \frac{2}{L} \sum_{j=1}^{\infty} V(j, t) \sin\left(\frac{j\pi x}{L}\right), \quad (4)$$

which satisfies the simply supported boundary conditions and where  $V(j, t)$  is the  $j$ -th Fourier coefficient at instant  $t$  which can be calculated by means of:

$$V(j, t) = \int_0^L w(x, t) \sin\left(\frac{j\pi x}{L}\right) dx. \quad (5)$$

Now, multiplying both sides of Eq. (1) by  $\sin(j\pi x/L)$ , and integrating over the beam length, results in the following system of differential equations, for  $j = 1, \dots, \infty$ :

$$\rho A \ddot{V}(j, t) + cA \dot{V}(j, t) + EI \frac{j^4 \pi^4}{L^4} V(j, t) = \left[ P - m \frac{w(vt, t)}{dt^2} \right] \sin\left(\frac{j\pi x}{L}\right) + \sum_{p=1}^{N_a} F_{ta,p} \sin\left(\frac{j\pi x_{a,p}}{L}\right). \quad (6)$$

The acceleration of the point mass can be obtained by differentiating Eq. (4) twice with respect to time and particularizing the position at  $x = vt$  expressed as:

$$\frac{d^2}{dt^2} \frac{w(vt, t)}{L} = \frac{2}{L} \sum_{k=1}^{\infty} \left[ \ddot{V}(k, t) \sin\left(\frac{k\pi vt}{L}\right) + \frac{2k\pi v}{L} \dot{V}(k, t) \cos\left(\frac{k\pi x}{L}\right) - \frac{k^2 \pi^2 v}{L} V(k, t) \sin\left(\frac{k\pi vt}{L}\right) \right], \quad (7)$$

which substituted in Eq. (5) yields:

$$\begin{aligned}
 \dot{V}(j, t) + \alpha \sum_{k=1}^{\infty} \dot{V}(k, t) \sin\left(\frac{j\pi vt}{L}\right) \sin\left(\frac{k\pi vt}{L}\right) & \quad (8) \\
 + \gamma \dot{V}(j, t) \\
 + 2\alpha \sum_{k=1}^{\infty} \frac{k\pi v}{L} \dot{V}(k, t) \sin\left(\frac{j\pi vt}{L}\right) \cos\left(\frac{k\pi vt}{L}\right) \\
 + EI \frac{j^4 \pi^4}{L^4} V(j, t) \\
 - \alpha \sum_{k=1}^{\infty} \frac{k^2 \pi^2 v}{L} V(k, t) \sin\left(\frac{j\pi vt}{L}\right) \sin\left(\frac{k\pi vt}{L}\right) \\
 = \frac{1}{\rho A} \sin\left(\frac{j\pi vt}{L}\right) \\
 + \frac{1}{\rho A} \sum_{p=1}^{N_a} F_{,p}(t) \sin\left(\frac{j\pi x_{a,p}}{L}\right),
 \end{aligned}$$

where  $\alpha = 2m/\rho AL$  and  $\gamma = c/\rho$ . The system shown in Eq. (7) can be arranged as follows:

$$[M]\{\ddot{V}\} + [C]\{\dot{V}\} + [K]\{V\} = \{F\} \quad (9)$$

where:

$$\begin{aligned}
 M_{jk} &= \delta_{jk} + \alpha \sin\left(\frac{j\pi vt}{L}\right) \sin\left(\frac{k\pi vt}{L}\right) & (10) \\
 C_{jk} &= \gamma \delta_{jk} + 2\alpha \frac{k\pi v}{L} \sin\left(\frac{j\pi vt}{L}\right) \cos\left(\frac{k\pi vt}{L}\right) \\
 K_{jk} &= EI \frac{j^4 \pi^4}{L^4} \delta_{jk} \\
 &- \alpha \frac{k^2 \pi^2 v}{L} \sin\left(\frac{j\pi vt}{L}\right) \sin\left(\frac{k\pi vt}{L}\right) \\
 &= \frac{1}{\rho A} \sin\left(\frac{j\pi vt}{L}\right) \\
 &+ \frac{1}{\rho A} \sum_{p=1}^{N_a} F_{,p}(t) \sin\left(\frac{j\pi x_{a,p}}{L}\right),
 \end{aligned}$$

in which  $\delta_{jk}$  represents Kronecker's delta.

In the case under study, a single VCD located at the midspan of the beam is considered; therefore,  $p = 1$  and  $x_{a,1} = L/2$ .

The displacement of any point of the beam can be calculated as a function of time by means of Eq. (5), whereas the velocity and the displacement may be obtained according to:

$$\frac{\partial w(x, t)}{\partial t} = \frac{2}{L} \sum_{j=1}^{\infty} \dot{V}(j, t) \sin\left(\frac{j\pi x}{L}\right), \quad (11)$$

$$\frac{\partial^2 w(x, t)}{\partial t^2} = \frac{2}{L} \sum_{j=1}^{\infty} \ddot{V}(j, t) \sin\left(\frac{j\pi x}{L}\right). \quad (12)$$

A convergence study has been conducted to determine the number of terms to be accounted for in the analysis. Figures 3 and 4 show the outcome of this study in terms of the displacement of the midspan point and the RMS error between number of terms, respectively; as it can be appreciated, the error diminishes with the number of considered terms. In this work 18 terms have been considered.

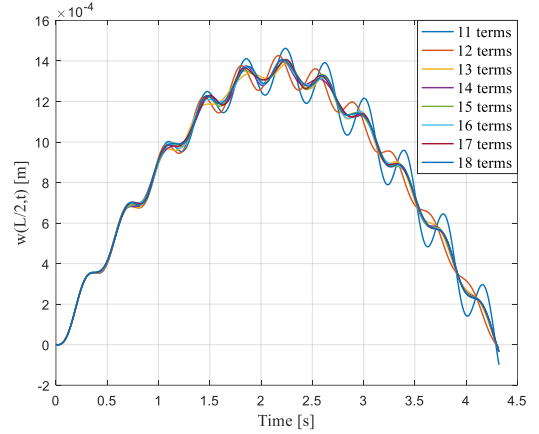


**Figure 3:** Displacement of the midspan point for different considered terms.

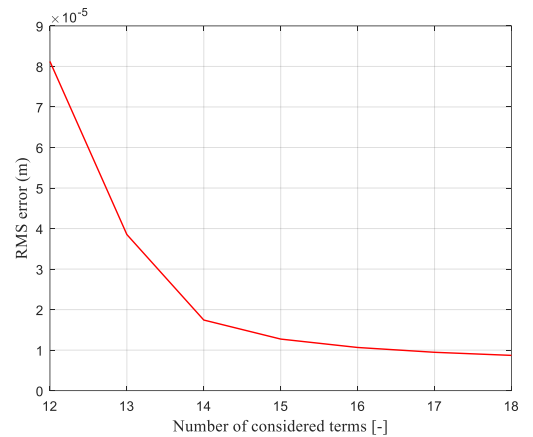


**Figure 4:** RMS error for different numbers of terms.

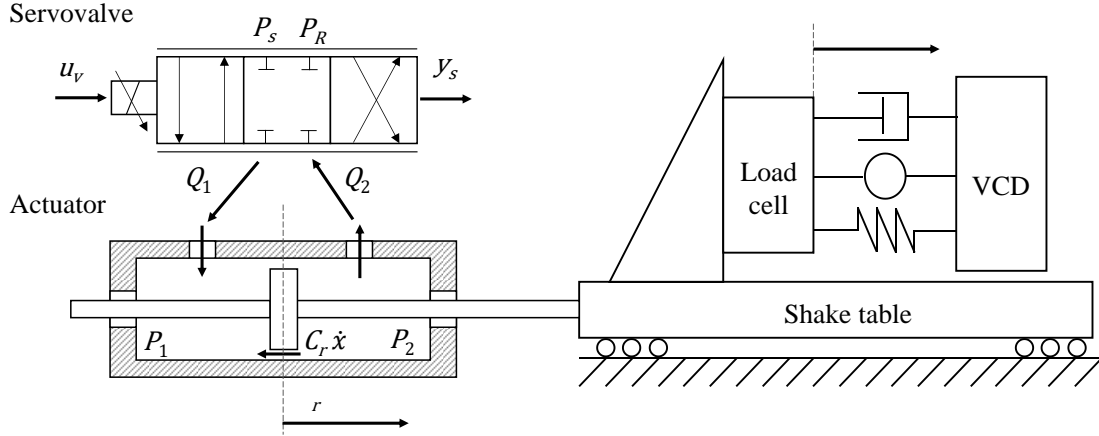


Figure 5. Servoactuator schematic, modeled variables and sign criterion.

## 2.2 Hydraulic servoactuator model

Figure 5 displays a scheme of the hydraulic servoactuator simulated in this work, along with the relevant variables and the sign criteria employed.

The servo valve spool motion has been modeled by means of the following first order system:

$$C_s u_v = \tau_s \dot{y}_s + y_s, \quad (13)$$

in which  $u_v$  is the input voltage to the servo valve,  $y_s$  is the spool position,  $C_s$  is the spool static gain and  $\tau_s$  is the time constant of the system.

The flow rates through the servo valve ports have been calculated according to the flow-rate equations for a symmetrical servo valve with matched orifices and critically lapped spool [4]:

$$Q = \begin{cases} C_d K_s y_s \operatorname{sgn}(P_s - P_1) \sqrt{2|P_s - P_1|/\rho_o}; & y_s \geq 0 \\ C_d K_s y_s \operatorname{sgn}(P_1 - P_s) \sqrt{2|P_1 - P_s|/\rho_o}; & y_s < 0 \end{cases} \quad (14)$$

$$Q = \begin{cases} C_d K_s y_s \operatorname{sgn}(P_2 - P_R) \sqrt{2|P_2 - P_R|/\rho_o}; & y_s \geq 0 \\ C_d K_s y_s \operatorname{sgn}(P_s - P_2) \sqrt{2|P_s - P_2|/\rho_o}; & y_s < 0 \end{cases} \quad (15)$$

where  $C_d$  represents the orifices discharge coefficient,  $K_s$  is the fluid passage area to spool position ratio,  $P_s$  and  $P_R$  are the pressures at

the inlet and outlet ports of the servoactuator's manifold,  $P_i$ ,  $Q_i$  are the pressures and flow rates associated to servoactuator chambers and  $\rho_o$  denotes oil density.

The evolution of the pressures in the chambers of the actuator has been obtained by applying the Continuity Equation to each servoactuator compartment [4]:

$$(v_{o1} + A_w x_p) \dot{P}_1 / \beta_1 + A_w \dot{x} = Q_1, \quad (16)$$

$$(v_{o2} - A_w x_p) \dot{P}_2 / \beta_2 - A_w \dot{x} = -Q_2, \quad (17)$$

where  $A_w$  is the effective area of the piston,  $v_{oi}$  are the initial volumes of the actuator chambers, which are calculated from the value of  $A_w$  and the cylinder stroke,  $s$ . Furthermore,  $\beta_i$  are the Bulk moduli of each chamber. In this work, leakage flows between actuator chambers and from chambers to their respective bearings have been neglected.

The acceleration of the actuator rod is governed by Newton's Second Law:

$$(m_r + m_s) \ddot{x}_r = (P_1 - P_2) A_w - C_r \dot{x}_r + \dots, \quad (18)$$

in which  $m_r$  and  $m_s$  represent respectively rod and VCD stator masses,  $\ddot{x}_r$  and  $\dot{x}_r$  are actuator rod acceleration and displacement,  $C_r$  stands for actuator viscous damping coefficient and

$F$  is the force transmitted by the VCD to rod-stator assembly.

By linearizing Eqs (13), (14), (15), (16), (17) and (18) around the mid-stroke equilibrium point and considering a completely symmetric actuator, the following state-space representation of the actuator system is obtained [5]:

$$\begin{Bmatrix} \dot{x} \\ \dot{\Delta P} \\ \dot{y}_s \end{Bmatrix} = [A] \begin{Bmatrix} x \\ \Delta P \\ y_s \end{Bmatrix} + [B] \begin{Bmatrix} u_v \\ F_p \end{Bmatrix}, \quad (19)$$

$$\begin{Bmatrix} \dot{x} \\ \dot{\Delta P} \\ \dot{y}_s \end{Bmatrix} = [C] \begin{Bmatrix} x \\ \Delta P \\ y_s \end{Bmatrix} + [D] \begin{Bmatrix} u_v \\ F_p \end{Bmatrix}. \quad (20)$$

As it can be noticed, the selected state-space variables have been the displacement and velocity of the rod, the difference of pressures across actuator chambers,  $\Delta P$ , and the spool displacement.

$$\begin{aligned} [A] &= \begin{bmatrix} 0 & 1 & 0 & 0 \\ 0 & -\frac{C}{m} & \frac{A_w}{m} & 0 \\ 0 & -\frac{2A_w\beta}{v_0} & 0 & \frac{2C_dK_s\beta\sqrt{\frac{P_s}{\rho}}}{v_0} \\ 0 & 0 & 0 & -\frac{1}{\tau_s} \end{bmatrix} \\ [B] &= \begin{bmatrix} 0 & \frac{1}{m_p} \\ 0 & 0 \\ \frac{C_s}{\tau_s} & 0 \end{bmatrix}, \\ [C] &= \begin{bmatrix} 1 & 0 & 0 & 0 \\ 0 & 1 & 0 & 0 \\ 0 & -\frac{C_r}{m_t} & \frac{A_w}{m_t} & 0 \end{bmatrix} \text{ and} \\ [D] &= \begin{bmatrix} 0 & 0 \\ 0 & 0 \\ 0 & \frac{1}{m} \end{bmatrix}. \end{aligned} \quad (21)$$

where  $m_t = m_r + m_s$ . Subindexes in  $\beta$  and  $v_0$  have been omitted in matrices in Eq. (21) because of the actuator symmetry assumption. Given the fact that the expected displacements of the actuator are small in comparison with its

stroke (see Table 1), the linearized version has been employed in the simulations.

So as to determine the size of the actuator, a campaign of simulations of the complete system may be run. The force rating of the actuator can be estimated by means of the acceleration values (Eq. (12)) multiplied by the total moving mass and accounting for the maximum force that the VCD can exert. The stroke of the actuator is estimated by Eq. (4). Finally, the flow rate, and consequently, the servovalve flow rate can be roughly estimated by Eq. (11). For an accurate sizing, of the servoactuation system a complete campaign of simulations, accounting for all the interest loading cases and target structures, needs to be carried out. In this work, a standard 25 kN actuator with a stroke of 150 mm and a servovalve with a nominal flow rate of 63 liters per minute with a pressure drop of 3.5 MPa per land have been considered. These represent a low cost solution, readily available in the market with which a wide range of tests can be performed.

The values of the servovalve and actuator parameters employed in the numerical simulations are shown in Table 1. These have been obtained respectively from [6] and [7].

### 2.3 Servoactuator controller model

A Three Variable Control scheme (TVC) has been implemented to ensure that the kinematic references output by the integration scheme are accurately tracked simultaneously (displacement, velocity and acceleration) [8]. The control order calculated by the TVC can be cast as:

$$\begin{aligned} u_v &= K_d(x_{r,ref} - x_r) + K_v(\dot{x}_{r,ref} - \dot{x}_r) + \\ &K_a(\ddot{x}_{r,ref} - \ddot{x}_r), \end{aligned} \quad (22)$$

where the subindex *ref* denotes the reference value and  $K_d$ ,  $K_v$  and  $K_a$  are respectively the displacement, velocity and acceleration control gains. The kinematic references for the

actuator have been calculated making use of Eqs. (4), (11) and (12) particularized to the midspan of the beam structure, where the VCD is assumed to be installed. The displacement can be sensed by means of an embedded displacement transducer, whereas the acceleration is provided by an accelerometer installed on the rod. Velocity values may be obtained by fusion of displacement and accelerometer transducers data through a Kalman filter [9]. However, in this work it has been considered that a direct measurement of the velocity is available to the controller. Table 1 shows the values of the control gains employed in the numerical simulations. These have been obtained by means of a trial and error procedure until satisfactory tracking of the reference waveforms has been obtained without compromising overall system stability.

## 2.4 Vibration absorber device model

An active vibration absorber has been considered as VCD in this study. The selected vibration control algorithm is the Direct Velocity Feedback Control (DVFC). The VCD has been assumed to be ideal, that is, with negligible internal dynamics and capable of reproducing instantaneously the target force calculated by the VCD controller [10]. Therefore, the force transmitted by the VCD to the actuator has been modeled by means of:

$$= -C_{DVFC}\dot{x}_r, \quad (23)$$

where  $C_{DVFC}$  is the control gain of the active VCD. Again, it has been assumed that a direct measurement of the velocity of the actuator rod is available to the control system of the VCD.

Table 1 shows the value of the VCD control gain employed in the numerical simulations.

## 3 SIMULATIONS RESULTS

The numerical simulation results obtained

with the model explained previously are presented in this section. A fourth order Runge-Kutta integration scheme with a step time  $\Delta t = 1e-4$  s has been employed for all the simulations.

First off, the beam structure subjected to an inertial moving load (5000 kg) traversing it at a speed  $v = 25$  km/h, without the VCD installed, has been simulated. Figure 6 displays the obtained displacement at the midspan point for both the simulated structure and for the hybrid test simulation. The error between the structure simulation and the simulated hybrid test is also presented. It is worth noting that this error coincides with the displacement tracking error achieved by the actuator control system. Figure 7 offers similar data for velocity at the midspan point and Figure 8 for acceleration. As it can be appreciated, the difference between the structural simulation and the hybrid experiment outcomes is small and remains within reasonable limits for the complete simulation timespan. This is due to the low error in displacement, velocity and acceleration tracking achieved by the TVC algorithm.

Secondly, the beam structure traversed by the same inertial moving load and equipped with a VCD has been simulated in the same scenarios: (i) the structure with the VCD and (ii) the hybrid experiment accounting for servoactuator system dynamics and its controller. As in the previous simulation case, the hybrid experiment yields results very similar to the ones obtained by the structure with VCD simulation due to the action of the TVC which successfully compensates for the dynamics of the actuator system.

As expected, the effect of the VCD is to effectively attenuate the maximum acceleration experienced by the midspan point by approximately a 43 %, see Figures (8) and (11). This attenuation even is more noticeable after the initial section of the simulation where an attenuation of around 83% is attained. In

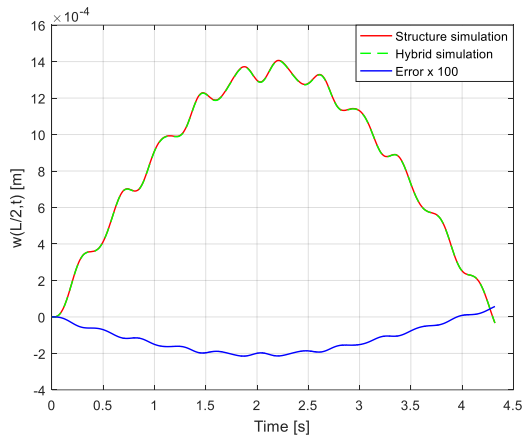


**Figure 6:** Displacement of midpoint without VSD

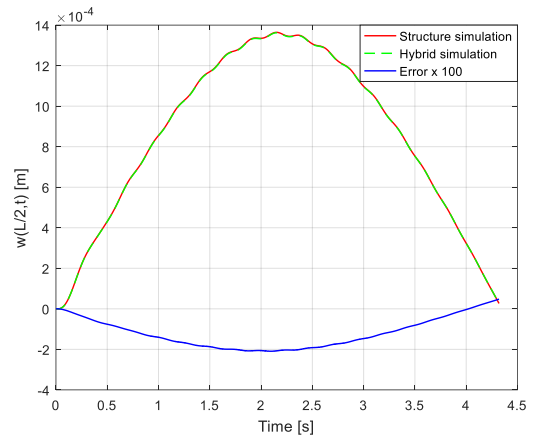


**Figure 9:** Displacement of the midpoint with VCD.

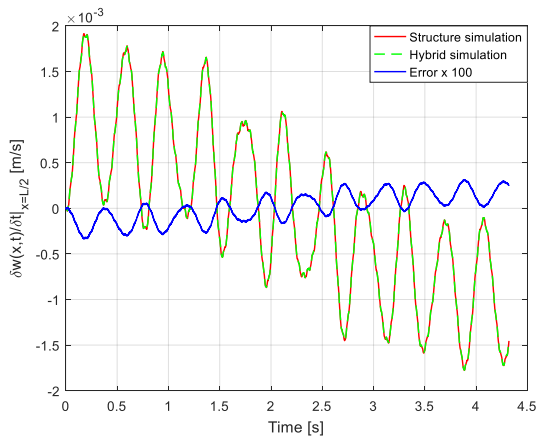


**Figure 7:** Velocity of the midspan point without VCD.

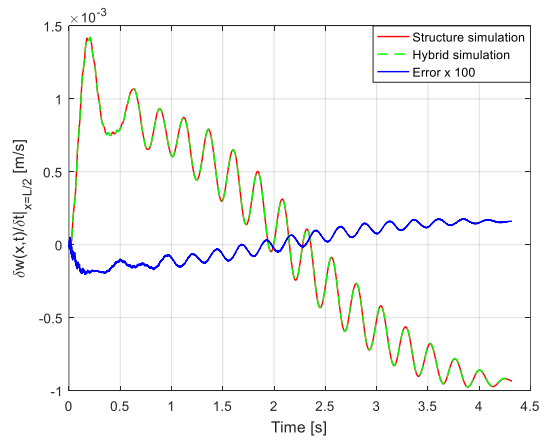


**Figure 10:** Velocity of the midpoint with VCD.

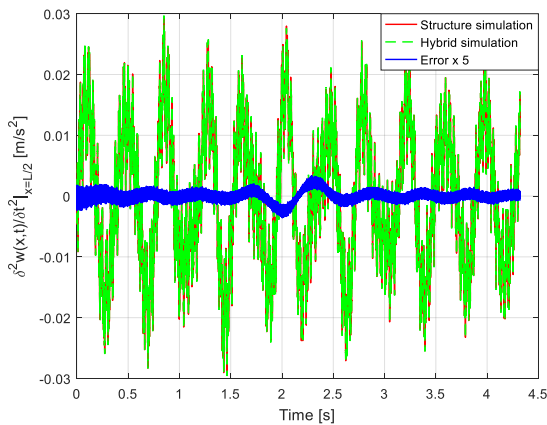


**Figure 8:** Acceleration of the midpoint without VCD.

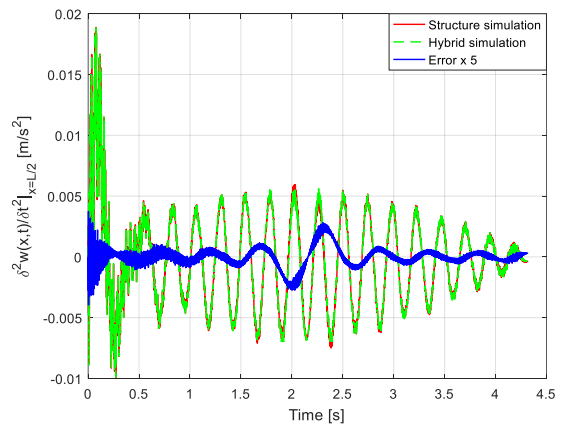


**Figure 11:** Acceleration of the midspan point with VCD.

any case, simulation results show that accurate predictions of the behavior of the structure equipped with the VCD system can be obtained by means of the HS procedure, provided that the semi-analytical integration scheme outputs correct results.

Parameter	Value	Parameter	Value
$A$ [m <sup>2</sup> ]	1.20e00	$m$ [kg]	5.00e03
$A_w$ [m <sup>2</sup> ]	1.20e-03	$m_r$ [kg]	7.96e00
$\beta$ [Pa]	1.00e09	$m_s$ [kg]	8.00e02
$c$ [Nsm <sup>-4</sup> ]	9.36e02	$L$ [m]	3.00e01
$C_d$ [-]	6.11e-01	[N]	4.91e04
$C_{DVFC}$ [Nm <sup>-1</sup> s]	1.00e06	$P_S$ [Pa]	6 2.80e07
$C_r$ [Nsm <sup>-1</sup> ]	5.00e01	$P_R$ [Pa]	0
$C_s$ [mV <sup>-1</sup> ]	1.80e-04	$\rho$ [kgm <sup>-3</sup> ]	7.85e03
$\Delta t$ [s]	1.00e-04	$\rho_o$ [kgm <sup>-3</sup> ]	8.50e02
$EI$ [Nm <sup>2</sup> ]	2.00e10	$s$ [m]	1.50e-01
$K_s$ [m]	1.20e-04	$\tau_s$ [s]	1.00e-02
$K_a$ [Vm <sup>-1</sup> s <sup>2</sup> ]	5.00e-02	$v$ [ms <sup>-1</sup> ]	6.94e00
$K_d$ [Vm <sup>-1</sup> ]	5.00e-01	$v_0$ [m <sup>3</sup> ]	8.69e-05
$K_v$ [Vm <sup>-1</sup> s]	5.00e00	$l_1$ [m]	1.50e01

**Table 1:** Values of the parameters employed in numerical simulations.

## 4 CONCLUSIONS

In this paper a methodology for the hybrid simulation of beam-like structures subjected to moving inertial loads and equipped with VCDs has been presented. The proposed approach may also be used for purely numerical simulations. In the hybrid case, the structure and the moving load are simulated numerically whereas the VCD is tested experimentally by means of a hydraulic servoactuator. The feasibility of the suggested procedure has been proved by means of numerical simulations.

The integration scheme used for the structure has been derived from the governing partial differential equation making use of the expansion in Fourier sine series; in this way, the solution is expressed as a sum of infinite terms in which spatial and temporal variables are separated. The family of time functions solves a system of ordinary differential equations of variable size; the solution to this

system must be obtained numerically. In order to obtain accurate results, the minimum number of terms to be accounted for in the solution must be determined by means of a convergence study.

The hydraulic servoactuation system candidate to be utilized in the hybrid tests has been modeled by means of a system linearized around its mid-stroke equilibrium point, given the fact that the expected displacements are small compared to maximum actuator displacement. A TVC algorithm has been employed to control simultaneously the displacement, velocity and acceleration response of the actuator.

Simulations of the beam-like structure have been performed with and without the VCD installed on it. The selected control philosophy for the VCD is a DVFC scheme in which the dynamics of the inertial vibration controller have been neglected.

Simulation results show that the proposed hybrid simulation test set-up is able to accurately reproduce the kinematic references output by the semi-analytical integration scheme, thus yielding a realistic estimate of the VCD device behavior when installed on structures assimilable to beams subjected to inertial moving loads.

The main features of the suggested approach are:

- Accurate and quick qualitative predictions of VCDs performance in moving load scenarios can be obtained for a wide range of load velocities, as long as the convergence of the integration method is ensured for the velocities whole range. This is in opposition to the traditional approach of detailed finite element modeling and proportional mass lumping in the load neighbor nodes, which may only be valid for very low load speeds.
- Any type of VCD device can be

simulated and tested according to HS procedure.

- The semi-analytical integration scheme may be modified to account for moving loads with associated dynamics or successive loads simulating a traffic flow.
- The application of the method to the assessment of multiple-input-multiple output vibration control strategies is straightforward.
- Actuators employed for hybrid simulation tests may be readily sized by running campaigns of purely numerical simulations.
- It is relatively easy to modify the proposed procedure to simulate different types of structures, i.e.: string, Timoshenko beam or plate-like structures with different boundary conditions.

Nevertheless, several factors must be evaluated to ensure a successful practical implementation. In particular, the hardware platform which executes the integration scheme must be carefully selected to ensure adequate processing capacity and real-time operation. Besides, the design of the actuator control algorithm based on a linearized system may not be sufficiently accurate for the actual realization of the system and more complex techniques may be required possibly implying sophisticated hardware.

#### ACKNOWLEDGEMENTS

The authors acknowledge the financial support provided by the Spanish Ministry of Science, Innovation and Universities through the project SEED-SD (RTI2018-099639-B-I00).

#### REFERENCES

- [1] Shing, P.B. Real-Time Hybrid Testing Techniques. In: Bursi O.S., Wagg D. (eds) *Modern Testing Techniques for Structural Systems*, pp. 259-292. CISM International Centre for Mechanical Sciences, vol 502. Springer, Vienna (2008).
- [2] Bajer, C.I. and Dyniewicz, B. *Numerical Analysis of Vibrations of Structures under Moving Inertial Load*. Springer-Verlag Berlin Heidelberg (2012).
- [3] Bajer, C.I. and Dyniewicz, B. *Numerical modelling of structure vibrations under inertial moving load*. Arch. Appl. Mech. 79:499-508 (2009).
- [4] Merrit, H.E. *Hydraulic Control Systems*. John Wiley & Sons, New York, USA (1967).
- [5] Ramírez-Senent, J., García-Palacios, J.H. and Díaz, I.M. Shaking table control via real-time inversion of hydraulic servoactuator linear state-space model. Proc. IMechE Part I: J Systems and Control Engineering. doi: 10.1177/09596518211007294 (2021)
- [6] Moog. *Servovalves with Integrated Electronics-D765 Series*. Moog GmbH, Böblingen, Germany (2020).
- [7] ISO 6022. Hydraulic fluid power. Mounting dimensions for single rod cylinders, 25 MPa (250 bar) series. International Organization for Standardization edition, 2006.
- [8] Yao, J., Dietz, M, Xiao, R., Yu, H., Wang, T. and Yue, D. *An overview of control schemes for hydraulic shaking tables*. J Vib Control, 22: 2807–2823 (2016).
- [9] Franklin, G.F., Powell, J.D. and Workman M.L. *Digital Control of Dynamic Systems*,

Second Edition, Addison-Wesley, 1990.

- [10] Díaz, I.M., Gallegos, C.A., Ramírez-Senent, J. and Renedo, C.M.A. *Interaction phenomena to be accounted for human-induced vibration control of lightweight structures*. *Frontiers in Built Environment* 7. doi: 10.3389/fbuil.2021.658529 (2021).

## ANALYSIS OF DYNAMIC LOADS IN STRUCTURES WITH NEURONAL NETWORK

Prendes-Gero M.B.\*, Gracia-Rodríguez J.†, Álvarez-Fernández I. <sup>a,\*</sup>,  
González-Nicieza C. \*, Rodríguez-Pereira, C. <sup>♦</sup>

\* Grupo de investigación DINROCK,  
Universidad de Oviedo  
<sup>a</sup>e-mail: inma@uniovi.es  
ORCID: 0000-0002-5681-6530

† Departamento de Construcción e Ingeniería de Fabricación,  
Universidad de Oviedo

<sup>♦</sup>Institute of Space Sciences and Technologies of Asturias (ICTEA)

**Abstract.** Safety criteria that currently exist use the peak particle velocity (PPV) and the fundamental frequency as damage criterion to limit the dynamic loads in the structures. However, some researchers prefer the use of particle acceleration. On the other hand, the energetic criteria started to be developed, but these do not take into account the dynamism of the phenomenon suitably, because they do not consider the concept of power or energy flux. In fact, the practice shows that none of the four indicators mentioned (velocity, frequency, acceleration and energy) is more suitable than the rest.

The identification of critical wave parameters for the occurrence of damage is a problem that has been unanswered for many years. A problem of this complexity cannot be addressed through the application of conventional techniques, but the use of new techniques invites optimism.

In this paper a neuronal network is employed as a predictive tool. The objective is to know the variation of the values of the different variables that characterize one wave, once this wave has gone through the structure (going into it by the foundations and going out by the beams of the roof). The analysed variables have been the acceleration, velocity, frequency and duration in the three axes (X, Y, Z) and the energy.

At the beginning, all the variables have been employed at the same time, that is, without deferring the values on each axis. The result was a neural network with two hidden layers of 13 neurons each one, a high computational time and poor results with correlation values below 0.8 and high mean square errors.

The analysis by axes gave good correlation values greater than 0.8 and low mean square errors. For the x axis the obtained results with a neuronal network with one hidden layer with 5 neurons or two hidden layer with 5 neurons each one were similar. But in the case of the y and z axes the results improve where two hidden layers are employed.

**Key words:** neuronal network, safety criteria, PPV criteria, energetic criteria.

### 1 INTRODUCTION

The vibration experienced at a certain distance from the blast is usually a complex

combination of several types of waves, which are difficult to separate [1]. Its characteristics can be described through the measurement in

time, in three orthogonal directions, of the acceleration, velocity or motion of a point. [2] adds frequency and velocity of wave propagation as necessary terms for his description.

Factors reflecting the intensity, frequency and duration of the wave and, on the other hand, factors inherent to the structure such as its damping coefficient and natural frequency should be taken into account when trying to establish structural safety against a seismic event (either a blast or an earthquake). A comprehensive review of the most recent developments in damage criteria has been carried out by [3, 4]. As this author emphasises, each country has its own standards, based on a greater or lesser number of case studies, and there is no common consensus to reconcile them.

The importance of the problem has meant that no effort has been spared in developing ground vibration transmission models [5 – 13] and of dynamic behaviour and damage in buildings [14 – 16].

In current standards, the PPV, which is the maximum velocity at which an individual particle moves in the passage of a given wave, is accepted as an indicator parameter of intensity, although some standards take into account only the largest component while others consider the modulus of the velocity vector. In some (but not all) cases, the frequency of vibration is also considered important. However, different elements of a structure can have very different natural frequencies. Thus, extensive studies [17, 18] have shown that walls have frequencies of 12 to 20 Hz, while superstructures have lower frequencies (5 to 10 Hz). In fact, these are very simplistic models that assume that the structure has only one degree of freedom for vibration.

However, there is a second set of damage criteria based on energy criteria. One of the first was proposed by [19], based on the hypothesis of a simple harmonic motion,

which considers the peak acceleration (not velocity) and the frequency at the peak (not the fundamental). This criterion was developed through the analysis of more than 1000 residential structures. [20] expressed this criterion in terms of velocity. In both cases, this is a very simplistic energy analysis. More recently [21] argue for the importance of taking into account the energy carried by the wave at the characteristic frequency of the structure. This energy would be obtained through the energy spectrum obtained through WPA (Wavelet Packed Analysis) of the signal. [22] have proposed another concept, obtaining the energy after analysing the complete waveform obtained through geophones.

On the other hand, the work of [23], who design large-scale equipment to induce vibrations in structures by means of hydraulic jacks, stands out. This review should not make us lose sight of the most important fact: neither the maximum particle velocity, nor the maximum acceleration, nor the Crandell (and later) energy criterion, nor the natural frequency of the structure allow us to correctly assess the effect of a wave on a structure. Nor does the wavelet analysis, as it is currently applied, solve the problem, since this analysis focuses more on the frequency field than on the amplitude of the wave, when in this problem both fields are important.

The aim of this work is to develop on neuronal network as a predictive tool. The end is to know the variation of the values of the different variables that characterize one wave, once this wave has gone through the structure (going into it by the foundations and going out by the beams of the roof). The analysed variables have been the acceleration, velocity, frequency and duration in the three axes (X, Y, Z) and the energy.

## 2 PREVIOUS STUDIES

Prior to the tests on full-scale structures,

small- and medium-scale studies were carried out.

### 2.1. Small-scale tests

Initially, small-scale laboratory tests were carried out [24 - 27] in order to control the different variables to be analysed. The tests were performed on isolated structural elements such as beams, columns, partitions (Figure 1). All the elements were fabricated in the laboratory with known and characterised materials. The dimensions of these first elements ranged from 10 to 40 cm.



**Figure 1.** 3D frame bonded with mortar.

These structural elements were instrumented with geophones and accelerometers and were subjected to states of static load and to states of dynamic load produced with a vibration generator.

The vibration generator developed by the Din-Rock Research Group allowed to regulate the intensity and frequency to obtain the desired vibratory wave.

The level of dynamic loading was modified (amplitude, different frequencies) until damage to the tested elements was obtained that triggered their rupture.

Damage assessment was carried out with acoustic emission, ultrasound tomography (to assess internal damage) and direct observation and measurement (where damage is visible).

From these small-scale studies it was concluded that

- Ultrasonic tests show no internal damage

after vibration.

- Fatigued structures have a lower fatigue strength.
- Joints are areas of great weakness, therefore, complex structures made up of several basic elements joined by joints have a worse vibration behaviour than solid elements.

### 2.2. Medium-scale tests

Next, work was carried out on more complex structures such as the foundation-column assembly where different materials were also used and a simple portal frame formed by two columns centred on two foundations.

The scale of the models is approximately 1:10. The cross-section of the columns and the beam is 4 cm x 2 cm and their length is 20 cm, being identical in all cases. The foundations are square, 12 cm on each side and 2 cm on each edge (Figure 2).



**Figure 2.** Medium-scale structures analysed.

These elements were instrumented with accelerometers and, as in the small-scale studies, were subjected to static and dynamic load states.

From these medium-scale studies it was concluded that:

- In the foundation-column assembly, the largest displacements are always concentrated in the weak axis of the column.

- The use of different materials hardly produces significant differences in the behaviour of the foundation-column assembly, with the exception of saturated sands that show liquefaction.
- For the single portal frame, disparity of results is observed between two of the accelerometers used. This shows that measurements in the field are affected by factors such as adhesion or surface regularity.
- In the portal frame, there is a change in the mode of oscillation from oscillating on its weak axis to oscillating more strongly on its strong axis, which increases the induced stresses by 25 %.

### • 3. CASE OF STUDY

Once the results of the small and medium scale tests have been analysed, a concrete structure with dimensions of 2 m high and 2.5 x 2.5 m base placed on a spread foundation is built. Figure 3 shows the construction process of the structure.



**Figure 3.** Construction of the structure.

The structure is located in the square of the Hanson quarry, located in Santa Marina de Piedramuelle near the city of Oviedo, capital of the Principality of Asturias in Northern Spain

(Figure 4).



**Figure 4.** Location of the quarry.

This location was chosen because blasting is carried out permanently in the quarry, which allows for a continuous study over time

Figure 5 shows the general layout of the structure, as well as the nomenclature used for each structural element:

- NLB: North lower beam.
- NUB: North upper beam.
- SUB: South upper beam.
- BA: base or structure slab.

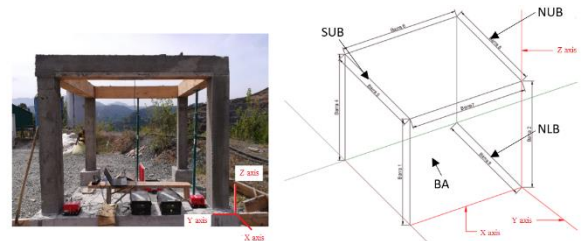


**Figure 5.** Structure and nomenclature of the beams.

### 3. METHODOLOGY

Once the structure to be tested has been defined:

- Accelerometers type Syscom, Etna, 9043 and 5033 are placed both in the input elements (NLB and BA) and in the output elements (NUB, SUB).
- Controlled blasting are carried out.
- The maximum acceleration, velocity, Fast Fourier Transform (FFT) and duration of

the event, as well as its energy, are obtained for each axis.

- The neural network capable of predicting the values recorded in the output elements knowing the values recorded in the input elements is calculated.

Table 1 shows the total load, the operating load, the distance from the blast to the structure and the scaled distance calculated according to [12], for three days of testing.

Date	Total load (kg)	Operating load (kg)	Distance (m)	Dscaled (m/kg <sup>1/2</sup> )
20/03/19	864	36	668	22.73
26/03/19	1680	67.2	641	15.64
06/04/19	888	74	501	16.81

**Table 1.** Blasting data for the dates collected.

It should be noted that all devices (except SYSCOM 3) directly measure acceleration (Table 2 and 3), so the velocity is obtained indirectly through the integration of acceleration and energy as the sum of the squares of the velocity components.

Date	Ele.	Ax (mm/s <sup>2</sup> )	Ay (mm/s <sup>2</sup> )	Az (mm/s <sup>2</sup> )
20/03/19	NLB	14.41	20.09	12.83
	NLB	16.03	29.08	178.46
26/03/19	NLB	377	672.63	1138.9
	NLB	169.49	191.49	422.18
06/04/19	NLB	46.01	60.26	25.19

**Table 2.** Maximum acceleration collected for each axis at the input elements.

Date	Ele.	Ax (mm/s <sup>2</sup> )	Ay (mm/s <sup>2</sup> )	Az (mm/s <sup>2</sup> )
20/03/19	NUB	49.63	74.95	74.9
	SUB	48.73	92.52	41.97
26/03/19	NUB	137.68	214.21	78.79
	NUB	71.85	54.94	35.28
06/04/19	SUB	67.73	52.73	29.85

**Table 3.** Maximum acceleration collected for each axis

at the output elements.

To obtain the FFT (Table 4 and 5), a MATLAB algorithm was used to calculate the dominant frequency from the recorded waveform. In addition, the value obtained is compared with the one obtained with the SismoSignal software that treats seismic signals coming from earthquake-type events. The objectives are:

- Determine the FFT and compare it with the one obtained in MATLAB verifying the implemented algorithm.
- Determine the event duration (Table 6 and 7) by the significant duration or interval in seconds, between 5% and 95% of the Husid function, where most of the energy is concentrated [28, 29].

Date	Ele.	FFT <sub>x</sub> (Hz)	FFT <sub>y</sub> (Hz)	FFT <sub>z</sub> (Hz)
20/03/19	NLB	11.71	11.42	12.3
	NLB	42.72	28.02	20.01
26/03/19	NLB	7.81	16.79	30.85
	NLB	8.05	8.05	23.92
06/04/19	NLB	16.3	16.45	32.27

**Table 4.** FFT for each axis at the input elements.

Date	Ele.	FFT <sub>x</sub> (Hz)	FFT <sub>y</sub> (Hz)	FFT <sub>z</sub> (Hz)
20/03/19	NUB	19.53	20.5	93.99
	SUB	19.53	20.26	93.5
26/03/19	NUB	20.38	0.24	0.73
	NUB	20.01	0.97	0.49
06/04/19	SUB	0.48	0.48	0.49

**Table 5.** FFT for each axis at the output elements.

Date	Ele.	tx (s)	ty (s)	tz (s)
20/03/19	NLB	1.48	1.2	1.73
	NLB	0.19	0.18	0.13
26/03/19	NLB	0.38	0.14	0.07
	NLB	0.33	0.27	0.14
06/05/19	NLB	0.66	0.57	0.60

**Table 6.** Event duration for each axis at the input

elements.

Date	Ele.	tx (s)	ty (s)	tz (s)
20/03/19	NUB	1.37	1.75	1.54
	SUB	1.12	1.51	0.97
26/03/19	NUB	2.15	2.74	2.10
	NUB	1.91	2.82	2.69
06/05/19	SUB	1.98	2.19	2.37

**Table 7.** Event duration for each axis at the output elements.

Once the acceleration, velocity, energy, FFT and event duration data are obtained, the neural network capable of predicting the values in the output elements from the values recorded in the input elements is calculated.

In the calculation of the network, the Fitting network function of the Matlab software is used, using 70% of the data as training data, 15% as validation data and the remaining 15% as check data. In addition, the Levenberg-Marquardt backpropagation function is used as the training function.

#### 4. RESULTS

Initially, the calculation of a neural network was approached with all input and output data, i.e. considering all axes at the same time.

The best result was obtained for a neural network with two hidden layers and 13 neurons in each layer, although the results are very poor with regressions below 0.8 except for the validation set (Figure 6).

The different attempts at improvement did not produce the desired result, so the calculation of different neural networks for each axis was proposed.

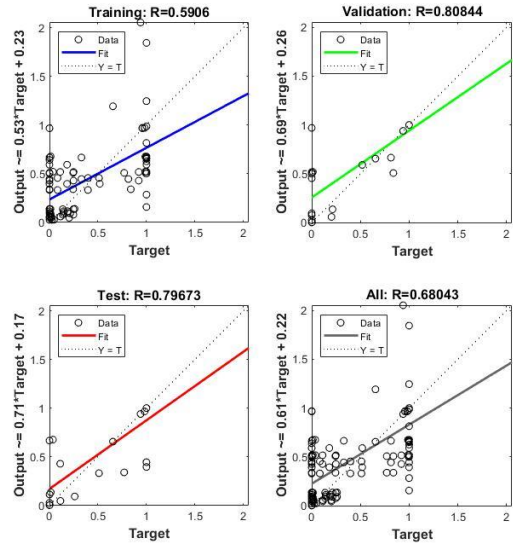


**Figure 6.** Regressions obtained by considering all input and output data simultaneously.

Neural networks with one and two hidden layers of 5 neurons in them were analysed.

On the X-axis, there is hardly any difference in the results obtained when one or two hidden layers are used, so as it is less computationally expensive, it is decided to work with the simplest network with regressions higher than 0.8 (Figure 7).

On the contrary, for both the Y-axis and the Z-axis, it is necessary to use the more complex prediction network with two hidden layers. In the case of the Y-axis, although the regression coefficient values present similar values for the two networks, the value of the mean square error committed is much lower when working with two hidden layers (Figure 8). On the Z axis, both the value of the regression coefficient and the value of the mean squared error is lower with two hidden layers.

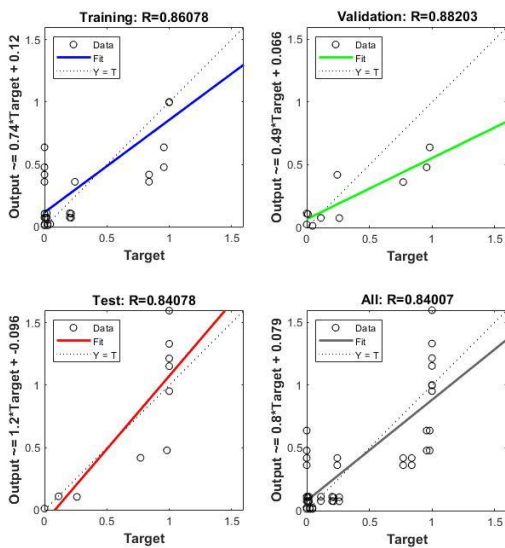


**Figure 7.** Regressions obtained for the X-axis with neural network with a hidden layer.

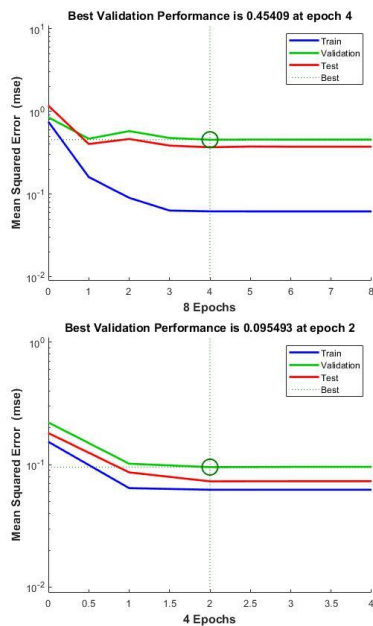


**Figure 8.** Minimum squared error on the y-axis for a neural network with one hidden layer (up) and two hidden layers (down).

## 5. CONCLUSIONS

The study shows that:

- One net should be used for each axis.

Preferably with two hidden layers.

- The results are not as expected, but the low volume of data available has to be taken into account. Therefore, a large improvement of the results can be expected when the training dataset is extended. This is expected to be done when the current situation stabilises.
- A larger volume of data will allow better filtering of the data, enabling the elimination of outliers.

## ACKNOWLEDGMENTS

The authors acknowledge the financial support provided by the Spanish Ministry of Economy and Competitiveness through the “Explora Project” VIBRASEC BIA2015-72928-EXP.

## REFERENCES

- [1] J.R. Brinkmann. *The control of ground vibration from colliery blasting during the undermining of residential areas*. Journal of the South African Institute of Mining and Metallurgy, 1987, 87 (2), 53-61
- [2] W.L. Bender. *Understanding Blast Vibration and Airblast, their Causes, and their Damage Potential*. Spring 2006 and Fall 2007 workshops of the Golden West Chapter of the International Society of Explosives Engineers.
- [3] T. Ngo; P. Mendis; A. Gupta; J. Ramsay. *Blast loading and blast effects on structures – an overview*. Electronic Journal of Structural Engineering, Special Issue 2007, (7), 79 – 91.
- [4] M. Mostafa. *Vibration Control*. Michael Lallart (Ed.), InTech. 2010, 355-380. ISBN: 978-953-307-117-6.
- [5] C. Caylak; A. Kocaslan; K. Gorgulu; A. Buyuksarac; E. Arpaz. *Importance of ground properties in the relationship of ground vibration – structural hazard and land application*. Journal of Applied

- Geophysic, 2014, 104, 6–16.
- [6] M. Khandelwal; T.N. Singh. *Evaluation of blasting induced ground vibration predictors*. Soil Dynamic Earthquake Engineering, 2007, 27, 116–125.
- [7] M. Khandelwal; M.A. Saadat. *Dimensional Analysis Approach to Study Blast-Induced Ground Vibration*. Rock Mechanics and Rock Engineering. 2014, DOI 10.1007/s00603-014-0604-y.
- [8] M. Ataei; M. Kamali. *Prediction of blast-induced vibration by adaptive neurofuzzy inference system in Karoun 3 power plant and dam*. Journal Vibration Control, 2012, 22, 1–9.
- [9] H.R.M. Azizabadi; H. Mansouri; O. Fouché. *Coupling of two methods, waveform superposition and numerical, to model blast vibration effect on slope stability in jointed rock masses*. Computers and Geotechnics, 2014, 61, 42–49.
- [10] D.P. Blair. *A probabilistic analysis of vibration based on measured data and charge weight scaling*. In: Proceedings of the 6th EFEE World Conference on Explosives and Blasting Technique, September 2011, Lisbon, Portugal. pp 319–337.
- [11] A.E. Álvarez-Vigil; C. González-Nicieza; F. López-Gayarre; M.I. Alvarez-Fernández. *Predicting blasting propagation velocity and vibration frequency using artificial neural network*. International Journal of Rock Mechanics and Mining Sciences, 2012, 55, 108-116.
- [12] C. González-Nicieza; M.I. Álvarez-Fernandez; A.E. Alvarez-Vigil; D. Arias-Prieto; F. López-Gayarre; F.L. Ramos-Lopez. *Influence of depth and geological structure on the transmission of blast vibrations*. Bulletin of Engineering Geology and Environmental, 2014, 73(4), 1211-1223.
- [13] M.T. Mohamed. *Performance of fuzzy logic and artificial neural network in prediction of ground and air vibrations*. International Journal of Rock Mechanics and Mining Science, 2011, 48, 845–851.
- [14] F. Faramarzi; F. Ebrahimi; A. Mohammad; H. Mansouri. *Simultaneous investigation of blast induced ground vibration and airblast effects on safety level of structures and human in surface blasting*. International Journal of Mining Science and Technology, 2014, 24, 663–669.
- [15] O. Dogan; O. Anil; S.O. Akbas; E. Kantar; R.T. Erdem. *Evaluation of blastinduced ground vibration effects in a new residential zone*. Soil Dynamic Earthquake Engineering, 2013, 50, 168–81.
- [16] C.H. Dowding. *Construction vibrations*. Prentice-Hall, Englewood Cliffs, 1996.
- [17] C.H. Dowding; W.K. Beck; D.K. Atmatzidis. *Blast Vibration Implications of Cyclic Shear Behavior of Model Plaster Panels*. Geotechnical Testing Journal, 1980, 3 (2).
- [18] K. Medearis. *The Development of Rational Damage Criteria for Low-Rise Structures Subjected to Blasting Vibrations*. Kenneth Medearis Associates, Final Rept. to National Crushed Stone Assn., August 1976, Washington, DC. 1996, p. 93.
- [19] F.J. Crandell. *Ground vibration due to blasting and its effect upon structures*. Journal Boston Soc. Civ. Engrs, April 1949, 222-245.
- [20] H.R. Nicholls; C.F. Johnson; W. Duvall. *Blasting vibrations and their effects on structures*. V.S. Bureau of Mines, Bulletin 1971, 656.
- [21] Z. Guosheng; L. Jiang; Z. Kui. *Structural safety criteria for blasting vibration based on wavelet packet energy spectra*. Mining Science and Technology (China) 2011, 21, 35-40.
- [22] K. Ram Chandar; V.R. Sastry. *A New Method of Estimating Wave Energy from*

- Ground Vibrations*. Geomaterials, 2015, 5, 45-55
- [23] L.K. Stewart; A. Freidenberg; T. Rodriguez-Nikl; M. Oesterle; J. Wolfson; B. Durant; K. Arnett; R.J. Asaro; G.A. Hegemier. *Methodology and validation for blast and shock testing of structures using high-speed hydraulic actuators*. Engineering Structures, 2014, 70, 168–180.
- [24] P. Fernández-Fidalgo. *Analysis of the transmission of vibrations originated by blasting in the ground*. Final project. Degree in Mining and Energy Resources Engineering. Polytechnic School of Mieres. University of Oviedo, 2018.
- [25] P. Fernández-Fidalgo. *Analysis of the affection to the structures of the vibrations induced by blasting*. Final project. Degree in Civil Engineering. Polytechnic School of Mieres. University of Oviedo, 2018.
- [26] A. Flores-Cordero. *Effect of vibrations caused by blasting on structural and support materials*. Master's Final Project. Master in Mining Engineering. School of Mining, Energy and Materials Engineering of Oviedo, 2018.
- [27] C. Lorenzana-García. *Structural damage induced by blasting*. Master's Final Project. Master in Mining Engineering. School of Mining, Energy and Materials Engineering of Oviedo, 2018.
- [28] M.D. Trifunac; A.G. brady. *A study on the duration of strong earthquake ground motion*. Bulletin of the Seismological Society of America. 1975, 65 (3), 581-626.
- [29] R. Husid. *Terremotos*. Andres Bello, Santiago de Chile, 1973

## **LOW-COST ARDUINO-BASED HORIZONTAL SENSOR AND DATA ACQUISITION SYSTEM FOR LOW-LEVEL AMBIENT VIBRATION MEASUREMENTS**

**Juan C. Galván\***, **Luis A. Padrón**, **Román Quevedo-Reina**, **Francisco J. Auyanet**,  
**Guillermo M. Álamo**

\* Instituto Universitario de Sistemas Inteligentes y Aplicaciones Numéricas en Ingeniería (SIANI),  
Universidad de Las Palmas de Gran Canaria  
Edif. Central del Parque Científico-Técnico. Campus Universitario de Tafira  
35017 Las Palmas de Gran Canaria, Spain  
e-mail: juancarlos.galvan@ulpgc.es

**Abstract.** The measurement of ambient vibrations to be used in system identification, model updating and structural health monitoring applications is already common practice in civil engineering. When the structure under study is very stiff, as in the case of concrete dams, and the level of ambient excitation is very small due to the absence of wind, running water or other vibration sources, the requirements and cost of the equipment needed to capture and process the vibrations tend to be elevated. At the same time, the deployment of the above-mentioned system identification, model updating and structural health monitoring applications may involve the use of a significant number of sensors or the need for keeping the sensors installed and acquiring data for long periods of time. In these cases, the economic cost of the sensors may represent a barrier to the use of this technology. At the same time, the availability of low-cost open platforms to perform this type of measurements is very useful not only in research but also in educational frameworks, because it allows students not only to use the technology but also to participate in its development and learn in the different fields (structural dynamics, electronics or programming) involved in a system of this kind. For these reasons, the paper presents the proposal of a low-cost horizontal sensor and data-acquisition system for low-level ambient vibration measurements. The mechanical sensor is based on the Lehman pendulum (or Garden Gate) design, with a coil-permanent magnet transducer and a data acquisition system based on the Arduino platform. The design of all elements involved in the system is presented in detail, and data obtained from a prototype of the design is presented and analyzed, showing the capabilities of the device.

**Key words:** Ambient vibrations, experimental structural identification, Arduino, experimental techniques

## 1 INTRODUCTION

Most civil structures, such as towers, bridges and dams, accumulate damage during their service life or can suffer a sudden damage due to natural disasters. So, an important issue is the detection of the structural damage since if the damage remains undetected the structure may have a reduced margin of safety. Formerly, the traditional procedure for evaluating the structural integrity was through visual inspections, and most recently, by means of destructive or forced vibration methods. Nowadays, numerous studies on damage detection use non-destructive evaluation methods such as Structural Health Monitoring (SHM) which can be conducted by means of ambient vibration through a sensor network that monitor the behaviour of the structures while they are in service, in order to extract information about displacement, velocity and acceleration from them. Commercially, there are a wide variety of seismic acquisition equipments but they are relatively expensive, which could restrict the number of stations that can be deployed simultaneously. However, the prices and accesibility to electronic components have helped to develop systems at low prices where geophones and accelerometers are the most widely used sensors. Thus, different research groups develop their own equipments. For instance, J.L. Soler-Llorens et al. [1] showed a low cost Arduino-based seismic recorder by means of vertical geophones and tested the system by comparing the registered signals with the ones obtained through different comercial data recording systems and different kind of geophones. In order to test the system, a sine wave was used as input signal where a function generator provided this input; S. Valenti et al. [2] proposed a low cost wireless sensor node for building monitoring by means of accelerometers where the performance of the sensor was evaluated through comparison

of results, in terms of modal frequencies and displacements, with those of a typical wired system using the Tower of the Engineering Faculty of the Università Politecnica delle Marche as demo structure.

This paper presents a low-cost Arduino-based horizontal sensor and data acquisition system to record low-level ambient vibration measurements with the following specifications (Fig.1):

- Electronic devices with very low power consumption.
- High sensitivity.
- Price of the sensor, amplifiers, filter, analog to digital converter and Arduino UNO board in their standard configuration is below 100 €.

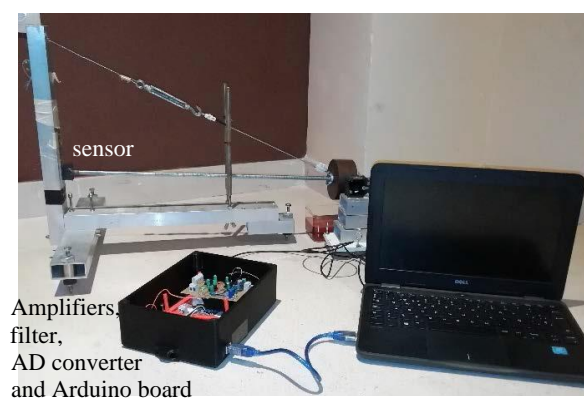


**Figure 1:** Proposed system.

The general design and the validation test of the system are reported in the paper to demonstrate its functionality. In order to validate it, two field tests have been conducted with ambient vibration comparing signals recorded by the proposed system with those obtained by a commercial high-precision and high-sensitivity seismograph. The outcome of those tests has shown the suitability of the proposed system to acquire and record low-levels signals and has also highlighted some of the limitations and areas for improvement of this proposal.

## 2 DESCRIPTION OF THE PROPOSED SYSTEM

The proposed system consists of four different parts: a) sensor; b) amplifiers, c) digital converter; and d) a microcontroller. This modular design allows more flexibility for future modifications (Fig.2).

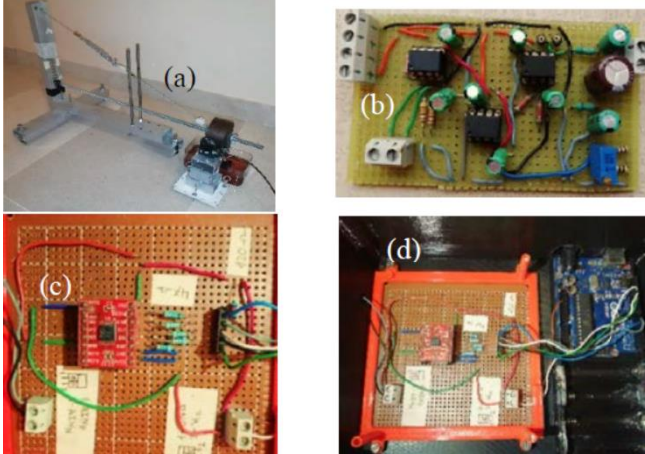


**Figure 2:** Components of the proposed system: (a) sensor (b) amplifiers and filter for signal conditioning (c) analog-to-digital converter (d) analog-to-digital converter connected to Arduino board microcontroller.

### 2.1. Sensor

A sensor is an instrument that measures the displacement of a vibrating body. The simplest type of sensor can be illustrated by a mass-spring-damper single-degree-of-freedom (SDOF) system mounted inside a box that is attached to the surface whose motion is to be measured, as shown in Fig. 3. The mass is connected to the box by a spring and a damper, while the box is attached to the ground. Since the spring and the damper are not rigid, the motion of the mass will be different to the motion of the ground. The relative motion between the mass and the box will relate to motion of the ground.

Thus, as illustrated in Fig. 3, the points 1 and 2 of the spring and damper, respectively, will have the same motion as the box (which is

to be measured,  $x_g$ ) and their vibration excites the mass into motion.

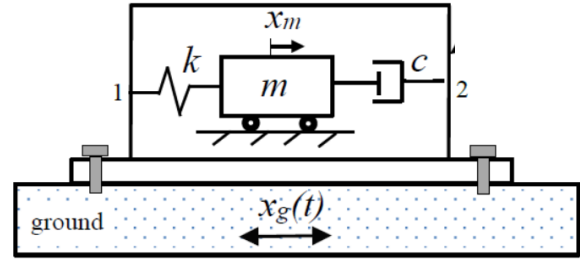


**Figure 3:** Simple mass-spring-damper sensor to record horizontal motions.

Being the displacement of the mass relative to the box  $x=x_m-x_g$ , where  $x_m$  denotes the horizontal displacement of the mass, the equation of motion of the mass  $m$  can be written as [3]:

$$m\ddot{x}_m + c(\dot{x}_m - \dot{x}_g) + k(x_m - x_g) = 0 \quad (1)$$

As mentioned above,

$$x = x_m - x_g \quad (2)$$

So, Eq. (1) can be written as

$$m\ddot{x} + c\dot{x} + kx = -m\ddot{x}_g(t) \quad (3)$$

If we assume the motion  $x_g$  to be harmonic,

$$x_g(t) = X_g(\omega)\sin(\omega t) \quad (4)$$

Here  $\omega$  is the circular frequency and  $X_g(\omega)$  is the amplitude of the base displacement. Thus, Eq. (3) becomes

$$m\ddot{x} + c\dot{x} + kx = m\omega^2 X_g(\omega)\sin(\omega t) \quad (5)$$

The particular solution of Eq. (5) is also harmonic; we assume the solution  $x_p(t)$

$$x_p(t) = X(\omega)\sin(\omega t - \phi) \quad (6)$$

Where  $X(\omega)$  and  $\phi$ , amplitude and phase angle of the response, respectively, are

constants to be determined. By substituting Eq. (6) into Eq. (5), we arrive at

$$X(\omega)[(k - m\omega^2) \sin(\omega t - \phi) + c\omega \cos(\omega t - \phi)] = m\omega^2 X_g(\omega) \sin(\omega t - \phi) \quad (7)$$

Using the trigonometric relations in Eq. (7)

$$\begin{aligned} \cos(\omega t - \phi) &= \cos(\omega t) \cos(\phi) + \sin(\omega t) \sin(\phi) \\ \sin(\omega t - \phi) &= \sin(\omega t) \cos(\phi) - \cos(\omega t) \sin(\phi) \end{aligned} \quad (8)$$

And equating the coefficients of  $\cos(\omega t)$  and  $\sin(\omega t)$  we obtain:

$$\begin{aligned} X(\omega)[(k - m\omega^2) \cos(\phi) + c\omega \sin(\phi)] &= m\omega^2 X_g(\omega) \\ X(\omega)[-(k - m\omega^2) \sin(\phi) + c\omega \cos(\phi)] &= 0 \end{aligned} \quad (9)$$

Solution of Eq. (9) gives:

$$\phi = \tan^{-1} \left( \frac{c\omega}{k - m\omega^2} \right) \quad (10)$$

$$\frac{X(\omega)}{X_g(\omega)} = \frac{m\omega^2}{\sqrt{(k - m\omega^2)^2 + (c\omega)^2}} \quad (11)$$

Eq. (10) and Eq. (11) can be expressed in a different form by introducing the notation

$$\omega_n = \sqrt{\frac{k}{m}} \quad (12)$$

$$\xi = \frac{c}{2m\omega_n} \quad (13)$$

$$r = \frac{\omega}{\omega_n} \quad (14)$$

Where  $\omega_n$  is the undamped natural circular frequency,  $\xi$  is the damping ratio and  $r$  is the frequency ratio. Thus, Eq. (10) and Eq. (11), can be rewritten as

$$\phi = \tan^{-1} \left( \frac{2\xi r}{1 - r^2} \right) \quad (15)$$

$$\frac{X(\omega)}{X_g(\omega)} = \frac{r^2}{\sqrt{(1 - r^2)^2 + (2\xi r)^2}} \quad (16)$$

Hence, when  $r \rightarrow \infty$ , Eq. (16) becomes

$$\lim_{r \rightarrow \infty} \frac{X(\omega)}{X_g(\omega)} = \frac{r^2}{\sqrt{(1 - r^2)^2 + (2\xi r)^2}} \approx 1 \quad (17)$$

So, according to Eq. (17), for larger values of  $r$ , the relative displacement ( $X$ ) and the base displacement ( $X_g$ ) have the same amplitude. Therefore, in order to satisfy Eq. (17), the natural frequency of the sensor must be low compared to that vibration to be measured.

The variations of  $X/X_g$  with respect to  $r$  are shown in Fig. 4 for different values of  $\xi$ . As can be seen, the damping ratio does not need to be present to satisfy Eq. (17), but its presence will improve the range of application of the instrument. For example, for  $\xi=0,7$ ,  $X(\omega) \cong Y(\omega)$  if  $r$  is greater than 2.

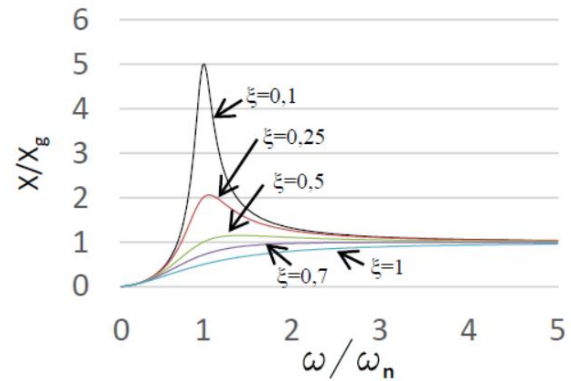


**Figure 4:** Response of a vibration-measuring instrument.

The device proposed here is based on the Lehman pendulum, sometimes also called the Garden Gate configuration, is a horizontal pendulum which is based on a system slightly tilted from horizontal where the mass of the system tends to remain suspended. When the ground moves, due to the vibrations caused by any excitation, the suspended mass of the system remains stationary, so we can directly measure the relative motion between the

ground and the suspended mass by a coil which converts that movement into a little current [4].

The sensor structure is made of extruded aluminum rectangle (5 cm x 2,5 cm) with two horizontal bars and one vertical bar joined between them by means of nuts and bolts. Fig. 5 shows a sensor structure picture, and the top, left side and front views of the structure.

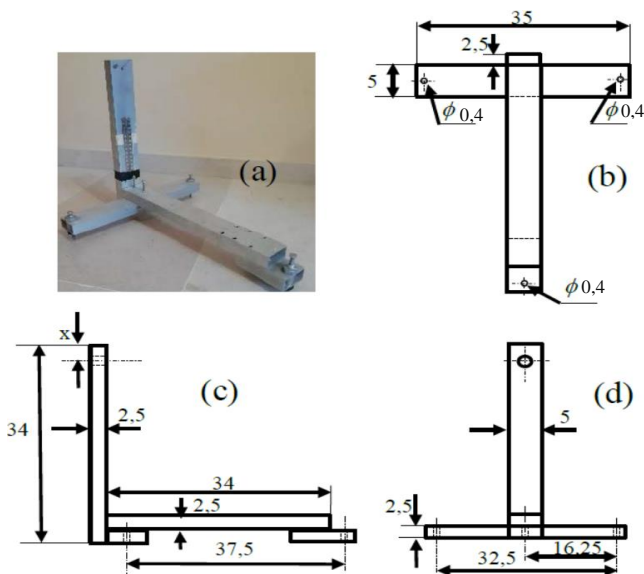


**Figure 5:** a) Sensor structure picture; b) Top, c) left side and d) front structure views (all dimensions in cm).

Fig. 6 presents a picture of the sensor. The movable arm (40 cm length) rests on a knife edge which is held against the vertical bar [5]. The knife edge is a very important part of the system since it avoids movable arm torsional oscillations. The other side of the movable arm, where it can swing freely, is hold up by a cable brake which is attached to the top of the vertical bar [6]. In this side, it can be seen the mass joined to the movable arm whose weight is 1,65 kg. In order to convert sensor structure movement into a little current, a neodymium magnet has been mounted on the mass (Fig. 7.a).

The oscillations of the movable arm must be damped. There are different damping

techniques, but in this work, the damping is obtained by means of two fins which are immersed in a tray filled (Fig. 7.b) with monograde diesel engine oil (SAE 30) insomuch as it is easier to control and to adjust than magnetic damping.

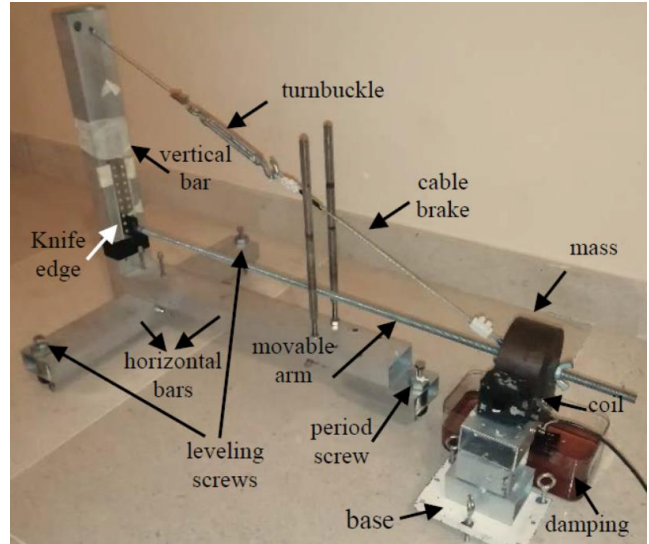


**Figure 6:** Proposed sensor.

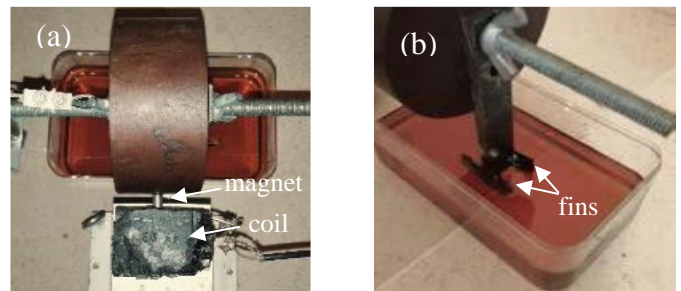


**Figure 7:** a) Coil mounted on the mass and magnet position. b) Fins immersed in a tray filled with monograde diesel engine oil.

On the other hand, the pickup coil has been mounted on a base which is independent from the sensor structure. When the ground moves, the sensor structure and the pickup coil move at the same time while the mass remains stationary. In this way, the relative motion between the magnet (mounted on the inertial mass) and the coil induces a small voltage in the coil which will be amplified and filtered.

One of the most important parts of the sensor are the screws. We can difference two screws types: Leveling and period screws. The two leveling screws have the purpose of leveling the movable arm while the period screw allows the adjustment of the movable arm inclination; this inclination gives us the sensor natural cyclic frequency (see section 2.1.1.). Periods of up to 6 to 8 seconds (equivalent to 0,12 Hz and 0,17 Hz), have been achieved, which allows to measure vibrations in structures with very low natural frequencies.

### 2.1.1. Sensor mathematical model

In order to obtain the sensor natural circular frequency and damping ratio, it will be considered the sensor showed in Fig.8

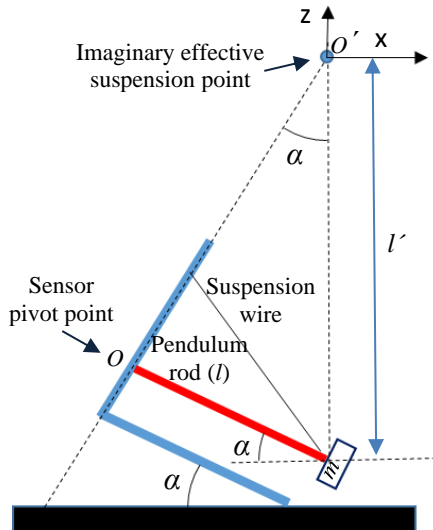


**Figure 8:** Schema of the sensor with angle of tilt ( $\alpha$ ) exaggerated [4].

The sensor is a horizontal pendulum which consists of a mass  $m$  swinging at the end of a rigid massless rod pivoted at point  $O$  with a length  $l$ ;  $l'$  is the effective pendulum length of a simple pendulum.

In Fig.9.a, the pendulum is in its equilibrium position; when the mass is displaced a small angle from its equilibrium

position and released, a restoring forces appear (Fig.9.b), being  $\vec{f}_d = -c \cdot \vec{v}$  the damping force which is acting at the end of the rigid massless rod (with  $v = l' \cdot \dot{\theta}'$ , tangencial component of the velocity of the mass  $m$ );  $a_t$  is the tangencial component of the acceleration of the mass  $m$  ( $a_t = l' \cdot \ddot{\theta}'$ ). Taking sum of moments respect to  $O'$ :

$$-mg \sin(\theta') l' - c \dot{\theta}' l' l' = m \ddot{\theta}' l' l' \quad (18)$$

The motion can be considered as a simple harmonic motion since  $\theta'$  is small, and we can say that  $\sin(\theta') \approx \theta'$ . Operating with Eq. (18) we have:

$$\ddot{\theta}' + \frac{c}{m} \cdot \dot{\theta}' + \frac{g}{l'} \cdot \theta = 0 \quad (19)$$

From the Fig. 8 we can obtain  $\sin(\alpha) = l/l'$ , and from Fig. 9.b we can get the relation  $\theta' = \theta \cdot l/l'$ , thus, operating with (19) we get:

$$\ddot{\theta} + \frac{c}{m} \cdot \dot{\theta} + \frac{g}{l} \cdot \sin \alpha \cdot \theta = 0 \quad (20)$$

Where Eq. (20) is the equation governing the free motion of the Lehman pendulum.

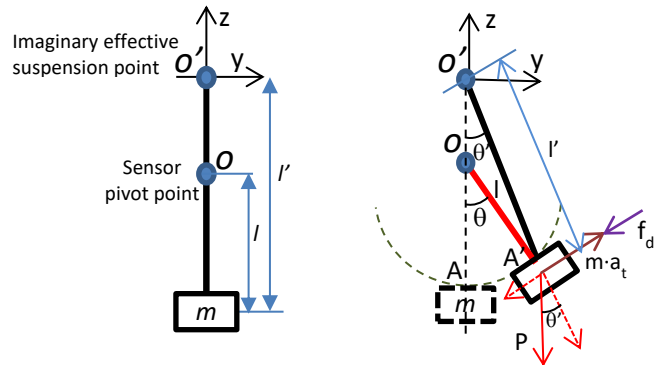


**Figure 9:** Pendulum from y-z plane: (a) equilibrium position (b) mass displaced a small angle  $\theta'$ .

The sensor undamped natural circular frequency will be obtained from Eq. (20) when  $c=0$ , so:

$$\ddot{\theta} + \frac{g}{l} \cdot \sin \alpha \cdot \theta = 0 \quad (21)$$

The solution of the linear, homogeneous, second-order differential equation with constant coefficients, Eq. (21), has the form  $\theta=e^{\lambda t}$ , thus, substituting into Eq. (21) yields:

$$\lambda^2 + \frac{g}{l} \cdot \sin \alpha = 0; \lambda_{1,2} = \pm i\omega_n \quad (22)$$

Where  $\omega_n$  is:  $\omega_n = \sqrt{\frac{g}{l} \sin \alpha}$  (23)

Thus, the differential equation of motion, Eq. (20), upon rearrangement and simplification, taking account Eq. (13), becomes:

$$\ddot{\theta} + 2\xi\omega_n\dot{\theta} + \omega_n^2\theta = 0 \quad (24)$$

Thereby, in according Eq. (23), the resonance frequency in a Lehman pendulum depends on the length of the movable arm and the angle of the structure ( $\alpha$ ) with respect to the horizontal plane. As can be seen in the spectra from Fig. 19 to Fig. 24, one frequency component, or peak, is highlighted in blue rectangle, being located between 0,12 Hz and 0,17 Hz; this peak

corresponds to the sensor natural frequency in each measure (using a movable arm 40 cm length).

## 2.2. Amplifiers and filter for signal conditioning

This part of the proposed system is formed by four stages (Fig.10): 1) a precision instrumentation amplifier; 2) an offset adjustment circuit; 3) an operational amplifier; and 4) an analog input filter; these four stages are powered with the same dual supplies, at least  $\pm 3.0$  V, using external batteries.

### 2.2.1. Precision instrumentation amplifier

The small signal induced in the pickup coil by the movement, proportional to ground velocity, is amplified using an instrumentation amplifier (Fig.10 – label 1 or Fig.11) which provides an amplified output signal ( $V_o$ ) with a single external resistor. The INA 114, which is a low cost, general purpose instrumentation

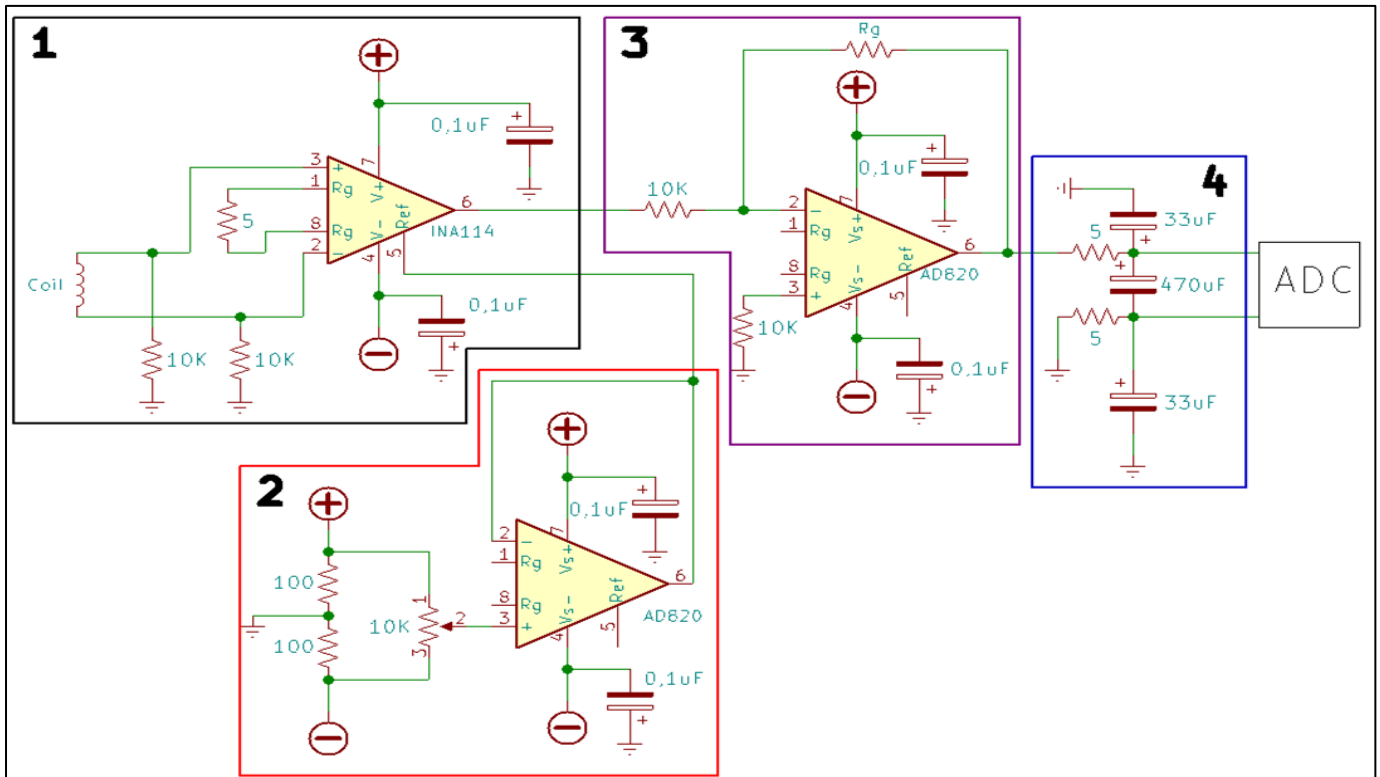


Figure 10: Electronic scheme for signal conditioning.

amplifier offering excellent accuracy and providing very low noise, has been selected. The single external resistor ( $R_G$ ) sets any gain from 1 to 10000 [7]; the gain is obtained by using the equation:

$$G = 1 + 50 \text{ K}\Omega / R_G \quad (25)$$

We have used a resistor of  $5 \Omega$  obtaining a gain of 10000 V/V, approximately. The output ( $V_o$ ) is referred to the output reference (Ref) terminal which is grounded through the offset adjustment circuit.

### 2.2.2. Offset adjustment circuit

The offset voltage will be trimmed with the circuit shown in Fig. 10 – label 2 or Fig.12. The voltage applied to Ref terminal is summed at the output.

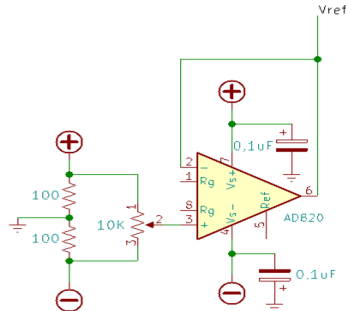


Figure 12: Offset adjustment circuit.

### 2.2.3. Operational amplifier

Then, a second amplification is carried out. The output signal from INA114 ( $V_o$ ) is amplified by an operational amplifier (Fig. 10 – label 3) being given the circuit gain by the relationship:

$$G' = R' / 10K \quad (26)$$

This gain is set means of  $R'$ . The AD820, which is a precision, low power FET input op

amp that can operate from a single supply of 5 V to 36 V, or dual supplies of  $\pm 2,5$  V to  $\pm 18$  V, has been chosen. In the AD820, N-channel JFETs are used to provide a low offset, low noise, high impedance input stage [8].

### 2.2.4. Analog Input filter

Analog input filtering serves three purposes: first, to limit the effect of aliasing during the sampling process, second, to reduce external noise from being a part of the measurement and third, to filter high frequency signals; therefore, a low pass resistor-capacitor (RC) filter will be placed at the input of the analog to digital converter for improve performance (Fig. 13).  $R_1/R_2$  and  $C_1/C_2$  form a bridge circuit so any mismatch between  $C_1$  and  $C_2$  will unbalance the bridge and reduce common-mode rejection; to avoid it, a differential input capacitor,  $C_{dif}$ , is placed, which mitigates the effects of mismatch in  $C_1$  and  $C_2$ , being the effect of mismatched reduced with a larger  $C_{dif}$  ( $C_{dif} \geq 10 \cdot C_1$ ,  $C_1 = C_2$ ) [9].

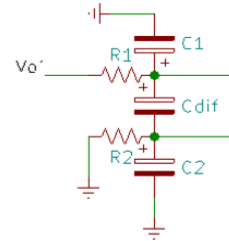


Figure 13: Low pass RC filter.

Considering that the frequencies we are interested in are under 10 Hz, the cutoff frequency has been configured to approximately 35 Hz, therefore, by applying (27) it results a  $C_{dif}$  of 470  $\mu\text{F}$ , and we can select a  $C_1(=C_2)$  of 33  $\mu\text{F}$  (Fig.10 – label 4 or Fig. 14). This output signal will be directly connected to the analog to digital converter.

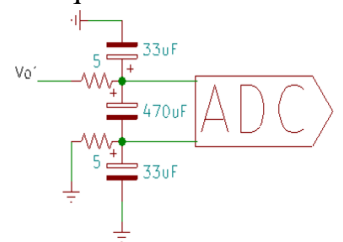


Figure 14: Analog Input filter.

$$f_{\text{cutoff}} = [2\pi(R_1+R_2) \cdot C_{dif}] \quad (27)$$

### 2.3. Analog-to-digital converter

Then, after the process of amplification and filtering, the signal will be connected to the analog-to-digital converter (ADC). In this system, we have selected the ADS1220 analog-to-digital converter, which is a precision, 24-bit, that offers many integrated features to reduce system cost and component count in applications measuring small sensor signals, with a wide supply range (2,3V to 5,5V). Moreover, the device features a low-noise, low-drift, high input impedance and programmable gain amplifier which is changed inside the device using a variable resistor [9]. In this case, we have selected a gain of 128 obtaining a full-scale input voltage of  $\pm 0,016V$ . The ADC operates with a single power supply provided through the 3,3V pin of the Arduino UNO. The principle serial interface connections for the ADS1220 are shown in Fig.15. It is important to remark that deviations in the internal clock of the ADS1220 of around 2% were found during the tests.

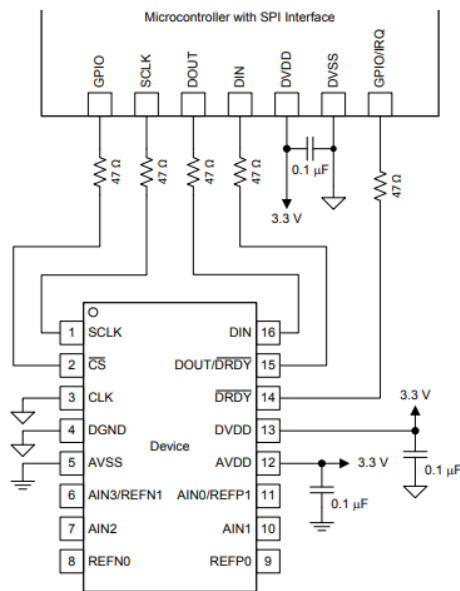


Figure 15: Serial Interface Connections [9]

### 2.4. Microcontroller

The Arduino Uno board has been used for commanding the analog-to-digital converter, process the information, and send the data to a computer through the USB port. The Arduino Uno is an open-source microcontroller board based on the Microchip ATmega 328P microcontroller and developed by Arduino.cc. The board is equipped with sets of digital and analog input/output (I/O) pins that may be interfaced to various expansion boards (shields) and other circuits. The arduino code is not presented herein due to space restrictions, but will be readily provided upon request to the authors by e-mail.

## 3 MATERIALS COST

Table 1 presents a list of materials and approximate costs at the time of assembly of the prototype. The total material cost lies below 100 €.

	Unit	Unit cost	Cost
<b>Sensor parts</b>			
Extruded aluminium (structure)	2 m	5,00 €/m	10,00 €
Mass	1,65 kg	2,50 €/kg	4,12 €
Turnbuckle	1	2,50 €	2,50 €
Screws	1 pack	1,50 €	1,50 €
Movable arm	1	1,50 €	1,50 €
Cable brake	1	1,00 €	1,00 €
Magnet (neodymium)	1 pack	4,60 €	4,60 €
<b>Amplifiers and digital converter</b>			
Resistors, capacitors, potentiometer and hook up wires			4,00 €
INA 114 (Instrumentation amplifier)	1	12,00 €	12,00 €
AD820 (Operational amplifier)	2	8,00 €	16,00 €
ADS1220 (analog-to-digital converter)	1	12,00 €	12,00 €
External batteries – AA, 1,5 V	4	0,50 €	2,00 €
<b>Arduino UNO.</b>	1	11,00 €	11,00 €
<b>TOTAL COST</b>			<b>82,22 €</b>

Table 1: Materials cost.

#### 4 EXPERIMENTAL VIBRATION TESTS AND ANALYSIS OF THE RESULTS

In order to test the behavior of the proposed low-cost acquisition system, this section presents comparison results between this acquisition system with the ones obtained by a commercial seismograph; the commercial seismograph used is Tromino® by MoHo s.r.l., which is a high-resolution all-in-one system for passive and active seismic surveys and vibration monitoring.

Two different campaigns have been carried out in the Island of Gran Canaria (Canary Island-Spain) conducted only with ambient vibration where the systems were configured with the following characteristics:

	First campaign	Second campaign
Recording time	15 min	15 min
Tromino ® - Sampling frequency	128 Hz	512 Hz
Lehman - Sampling frequency	88,2 Hz	88,2 Hz

**Table 2:** Systems configuration.

The first campaign took place on June 20<sup>th</sup> 2019. The seismographs were installed on the third floor of a five-storey building located in Las Palmas city where the distribution of the measurement points is shown in Fig. 16. The data acquisition systems were installed at the same place but the measurements were carried out at different times with a difference of 30 minutes between one and the other.

The second campaign was carried out in a dam, called Soria dam, located in the south of the Island and it took place on June 27<sup>th</sup> 2019. The distribution of the measurement points is shown in Fig.17. The proposed system has been protected from wind using a box (Fig.18). The proposed system and the data acquisition

systems were installed close to each other so the measurements were carried out at the same time.

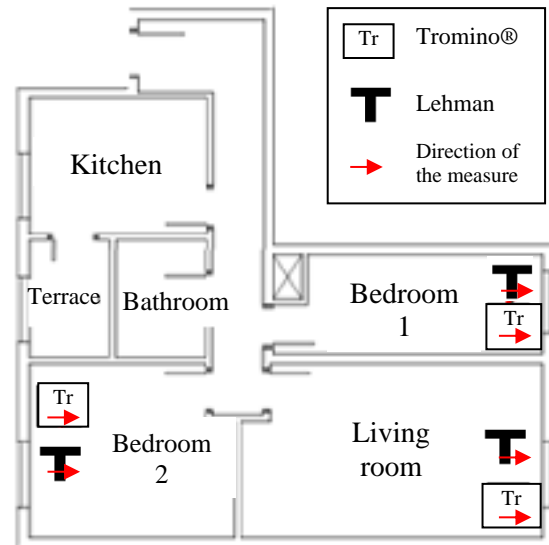


**Figure 16:** House plan. First campaign.

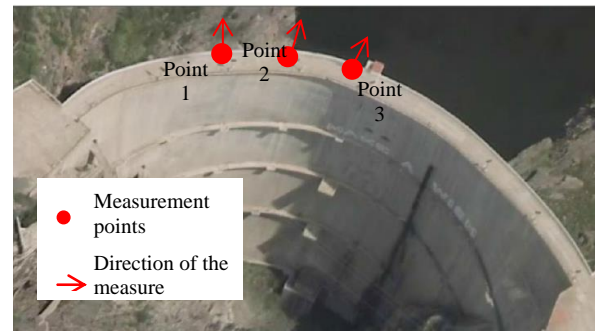


**Figure 17:** Soria dam. Second campaign.



**Fig.18:** (a) Proposed system inside the box (b) Proposed system box and Tromino®.

Figures 19 to 21, and Figures 22 to 24, present the Power Spectral Density plots corresponding to the signals recorded at the building and the dam respectively. We can observe a very good agreement between the two systems, in terms of both frequency and

amplitude, being the frequencies from both devices very close with a maximum divergence of 0,06 Hz which contributes to validate the proposed system.

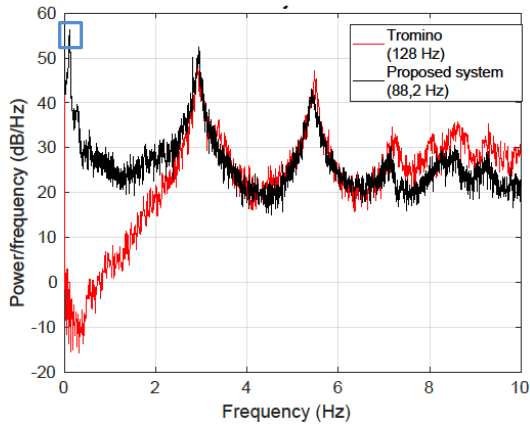


**Fig.19:** PSD of the recording. Bedroom 1.

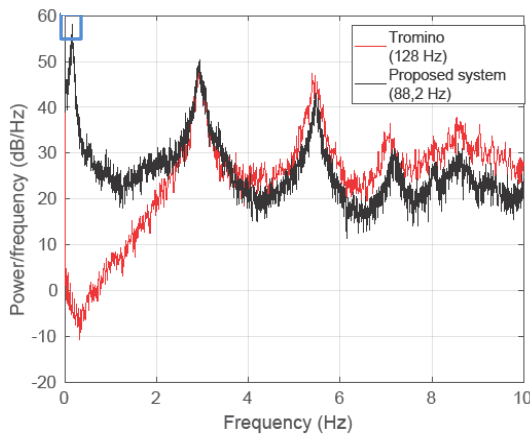


**Fig.20:** PSD of the recording. Living room.

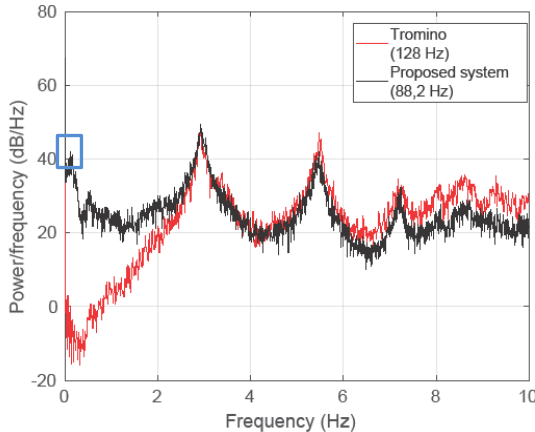


**Fig.21:** PSD of the recording. Bedroom 2.

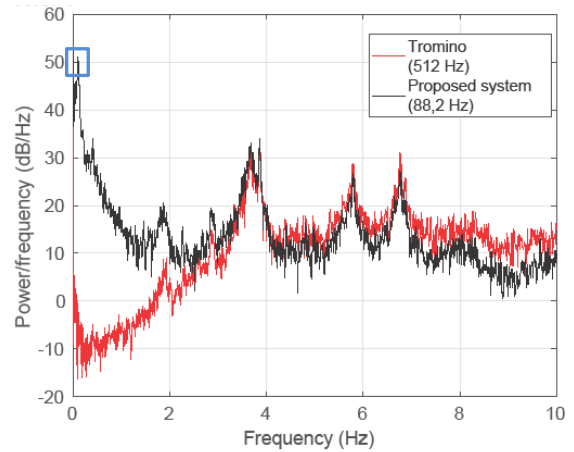


**Fig.22:** PSD of the recording. Dam, point 1.

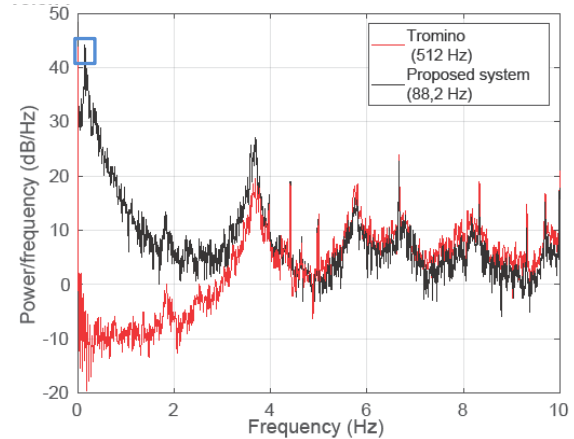


**Fig.23:** PSD of the recording. Dam, point 2.

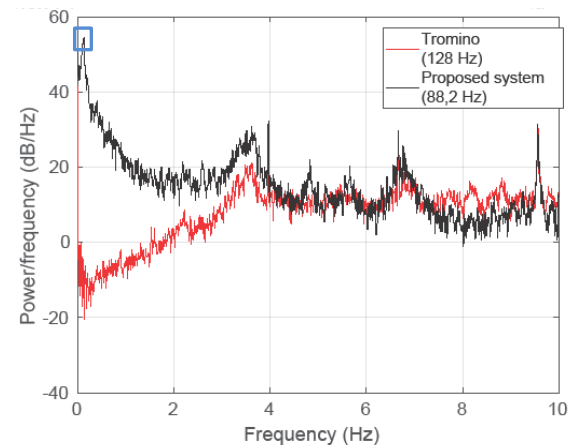


**Fig.24:** PSD of the recording. Dam, point 3.

## 5 CONCLUSIONS

This paper presents the design and preliminary results of a low-cost arduino-based

prototype system for measurement of structural low-level vibrations. The cost of the proposed system is below 100 €. In order to test the accuracy of the design, two in situ tests were conducted for field validation of the system where the data obtained with the proposed system were compared with data recorded by commercial seismograph (Tromino®). The results obtained from these experiments surpassed our expectations: the match in terms of frequency response is very high, and the sensitivity of the device is also really good. On the other hand, the device present several important drawbacks: the time needed for the set-up (as it must be disassembled for transportation), its sensitivity to wind and its size and weight. There are also some areas that would need improvement and/or further development, especially the calibration and reproducibility in terms of amplitude of the measured vibrations.

All in all, the proposal can be used as a basis to teach, learn, measure vibrations and develop other types of devices for this purpose.

## ACKNOWLEDGEMENTS

The authors acknowledge the support provided by the Laboratorio de ensayo de materiales of the Department of Civil Engineering of the ULPGC and want to thank Jacob Montesdeoca García and Cristóbal Melián Machín for their help to build the sensor structure and the sensor protection box, respectively. Additionally, the authors thank to Silvia Castellaro and Stefano Gianessi for providing the Tromino data. And finally, the authors also wish to thank to Cerrajería y Carpintería Metálica Ramírez Lemes for the knife edge welding. R. Quevedo is recipient of the FPU fellowship FPU19-04170 from the Ministerio de Universidades.

## REFERENCES

- [1] J. L. Soler-Llorens, J. J. Galiana-Merino, J. Giner-Caturla, P. Jauregui-Eslava, S. Rosa-Cintas, J. Rosa-Herranz. *Development and programming of Geophonino: A low cost Arduino-based seismic recorder for vertical geophones*. Computers & Geosciences. Volume 94, Pages 1-10, September 2016.
- [2] S. Valenti, M. Conti, P. Pierleoni, L. Zappelli, A. Belli, F. Gara, S. Carbonari, and M. Regni. *A low cost wireless sensor node for building monitoring*. Environmental, Energy, and Structural Monitoring Systems, Proceedings, art. no. 8405827, Pages 1-6, 2018.
- [3] Singiresu S. Rao. *Mechanical vibrations* (fifth edition). Addison-Wesley Publishing Company, 2011.
- [4] Paul Denton. *Building a simple seismometer*. British Geological Survey. Natural environment research council.
- [5] Knight K. "Instructions for construction of a Lehman Seismometer", Redwood city public seismic network (<http://www.seismicnet.com/lehman.html>), 2000
- [6] Bernd Ulmann. *Grundlagen und Selbstbau geophysikalischer Meßinstrumente*, Der Andere Verlag, 2004 (also in [http://www.vaxman.de/projects/lehman\\_seismometer/seismometer.html](http://www.vaxman.de/projects/lehman_seismometer/seismometer.html))
- [7] Burr-Brown Corporation; INA 114. Precision instrumentation amplifier. Technical datasheet printed in U.S.A., March, 1998.
- [8] Analog devices; AD 820. Single-Supply, Rail-to-Rail, Low Power, FET Input Operational Amplifier.
- [9] Texas Instruments; ADS1220. 4-Channel, 2-kSPS, Low-Power, 24-Bit ADC with Integrated PGA and Reference. Technical datasheet revised august 2016.

## MODAL MASS IN SYSTEMS WITH TWO PARTS OF DIFFERENT MASS-DENSITY

R. Stufano<sup>a</sup>, A. Fraddosio<sup>b</sup>, M. Aenlle<sup>c</sup>, F. Pelayo<sup>c</sup> and R. Brincker<sup>d</sup>

<sup>a</sup> Department of Civil, Environmental, Construction and Chemical Engineering  
Polytechnic University of Bari  
70125 Bari, Italy  
E-mail : r.stufano1@studenti.poliba.it

<sup>b</sup> Department of Civil Engineering Sciences and Architecture  
Polytechnic University of Bari  
70125 Bari, Italy

<sup>c</sup> Department of Construction and Manufacturing Engineering  
University of Oviedo  
33204 Gijón, Spain

<sup>d</sup> Department of Civil Engineering  
Technical University of Denmark  
2800 Kongens Lyngby, Denmark

**Abstract.** The modal mass in constant mass-density systems is equal to the product between the total mass of the structure and the length of the mode shapes squared. However, in non-constant mass-density systems, the modal mass is equal to the product between an apparent mass and the squared length of the mode shapes. This apparent mass is different for each mode and depends on the mode shape and how the mass is distributed in the structure. However, if a limited number of volumes with different mass-densities can be identified, a relationship between the modal masses of the different modes can be established. In this paper, numerical simulations on different structures with non-constant mass-density were performed. The length of the mode shapes was estimated using an approximate equation and the effect of the number of DOF's was investigated. Then, the apparent masses corresponding to each mode were estimated. Finally, the analytical relationship between the modal masses of the different modes was verified.

**Key words:** Modal Mass, Dynamics of Structures, Mode shapes, Normalization

### 1 INTRODUCTION

In discrete systems, the modal mass corresponding to the mode shape  $\psi$  can be calculated with the equation [1-4]:

$$m = \psi^T M \psi \quad (1)$$

In constant mass-density systems, Eq. (1)

can be expressed as [1,2]:

$$m = M_T L^2 \quad (2)$$

Where  $M_T$  is the total mass of the system and  $L^2$  is the squared length of the mode shape given by:

$$L^2 = \frac{\psi^T V \psi}{V_T} \quad (3)$$

Where  $V_T$  is the total volume of the system and  $V$  is the volume matrix. The length depends on the mode shape  $\psi$  and on how the volume is distributed in the structure.

### 1.1 Two constant mass-density systems.

If the structure is constituted by two parts with the two volumes,  $V_1$  with the mass density  $\rho_1$ , and  $V_2$  with the mass density  $\rho_2$ , the modal mass is obtained with the equation [1]:

$$m = M_1 L_1^2 + M_2 L_2^2 \quad (4)$$

Where  $L_1^2$  and  $L_2^2$  are the partial squared lengths of the mode shape  $\psi$  over the partial volumes  $V_1$  and  $V_2$ , respectively, i.e.:

$$L_1^2 = \frac{\psi_{V_1}^T V_1 \psi_{V_1}}{V_1} \quad (5)$$

And

$$L_2^2 = \frac{\psi_{V_2}^T V_2 \psi_{V_2}}{V_2} \quad (6)$$

With respect to the total squared length  $L^2$ , it can be obtained from the partial lengths by means of the equation [1]:

$$L^2 V_T = L_1^2 V_1 + L_2^2 V_2 \quad (7)$$

Eq. (1) can also be expressed as:

$$m = M_a L^2 \quad (8)$$

Where  $M_a$  is an apparent mass, given by:

$$M_a = V_T \frac{M_1 L_1^2 + M_2 L_2^2}{L_1^2 V_1 + L_2^2 V_2} \quad (9)$$

This apparent mass is different for each mode and depends on the mode shape and how the mass is distributed in the structure.

With respect to the squared cross-length [2] between the mode shapes  $\psi_i$  and  $\psi_j$ , it is defined as:

$$L_{ij}^2 = \frac{\psi_i^T V \psi_j}{V_T} \quad (10)$$

The total squared cross-length  $L_{ij}^2$  is related with the partial squared cross-lengths by means of:

$$L_{ij}^2 V_T = L_{ij1}^2 V_1 + L_{ij2}^2 V_2 \quad (11)$$

The squared cross-length  $L_{ij}^2$  is zero in constant mass-density systems, which means that the mode shapes are orthogonal. On the contrary, non-orthogonality is an indicator of non-constant mass-density.

Due to the fact that the mode shapes are orthogonal with respect to the mass matrix, the following relationship, relating the squared cross-lengths, is derived from Eq. (1):

$$0 = M_1 L_{ij1}^2 + M_2 L_{ij2}^2 \quad (12)$$

### 1.2 Arbitrary number of constant mass distributions

The equations formulated in section 1.1 can be generalized for an arbitrary number of constant mass distributions as:

$$m = \sum_n M_n L_n^2 \quad (13)$$

$$L^2 = \frac{1}{V_T} \sum_n V_n L_n^2 \quad (14)$$

$$L_{ij}^2 = \frac{1}{V_T} \sum_n V_n L_{ijn}^2 \quad (15)$$

In this paper, numerical simulations on different structures (beams, shells, and 3D solids) composed of two parts with different mass-densities were performed. An approximate formulation was used to calculate the length and the cross-length of the mode shapes. Using the modal masses of the first two modes and the length of the mode shapes, the

modal masses of the rest of the modes were estimated demonstrating that the technique is reasonable accurate.

### 3 NUMERICAL SIMULATIONS

#### 3.1. Cantilever Beam: Different mass-density in section.

A three-dimensional cantilever beam, 1 meter long and with constant cross-section  $4\text{ cm} \times 5\text{ cm}$ , with two different constant mass-density parts (steel and concrete) along the beam (see Fig. 1) was assembled in ABAQUS [5]. Both materials were considered linear-elastic and the material properties presented in Table 1 were assumed.



**Figure 1:** Steel-Concrete cantilever beam. Concrete green color. Steel grey color.

Material	Mass-density $\rho \left( \frac{kg}{m^3} \right)$	Young's modulus $E (GPa)$	Poisson ratio $\nu$
Steel	7850	210	0.3
concrete	2400	20	0.18

**Table 1:** Material properties considered for the steel-concrete cantilever.

The beam was meshed with twenty-node quadratic hexahedral elements (C3D20R) with an approximate global size of 0.0025 m (see Fig. 1). The natural frequencies and modal masses (mode shapes normalized to the largest component equal to unity) corresponding to the first eight modes are presented in Table 2. The total mass of the beam is  $M_T = 10.25\text{ kg}$ , where  $M_{T_s} = 7.85\text{ kg}$  corresponds

to the steel part and  $M_{T_c} = 2.4\text{ kg}$  corresponds to the concrete part.

Mode	Frequency [Hz]	Modal mass [kg] ABAQUS	Apparent mass [kg]
1	21.41	2.56	10.23
2	38.24	2.56	10.23
3	133.46	2.58	10.20
4	236.82	2.59	10.19
5	370.51	2.62	10.16
6	529.14	2.37	8.08
7	651.13	2.60	10.15
8	717.41	2.66	10.11

**Table 2 :** Natural frequencies and modal masses.

The squared length of the steel and concrete parts of the structure were calculated with the equations [2]

$$L_s^2 \cong \frac{\psi_s^T \psi_s}{N_s} \quad (16)$$

and

$$L_c^2 \cong \frac{\psi_c^T \psi_c}{N_c} \quad (17)$$

Where the sub-indexes 's' and 'c' indicate steel and concrete, respectively.

The total squared length (Table 5) is given by [1]:

$$L^2 \cong \frac{L_s^2 N_s + L_c^2 N_c}{N} \quad (18)$$

Where  $N = N_s + N_c$ . The apparent mass corresponding to each mode (Eq. (8)) is presented in Table 2.

Although the mass-density is not constant ( $\rho \neq const$ ) in this model, it is constant the mass-density for unit length, and the equation [2]:

$$L^2 \cong \frac{\psi^T \psi}{N} \quad (19)$$

can still be used to calculate the squared length

of the bending modes. This also means that the apparent mass of the bending modes is equal to the total mass of the system (see Table 2).

With respect to the cross-length (see Table 5), it is close to zero between the bending modes, but this is not case, as expected, between the torsional and the bending modes.

### 3.2. Cantilever Beam: Different mass-density in length.

A three-dimensional cantilever beam with the same dimensions and same material properties as the structure studied in section 3.1, but with material distribution as shown in Fig. 2, is considered in this section. The encastre boundary condition is placed at the end of the steel part.

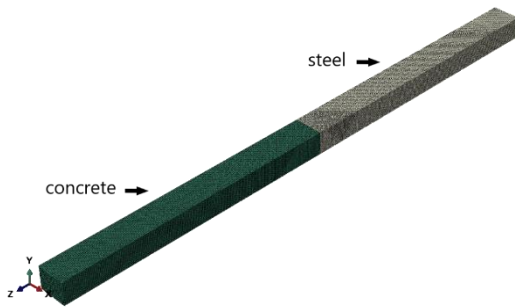


**Figure 2:** Steel-Concrete cantilever beam. Concrete green color. Steel grey color

The beam was meshed with twenty-node quadratic hexahedral elements (C3D20R) with an approximate global size of 0.0025 m (see Fig. 2). The natural frequencies and modal masses (mode shapes normalized to the largest component equal to unity) corresponding to the first eight modes are presented in Table 3. The total mass of the beam is again  $M_T = 10.25 \text{ kg}$ . distributed as  $M_{T_S} = 7.85 \text{ kg}$  and  $M_{T_C} = 2.4 \text{ kg}$

	Mode	Frequency [Hz]	Modal mass [kg]
1	1 <sup>st</sup> Bending Y	47.81	0.93
2	1 <sup>st</sup> Bending X	59.66	0.93
3	2 <sup>nd</sup> Bending Y	148.44	1.32
4	2 <sup>nd</sup> Bending X	184.83	1.32
5	3 <sup>rd</sup> Bending Y	440.37	0.90
6	3 <sup>rd</sup> Bending X	542.98	0.91
7	Torsion	743.98	0.79
8	4 <sup>th</sup> Bending Y	798.21	1.56

**Table 3 :** Natural frequencies and modal masses of the structure in Fig. 2

The contribution of the steel and concrete parts to the total modal mass (using the squared lengths estimated with Eqs. (16) and (17)), the total modal masses, and the apparent mass (different for each mode) are presented in Table 4.

Mode	Modal mass [kg]			Apparent mass [kg]
	Steel $M_{T_S}L_S^2$	Concrete $M_{T_C}L_C^2$	$M_{T_S}L_S^2 + M_{T_C}L_C^2$	
1	0.07	0.86	0.93	5.05
2	0.07	0.86	0.93	5.05
3	0.69	0.63	1.32	7.54
4	0.70	0.63	1.33	7.54
5	0.30	0.61	0.90	6.21
6	0.30	0.62	0.92	6.21
7	0.06	0.80	0.86	5.04
8	0.87	0.70	1.56	7.79

**Table 4 :** Modal masses and apparent masses for the cantilever beam in Fig. 2

The partial squared lengths, cross-lengths, and the total squared lengths, estimated with eqs. (16-18) are shown in Tables 6-8. In this case the mass-density is not constant, different squared lengths are expected for each mode, and non-zero values are expected for the cross-length (except for orthogonal mode shapes).

1	1 <sup>st</sup> Bending Y	0.25	0	0.0011	0	0.0011	0	0	0.0012
2	1 <sup>st</sup> Bending X	0	0.25	0	0.0002	0	0.0693	0	0
3	2 <sup>nd</sup> Bending Y	0.0011	0	0.25	0	0.0015	0	0	0.0014
4	2 <sup>nd</sup> Bending X	0	0.0002	0	0.25	0	0	0.0009	0
5	3 <sup>rd</sup> Bending Y	0.0011	0	0.0015	0	0.26	0	0	0.0019
6	Torsion	0	0.0693	0	0	0	0.29	0.0025	0
7	3 <sup>rd</sup> Bending X	0	0	0	0.0009	0	0.0025	0.26	0
8	4 <sup>th</sup> Bending Y	0.0012	0	0.0014	0	0.0019	0	0	0.26

**Table 5:** Squared Length Matrix of the Steel-Concrete cantilever beam (Fig. 1).

1	1 <sup>st</sup> Bending Y	0.01	0	-0.0271	0	0.0150	0	0	-0.0020
2	1 <sup>st</sup> Bending X	0	0.01	0	-0.0273	0	0.0152	0	0
3	2 <sup>nd</sup> Bending Y	-0.0271	0	0.09	0	-0.0510	0	0	0.0145
4	2 <sup>nd</sup> Bending X	0	-0.0273	0	0.09	0	-0.0516	0	0
5	3 <sup>rd</sup> Bending Y	0.0150	0	-0.0510	0	0.04	0	0	-0.0377
6	3 <sup>rd</sup> Bending X	0	0.0152	0	-0.0516	0	0.04	0	0
7	Torsion	0	0	0	0	0	0	0.01	0
8	4 <sup>th</sup> Bending Y	-0.0020	0	0.0145	0	-0.0377	0	0	0.11

**Table 6 :** Squared length of the steel part of the structure (Fig. 2).

1	1 <sup>st</sup> Bending Y	0.36	0	0.0898	0	-0.0470	0	0	0.0094
2	1 <sup>st</sup> Bending X	0	0.36	0	0.0902	0	-0.0474	0	0
3	2 <sup>nd</sup> Bending Y	0.0898	0	0.26	0	0.1684	0	0	-0.0482
4	2 <sup>nd</sup> Bending X	0	0.0902	0	0.26	0	0.1705	0	0
5	3 <sup>rd</sup> Bending Y	-0.0470	0	0.1684	0	0.25	0	0	0.1259
6	3 <sup>rd</sup> Bending X	0	-0.0474	0	0.1705	0	0.26	0	0
7	Torsion	0	0	0	0	0	0	0.33	0
8	4 <sup>th</sup> Bending Y	0.0094	0	-0.0482	0	0.1259	0	0	0.29

**Table 7** Squared length of the concrete part of the structure (Fig. 2).

1	1 <sup>st</sup> Bending Y	0.18	0	0.0313	0	-0.0160	0	0	0.0037
2	1 <sup>st</sup> Bending X	0	0.18	0	0.0315	0	0	0	0
3	2 <sup>nd</sup> Bending Y	0.0313	0	0.18	0	0.0587	0	0	-0.0168
4	2 <sup>nd</sup> Bending X	0	0.0315	0	0.18	0	0	0	0
5	3 <sup>rd</sup> Bending Y	-0.0160	0	0.0587	0	0.14	0	0	0.0441
6	3 <sup>rd</sup> Bending X	0	0	0	0	0	0.15	0	0
7	Torsion	0	0	0	0	0	0	0.17	0
8	4 <sup>th</sup> Bending Y	0.0037	0	-0.0168	0	0.0441	0	0	0.20

**Table 8** Total squared length of the structure (Fig. 2).

In systems consisting of two parts of constant mass-density, the following relationship between the squared cross-lengths and the total

masses of the concrete and steel parts, is derived (for all the modes) from Eq. (12):

$$\frac{M_{Ts}}{M_{Tc}} = -\frac{L_{ijc}}{L_{ijs}} \quad (20)$$

It is inferred from Tables 6 and 7 that Eq. (20) is fulfilled for all the modes (except if they are orthogonal) with an error less than 20%. However, the error decreases as increasing the magnitude of the squared cross-length components.

Using the squared lengths of Tables 6 and 7, and the modal masses presented in Table 3, the total masses of the concrete and the steel parts were estimated using Eq. (4), obtaining  $M_{Ts} = 7.98 \text{ kg}$  and  $M_{Tc} = 2.34 \text{ kg}$ , respectively. This demonstrates that the mass distribution can be known if the modal masses and the partial squared lengths can be estimated from the experimental or the numerical data. Alternatively, the modal masses can be estimated if the partial squared lengths and the total mass of each part (with different mass-density) are known.

### 3.3. Two-story building model.

A two-storey building made of steel columns (section  $0.1 \text{ m} \times 0.1 \text{ m}$  and length  $2.9 \text{ m}$ ) and rectangular concrete storeys (dimensions  $4 \text{ m} \times 10 \text{ m}$  and thickness  $0.3 \text{ m}$ ) was assembled in ABAQUS [5] (see Fig. 3). The same material properties as those considered in the previous sections were utilized in the simulations.

A fix boundary condition was considered at the foundation, and the model was meshed with 3D elements C3D20R with a global size of  $0.1 \text{ m}$  for the storeys and  $0.05 \text{ m}$  for the columns. The natural frequencies and modal masses (mode shapes normalized to the largest component equal to unity) corresponding to the first 8 modes are presented in Table 9. The total mass of the structure is  $M_T = 60332 \text{ kg}$ .

distributed as  $M_{Ts} = 2732 \text{ kg}$  for the columns and  $M_{Tc} = 57600 \text{ kg}$  for the storeys. The squared length of the mode shapes is shown in Table 10.

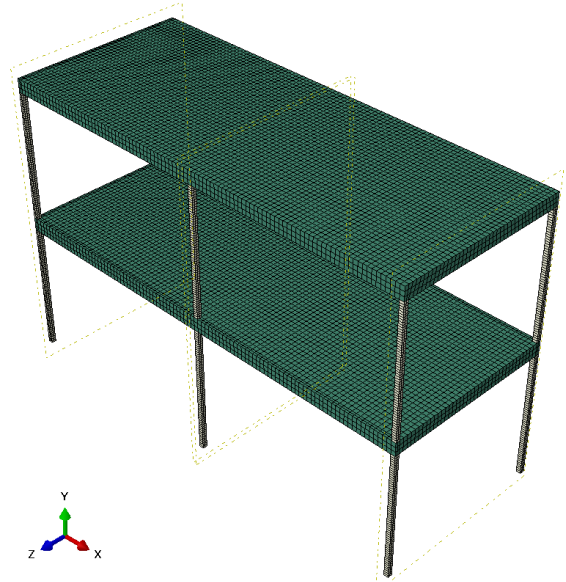


**Figure 3:** Mesh of the steel concrete building model meshed with C3D20R.

	Mode	Frequency [Hz]	Modal mass [kg]	Apparent mass [kg]
1	1 <sup>st</sup> Bending Z	1.06	37789	62113
2	1 <sup>st</sup> Bending X	1.07	38035	62102
3	1 <sup>st</sup> Torsion	1.52	15074	57375
4	2 <sup>nd</sup> Bending Z	2.69	38063	62425
5	2 <sup>nd</sup> Bending X	2.74	38298	62414
6	2 <sup>nd</sup> Torsion	3.89	15297	57837
7	3 <sup>rd</sup> Bending Y	14.62	15642	65035
8	3 <sup>rd</sup> Bending Y	15.19	15237	64882

**Table 9** Natural frequencies, modal masses and apparent masses for the building model meshed with C3D20R.

Due to the fact that most of the mass of the system is concentrated at the storeys, the length of the mode shapes can be approximated as:

$$L^2 \cong L_c^2 \quad (20)$$

And the modal mass as:

$$m \cong M_{Tc} \cdot L_c^2 \quad (21)$$

Which for this case results in:

$$m \cong M_{Tc1} \cdot L_{c1}^2 + M_{Tc2} \cdot L_{c2}^2 \quad (22)$$

Where sub-indexes 1 and 2 indicate 1<sup>st</sup> and 2<sup>nd</sup> storeys. respectively. For bending modes with stories moving as solid rigid. Eq. (22) simplifies to:

$$m \cong M_{Tc1} \cdot \psi_1^2 + M_{Tc2} \cdot \psi_2^2 \quad (23)$$

Mode	Squared Length		Modal mass [kg]	
	full model	Only storeys	full model	Only storeys
1 <sup>st</sup> Bending Z	0.61	0.64	37789	36834
1 <sup>st</sup> Bending X	0.61	0.64	38035	37068
1 <sup>st</sup> Torsion	0.26	0.26	15074	14878
2 <sup>nd</sup> Bending Z	0.61	0.65	38063	37217
2 <sup>nd</sup> Bending X	0.61	0.65	38298	37441
2 <sup>nd</sup> Torsion	0.26	0.26	15297	15250
3 <sup>rd</sup> Bending Y	0.24	0.27	15642	15305
3 <sup>rd</sup> Bending Y	0.23	0.26	15237	14793

**Table 10** : Squared length and modal masses of the building model

From Table 9 it is inferred that the apparent mass for all the modes is roughly equal to the mass of the stories, i.e. to the total mass of the concrete ( $M_{Tc} = 57600 \text{ kg}$ ). With respect to the total mass, it can be determined accurately with Eq. (21).

This structure was also meshed with beam elements B31 for the columns and shell elements S8R for the stories (see Fig. 4). Similar modal parameters were obtained with both models (3D and beam+shell). The squared length of the mode shapes was

estimated using only the translational DOF's. It can be observed in Table 11 that the squared length was estimated with a good accuracy using this model, the error being less than 7.5%.

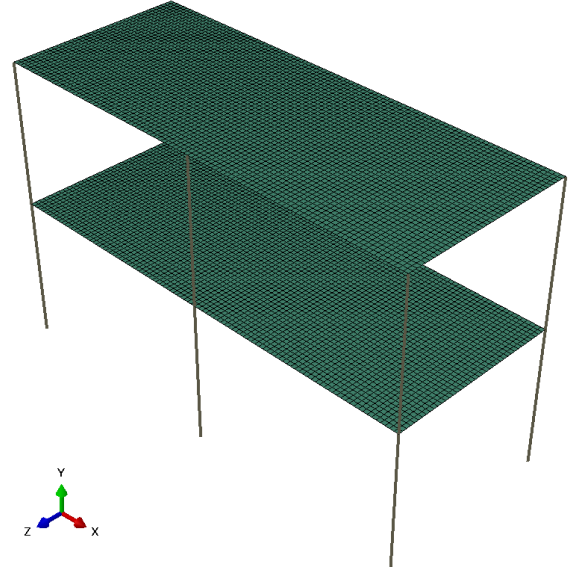


**Figure 4**: Mesh of the steel concrete building model meshed with beams and shells.

Mode	Squared Length		Apparent mass [kg]	
	3D	Beam-shell	3D	Beam-shell
1 <sup>st</sup> Bending Z	0.61	0.65	62113	59716
1 <sup>st</sup> Bending X	0.61	0.65	62102	59716
1 <sup>st</sup> Torsion	0.26	0.25	57375	60145
2 <sup>nd</sup> Bending Z	0.61	0.66	62425	59668
2 <sup>nd</sup> Bending X	0.61	0.66	62414	59668
2 <sup>nd</sup> Torsion	0.26	0.26	57837	60096
3 <sup>rd</sup> Bending Y	0.24	0.26	65035	59165
3 <sup>rd</sup> Bending Y	0.24	0.26	64882	59345

**Table 11** : Squared length and apparent mass using 3D and beam-shell elements.

## 11 CONCLUSIONS

In constant mass-density systems, the modal mass is equal to the product between the total mass of the structure and the length

squared. If the structure is constituted by two parts with the two volumes.  $V_1$  with the mass density  $\rho_1$ , and  $V_2$  with the mass density  $\rho_2$ , the modal mass is obtained with Eq. (4) [1].

If the mass density is not constant, the ratio modal mass/squared length is equal to an apparent mass. which is different for each mode and depends on the mode shape and how the mass is distributed in the structure.

In this paper, two steel cantilever structures made of steel and concrete and a two-story building model have been assembled in ABAQUS [5] and meshed with 3D, beam, and shell elements.

The squared length of the mode shapes has been estimated with a good accuracy using Eq. (18).

In structures constituted by two parts of different mass-density, the cross-length is non-zero (except for orthogonal mode shapes). Moreover, the ratio of squared cross-lengths is constant for all the modes and equal to the ratio of total masses of the two different materials.

In some particular cases and in some specific modes, the assumption of constant mass density is still valid. This is the case with two of the structures studied in his paper: beams with constant mass per unit length and building models with most of the mass concentrated at the stories.

## ACKNOWLEDGES

The economic support given by the Spanish Ministry of Education through the project MCI-20-PID2019-105593GB-I00/AEI/10.13039/501100011033 are gratefully appreciated.

## REFERENCES

- [1] M. Aenlle. Martin Juul. R. Brincker. "Modal Mass and Length of Mode Shapes in Structural Dynamics". *Shock and Vibration*. vol. 2020. Article ID 8648769. 16 pages. 2020.
- [2] M. Aenlle. Martin Juul. R. Brincker. "Modal Mass in Constant Mass-Density Systems". In these proceedings. 2021.
- [3] Clough R.W. and Penzien J. (1993) *Dynamics of structures*. 2nd edition. New York: McGraw-Hill
- [4] Chopra A.K. (1995) *Dynamics of Structures*. New Jersey: Prentice Hall
- [5] ABAQUS UNIFIED FEA. Dassault Systems

## MODAL MASS IN CONSTANT MASS-DENSITY SYSTEMS

R. Stufano<sup>a</sup>, A. Fraddosio<sup>b</sup>, M. Aenlle<sup>c</sup>, F. Pelayo<sup>c</sup> and R. Brincker<sup>d</sup>

<sup>a</sup> Department of Civil, Environmental, Construction and Chemical Engineering  
Polytechnic University of Bari  
70125 Bari, Italy  
e-mail: r.stufano1@studenti.poliba.it

<sup>b</sup> Department of Civil Engineering Sciences and Architecture  
Polytechnic University of Bari  
70125 Bari, Italy

<sup>c</sup> Department of Construction and Manufacturing Engineering  
University of Oviedo  
33204 Gijón, Spain

<sup>d</sup> Department of Civil Engineering  
Technical University of Denmark  
2800 Kongens Lyngby, Denmark

**Abstract.** Mass normalized mode shapes (scaled mode shapes) contain information of both the modal mass (magnitude of the vector) and the shape of the mode (deflection shape). In scaled mode shapes the modal mass is dimensionless unity. On the other hand, a mode shape is said to be un-scaled if it is not mass normalized. Un-scaled mode shapes only contain information of the shape of the mode and a scaling factor (or modal mass) is needed to define completely the mode shape. It has been demonstrated that the modal mass in constant mass-density systems is equal to the product between the total mass of the structure, and the length of the mode shapes squared. This means that a relation between the modal masses of the different modes exists, i.e. when using modal analysis only the modal mass of one mode is needed because all the modal masses can be estimated from such a mode. In this paper, numerical simulations on different structures (beams, plates and 3D solids) with constant mass-density were performed. It is demonstrated that using the modal mass of the first mode, and the length of the mode shapes normalized to the largest component equal to unity, the modal masses for the rest of the modes can be estimated with a good accuracy.

**Key words:** Modal Mass, Dynamics of Structures, Mode shapes, Normalization

### 1 INTRODUCTION

A modal model is a mathematical model formulated to describe the dynamic behavior of a structure in terms of modal parameters, namely natural frequencies, damping ratios, mode shapes and modal masses.

Mode shapes can be normalized in many different ways, the most common techniques being mass normalization, normalization to the unit length of the mode shape (length scaling) and normalization to a component (usually to the largest component) equal to unity (DOF scaling) [1,2,3]. For this reason, the magnitude

and the units of the modal mass depend on the normalization method.

In case of normalization to the mass matrix (mass normalization), the mode shapes contain information of both the shape of the mode and the scale (scaling factor or modal mass).

The modal mass of mass-normalized mode shape is dimensionless unity for all the modes, whereas the units of the mode shapes are  $1/\sqrt{kg}$  for the translational DOF's and  $1/(m\sqrt{kg})$  for the rotational DOF's.

A mode shape is said to be normalized to the unit length if its length is unity. In discrete systems, the length of the mode shape vector  $\boldsymbol{\psi}$  (length of a vector in an Euclidean space) is defined as [2,4]:

$$L_E^2 = \sqrt{\boldsymbol{\psi}^T \boldsymbol{\psi}} \quad (1)$$

However, the modal mass estimated using the length defined by Eq. (1) is dependent upon the number of DOF's in the model.

Another approach to normalize mode shapes is to scale the largest component (or some other component) to a certain value (for instance equal to unity) [1,2]. If the modal masses (normalization to the largest component equal to unity) of a numerical and an experimental model are going to be compared, the DOF used for normalization should be the same in the FE model and the test. i.e. the DOF must be shared. If this is not the case, then the modal mass is dependent upon selected DOF.

In this paper, numerical simulations on different structures (beams and 3D solids) with constant mass-density were performed. An approximate formulation to calculate the length of the mode shapes is proposed, which uses only the nodal components of the mode shapes. It has been proved that the modal masses of the structure can be estimated with a good accuracy when the length of the mode

shapes and the modal mass of one mode is known. Moreover, it has been proved that the cross-length for all the modes is zero.

## 2 BASIC THEORY

In discrete systems, the mode shapes are vectors and the modal mass corresponding to an un-scaled mode shape ( $\boldsymbol{\psi}$ ) can be calculated with the equation [1,2,3]:

$$m = \boldsymbol{\psi}^T \mathbf{M} \boldsymbol{\psi} \quad (2)$$

Where  $\mathbf{M}$  is the mass matrix and  $m$  the modal mass.

If the mass-density  $\rho$  of the system is constant, Eq. (2) can be expressed as [2]:

$$m = \rho \boldsymbol{\psi}^T \mathbf{V} \boldsymbol{\psi} \quad (3)$$

Where  $\mathbf{V}$  is the volume matrix. If the total volume of the system is denoted as  $V_T$ , Eq. (2) can also be formulated as:

$$m = M_T \frac{\boldsymbol{\psi}^T \mathbf{V} \boldsymbol{\psi}}{V_T} \quad (4)$$

Where the term:

$$L^2 = \frac{\boldsymbol{\psi}^T \mathbf{V} \boldsymbol{\psi}}{V_T} \quad (5)$$

is the length of the mode shape  $\boldsymbol{\psi}$ , which depends on the volume of the structure and on the mode shapes. Eq. (4) can also be expressed as:

$$m = M_T L^2 \quad (6)$$

which indicates that in constant mass-density systems the modal mass is equal to the product between the total mass of the structure and the length squared.

From Eq. (6) it is derived that:

$$\frac{m_1}{L_1^2} = \frac{m_2}{L_2^2} = \dots = \frac{m_r}{L_r^2} = \dots = M_T \quad (7)$$

Where the subindex ‘r’ indicates the order of the mode.

From Eq. (6) is inferred that if the length of the mode shapes is known:

- Only one modal mass needs to be known. The rest of the modal masses can be estimated with Eq. (7).
- The modal masses can be estimated if the total mass of the structure is known.

If a structure is discretized with many finite elements of equal volume, Eq. (5) can be accurately approximated by:

$$L^2 \cong \frac{\Delta V \sum_{k=1}^{N_V} \psi_k^2}{N_V \Delta V} = \frac{\sum_{k=1}^{N_V} \psi_k^2}{N_V} \quad (8)$$

Where  $N_V$  is the number of elements (number of volumes) of the structure. As the components of the mode shapes are commonly known at the nodes of the elements, Eq. (8) can also be approximated by means of the expression:

$$L^2 \cong \frac{\Delta V \sum_{k=1}^N \psi_k^2}{N \Delta V} = \frac{\psi^T \psi}{N} \quad (9)$$

Where  $N$  is the number of nodes of the model.

The cross-length between the mode shapes  $\psi_i$  and  $\psi_j$  is defined as:

$$L_{ij}^2 = \frac{\psi_i^T V \psi_j}{V_T} \quad (10)$$

Which can be approximated (for constant mass-density systems) by:

$$L_{ij}^2 = \frac{\psi_i^T \psi_j}{N} \quad (11)$$

From Eq. (11) is inferred that the all the mode shapes in constant mass-density systems are orthogonal, i.e. non-orthogonality is an indicator of non-constant mass-density.

### 3 NUMERICAL SIMULATIONS

#### 3.1. Cantilever Beam. 3D model.

A steel cantilever beam with rectangular cross-section ( $4 \text{ cm} \times 5 \text{ cm}$ ) and 1 meter long, was assembled in the finite element software ABAQUS [5]. The steel was considered linear -elastic and the following material properties were assumed: mass-density  $\rho = 7850 \text{ kg/m}^3$ , Young’s modulus  $E = 210 \times 10^9 \text{ N/m}^2$ , and Poisson ratio  $\nu = 0.3$ . The total mass of the system is  $M_T = 15.7 \text{ kg}$ .

The beam was initially meshed with eight-node linear hexahedral elements (C3D8R) with an approximate global size of 0.005 m (see Figs 1 to 8). The natural frequencies and modal masses (mode shapes normalized to the largest component equal to unity) corresponding to the first eight modes are presented in Table 1, whereas the mode shapes are shown in Figures 1 to 8.

mode	frequency [Hz]	modal mass [kg]
1	33.19	3.93
2	41.57	3.93
3	206.48	3.97
4	257.52	3.99
5	571.56	4.03
6	708.42	4.09
7	708.60	4.39
8	1102.10	4.13

**Table 1** : Natural frequencies and modal masses.

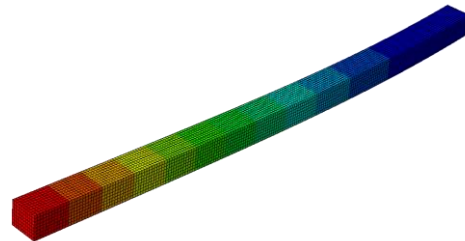


**Figure 1** : First Bending Y

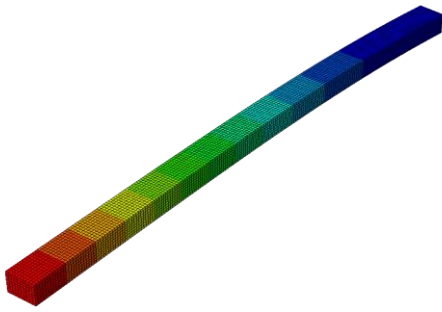


Figure 2 : First Bending X

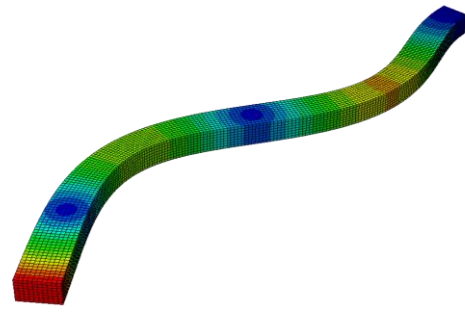


Figure 6 : Third Bending X

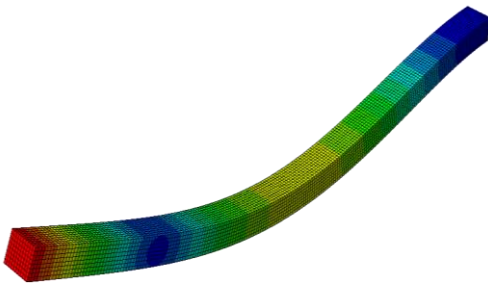


Figure 3 : Second Bending Y

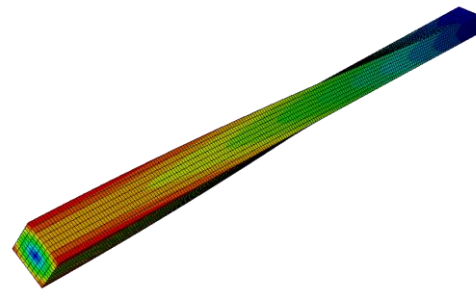


Figure 7 : Torsion

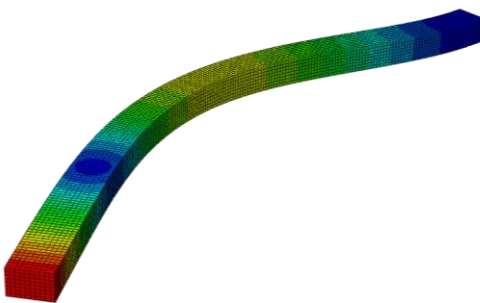


Figure 4: Error! No hay texto con el estilo especificado en el documento. : Second Bending X

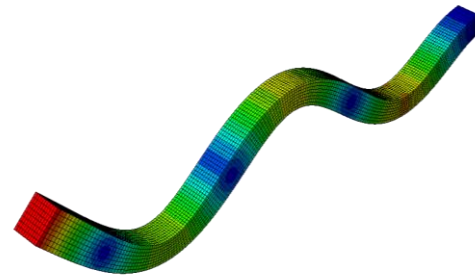


Figure 8 : Fourth Bending Y

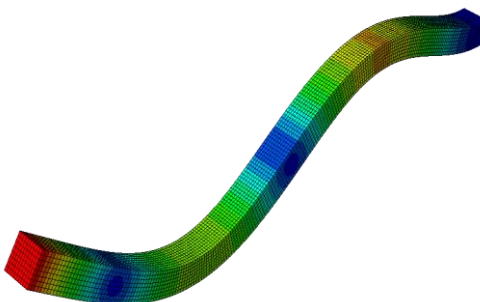


Figure 5 : Third Bending Y

The analytical expressions of the mode shapes of a cantilever beam can be found in the literature [1,3], from which is derived that the analytical squared length of all the bending modes is  $L^2 = 0.25$ , whereas the squared length of the torsional mode as  $L^2 = 0.2729$ . The squared lengths estimated with Eq. (9) and the cross-lengths estimated with Eq (11) are presented in Table 2, where the diagonal terms indicate the length and the off-diagonal ones indicate the cross-length. From Table 2 is inferred that Eq. (9) provides a good accuracy in the estimation of the length

of the mode shapes, the maximum error in bending modes being 5.7%.

Due to the fact that the mass-density is constant, the cross-length for all the modes must be zero. It can be observed in Table 2 that, as expected, all off-diagonal terms are very close to zero.

First Bending Y	0.25	0	0.0025	0	0.0025	0	0	0.0025
First Bending X	0	0.25	0	0.0026	0	0.0025	0	0
Second Bending Y	0.0025	0	0.25	0	0.0027	0	0	0.0026
Second Bending X	0	0.0026	0	0.26	0	0.0027	0	0
Third Bending Y	0.0025	0	0.0027	0	0.26	0	0	0.0028
Third Bending X	0	0.0025	0	0.0027	0	0.26	0	0
Torsion	0	0	0	0	0	0	0.33	0
Fourth Bending Y	0.0025	0	0.0026	0	0.0028	0	0	0.27

**Table 2 :** Length Matrix of the Cantilever beam.

Due to the fact that the system has constant mass-density, Eq. (6) has to be fulfilled, i.e. the ratio  $\frac{m}{L^2}$ , shown in Table 3, must be the same for all the modes and equal to the total mass of the system. It can be observed in Table 3 that the maximum error is 0.86% for the bending modes, whereas a larger error has been obtained for the torsional mode (16%), indicating that a more refined mesh is needed in order to calculate the length with a better accuracy.

Mode	$M_T$
1	15.62
2	15.62
3	15.61
4	15.61
5	15.59
6	15.59
7	13.19
8	15.56

**Table 3 :** Total mass Matrix of Cantilever beam.

The model was also meshed using twenty-node hexahedral elements (C3D20R). Moreover, in

order to study the influence of the size of the finite elements, simulations were performed using finite elements (C3D8R and C3D20R) of the following size: 0.0025 m, 0.005 m, 0.010 m, 0.020 m, and 0.030 m. The squared lengths obtained with Eq. (9) for all the simulations are presented in Figs 11 to 18.

As expected, the accuracy of the technique increases as the size of the elements diminishes, and better accuracy is obtained with the quadratic elements C3D20R. However, the discrepancies between the squared lengths obtained with both types of elements decrease as the size of the elements diminishes.

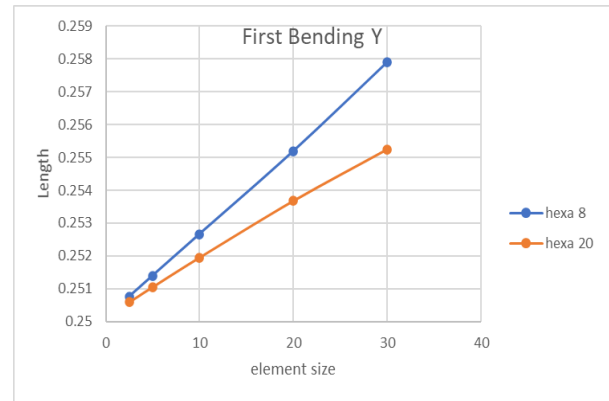


**Figure 11 :** Squared lengths obtained for different sizes of finite elements (First Bending Y)

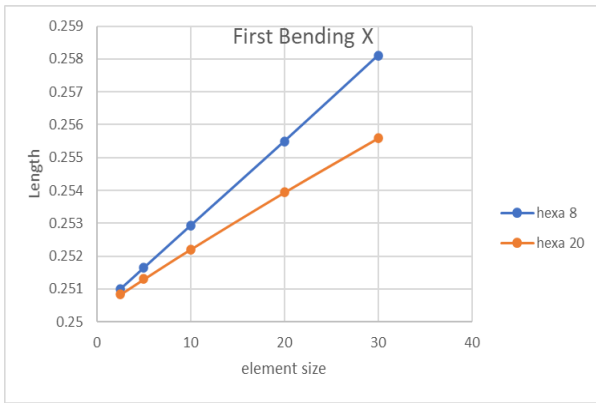


**Figure 12** : Squared lengths obtained for different sizes of finite elements (First Bending X)

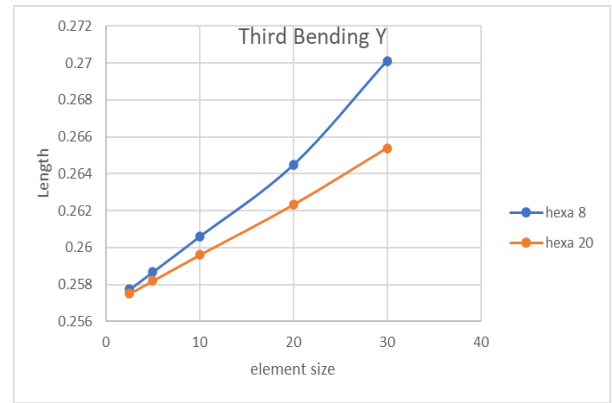


**Figure 15** : Squared lengths obtained for different sizes of finite elements (Third Bending Y)

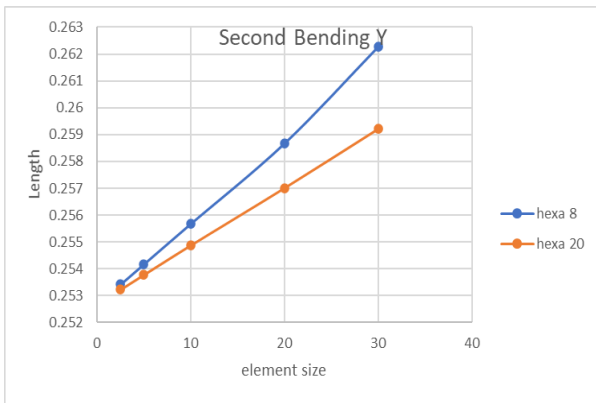


**Figure 13** : Squared lengths obtained for different sizes of finite elements (Second Bending Y)

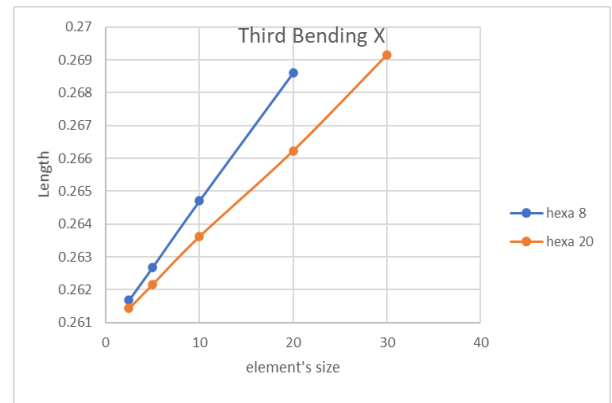


**Figure 16** : Squared lengths obtained for different sizes of finite elements (Third Bending X)

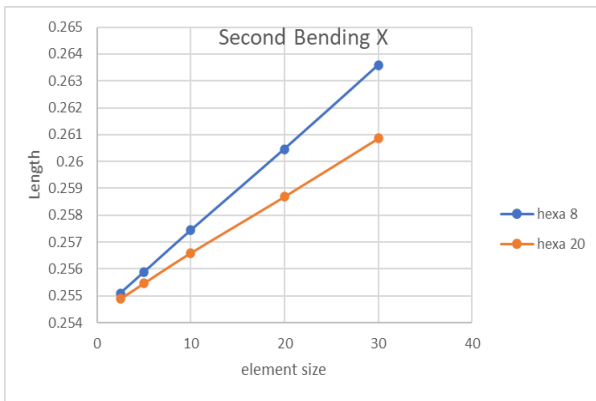


**Figure 14** : Squared lengths obtained for different sizes of finite elements (Second Bending X)

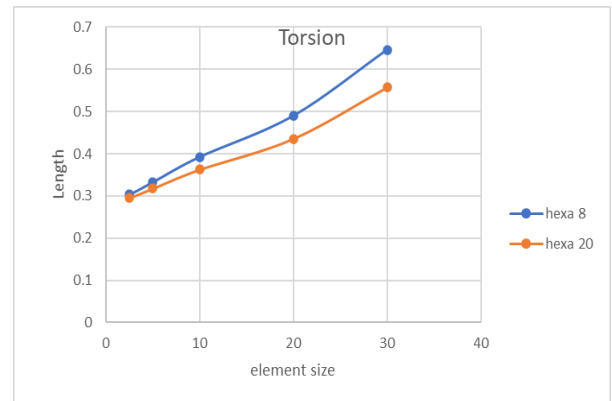


**Figure 17** : Squared lengths obtained for different sizes of finite elements (Torsion)

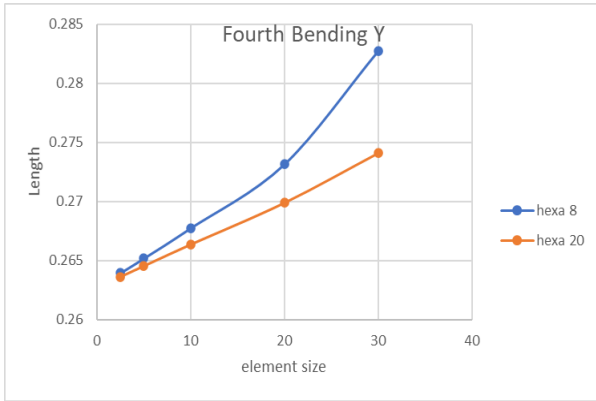


**Figure 18** : Squared lengths obtained for different sizes of finite elements (Fourth Bending Y).

In order to study the effect of the elements aspect ratio, the model was meshed with elements C3D20R and dimensions (mm)  $2.5 \times 2.5 \times 2.5$ ,  $2.5 \times 2.5 \times 5$  and  $2.5 \times 2.5 \times 10$ . It can be observed in Table 4, where the ratio  $m/L^2$  is presented, that similar results have been obtained with the different meshes, the accuracy being slightly better with cubic elements.

Mode	Ratio $m/L^2$		
	Size 2.5*2.5	Size 2.5*5	Size 2.5*10
1	15.67	15.64	15.58
2	15.67	15.64	15.58
3	15.66	15.64	15.58
4	15.66	15.64	15.58
5	15.66	15.63	15.57
6	15.66	15.63	15.57
7	14.51	14.51	14.51
8	15.65	15.62	15.56

**Table 4** : Ratio  $m/L^2$  for different finite element sizes.

### 3.3. Cantilever Beam. Beam model.

The aforementioned cantilever beam was also meshed with ABAQUS beam elements B32 with an approximate length of 0.0025 m, obtaining the same modal parameters. The length of the mode shapes, calculated with Eq. (9) and using only the translational DOF's, is

presented in Table 5, together with those obtained with the 3D model.

Mode	Squared length	
	Model B32	Model C3D20R
First Bending Y	0.25	0.25
First Bending X	0.25	0.25
Second Bending Y	0.25	0.25
Second Bending X	0.25	0.25
Third Bending Y	0.25	0.26
Third Bending X	0.26	0.26
Torsion	0.5*	0.30+
Fourth Bending Y	0.26	0.26

**Table 5** : Squared lengths obtained with beam and 3D models. \* with rotational DOF's. + Calculated with translational DOF's.

The bending mode shapes were normalized to the largest component equal to unity, which means that the translational DOF's are dimensionless, whereas the rotational DOF's have the units  $[\frac{1}{m}]$ .

However, the torsional mode was normalized to the largest rotation equal to unity, which means that the squared length of the torsional mode ( $L_\theta^2$ ) is also dimensionless. With respect to the modal mass, it is given in units of  $kg\ m^2$  and obtained with the expression:

$$m_\theta = I_M L_\theta^2 \quad (12)$$

Where  $I_M$  is the mass moment inertia of the structure with respect to the longitudinal axes of the beam, which for a rectangular section of dimensions  $a \times b$  is given by:

$$I_M = M_T \frac{(a^2 + b^2)}{12} \quad (13)$$

From the finite element model it has been obtained that  $L_\theta^2 = 0.5$  and  $m_\theta = 2.682 \times 10^{-3} kg\ m^2$

The modal masses and the squared lengths of the torsional mode, obtained with the 3D

model and with the beam model, can be related as:

$$M_T = \frac{m}{L^2} = \frac{m_\theta}{\frac{(a^2 + b^2)}{12} L_\theta^2} \quad (14)$$

### 3.4. Cantilever Cross Beam.

A steel cantilever beam with two short beams (rectangular section 4 cm × 5 cm and length 4 cm) attached near the free end, was assembled in ABAQUS [5] and meshed with elements C3D20R of size 0.0025 m (Fig. (23)). The same mechanical properties as those considered in the previous models were used in the simulations, the total mass of the beam being  $M_T=17.27$  kg.

The lengths of the mode shapes (Eq. (9)), the modal masses and the total mass estimated with Eq. (7) are presented in Table 5. The modal masses (kg) are presented in Table 6.

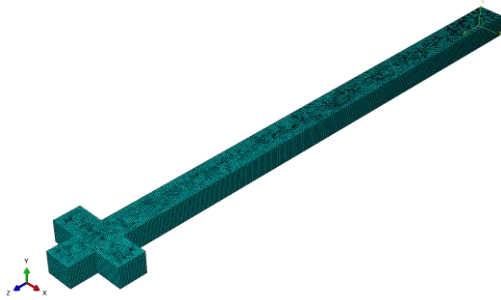


**Figure 23** : Cantilever cross beam: 3D model

This structure was also meshed with beam elements B32 with an approximate length of 0.0025 m. The beam was modelled with constant cross section and the effect of the attached beams were considered as concentrated masses and rotary inertias.

The length of the bending mode shapes were calculated with Eq. (9) using only the translational DOF's (the contribution of the rotational DOF's is neglected). However, Eq. (9) only considers the components of the mode

shapes at the nodes, i.e, the volume of lumped masses is not taken into account. This means that the effect of the attached masses is not considered and Eq. (5) must be reformulated as:

$$L^2 \cong \frac{L_1^2 V_1 + L_{\Delta M}^2 V_{\Delta M}}{V_1 + V_{\Delta M}} \quad (15)$$

Where  $L_1^2$  and  $V_1$  indicate length and volume of the beam (calculated with Eq. (9) and without considering the lumped masses) and  $L_{\Delta M}^2$  and  $V_{\Delta M}$  refer to the length and the volume of the lumped masses. A better accuracy can be obtained if the effect of the rotary inertias are considered in Eq. (13).

Mode	Squared length	
	Model B32	Model C3D20R
first bending Y	0.30	0.30
first bending X	0.30	0.30
second bending Y	0.38	0.37
second bending X	0.39	0.37
torsion	0.07	---
third bending Y	0.37	0.36
third bending X	0.40	0.36
fourth bending Y	0.32	0.30

**Table 5** : Cantilever cross beam: squared length.

Mode	Modal mass	
	Model B32	Model C3D20R
first bending Y	5.1484	5.1525
first bending X	5.1587	5.1623
second bending Y	6.4947	6.4873
second bending X	6.6568	6.6410
torsion	1.1925	---
third bending Y	6.3863	6.3192
third bending X	6.9497	6.7775
fourth bending Y	5.5411	5.3900

**Table 6** : Cantilever cross beam: modal masses (kg)

It can be observed in Table 5 that the length of

the mode shapes is estimated with a good accuracy using the beam model, the error increasing with the order of the mode. With respect to the ratio  $m/L^2$  (Table 6), a good accuracy has been obtained for all the modes with both the 3D and the beam model.

Mode	Total mass $M_T = m/L^2$	
	Beam	3D
first bending Y	17.28	17.15
first bending X	17.31	17.15
second bending Y	17.47	17.26
second bending X	17.84	17.25
torsion	---	16.58
third bending Y	17.64	17.36
third bending X	18.62	17.32
fourth bending Y	17.83	17.20

**Table 7** : Cantilever cross beam : total mass.

## 11 CONCLUSIONS

In constant mass-density systems, the modal mass is equal to the product between the total mass of the structure and the length squared. This means that the modal masses of experimental systems can be estimated if the total mass is known and the length of the experimental mode shapes can be estimated with a reasonable accuracy.

In this paper, two steel cantilever structures have been assembled in ABAQUS [5], which have been meshed with 3D and beam elements.

The length of the mode shapes when the model is meshed with 3D elements can be estimated with a good accuracy using Eq. (9), where the components of the mode shapes at the nodes have to be known.

When using beam elements, the length of the bending modes can also be calculated with Eq. (9) considering the translational DOF's. The contribution of the rotations can be neglected if the elements are small.

When using beam elements, Eq. (9) can also be used to calculate the length of the torsional modes, considering the rotational DOF's.

When the length is calculated with Eq. (9), lumped masses and inertias are not considered. Their contribution to the length of the mode shapes have to be considered separately.

For equal size of finite elements, Eq. (9) is more accurate for bending modes than for torsional modes.

The beam models allow to estimate the length of the mode shapes with a good accuracy with less computational time.

## ACKNOWLEDGES

The economic support given by the Spanish Ministry of Education through the project MCI-20-PID2019-105593GB-I00/AEI/10.13039/501100011033 are gratefully appreciated.

## REFERENCES

- [1] Clough R.W. and Penzien J. (1993) Dynamics of structures, 2nd edition. New York: McGraw-Hill
- [2] M. Aenlle, Martin Juul, R. Brincker, "Modal Mass and Length of Mode Shapes in Structural Dynamics", Shock and Vibration, vol. 2020, Article ID 8648769, 16 pages, 2020.
- [3] Chopra A.K. (1995) *Dynamics of Structures*. New Jersey: Prentice Hall
- [4] Dianat S.A and Saber E. (2009) *Advanced Linear Algebra for Engineers with MATLAB*, New York: CRC Press.
- [5] ABAQUS UNIFIED FEA. Dassault Systems

## **Section 2: Seismic engineering**

---

## MAGNETO RHEOLOGICAL FLUIDS IN CIVIL ENGINEERING

**Andrea Vázquez Greciano\***, **José Ignacio Hernando García\***, **Jesús Ortiz Herrera\*** and  
**Antonio Aznar López\***

\* Escuela Técnica Superior de Arquitectura de Madrid,  
Universidad Politécnica de Madrid  
28040 Madrid, Spain  
e-mail: andrea.vazquez.greciano@upm.es  
ORCID: 0000-0001-9623-0721

**Abstract.** Seismic activity and vibrations may be predictable, but changes in the structure such as a variation in the stiffness during a seismic event or different induced load patterns in footbridges and bridges may require a damping response that varies in time as well. In this field of study, the incorporation of magneto rheological materials could be useful.

Magneto Rheological Fluids (MRF) are characterized by being capable of changing their physical properties when subjected to a magnetic field. MRFs are made of micron-sized ferrous particles suspended in a base fluid. With a magnetic field in place, the particles align in chain-like structures that show greater resistance to flow, which causes a change in viscosity from liquid to visco-elastic solids in just milliseconds and back to fluid when the magnetic field is no longer present. These fluids show outstanding features like fast response, reversibility and controllability.

This work presents a rheological background to the MRF technology through different types of fluids, as well as the MRFs' characteristics, operational modes, etc. The study presented in this work opens the door to real applications mostly related to structural engineering. A remarkable case study of the use of MRF is presented: the damper located in the Dongting Lake Bridge. The system reduces wind-rain induced vibrations on cables taking advantage of MRF, with regards to that both reliability and maintenance along with aesthetics are factors that determine the project.

**Key words:** Magneto Rheological Fluids, Vibrations, Viscosity, Electromagnetism.

### 1 INTRODUCTION

In the event of seismic activity, building protection objectives may be summarised as: maintaining enough stiffness so that the construction behaves within the elastic range and ensuring ductility energy dissipation when it reaches the inelastic range.

On the one hand, resistant design aim is to make the structure withstand seismic forces with as little damage as possible, depending on the magnitude of the earthquake and on the

type of building considered. A resistant design takes into account both the materials used and their mechanical characteristics, and the floor plan and elevation geometry, configuration, slenderness, its joints...

On the other hand, control systems either dissipate energy produced by dynamic loading or modify the energy that gets in the structure. This way, constructions withstand smaller stress.

## 1.1 Control systems

According to ISO 3010:2017<sup>[1]</sup>, control systems can be classified as follows:

- Passive systems. These are widely used due to their reduced cost and because there is no energy input requirement. They are automatically activated by the energy produced by the excitation. Major drawback is these systems are not capable of modifying the response under changing stimulus or structure damage.

- Active systems. They are powered mechanisms capable of adjusting the control forces applied. A series of sensors measure the structure response that is analysed by controllers which establish the amount of force the actuator is to exert. A serious drawback is that energy supply could be shut down during a seismic event, therefore leaving the building unprotected.

- Hybrid systems. These consist of a combination of active and passive systems. While the passive part reduces the response, the active one is used to further decrease the acceleration or displacement. For this reason, control forces are smaller than those in active systems. Therefore, the energy input required is much lower, resulting in more reliable systems.

- Semi-active systems. The sensor-controller-actuator operating principle is similar to that in active systems, only semi-active ones are not designed to exert a force in the structure. Consequently, these mechanisms are generally smaller and the amount of energy required is lower. Semi-active systems provide with fast changing response in case of varying conditions.

Seismic activity and vibrations may be predictable, but changes in the structure such as a variation in the stiffness during a seismic event or different induced load patterns in footbridges and bridges may require a damping response that varies in time as well. In this field

of study, the incorporation of magneto rheological materials in semi-active fluid devices could be useful, resulting in an improvement in functionality and costs.

## 2 RHEOLOGICAL BACKGROUND

Rheology is the study of flow and deformation of matter in response to the influence of stresses. Fluids have no fixed shape of their own and flow when an external force is applied, this is, while a solid can resist an applied shear stress by deforming, a fluid deforms continuously under the influence of shear stress. For this reason, fluids behaviour is analysed in terms of stress and strain rate. Therefore, fluids can also be defined as substances that can resist an applied shear stress by moving<sup>[2]</sup>.

Substances are composed of molecules between which act cohesive forces. Solid molecules are closely packed together and so its bonds are the strongest, keeping the molecules at fixed positions. Liquid molecules can move relative to each other although the volume remains constant due to strong cohesive forces. Gas molecules are widely spaced and their cohesive forces are small, which is the reason these fluids can move about at random<sup>[2,3]</sup>.

Individual molecule dynamics should be considered enough to define a fluid sample. However, it is convenient to disregard the atomic nature of a substance and consider it as continuous and homogeneous, this is, a continuum. This idealization is valid as long as the molecular structure is very small compared to the size of the system considered. This way, substances can be described by their properties as point functions<sup>[2,3]</sup>.

One of these properties is the viscosity, which represents the internal resistance of a fluid to motion. It is a consequence of the cohesive forces between molecules. Fluids can be classified based on their viscosity as follows

(figure 1):

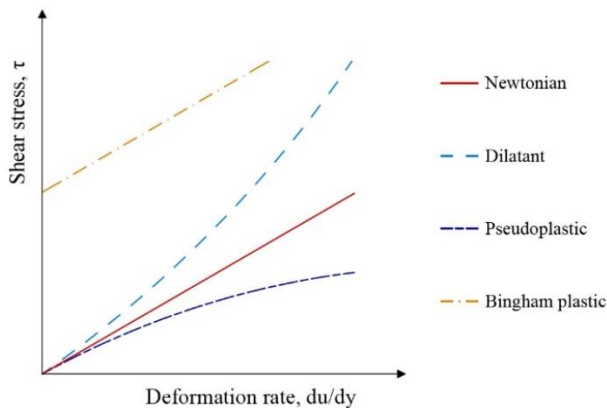


**Figure 1:** Types of fluids. Variation of shear stress with the rate of deformation.

- Ideal fluids are incompressible and have no viscosity, hence the lack of resistance to shear stress ( $\tau$ ).
- Ideal solids overcome shear stress with no deformation rate, having infinite viscosity.
- Newtonian fluids are those for which the shear stress is proportional to the deformation rate ( $du/dy$ ). The constant of proportionality is called dynamic viscosity ( $\mu$ ).
- Non-Newtonian fluids are those in which the relationship between shear stress and deformation rate is not linear. In dilatant fluids,  $\mu$  increases with  $du/dy$ . On the other hand, in pseudoplastic fluids,  $\mu$  decreases with  $du/dy$ . If the material behaves as a solid up to the yield stress and then deforms continuously as a fluid, it is called Bingham plastic.

### 3 MAGNETORHEOLOGICAL FLUIDS

Magnetorheological (MR) fluids were first described in the 1940's by Jacob Rabinow<sup>[4-6]</sup>.

MR fluids are dispersions composed of micron-sized magnetizable particles (1-10  $\mu\text{m}$ ) suspended in an organic or aqueous liquid carrier.

These smart materials have the ability to modify some aspects of their rheology when an external magnetic field is applied.

### 3.1 MR fluid components

MR fluids are made up of three basic components: magnetizable particles, base fluid and additives<sup>[4-9]</sup>.

As for the magnetically active phase, different ceramic, metal and alloy compositions such as iron-cobalt alloys, manganese zinc ferrite or nickel zinc ferrite have been described to prepare MR fluids<sup>[4]</sup>. However, the most common magnetic material used for these dispersions is high purity iron powder (carbonyl iron, figure 2) due to its purity (>99%), high saturation magnetisation and non-abrasive spherical shape.

The base fluid is a carrier in which the magnetic particles are suspended, such as silicon oil, synthetic oil or mineral oil<sup>[5]</sup>. It should present temperature-independent low viscosity and be non-reactive towards the magnetic particles and the materials used in the device.

Additives include stabilizers and surfactants. These are required to control the settling and suspension of particles or to provide anti-wear properties.

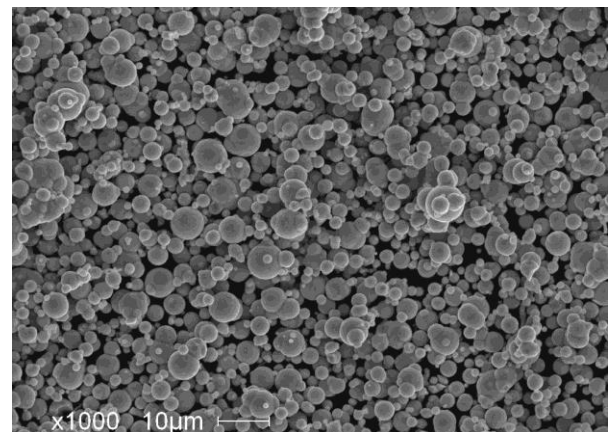


**Figure 2:** Scanning electron micrograph of carbonyl iron powder<sup>[10]</sup>.

### 3.2 MR fluids rheology

The viscosity of MR fluids varies when a magnetic field is applied. In the off-state (no

magnetic field) MR fluids flow freely, with low viscosity. When an external magnetic field is applied (on-state), there is a polarization of the magnetizable particles which rearrange into chain-like structures in the direction of the magnetic field <sup>[3,4,11,12]</sup>, as seen in figure 3. The chain structure restricts the movement and the yield strength increases. As a result, the fluid exhibits greater resistance to flow, which causes a change in viscosity from liquid to visco-elastic solids in just milliseconds.

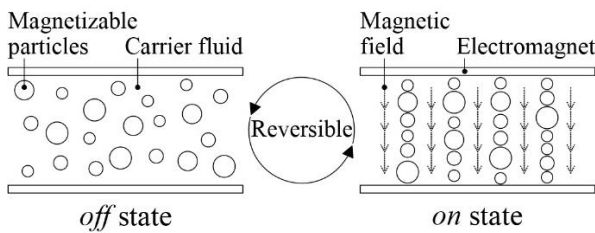


Figure 3: MR fluid mechanism.

This is a reversible process since MR fluids switch back to liquid when the magnetic field is no longer activated. The degree to which the fluid changes to a semi-solid is proportional to the strength of the magnetic field, giving MR fluids great controllability and precision <sup>[12]</sup>. This is the reason MR fluids make an outstanding semi-active control system, the response can be modified in milliseconds for the specific requirements. Moreover, if the magnetic field were damaged, it would behave as a passive system, providing the structure with protection.

MR fluids behave as Non-Newtonian fluids during the on-state. They often exhibit shear-thinning behaviour (pseudoplastic fluid) <sup>[3]</sup> or Bingham plastic behaviour <sup>[8,11]</sup>. Table 1 shows the characteristic dynamic viscosity values for different materials. The dynamic viscosity of MR fluids can reach values  $10^5$  times greater than water and up to  $10^3$  times greater than engine oil.

Material (20°C)	Dynamic viscosity $\mu$ (Pa·s)
Water	0.001
Mercury	0.0015
Olive oil	0.01
Engine oil	0.1
Silicon oil	0.35
Glycerin	1.50
Honey	1-10
MR fluid	1-100

Table 1: Dynamic viscosity (order of magnitude) of various materials.

## 4 MR FLUIDS OPERATIONAL MODES

MR fluids standard operating modes are: valve mode, direct shear mode, and squeeze mode <sup>[5,12,13,14]</sup>, depending on the type of deformation employed.

### 4.1 Valve mode

In valve mode, the MR fluid flows between two static plates (or an orifice) as a consequence of a pressure drop. The magnetic field applied is perpendicular to the flow and controls the viscosity, therefore modifying the velocity profile <sup>[14-15]</sup>. Valve mode scheme is defined in figure 4.

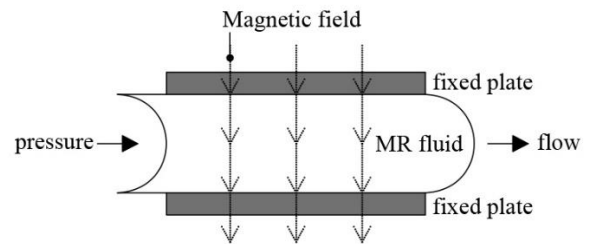


Figure 4: Valve mode.

The pressure drop ( $\Delta P$ ) is caused by both the pure rheological ( $\Delta P_{\mu}$ , viscous) component and the magnetorheological component ( $\Delta P_{mr}$ , magnetic field-dependent). The value of the pressure drop is defined in equation 1 <sup>[5, 16]</sup>:

$$\Delta P = \Delta P_{\mu} + \Delta P_{mr} \quad (1)$$

$$\Delta P = \frac{12 \cdot \mu \cdot Q \cdot L}{g^3 \cdot w} + \frac{\tau_{mr} \cdot L \cdot f}{g}$$

Equation 1 shows that the pressure drop is dependent on the dynamic viscosity ( $\mu$ , Pa·s) with no applied field, the flow rate ( $Q$ , m<sup>3</sup>·s) and the length ( $L$ , m) fluid gap ( $g$ , m) and width ( $w$ , m) of the flow channel in the viscous component. The magnetic field-dependent component depends on the variable yield stress ( $\tau_{mr}$ , N/mm<sup>2</sup>) developed in response to the applied magnetic field,  $L$  and  $g$  form the geometrical data and an empirical factor ( $f$ ). The parameter  $f$  is a function of the flow velocity profile and has a value from 2 (if  $\Delta P_{mr} / \Delta P_{\mu} < 1$ ) to 3 (if  $\Delta P_{mr} / \Delta P_{\mu} > 100$ )<sup>[16]</sup>.

The minimum volume of active fluid is defined in equation 2, in order to achieve the desired effect at a certain flow rate:

$$V = L \cdot g \cdot w \quad (2)$$

$$V = \frac{12 \cdot \mu}{f^2 \cdot \tau_{mr}^2} \cdot \frac{\Delta P_{mr}}{\Delta P_{\mu}} \cdot Q \cdot \Delta P_{mr}$$

This operational mode is widely spread and some applications are dampers, actuators and shock absorbers<sup>[14,15]</sup>.

#### 4.2 Shear mode

In shear mode, MR fluid is placed between two surfaces, a fixed one and a moving one. The magnetic field is applied perpendicularly to the motion of the surface<sup>[5, 12, 14]</sup>. Shear mode scheme is displayed in figure 5.

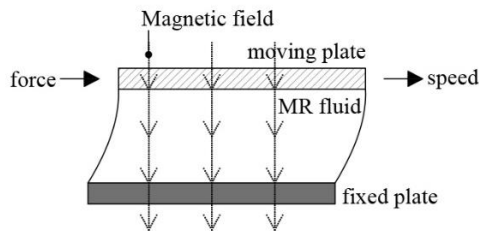


Figure 5: MR Direct-shear mode.

The force ( $F$ ) can be divided into a pure

rheological ( $F_{\mu}$ , viscous) component and a magnetorheological component ( $F_{mr}$ , magnetic field-dependent). The value of the total force is defined in equation 3<sup>[5, 14]</sup>:

$$F = F_{\mu} + F_{mr} = \frac{\mu \cdot S \cdot L \cdot w}{g} + \tau_{mr} \cdot L \cdot w \quad (3)$$

Equation 3 shows that the force depends on the dynamic viscosity ( $\mu$ , Pa·s) with no applied field, the relative speed ( $S$ , m/s), the length ( $L$ , m), fluid gap ( $g$ , m) and width ( $w$ , m) of the flow channel in the viscous component, and the variable yield stress ( $\tau_{mr}$ , N/mm<sup>2</sup>) developed in response to the applied magnetic field.

The minimum volume of active fluid is defined in equation 4, in order to achieve the desired effect at a certain speed:

$$V = L \cdot g \cdot w = \frac{\mu}{\tau_{mr}^2} \cdot \frac{F_{mr}}{F_{\mu}} \cdot S \cdot F_{mr} \quad (4)$$

This operational mode is likewise widely spread and used in brakes, clutches or chocking devices<sup>[5]</sup>.

#### 4.3 Squeeze mode

In squeeze mode, a force is applied in the same direction as the magnetic field to either reduce or increase the distance between parallel plates which causes a squeeze flow<sup>[14,15]</sup>. Squeeze mode scheme can be seen in figure 6.

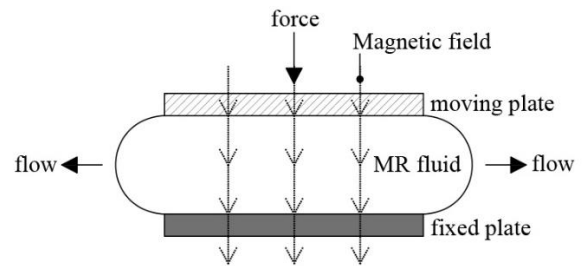


Figure 6: Squeeze mode.

Squeeze mode has not been so widely spread as the previous modes, and it is generally used in small-amplitude vibration

dampers. This mode allows the application of very large forces with small motion <sup>[14]</sup>.

## 5 CASE STUDY: DONGTING LAKE BRIDGE

A remarkable case study of the use of MR fluid is presented: the dampers located in the Dongting Lake Bridge (figure 7), southern - central China.



Figure 7: Dongting Lake bridge <sup>[17]</sup>.

The Dongting Lake bridge is a three-tower prestressed concrete cable-stayed bridge. It consists of two central spans measuring 310 m long each and two side spans measuring 130 m each. The central tower is 125.7 m high and the side towers measure 99.3 m. The deck is 23.4 m wide. A total of 222 cables support the bridge. These are 28-210 m long and 99-159 mm in diameter <sup>[18]</sup>. A scheme of Dongting Lake bridge is shown in figure 8.



Figure 8: Dongting Lake bridge. Elevation <sup>[18]</sup>.

The bridge was completed in 2000, when severe rain-wind induced vibration was observed <sup>[19]</sup> in nearly all cables. For this reason, it was decided to include a MR damper

system, whose yield force could be monitored and adjusted for varying vibration conditions. It constituted the world's first full-scale implementation of MR damping for bridge structures <sup>[20]</sup>.

The system reduces wind-rain induced vibrations on cables taking advantage of MR fluid, with regards to that both reliability and maintenance along with aesthetics are factors that determine the project <sup>[19]</sup>.

The dampers selected for the bridge were manufactured by Lord Corporation. RD-1005 MR dampers, which are no longer commercially available, were used. However, their behaviour can be described by typical MR dampers which run in valve mode (figures 9 and 10). RD-1005 included an outer case for protection against dust or rain.

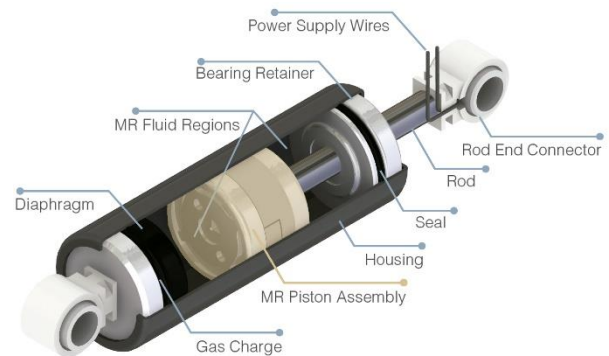


Figure 9: Valve mode MR damper <sup>[12]</sup>.

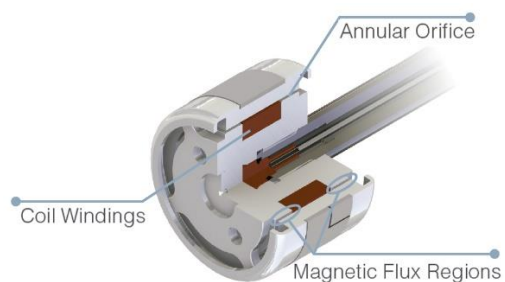


Figure 10: MR piston assembly <sup>[12]</sup>.

Several tests were performed on various cables. Results showed that the modal damping ratios were significantly increased when MR

dampers were installed <sup>[19]</sup>, and so the resulting vibrations were so small they had no visible movement. Since the maximum damping ratio did not reach the same value for different modes, the usefulness of semi-active was made clear.

The final assembly of the dampers can be seen in figure 11, in triangular shape in order to control in and out-plane vibrations. The electrical power supply reaches each cable and an A/D rectifier provides the required current, hence ensuring an optimal performance <sup>[19]</sup>.



**Figure 11:** Dongting Lake bridge. Assembly of the dampers <sup>[20]</sup>.

## 6 CONCLUSIONS

MRF show outstanding features like fast response, reversibility and controllability.

The viscosity of MR fluids can be considerably increased in just milliseconds and switched back to normal when the magnetic field is no longer present.

Various operational modes are currently widely spread. A combination of these modes or new operation modes can be developed, taking into account MRF characteristics.

The MRF technology proves itself useful as a semi-active control system. Variations in external inputs such as seismic forces or vibrations and internal modifications such as stiffness alteration can be overcome by a time-varying response.

## REFERENCES

- [1] ISO 3010:2017 *Bases for design of structures-Seismic actions on structures.*
- [2] P.M. Gerhart, R.P. Gross & J.I. Hochstein. *Fundamentos de mecánica de fluidos.* Addison-Wesley Iberoamericana, 1995.
- [3] Y.A. Çengel & J.M. Cimbala. *Fluid mechanics: fundamentals and applications.* McGraw-Hill, 2006.
- [4] P.P. Phulé. *Magnetorheological (MR) fluids: Principles and applications.* Smart Materials Bulletin, 2001.
- [5] A.G. Olabi & A. Grunwald. *Design and application of magneto-rheological fluid.* Materials and Design, Elsevier, 2007.
- [6] S. Sharma & S. Khurana. *Investigation on Magnetorheological Damper for its Various Applications.* IJLTEMAS, Vol. VI, Issue XI, 2017.
- [7] Agrawal A.K. & Amjadian M. *Innovative Bridge Design Handbook. Construction, Rehabilitation and Maintenance.* Chapter 20: *Seismic component devices.* Butterworth-Heinemann, Elsevier, 2016.
- [8] Tamizharasi G. et al. *Testing of fluids for making magnetorheological damper: an experimental study.* NITK Research Bulletin, Vol. 21 No. 1, 2012.
- [9] S. Khuntia et al. *Design, development and analysis of a magnetorheological damper.* IOP Conf. Series: Materials Science and Engineering 804, 2020.
- [10] Royalink Industries Corp. <http://www.royalinkindustries.com/raw-materials/carbonyl-iron-powder/>.
- [11] M.T Lopez-Lopez, J.D.G. Duran & A.Y. Zubarev. *Rheological Analysis of Magnetorheological Fluids.* Encyclopedia of Smart Materials, Elsevier, 2019.
- [12] LORD Corporation. *How does an MR Damper work?* <https://www.lord.com/products-and-solutions/active-vibration-control/industrial-suspension-systems/how-does-mr-damper-work>.

- [13] J. de Vicente, D.J. Klingenberg & R. Hidalgo-Alvarez. *Magnetorheological fluids: a review*. The Royal Society of Chemistry, Soft Matter, 2011.
- [14] A. Hajalilou, S.A. Mazlan, H. Lavvafi & K. Shameli. *Field Responsive Fluids as Smart Materials*, Engineering Materials. Springer, 2016.
- [15] S.A. Mazlan. *The behaviour of Magnetorheological Fluids in Squeeze Mode*. Dublin City University, 2008.
- [16] M.R. Jolly, J. W. Bender & J. D. Carlson. *Properties and Applications of Commercial Magnetorheological Fluids*. Journal of Intelligent Material Systems and Structures, 1999.
- [17] Hunan Communication & Water Conservancy Group Ltd. <http://www.hncc-china.com>.
- [18] Y. Q. Ni, X. Y. Wang, Z. Q. Chen & J. M. Ko. *Field observations of rain-wind-induced cable vibration in cable-stayed Dongting Lake Bridge*. Journal of Wind Engineering and industrial Aerodynamics 95, 2007.
- [19] Z.Q. Chen et al. *MR damping system for mitigating wind-rain induced vibration on Dongting Lake Cable-Stayed Bridge*. Wind and Structures, Vol. 5, No. 5, 2004.
- [20] K. Morita & S. McCabe. *US-Japan Cooperative Structural Testing Research Program on Smart Structural Systems*. UJNR Panel on Wind and Seismic Effects, Vol. 1 No. 5, 2004.

## REINFORCEMENT OF ADOBE CONSTRUCTION DAMAGED BY SEISMIC LOADS

Andrea Vázquez Greciano\* and Antonio Aznar López\*

\* Escuela Técnica Superior de Arquitectura de Madrid  
Universidad Politécnica de Madrid  
28040 Madrid, Spain  
e-mail: andrea.vazquez.greciano@upm.es  
ORCID: 0000-0001-9623-0721

**Abstract.** This work presents a new possibility of reuse of Polyethylene terephthalate (PET) as a reinforcement on adobe structures. The ever-growing global demand of PET bottles, along with the impossibility of recycling processes to keep up with their consumption pace, are the reasons to define a new use that ensures its reuse. The implementation of PET-fibres structural reinforcement on adobe building structures seeks a better adobe tensile strength behaviour, that may be decreased due to earthquakes or landslide.

This work is focused on adobe building on the specific location Keur Bakar Diahité in Senegal. Nonetheless, it is believed that this structural reinforcement may be applicable to other locations.

Mechanical tensile strength, compressive strength and pull-out tests have been performed with and without PET reinforcement. Using the laboratory obtained data, Finite Element Method (FEM) has been applied to simulate the effect of the reinforcement.

First, a single PET-reinforced brick has been analysed. The effect of the PET reinforcement has shown to improve the compressive strength on the adobe brick by a hoop-effect similar to that caused by steel hoops in concrete.

Then, a single-storey, both PET-reinforced and non-reinforced, adobe brick dwelling has been analysed and subjected to a seismic event. FEM simulations show that the base shear on PET-reinforced adobe housing was halved, compared to those with no reinforcement.

The results demonstrate that the inclusion of strip-shaped PET reinforcement on adobe constructions improves their mechanical behaviour, show that the yield strength tolerated by the reinforced adobe is 40% greater than the non-reinforced adobe, and manifest that the fracture energy of braided-reinforced adobe samples is 6 times greater than non-reinforced adobe.

**Key words:** Method of finite elements, Reinforcement, PET, Adobe.

### 1 INTRODUCTION

The ever-growing global demand of PET bottles, along with the impossibility of

recycling processes to keep up with their consumption pace, are the reasons to define a new use that ensures its reuse. This work

presents a new possibility of reuse of Polyethylene terephthalate (PET) as a reinforcement on traditional adobe structures which seeks reducing energy waste derived from recycling processes [1].

The implementation of PET-fibres structural reinforcement on adobe building structures seeks a better adobe tensile strength behaviour, that may be decreased due to earthquakes or landslide. Both laboratory tests and model simulations were carried out in order to evaluate the effect of the reinforcement [2].

## 2. LOCATION

This research seeks to improve adobe traditional construction by means of reusing PET waste products. It is focused on the buildings on the specific location Keur Bakar Diahité in southern Senegal.

Locals build on-site compressed blocks made of cement, water and soil. Different requirements such as climate conditions and seismic resistance define a dwelling sample: cylindrical spaces with small openings provide thermal and solar conditioning, mass and stability against seismic events [3].

It is believed that this structural reinforcement may be applicable to other locations as well.

## 3 MECHANICAL TESTS

Mechanical tensile strength, compressive strength and pull-out tests were performed with and without PET reinforcement in order to evaluate the reinforcement strength.

### 3.1 Tensile strength

Tensile strength tests were carried out by a INSTRON 8501 with a 10 kN load cell at a speed of 10 mm/minute with displacement control. A mechanical swivel joint was used to nullify the eccentricity of loading. PET samples were fastened by grips. The

deformation was measured by an Instron extensometer ranging from -2500 to +2500 micron.

The PET samples measured 20 mm high, 10 mm wide and 0.34 mm thick and were obtained from PET bottles (figure 1).



**Figure 1:** PET sample : before (left) and after (right) tensile strength test.

The yield strength obtained was 75 MPa and the ultimate strength 128 MPa. Young's Modulus was 2500 MPa average (figure 2).

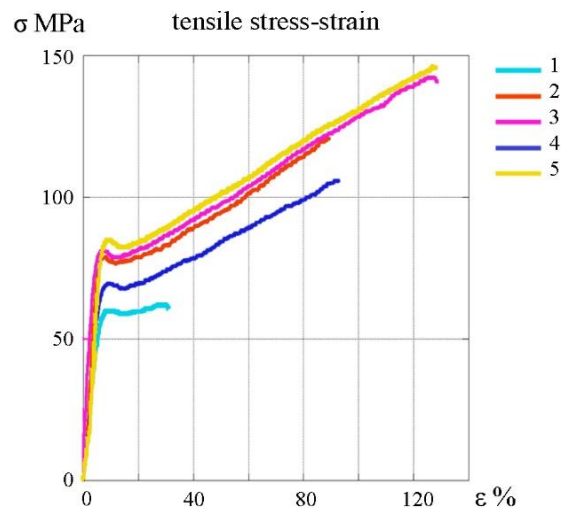


**Figure 2:** Vertical PET samples stress-strain graph.

### 3.2 Compressive strength

Compressive strength tests were developed

in order to compare the behaviour between non-reinforced and PET-reinforced adobe samples. The tests were carried out by a INSTRON 8501 with a 100 kN load cell at a speed of 0.2 mm/minute. The normalised samples were placed between two parallel compression plates.

Adobe was placed in cylindrical normalised moulds measuring 150 mm high and 75 mm diameter. PET reinforced adobe consisted of a 1.1 m long PET strip coiled around the adobe and secured by folding the end points into the mortar. The samples were cured for 10 days at constant 20°C.

Non-reinforced adobe showed an average yield strength of 1.05 MPa and an average Young's Modulus of 330 MPa (figure 3) at 10 days of curing.

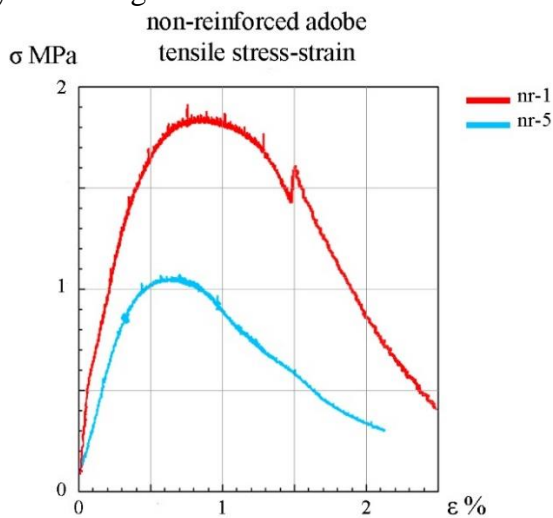


Figure 3: Non-reinforced adobe stress-strain graph (10 days).

Taking into consideration 28 days of curing, the value of the yield strength triples. Therefore, the yield strength considered for adobe was set at 3.15 MPa.

As for PET-reinforced adobe, the average yield strength obtained was 1.5 MPa, 43% greater than the non-reinforced samples. Its average Young's Modulus was 374 MPa (figure 4).

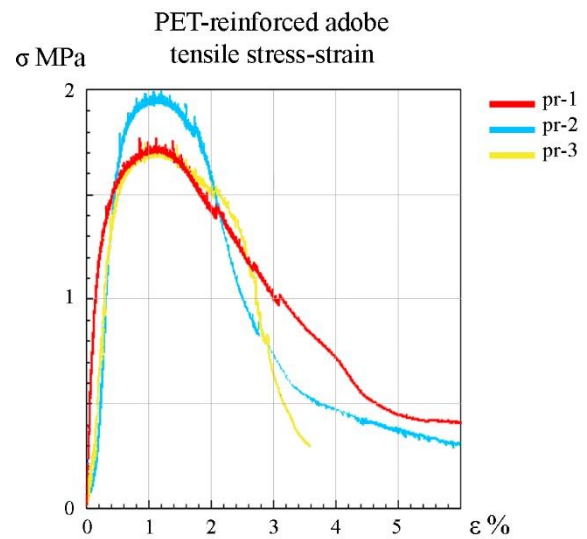


Figure 4: PET-reinforced adobe stress-strain graph (10 days).

Regarding braided PET-reinforced adobe, the average yield strength obtained was 0.7 MPa, the lowest value because of a smaller diameter of adobe available due to the inclusion of braided PET. Its average Young's Modulus was 174 MPa (figure 5).

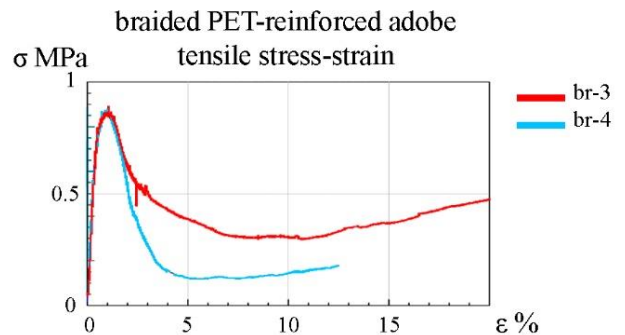


Figure 5: PET-reinforced adobe stress-strain graph (10 days).

It is worth mentioning the value obtained for the fracture energy, calculated as the area below the stress-strain line. Braided PET-reinforced samples fracture energy was 2.5 times greater than those with PET-reinforcement, and 6 times greater than non-reinforced ones.

### 3.3 Pull-out tests

Pull-out tests were carried out in order to evaluate the adherence between PET and adobe. These were performed by a INSTRON 8501 with a 50 kN load cell at a speed of 0.2 mm/minute.

Plain and knotted PET strips were introduced in adobe bricks measuring 150 mm long, 75 mm wide and 75 mm tall. The adhesion coefficient obtained was 0.034 N/mm<sup>2</sup> for plain strips. Knotted PET samples resulted in the typical breakout failure.

## 4 MODEL ANALYSIS

Using the laboratory obtained data from the mechanical tests, Finite Element Method (FEM) was applied to simulate the effect of the reinforcement. Ansys software was used.

The FEM can be defined as a *general discretization procedure of continuum problems posed by mathematically defined statements*<sup>[4]</sup>. This method of approximation to continuum problems involves dividing the continuum into a finite number of parts (elements), whose behaviour is specified by a finite number of parameters. These elements are assumed to be interconnected at a discrete number of nodal points.

The first step is the determination of element properties from the geometric material and loading data. Therefore, both a single PET-reinforced adobe brick and a single-storey adobe dwelling were defined.

### 4.1 PET-reinforced adobe brick

The geometry modelling of the adobe brick was made according to the Solid-285 Ansys element. This element is a tetrahedron defined by four nodes. Each node has three degrees of freedom (DOFs): translations in the nodal x, y, and z directions<sup>[5]</sup>. The geometry, node locations and coordinate system for this element are shown in figure 6.

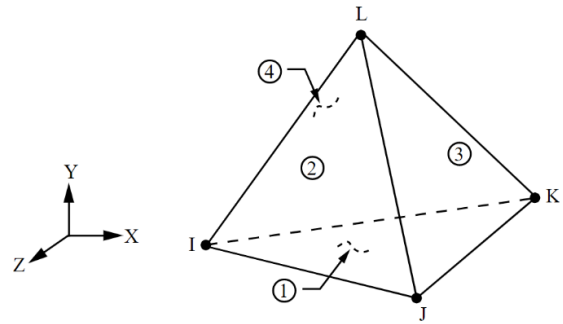


Figure 6: Solid-285 Ansys element.

Solid-285 element proved itself useful since it is suitable for modelling irregular meshes.

The adobe brick was modelled based on a cuboid measuring 295 mm long, 140 mm wide and 90 mm high. Three cylinders of diameter 45 mm represent the hollow section of the adobe cored brick described in [6] (figure 7).

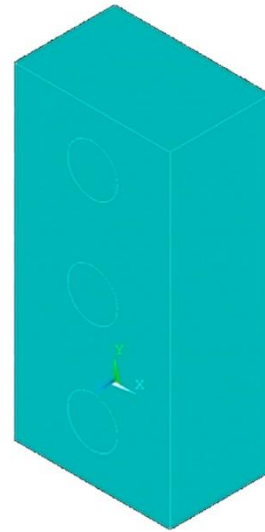
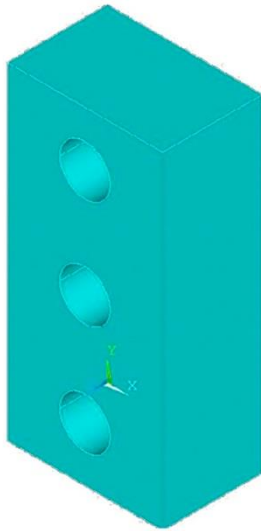


Figure 7: Solid element.

Boolean subtraction operations were used to obtain the final adobe brick shape as seen in figure 8. The distance between the cylindrical hollow sections is 98 mm each, and the outer ones are 49 mm apart from the edge of the brick. These hollow sections are all aligned along the longitudinal axis of the brick.



**Figure 8:** Adobe brick.

Ansys ‘Mesh tool’ was used to create an all-tetrahedral mesh, as seen in figure 9. The spatial subdivision algorithm ensures refinement of the mesh where necessary (in this case along the hollow sections), but maintains larger elements where possible (outer perimeter of the brick) allowing for faster computation [7].

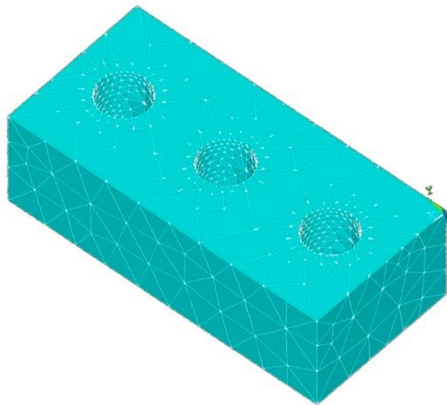


**Figure 9:** Adobe brick meshing.

The geometry modelling of the PET reinforcement was made according to the Shell-281 Ansys element. This element is suitable for analyzing composite shell

structures, for linear and nonlinear applications and it accounts for follower effects of distributed pressures [8]. The element has eight nodes having each six DOFs: translations in the nodal x, y, and z axes, and rotations about the x, y, and z axes [5]. The geometry, node locations and coordinate system for this element are shown in figure 10.

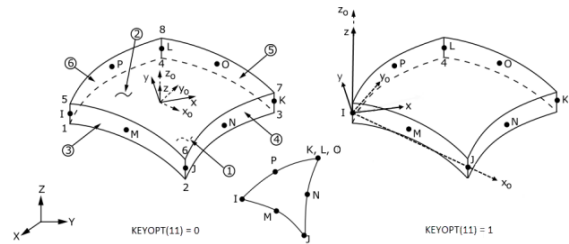


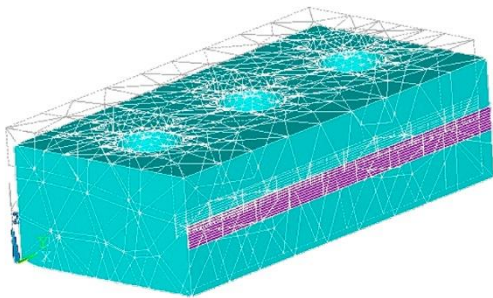
**Figure 10:** Shell-281 Ansys element.

The PET reinforcement strips were modelled according to the dimensions obtained in the PET-bottle recycling process. Therefore, a shell of 100 mm wide and 0.34 mm thick was placed along the stretcher face of the brick on each side.

Once the geometry was modelled, the various mechanical characteristics were defined according to the laboratory obtained data for each material. Regarding the adobe, Young’s modulus was set at 1089 MPa (considering 28 days of curing) and Poisson’s ratio was set at 0.2. As for the PET, Young’s modulus was set at 2500 MPa and Poisson’s ratio was set at 0.31. In order to simulate the interaction between materials, a surface-to-surface contact element was defined [9] and the coefficient of friction was set at 0.3 as derived from the pull-out tests.

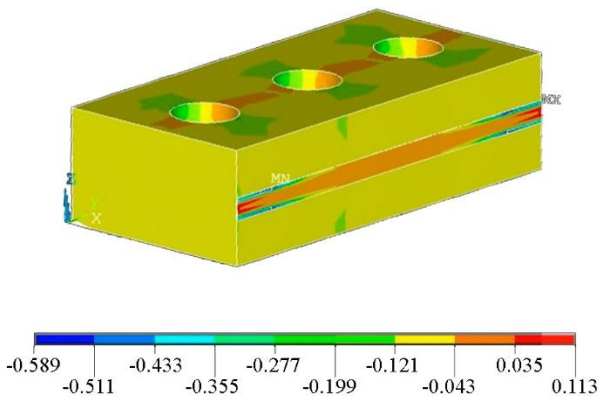
The PET contribution was studied through the model analysis carried out on a reinforced and a non-reinforced adobe brick. The displacements on the bed of the brick nodes were blocked and vertical loads were applied on the top bed nodes. The load was estimated taking into account the weight of the ceiling (2 kN/m<sup>2</sup>) and the adobe weight (whose density is 18.5 kN/m<sup>3</sup>).

Figure 11 shows the amplified deformation due to the applied loads. Vertical loads produce vertical deformations, and these, in turn, produce horizontal deformations along the x axis (along the y axis the adjacent blocks would prevent the displacement). In this situation the PET reinforcement begins to act and reduces the brick flattening. In a way, it resembles the clamping effect steel produces in reinforced concrete structures, which increases the strength up to 3.3 times.



**Figure 11:** Deformation of the block due to the applied loads.

Figure 12 shows the stress along the x axis. The tensile stress greatest values are located at the PET strips end points (0,11 MPa), which are rather low compared to the yield strength (75 MPa), representing the 0.0015% capacity.



**Figure 12:** X axis stress.

The ‘hoop-effect’ can be observed in the adobe surrounding the PET reinforcement. The

compressive stress reaches -0.58 MPa, again a very modest value compared to the adobe yield stress (-315 MPa). It represents the 0.0018% of the total capacity.

Regarding the interaction between materials, figure 13 shows mostly near contact, and also and sliding at some points. There are superpositions (Far Open) and it is worth mentioning there is no sticking between PET and adobe. This may be due to the low friction coefficient modelled, or more probably as a result of the significant PET effect.

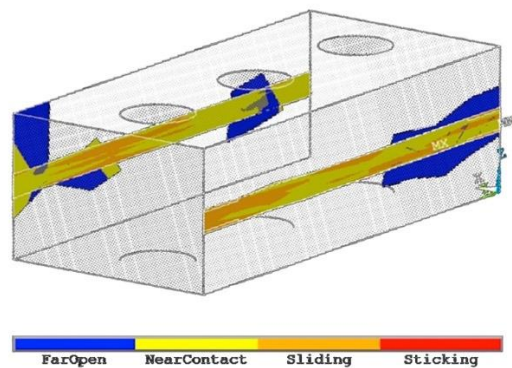


**Figure 13:** Interaction between PET and adobe.

## 4.2 Adobe dwelling

A simplified one-storey dwelling was subjected to a seismic simulation. Various studies are taken into consideration [8, 10, 11] in order to model the construction. In this case both Ansys and manual calculation were required since it was not possible for the programme to take fracture energy or deformation capacity into consideration [12]. Therefore, Ansys was helpful in calculating the vibration eigenmodes and in obtaining the mechanical response of the non-reinforced adobe dwelling. The contribution of the PET was manually obtained following the Spanish Code [13].

The geometry modelling of the adobe dwelling was made according to the Soild-185 Ansys element. This element is used for 3-D

modeling of solid structures and provides creep and large deflection. The element has eight nodes having three DOFs at each node: translations in the nodal x, y, and z axes [5]. The geometry, node locations and coordinate system for this element are shown in figure 14.

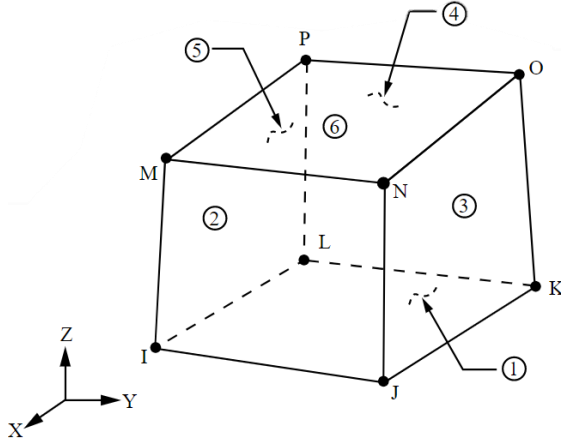


Figure 14: Solid-185 Ansys element.

The geometry was defined as a hollow cylinder measuring 1500 mm outer radius, 1205 mm inner radius (295 mm brick thickness) and 2300 mm high. A homogeneous rectangular mesh was applied and the mechanical properties of the material remained the same as in the previous section.

Then, a modal analysis was carried out in order to calculate the modes of vibration of the structure, considering that the modes obtained are valid for both the reinforced and non-reinforced adobe dwelling. The results can be seen in table 1.

Mode	Analytical Freq. [Hz] ( $w_i$ )
1	0.4305
2	0.4625
3	0.7056
4	0.9112
5	1.0813

Table 1: Modes of vibration.

Figure 15 represents the first mode of vibration, its displacements and frequency.

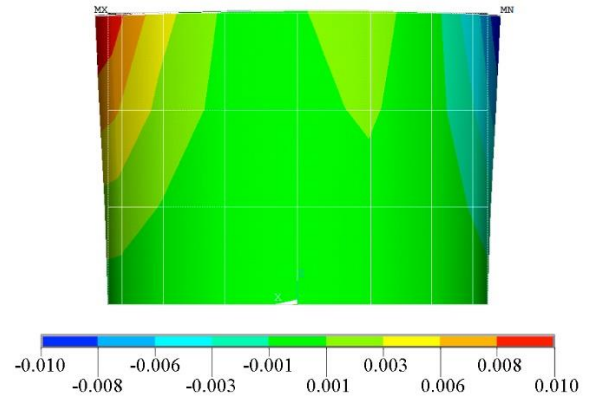


Figure 15: First mode of vibration.

The response spectrum is then calculated according to NCSE-02 [13].

Equation (1) is used to graph the response spectrum:

$$\alpha(T) = 1 + 1.5 \cdot \frac{T}{T_A} \quad \text{if } T < T_A \quad (1)$$

$$\alpha(T) = 2.5 \quad \text{if } T_A < T < T_B$$

$$\alpha(T) = K \cdot C/T \quad \text{if } T > T_B$$

$T_A$  and  $T_B$  are the spectrum characteristic periods (figure 16), and are calculated in (2):

$$T_A = K \cdot C/10 \quad (2)$$

$$T_B = K \cdot C/2.5$$

where:

- $K$ : contribution coefficient = 1.2
- $C$ : geotechnical ground coefficient = 1

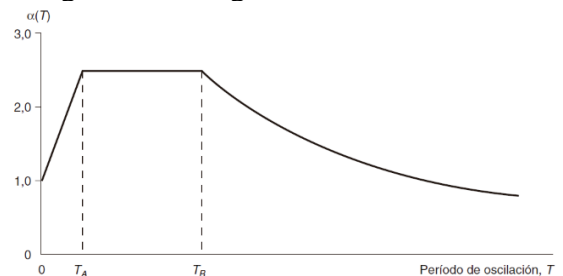


Figure 16: Response spectrum.

Therefore,  $T_A = 0.12$  and  $T_B = 0.48$  seconds.

The various values of  $\alpha(T)$  can be seen in table 2. These result in the response spectrum plotted in figure 17.

T [s]	$\alpha(T)$
0	1.00
0.5	2.50
1	1.20
1.5	0.80
2	0.60
2.5	0.48
3	0.40

**Table 2:** Values for T and  $\alpha(T)$ .

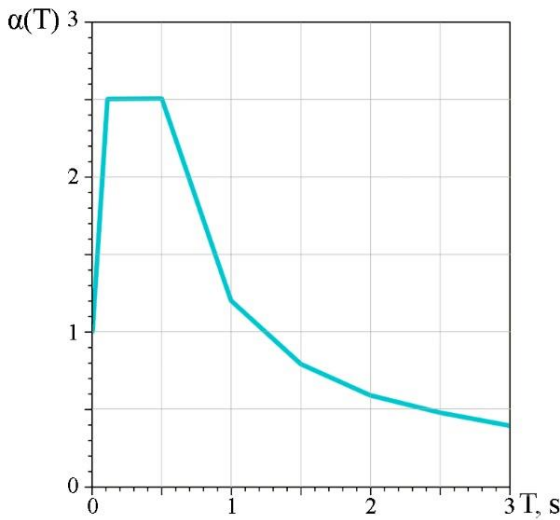


**Figure 17:** Response spectrum  $\alpha(T)$ -T.

Then the equivalent static force, *fuerza sísmica estática equivalente*, ( $F_{ik}$ ) was calculated as in (3) for the first mode of vibration:

$$F_{ik} = s_{ik} \cdot P_k \quad (3)$$

where:

- $s_{ik}$ : seismic coefficient corresponding to the selected floor and mode of vibration
- $P_k$ : weight of the floor

The weight of the single-floor construction ( $P_1$ ) was calculated multiplying the density of adobe ( $18.5 \text{ kN/m}^3$ ) times the volume of the

hollow cylinder, resulting in 106.8 kN. The value for  $s_{11}$  was calculated in equation (4):

$$s_{ik} = (a_c/g) \cdot \alpha \cdot \beta \cdot \eta_{ik} \quad (4)$$

where:

- $a_c$ : acceleration calculation value
- $\alpha$ : period-dependent coefficient
- $\beta$ : response coefficient
- $\eta_{ik}$ : distribution factor for k-storey in i-vibration mode

The *aceleración de cálculo* ( $a_c$ ) is defined in equation (5):

$$a_c = S \cdot \rho \cdot a_b \quad (5)$$

where:

- S: ground coefficient
- $\rho$ : risk coefficient
- $a_b$ : seismic horizontal ground acceleration, *aceleración sísmica básica*, corresponds to Sokone city, 15 km apart from Keur Bakar Diahité.

S takes the value 1.0,  $\rho$  is 1.0 as the dwelling is considered as a normal construction, and  $a_b$  is calculated in (6):

$$a_b = 0.04 \cdot g \quad (6)$$

where:

- g: gravity

Following equations (5) and (6) the final value for  $a_c$  is  $0.39 \text{ m/s}^2$ .

The period-dependent coefficient ( $\alpha_i$ ) is calculated in equation (7):

$$\begin{aligned} \alpha &= 2.5 && \text{if } T_i < T_B \\ \alpha &= 2.5 \cdot (T_b/T_i) && \text{if } T_i > T_B \end{aligned} \quad (7)$$

$T_i$  refers to the period considered, in this case for the first mode, being the period (T) the inverse of the frequency ( $w$ ). Therefore  $T_1=2.32$  seconds.

Introducing the values of  $T_1$  and  $T_B$  in (7) we obtain the value for  $\alpha_1=0.517$ .

The response coefficient ( $\beta$ ) is calculated as follows (8):

$$\beta = v/\mu \quad (8)$$

where:

- $v$ : damping modification factor = 1 for damping equal to 5% of critical damping
- $\mu$ : ductility behaviour coefficient

The value for  $\mu$  depends on the organization of the structure, materials used and the detailed construction. Therefore, two values of  $\mu$  were considered: both the adobe and the PET-reinforced adobe construction. Masonry walls use  $\mu=1$  (non-reinforced) and high energy dissipation structures use  $\mu=2$  (PET-reinforced), as indicated in the Spanish Code. Consequently,  $\beta_{\text{non-r}} = 1$  and  $\beta_{\text{PET-r}} = 0.5$ .

The distribution factor for  $k$ -storey in  $i$ -vibration mode ( $\eta_{ik}$ ) is defined in equation 9:

$$\eta_{ik} = \Phi_{ik} \cdot \frac{\sum_{k=1}^n m_k \cdot \Phi_{ik}}{\sum_{k=1}^n m_k \cdot \Phi_{ik}^2} \quad (9)$$

where:

- $\Phi_{ik}$ : shape coefficient for  $k$  floor in  $i$  vibration mode
- $\beta$ : response coefficient

The shape ( $\Phi_{ik}$ ) coefficient is defined in equation 10:

$$\Phi_{ik} = \sin [(2i - 1) \cdot \pi \cdot h_k/2H] \quad (10)$$

where:

- $h_k$ :  $k$  floor height above ground level
- $H$ : total height of the building

As mentioned previously, the simplified one-storey dwelling  $h_k=H= 2.3$  m.

The values obtained for equations (3, 4, 5, 7, 8, 9 & 10) are shown in table 3. The equivalent static forces  $F_{11}$  for both reinforced and non-reinforced one-storey dwellings are, in this case, equivalent to the static base shear  $V_1$ .

Non-reinforced dwelling		PET-reinforced dwelling	
$\Phi_{11}$	1	$\Phi_{11}$	1
$\eta_{11}$	1	$\eta_{11}$	1
$\beta$	1	$\beta$	0.5
$\alpha_1$	0.517	$\alpha_1$	0.517
$a_c$	0.39 m/s <sup>2</sup>	$a_c$	0.39 m/s <sup>2</sup>
$s_{11}$	0.0206	$s_{11}$	0.0103
$P_1$	106.8 kN	$P_1$	106.8 kN
$F_{11}$	2200 N	$F_{11}$	1100 N
$V_1$	2200 N	$V_1$	1100 N

**Table 3:** values.

These results showed that the base shear stress on PET-reinforced adobe housing was halved, compared to those with no reinforcement.

The simplified one-storey dwelling was subjected to the seismic ‘spectrum’ simulation caused by Response spectrum  $\alpha(T)$ -T (figure 17). Figure 18 shows the horizontal deformation of the building and figure 19 represents the tangential stress due to said input.

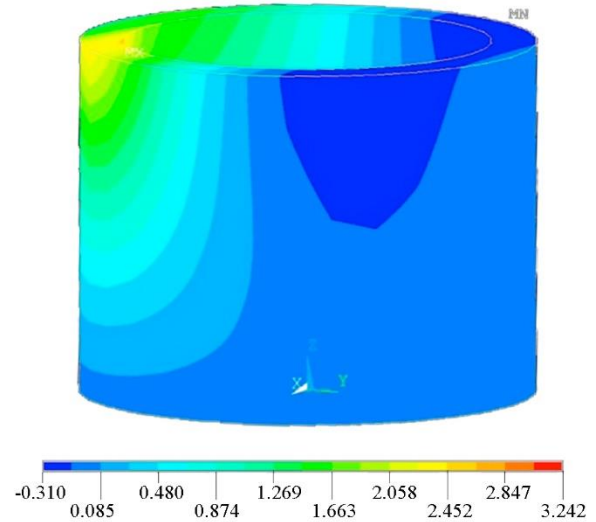


**Figure 18:** Horizontal deformation.

Then, the model analysis results were compared to the laboratory obtained data.

The tests revealed an average yield

compressive strength ( $\sigma$ ) of adobe of value 1.05 MPa during its early days of curing. Von Mises theory was used to estimate the shear stress ( $\tau$ ) the structure is submitted to as follows (equation 11):

$$\tau = \sigma/\sqrt{3} \quad (11)$$

resulting in  $\tau=0.6$  MPa. According to [14], the tangential strength of the mortar joint is a tenth of  $\tau$ . For this reason, a tension greater than 0.06 MPa would not bear the studied seismic event. It is clear from the data in figure 19 that various regions go over 0.06 MPa, resulting in weak areas when no reinforcement is applied.

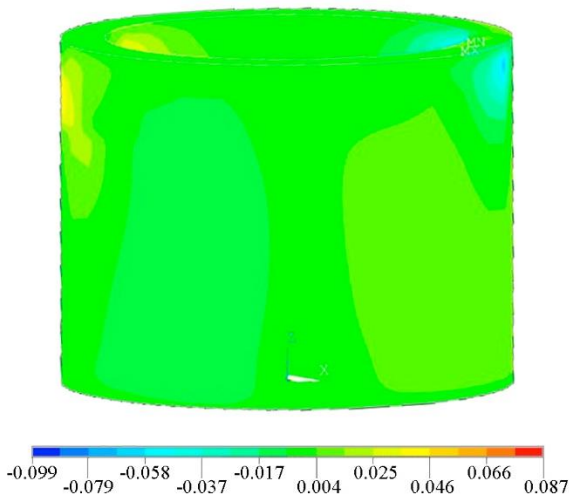


**Figure 19:** Tangential stress of non-reinforced construction.

Similarly, the construction was then analysed taking into account the PET reinforcement of adobe. It was not possible for Ansys to take fracture energy or deformation capacity into consideration. Consequently, a static analysis was carried out. A base shear of  $V_1=1100$  N was applied.

Figure 20 shows the tangential stress thereby obtained. It was observed that the PET reinforcement reduced these stress values, compared to the non-reinforced construction.

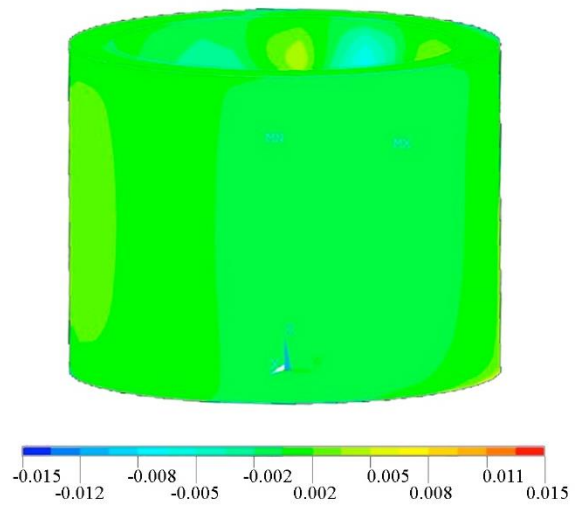


**Figure 20:** Tangential stress of PET-reinforced construction.

## 5 CONCLUSIONS

- The results derived from mechanical tests showed how PET-reinforcement on adobe improves the mechanical behaviour of this kind of mixed structures. Tensile strength increased along with a greater fracture energy.
- The model analysis showed a better behaviour of PET-reinforced adobe structures under seismic excitations.
- The reuse of materials combined with traditional construction improve the quality of the dwellings.

## REFERENCES

- [1] Siddique R. Khatib J. & Kaur I. *Use of recycled plastic in concrete: a review*. Elsevier, 2007.
- [2] A. Vázquez. *Refuerzo estructural con PET reutilizado: aplicación en adobe*. Trabajo Fin de Grado, Universidad Politécnica de Madrid, Escuela Técnica Superior de Arquitectura, 2018.
- [3] C. Blanco & P. Morales. *Ficha técnica: Sistema constructivo adobe/tapial*, Arquitectos Sen Fronteiras.

- [4] O.C. Zienkiewicz, R.L. Taylor & J.Z. Zhu. *The Finite Element Method: Its Basis and Fundamentals*, 6th Ed. Elsevier Butterworth-Heinemann, 2005.
- [5] Budapest University of Technology and Economics, Faculty of Mechanical Engineering, Department of Applied Mechanics. *Ansys Manual*. 21 February 2018. [https://www.mm.bme.hu/~gyebro/files/ans\\_help\\_v182/ans\\_elem/](https://www.mm.bme.hu/~gyebro/files/ans_help_v182/ans_elem/)
- [6] V. Rodríguez. *Locally Sourced and Processed Insulation Materials for Building Construction in Developing Countries*. Proyecto Fin de Máster, Universidad Politécnica de Madrid, Escuela Técnica Superior de Ingenieros de Caminos, Canales y Puertos, 2016.
- [7] ANSYS, Inc. *ANSYS Meshing User's Guide*. Release 13.0, 2010.
- [8] F. M. Nazri, *Seismic Fragility Assessment for Buildings due to Earthquake Excitation*. Springer, 2018.
- [9] ANSYS, Inc. *ANSYS Contact Technology Guide*. Release 9.0, 2004.
- [10] M. R. Hatch. *Vibration Simulation Using MATLAB and ANSYS*. Chapman and Hall/CRC, 2001.
- [11] T. Paulay & M. J. N. Priestley. *Seismic Design of Reinforced Concrete and masonry Buildings*. Joh Wiley & Sons, INC, 1992.
- [12] P. Kohnke, Ph. D. *Theory Reference*. ANSYS Release 5.6, 1999.
- [13] NCSE-02. *Norma de Construcción Sismorresistente: Parte General y edificación*. 2009.
- [14] B. Saavedra & J. Marcial. *Análisis sísmico de módulos de adobe reforzado con malla de polímero, Proyecto DAI-2987*. Pontificia Universidad del Perú, Departamento de Ingeniería, Sección Ingeniería Civil, 2006.

### **Section 3: Railway dynamics**

---

## RAILWAY INDUCED VERTICAL VIBRATIONS IN TWO-SPAN CONTINUOUS BRIDGES

M.D. Martinez-Rodrigo\*, A. Andersson†, C. Pacoste†, R. Karoumi†

\* Departamento de Ingeniería Mecánica y Construcción,  
Universitat Jaume I  
12006 Castellón, Spain  
e-mail: mrodrigo@uji.es  
ORCID: 0000-0003-4748-9133

† Division of Structural Engineering and Bridges,  
KTH Royal Institute of Technology  
10044 Stockholm, Sweden

**Abstract.** In this study the vibratory response of two-span continuous beams subjected to moving loads is investigated. The main practical interest is the evaluation of the maximum vertical acceleration in railway bridges, which is one of the most demanding Serviceability Limit States for traffic safety. Two-span continuous bridges exhibit antisymmetric and symmetric modes with closely spaced natural frequencies, leading to a more involved dynamic behavior than that of simply-supported bridges. First, the free vibration response of a Bernoulli-Euler two-span beam after the passage of a single load is formulated analytically, and cancellation and maximum free vibration response conditions are obtained. These results are used to determine length-to-train characteristic distance ratios leading to cancelled resonances or remarkably prominent ones. Then a methodology for detecting which could be the most aggressive trains for a particular structure based on pure geometrical considerations is discussed. Finally, the applicability of the theoretical derivations is shown through the numerical analysis of two real bridges belonging to the Swedish railway network.

**Key words:** Two-span continuous railway bridges, Moving loads, Resonance, Cancellation.

### 1 INTRODUCTION

Among the longitudinal typologies of railway viaducts, both bridges with continuous decks resting on multiple supports and bridges composed of simply-supported (SS) spans coexist. The former are structurally more efficient and able to transmit the horizontal break and acceleration forces to the ground with the collaborative action of the substructure elements. The latter may be constructed in a rather systematic way, allow possible prefabrication, partial replacement of the SS decks and facilitate continuous rails. Nevertheless, the higher number of joints and

supporting devices increases the maintenance costs and these structures are usually appropriate only when piers have a limited height. This work is devoted to two-span continuous bridges, as the simultaneous contribution to the transverse vibrations of antisymmetric and symmetric modes constitutes a more complex problem and these structures may still experience important amplifications under railway traffic [1]-[2].

The basic phenomenon governing the vertical vibrations induced in a bridge by a railway convoy is the amplitude of the free vibrations that each axle leaves on the structure

after its passage, as these free vibration waves accumulate and may add in phase for certain speeds. Depending on the ratio between the travelling time of the load and the natural period of the structure, the amplitude of the free vibrations in that particular mode may be maximum or may be cancelled out, implying that the structure will remain at rest under certain ideal conditions. This basic problem has been analyzed in the past for simply- and elastically-supported beams [3]-[5]. The interest of knowing these conditions a priori is that when resonance, caused by series of loads, takes place at a maximum free vibration velocity or, on the contrary, close to a cancellation condition, the train will induce either a very prominent response or an almost imperceptible one, respectively.

The objectives of this study are to (i) investigate analytically the problem of free vibrations in two-span continuous beams; (ii) verify whether maximum free vibration and cancellation conditions take place and, if so, to determine their value for any longitudinal bending mode and for any structure; (iii) obtain geometrical ratios leading to maximum resonance and cancellation of it for symmetric and antisymmetric modes and to prove their applicability when ideal conditions are not met; and (iv) apply the former theoretical derivations to the application of two-span bridges under High-Speed traffic by proposing a methodology to detect which could be the most and least aggressive trains for a particular design speed of the line, and what kind of resonance is responsible for it.

Being able to predict velocities leading to maximum free vibration or cancellation is of practical interest as not only the most and least aggressive trains may be detected for a particular structure but, in addition, this information could also be useful when planning experimental campaigns on bridges with the aim of identifying amplitude-dependent magnitudes (e.g. modal damping).

## 2 FREE VIBRATIONS OF TWO-SPAN BEAM UNDER MOVING LOAD

The partial differential equation governing the undamped transverse vibrations  $w(x,t)$  of a two-span Bernoulli-Euler beam, neglecting shear deformation and rotatory inertia, traversed by a constant-valued load  $P$  moving at constant speed  $V$  is given by

$$\rho A(x) \frac{\partial^2 w(x,t)}{\partial t^2} + \frac{\partial^2 EI(x)}{\partial x^2} \frac{\partial^2 w(x,t)}{\partial x^2} = -P\delta(x-Vt) \left[ H(t) - H\left(t - \frac{2L}{V}\right) \right] \quad (1)$$

The solution to Eq. (1) may be expressed as a linear combination of the normal modes  $\phi_i(x)$  represented in Fig. (1) along with the corresponding roots of the frequency equations for antisymmetric  $\lambda_i^a$  and symmetric modes  $\lambda_i^s$ :

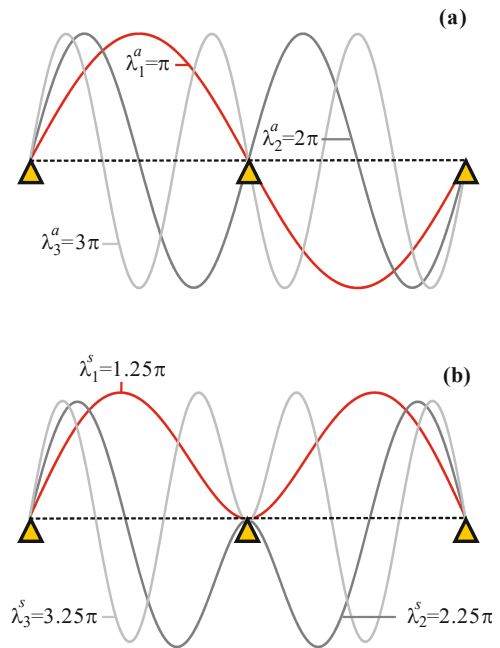


**Figure 1:** First three (a) antisymmetric and (b) symmetric normal modes of the two-span beam.

In two-span continuous beams antisymmetric and symmetric modes alternate with the frequency number, and each modal frequency increases in relation to the fundamental one  $f_1^a$  according to the factors

$$f_1 = f_1^a [1, 1.56, 4, 5.06, 9, 10.56, \dots] \quad (2)$$

In virtue of the modes orthogonality, modal equations become uncoupled and the amplitude of the free vibrations normalized by the modal static displacement once the load leaves the beam,  $R_n$ , may be obtained in closed form neglecting structural damping as

$$R_n = \frac{\omega_n^2 M_n}{-P} \sqrt{\frac{\xi_n^2}{\omega_n^2} + \xi_n^2} \Big|_{t=\frac{2L}{V}} \Rightarrow R_n = f\left(K_n = \frac{\lambda_n V}{\omega_n L}\right) \quad (3)$$

In Eq. (2),  $\xi_n$ ,  $\omega_n$  and  $M_n$  are  $n$ -th modal amplitude, circular frequency and modal mass, respectively,  $L$  is the length of each span and a dot indicates differentiation with respect to time. Fig. (2) shows the evolution of  $R_n$  for the first antisymmetric and first symmetric modes vs. the speed parameter  $K_1$ . As both  $R_n$  and  $K_1$  are non-dimensional, these representations and the conclusions derived hereafter are applicable to any two-equal-span uniform beam.

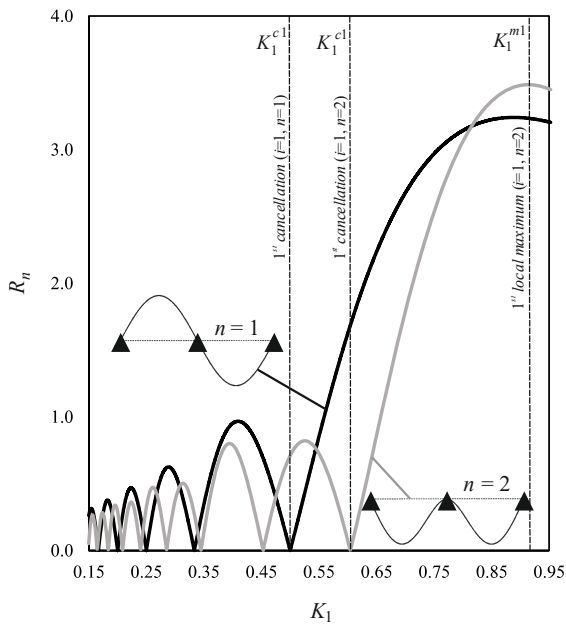


Figure 2:  $R_n$  for first two modes vs.  $K_1$ .

From the analysis of Fig. (2) it can be concluded that (i) depending on the travelling

speed, the amplitude of the free vibrations that a particular beam undergoes in a certain mode once the load leaves the structure can be maximum or cancelled out, taking into account that no damping is present in the system. The speed parameters for these conditions can be obtained analytically. (ii) The velocities cancelling out the free vibrations of the fundamental mode also cancel out the response of the remaining antisymmetric modes. This does not occur among the symmetric modes or among these and the fundamental mode. (iii) When damping is present and for moderate levels of it, the evolution of  $R_n$  is similar, the amplitudes at local maxima are lower, and the response is not completely cancelled out at cancellation speeds, although the response is remarkably low. From the solution to Eq. (3) cancellation and maximum free vibration non-dimensional speeds may be calculated as

$$R_n(K_n) = 0 \Rightarrow K_n^{ci} \quad \frac{\partial R_n(K_n)}{\partial K_n} = 0 \Rightarrow K_n^{mi} \quad i \geq 1 \quad (4)$$

In Table 1 the first four values of  $K_n^{ci}$  and  $K_n^{mi}$  are given for the first four modes. As it should be expected the speed parameters for the fundamental mode coincide with those of the SS beam for the second bending mode if  $L$  is the span length [5]. It should be indicated that a realistic upper limit for  $K_1$  can be estimated in 0.5. Therefore,  $K_n^{m1}$  will never be reached in a practical situation.

$n$	$K_n^{c1}$	$K_n^{c2}$	$K_n^{c3}$	$K_n^{c4}$
1	0.5000	0.3333	0.2500	0.2000
3	0.6667	0.5000	0.4000	0.3333
2	0.4835	0.3624	0.2758	0.2282
4	0.6201	0.5107	0.4044	0.3488
$n$	$K_n^{m1}$	$K_n^{m2}$	$K_n^{m3}$	$K_n^{m4}$
1	0.8883	0.4094	0.2886	0.2235
3	0.9653	0.5812	0.4478	0.3652
2	0.7312	0.4202	0.3157	0.2509
4	0.8409	0.5625	0.4542	0.3758

Table 1: Cancellation and maximum free vibration speeds of first two antisymmetric ( $n=1,3$ ) and first two symmetric ( $n=2,4$ ) modes.

### 3 FORCED VIBRATIONS UNDER EQUIDISTANT LOADS

#### 3.1 $L/d$ ratios for maximum resonance and cancellation of resonance

In what follows the dynamic response of the two-span beam is investigated under trains of equidistant loads travelling at constant speed  $V$ . When the time interval between the passage of two consecutive loads is a multiple of one of the beam natural periods, resonance is induced. Depending on the amplitude of the free vibrations, resonance could result in a remarkably amplified response (if the resonant speed coincides with a maximum free vibration speed) or may not even be perceptible (if it coincides with or is close to a cancellation condition). Ideally, a train of equidistant loads with characteristic distance  $d$  induces a  $j$ -th order resonance of the  $n$ -th mode as per Eq. (5), which may be expressed non-dimensionally as

$$V_{nj}^r = \frac{d \cdot f_n}{j} \Rightarrow K_{nj}^r = \frac{\lambda_n}{\omega_n L} \frac{d \cdot f_n}{j} \quad (5)$$

By equating  $K_{nj}^r$  to the cancellation or maximum free vibration speed parameters in Table 1, for any mode  $n$  and event  $i$ ,  $L/d$  ratios leading to the cancellation or maximum of the  $j$ -th resonance of the  $n$ -th mode of the two-span continuous beam are obtained according to

$$K_{nj}^r = K_n^{ci} \Rightarrow \left(\frac{L}{d}\right)_{nj}^{ci} = \frac{\lambda_n}{2\pi j} \frac{1}{K_n^{ci}} \quad (6a)$$

$$K_{nj}^r = K_n^{mi} \Rightarrow \left(\frac{L}{d}\right)_{nj}^{mi} = \frac{\lambda_n}{2\pi j} \frac{1}{K_n^{mi}} \quad (6b)$$

In Tables 2 and 3 these ratios are given for the first two normal modes  $n=1, 2$ , i.e. first antisymmetric and first symmetric modes, which will have the highest participation in the transverse acceleration, as will be shown later on. Ratios for higher modes could also be obtained analytically by applying Eq. (6). These ratios are valid for any beam or bridge

due to the non-dimensional nature of the formulation.

$j$	$\left(\frac{L}{d}\right)_{1j}^{c1}$	$\left(\frac{L}{d}\right)_{1j}^{c2}$	$\left(\frac{L}{d}\right)_{1j}^{c3}$	$\left(\frac{L}{d}\right)_{1j}^{c4}$
1	1.000	1.500	2.000	2.500
3	0.500	0.750	1.000	1.250
2	0.333	0.500	0.667	0.833
4	0.250	0.375	0.500	0.625
$n$	$\left(\frac{L}{d}\right)_{1j}^{m1}$	$\left(\frac{L}{d}\right)_{1j}^{m2}$	$\left(\frac{L}{d}\right)_{1j}^{m3}$	$\left(\frac{L}{d}\right)_{1j}^{m4}$
1	0.563	1.221	1.733	2.238
3	0.281	0.611	0.866	1.119
2	0.188	0.407	0.578	0.746
4	0.141	0.305	0.433	0.559

**Table 2:**  $L/d$  ratios for cancellation of resonance and maximum resonance of the first mode (antisymmetric).

$j$	$\left(\frac{L}{d}\right)_{2j}^{c1}$	$\left(\frac{L}{d}\right)_{2j}^{c2}$	$\left(\frac{L}{d}\right)_{2j}^{c3}$	$\left(\frac{L}{d}\right)_{2j}^{c4}$
1	1.293	1.725	2.266	2.739
3	0.646	0.862	1.133	1.369
2	0.431	0.575	0.755	0.913
4	0.323	0.431	0.567	0.685
$n$	$\left(\frac{L}{d}\right)_{2j}^{m1}$	$\left(\frac{L}{d}\right)_{2j}^{m2}$	$\left(\frac{L}{d}\right)_{2j}^{m3}$	$\left(\frac{L}{d}\right)_{2j}^{m4}$
1	0.855	1.487	1.980	2.491
3	0.427	0.744	0.990	1.246
2	0.285	0.496	0.660	0.830
4	0.214	0.372	0.495	0.623

**Table 3:**  $L/d$  ratios for cancellation of resonance and maximum resonance of the second mode (symmetric).

#### 3.2 Contour plots of maximum response

In what follows, the previous derivations are exemplified through numerical parametric analyses including the presence of structural damping and considering the simultaneous contribution of several modes of vibration in the computation of the transverse response.

A particular beam is selected with the properties of an existing railway bridge that will be analysed in section 4. In particular  $L=23.5$  m,  $EI=7.14 \cdot 10^{10}$  Nm<sup>2</sup>,  $\rho A=23010$  kg/m and modal damping  $\zeta_n=1\%$ . The bridge vertical response is obtained in the time domain by numerical integration applying the

Newmark- $\beta$  linear acceleration algorithm under the circulation of artificial trains of equidistant loads. The analytical expressions for the normal modes are used to represent the deformation of the beam and, therefore, no spatial discretization is needed. The vertical response of the bridge is obtained under the circulation of 201 independent trains each composed of 25 loads of 210 kN separated by a distance  $d$ . Characteristic distances,  $d$ , are selected so that the range  $(L/d) \in [0.5, 2.5]$  is covered using a fine increment  $\Delta(L/d) = 0.01$ . For each of the trains, the maximum displacement and acceleration are obtained at different sections of the beam in a range of circulating velocities such that the first three resonances ( $j=1,2,3$ ) of the first and of the second modes are excited. The maximum response is obtained considering the first six modes of vibration with natural frequencies up to 60 Hz. The natural frequencies of the modes in the particular case under study are the following:

$$f_n = \{5.01, 20.04, 45.09\} \text{ Hz } i = 1, 3, 5 \quad (7a)$$

$$f_n = \{7.83, 25.37, 52.92\} \text{ Hz } i = 2, 4, 6 \quad (7b)$$

In Fig. (3), contour plots of the maximum transverse displacement (a) and acceleration (b) at the mid section of the second span in absolute value due to the contribution of the first six modes ( $N=6$ ) are included. Each point in the contour representation corresponds to a particular train, defined by its characteristic distance  $d$  and a particular circulating velocity  $V$  of that train. The maximum response for each train and velocity is plotted in terms of two ratios:  $L/d$  and the speed  $V$  divided by the product of the fundamental frequency times the characteristic distance. This representation is not only non-dimensional, but it also facilitates the visualization of a particular mode resonant order, as the corresponding peaks appear vertically aligned for each value of  $j$ . In all the plots a series of maxima appear

at  $V/f_1 d = \{1, 0.5, 0.333, \dots\}$  for different  $L/d$  values corresponding to resonances of the fundamental antisymmetric mode for  $j=1, 2, 3, \dots$ . Series of peaks are also visible in the vicinity of  $V/f_1 d = \{1.56, 0.78, 0.52, \dots\}$ , coinciding with resonances of the second mode (first symmetric mode), as well for  $j=1, 2, 3, \dots$ . These values are consistent with the fact that  $f_2 = 1.56 \cdot f_1$ .

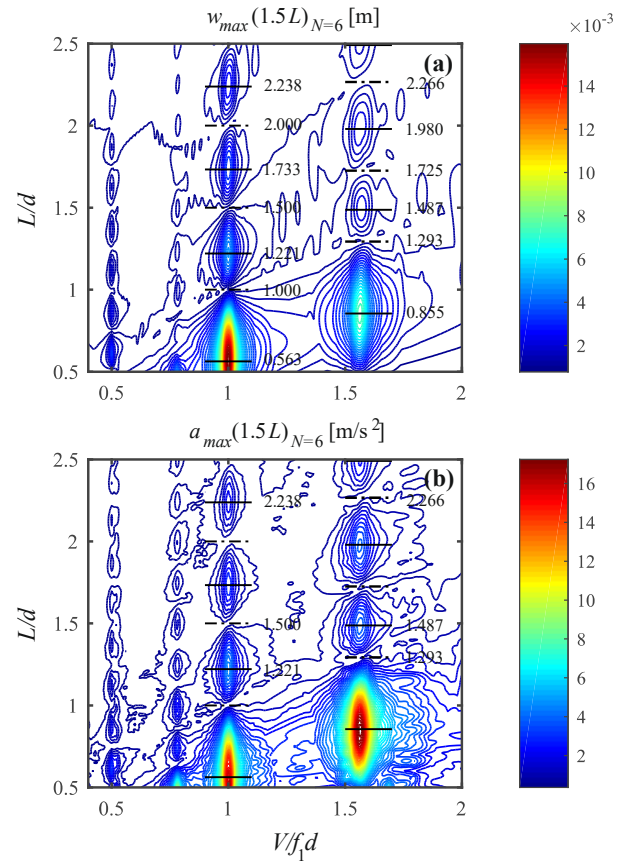


**Figure 3:** Contour plots for maximum displacement and acceleration under trains of equidistant moving loads.

At resonance, as  $L/d$  increases maximum resonance peaks and cancelled resonances take place alternatively. Also, as  $L/d$  increases, the amplification at resonance reduces, since shorter characteristic distance trains excite the same resonance at a lower velocity, and lower velocities imply lower amplitude local maxima

of the free vibration response, as shown in section 2.

The actual value of the maximum response in Fig. 3 is not relevant for this study, as no upper limit for the train speed is considered. In all plots and for the first resonance order ( $j=1$ ) of the first two modes, corresponding to  $V/f_1d=1$  and 1.56,  $L/d$  analytical ratios for maximum resonance and cancellation of resonance have been highlighted in thick and discontinuous horizontal segments along with the specific value, which is that included in Tables 2 and 3. The analytical predictions are accurate, despite the simultaneous contribution of the six modes and despite the presence of structural damping. It is also worth mentioning that these ratios predict cancelled and maximum resonances adequately both in the displacement and in the acceleration response.

The effect of modes higher than the second one is visible far from resonance, for moderate values of the response, especially in the acceleration plots. The displacement response is mildly affected by modes higher than  $n=2$ , which is to be expected and consistent with previous works. The overall maximum acceleration takes place at the first resonance of the second mode ( $V/f_1d=1.56$ ) in the vicinity of the first theoretical maximum, i.e.  $L/d=0.855$ , leading to  $17.72 \text{ m/s}^2$ .

From the previous analysis it can be concluded that when resonance is induced on a two-span continuous beam or bridge by a train of equidistant loads, its amplification will depend on the level of free vibrations associated with the particular velocity. Resonances of either the first (antisymmetric) or second (symmetric) mode are prone to be responsible for the overall maximum vertical acceleration of the bridge. The same train will require a higher speed in order to induce the same resonance of the second mode (when compared to that of the fundamental), with a higher level of free vibrations left by each axle load. Therefore, the second mode can be the

one responsible for the maximum response as long as the train speed is sufficiently high. In other words, the mode causing the maximum overall response of the bridge will depend on the maximum train speed.

Depending on the ratio between the length and the train characteristic distance, the response at resonance may be rather prominent or almost imperceptible. Furthermore, the analytical predictions of these  $L/d$  ratios leading to maximum resonance or cancellation of it, which were obtained in closed form in the absence of damping and admitting separate modal contributions, show themselves to be good estimates of the real values. This is due to the moderate damping values in railway bridges and also to the fact that, at resonance, the contribution of modes other than the one undergoing resonance is very limited.

#### 4 CASE STUDIES

In this section, the analysis of the dynamic performance of two real bridges is presented under the circulation of articulated load trains considering realistic design speeds. The bridges belong to the Swedish railway network, in particular, to the Bothnia and to the West Coast lines, respectively. The maximum train speed at both sites is at present 200 km/h. The possibility of increasing the operating speed on these lines with a target of 250 km/h is currently under study, and the evaluation of the performance of the bridges if these lines are upgraded is a topic of major interest for the Swedish railway administration [6].

	Lögde Br.	Förlöv Br.
$L$ (m)	43.0	23.5
$EI$ (GNm <sup>2</sup> )	105	71.4
$\rho A$ (kg/m)	13816	23010
$\zeta_n$ (%)	0.50	1.00
$f_1, f_2$	2.34, 3.66	5.01, 7.83

**Table 4:** Properties of the bridges under study.

The structures under study are single-track

and, in a first approach, the contribution of modes other than the longitudinal bending ones is disregarded. The main properties of the beams model for the two bridges and first two bending frequencies are included in Table 4.

The response of the bridges under the circulation of the High Speed Load Model-A (HSLM-A) from Eurocode (EC) is obtained by time integration using analytical mode shapes. The design speed considered for both bridges is 300 km/h (i.e. 1.2 times the target operating speed).

#### 4.1 Case 1. Bridge over River Lögde

The first structure under study is a continuous bridge with two 43 m identical spans and a uniform steel-concrete composite deck, as shown in Fig. 4.

The critical speeds for the ten HSLM-A trains' characteristic distances (from 18 to 27 m) for the lowest resonance order attainable given the design speed, and for the first two modes, which will be the ones that contribute most to the acceleration response, are represented in Fig. 5(a). The reader is referred to [7] for numerical details. All the trains induce first resonance of the fundamental mode under 300 km/h. Nonetheless, only the first five trains, with smaller characteristic distances, are able to do so in the case of the second mode, due to its higher frequency.

In order to compare the level of free vibrations associated to each train at the resonant speeds, the values of  $K_{1j}^r$  are superimposed to the normalised amplitude of the free vibrations for the first two modes,  $R_1$  and  $R_2$ . The vertical black lines stand for the resonant speeds of the fundamental mode and the grey vertical ones to those of the second mode. The intersection of each vertical line with either  $R_1(K_1)$  or  $R_2(K_1)$  (only intersections of traces of the same color should be considered) provides an estimation of the level of acceleration experienced by the bridge in a

certain mode at resonance. Moreover, the amplitude of either  $R_1$  or  $R_2$  is multiplied by the factor  $P_k/P_1$  in order to account for the different axle load modulus of the HSLM-A trains,  $P_k$  being the axle load of the  $k$ -th train and  $P_1=170$  kN, which is the minimum value. This corrected product is shown with a red circle that has a black border in the case of resonances of the first antisymmetric mode and a grey border in the case of resonances of the second mode.

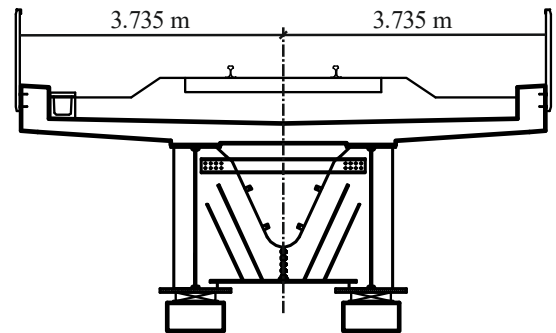


Figure 4: Bridge over River Lögde Rover. Elevation view and cross section.

Admitting that the number of loads is sufficient and that the resonance state has reached a constant amplitude due to the presence of damping, this may be used to compare the relative amplitudes of the acceleration at resonance induced by different trains on the first two modes of vibration. This is of course an estimation that only takes into account the lengths of the passengers' coaches and admits similar modal damping ratios for both modes, but it allows a preliminary prediction of which train will induce the most detrimental resonance and which mode will be the one undergoing it, taking into consideration

all cancellation and maximum free vibration situations. According to this the maximum acceleration may take place at first resonance of the second mode induced by train A4. This train should be one of the most aggressive trains for the particular structure and speed limit according to the Serviceability Limit State for traffic safety.

The response of the Lögde bridge to the circulation of the ten HSLM-A trains is computed and presented. The overall maximum acceleration takes place at mid-span of the second span. In Fig. 6 the maximum transverse displacement (a) and acceleration (b) are plotted in absolute values at this most critical section versus the non-dimensional speed  $V/f_1d$  for the ten HSLM-A trains. The maximum response induced by the HSLM-A4

is represented with a red trace. The overall maximum acceleration exceeds the limit for ballasted tracks according to EC. Therefore, this bridge may need to be improved in order to allow increased train speeds. As predicted, for the admitted design velocity the maximum response in terms of accelerations is due to a first resonance of the second mode ( $V/f_1d=1.56$ ), and it is induced by the HSLM-A4 train (red trace). In Fig. 6 it can also be observed that train A2 does not induce first resonance of the symmetric mode. For this train  $L/d_k=2.26$ , very close to the theoretical value for cancellation of the second mode first resonance. Finally, it should be said that the effect of modes higher than the second one is very low, especially at resonance, especially for the displacement response.

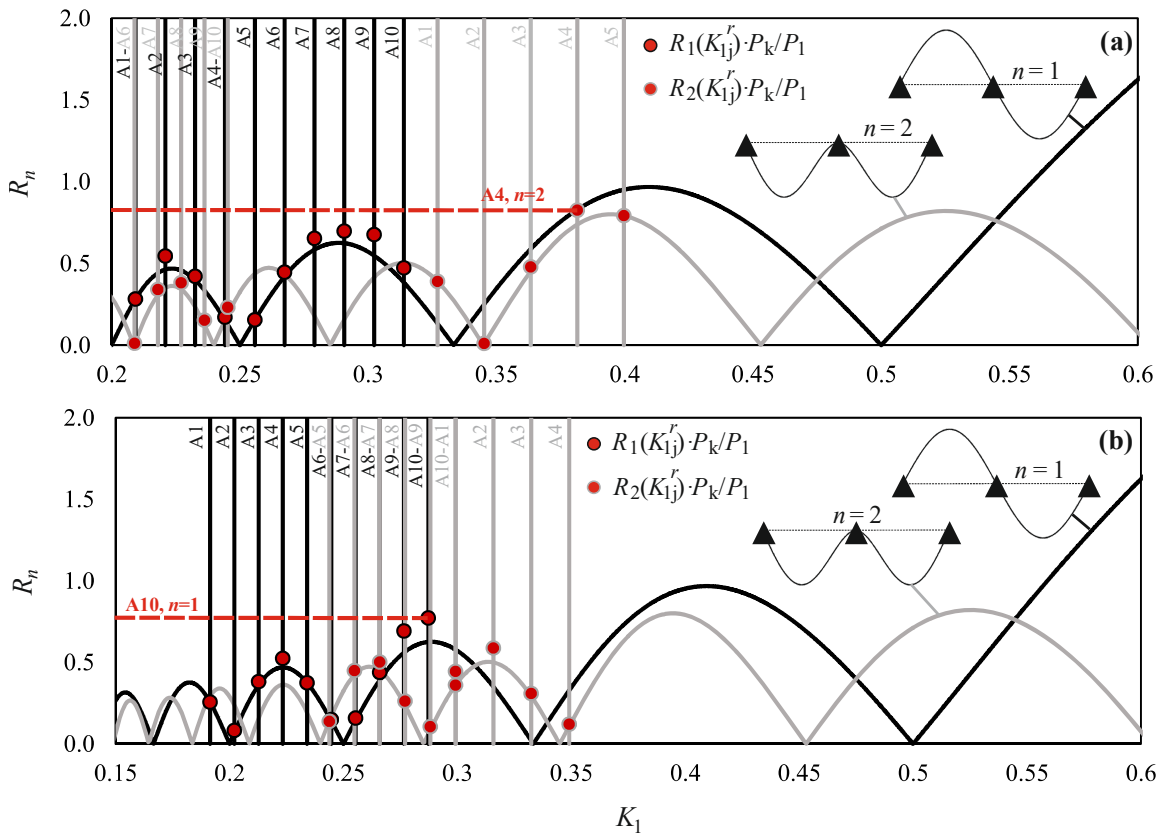


**Figure 5:**  $R_n$  vs.  $K_1$  for  $n=1,2$  and most critical resonant speeds from HSLM-A under 300 km/h: (a) Lögde Bridge and (b) Förslöv Bridge.

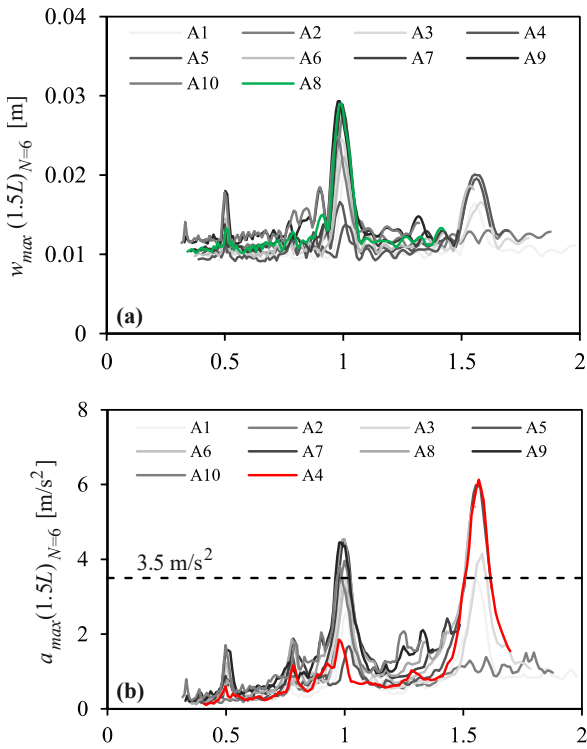


Figure 6: Lögde Bridge. (a)  $w_{max}$  and (b)  $a_{max}$  at  $x=1.5L$ . HSLM-A,  $V_{max}=300$  km/h.

#### 4.2 Case 2. Förslöv Bridge

As a second example, the case of a prestressed concrete railway bridge from the West Coast line located between the cities of Gothenburg and Copenhagen is presented. A modified version of the real structure is analyzed, with two identical spans of 23.5 m.

The first two natural frequencies of the bridge calculated analytically are 5.01 Hz and 7.83 Hz, respectively. Again, the theoretical resonant frequencies are computed for the first two modes and the first resonant orders. In this case study the natural frequencies are higher than in the previous one. For this reason, the critical velocities leading to first resonance of the first two modes exceed the maximum design speed of 300 km/h assumed for all the HSLM-A trains. In Fig. 5(b) the highest attainable non-dimensional resonant speeds for each train are represented with vertical solid

traces for the first and second modes. In this case, all the trains in the HSLM model are capable of inducing a second-order resonance of the first antisymmetric mode, but only the first four have a sufficiently low characteristic distance to induce second-order resonance of the first symmetric mode below 300 km/h. It can be verified graphically that train HSLM-A10 is the one leading to a highest value of  $R_n \cdot P_k / P_1$ , in particular for the first mode, as its associated second resonance speed coincides with the third local maximum of the free vibrations for  $n=1$ . Therefore, this train could be one of the most aggressive.

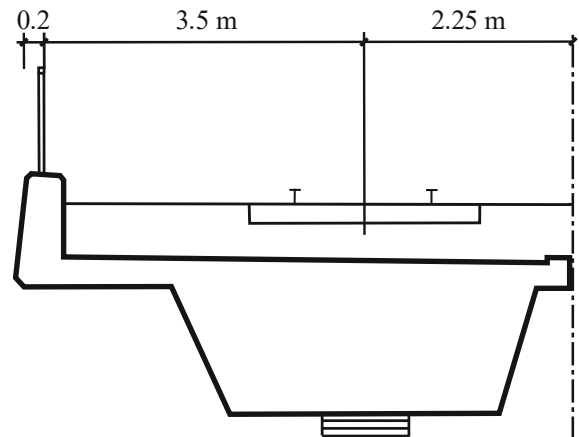
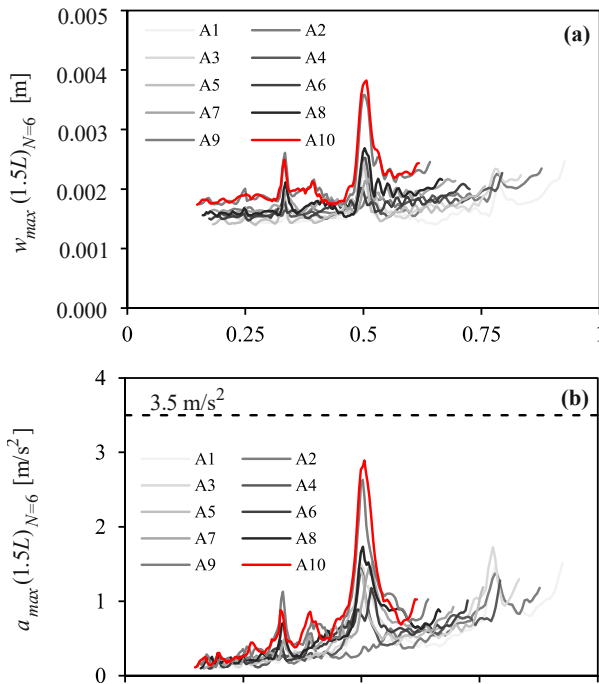


Figure 7: Förslöv Bridge. Elevation view and cross-section.

In what follows, the response of the bridge is obtained numerically under the ten HSLM-A trains. Fig. 8 shows the maximum displacement and acceleration responses of the Förslöv bridge taking into account the contribution of the first six modes of vibration. The overall maximum acceleration takes place

at the mid-span section of the second span, as in the previous example.



**Figure 8:** Förlöv Bridge. (a)  $w_{\max}$  and (b)  $a_{\max}$  at  $x=1.5L$ . HSLM-A,  $V_{\max}=300$  km/h.

The maximum acceleration reaches  $2.89$   $\text{m/s}^2$ , below the recommended limit for traffic safety on ballasted tracks. The maximum acceleration is associated to a second resonance of the fundamental mode, as predicted in the previous analysis of the level of free vibrations. The train leading to the maximum acceleration response is A10, with  $L/d_k=0.87$ , close to the theoretical ratio for the maximum second resonance of the fundamental mode (see Table 2) and also consistent with what is shown in Fig. 5(b). This train is also the one responsible for the maximum displacement, which is also caused by the second resonance of the fundamental mode. Only a few trains are able to induce second resonance of the second mode (i.e.  $V/f_1d=0.78$ ) and the response in terms of accelerations is much lower than that induced by the most aggressive train in the first mode.

In Fig. 8 it can also be observed that train A2 does not induce second resonance of the fundamental mode. For this particular train and bridge  $L/d_k=1.24$ , very close to the theoretical value of 1.25 of cancellation of this particular resonance (see Table 2). It is important to state, again, that the maximum response is mainly governed by the first two modes of vibration of the two-span beam, and that the contribution of higher modes in the acceleration response at resonance is negligible.

## 11 CONCLUSIONS

The main conclusions derived from the research conducted are:

- When a load moving at constant speed travels on a two-span continuous beam, the level of free vibrations left by the load in a certain mode may be maximum or negligible, depending on the ratio between the load velocity and the beam frequency. These conditions for maximum free vibration and cancellation can be obtained analytically in a non-dimensional format.
- Linear velocities that cancel out the free vibrations in the first antisymmetric mode also cancel out the response of the remaining antisymmetric modes. This does not occur among the symmetric modes or among these and the fundamental one.
- When resonance is induced on a two-span continuous beam or bridge by a train of equidistant loads, its amplification will depend on the level of the free vibrations associated to the particular velocity. Moreover, depending on the ratio between the length and the train characteristic distance, the response at resonance may be rather prominent or almost imperceptible.

- The analytical predictions of the  $L/d$  ratios leading to maximum resonance or its cancellation, obtained in the absence of damping and admitting separate modal contributions, show themselves to be excellent estimates of the real values when several modal contributions and modal damping are considered.
- The maximum acceleration response in a two-identical-span railway bridge is mostly governed by the first antisymmetric and first symmetric modes. If a bridge undergoes resonance of the first two modes, the one leading to the maximum acceleration will depend on the maximum design speed. The non-dimensional free vibration amplitudes at the actual resonant speeds may be used to estimate the particular train, resonance order and mode number leading to the overall maximum acceleration response in the structure.

## ACKNOWLEDGEMENTS

The authors acknowledge the Spanish Ministry of Culture and Sport and the Ministry of Science, Innovation and Universities for the financial support received in the framework of (i) programme José Castillejo with reference number CAS18/00080 for mobility of researchers; and research project (ii) [PID2019-109622RB].

## REFERENCES

- [1] Y. Wang, Q. Wei, J. Yau. *Interaction response of train loads moving over a two-span continuous beam*. Int J Struct Stab Dyn 13(1):1-18, 2013.
- [2] J. Yau. *Resonance of continuous bridges due to high-speed trains*. J Mar Sci Technol 9(1):14-20, 2001.
- [3] Y. Yang, J. Yau, Y. Wu. *Vehicle-bridge interaction dynamics: with applications to High-Speed railways*. World Scientific, 2004.
- [4] E. Savin. *Dynamic amplification factor and response spectrum for the evaluation of vibrations of beams under successive moving loads*. J Sound Vib 248(2):267-288, 2001.
- [5] P. Museros, E. Moliner, M.D. Martínez-Rodrigo. *Free vibrations of simply-supported beam bridges under moving loads: Maximum resonance, cancellation and resonant vertical acceleration*. J Sound Vib 332(2):326-345, 2013.
- [6] C.P.C. Johansson, N.A. Nualláin, A. Andersson. *A methodology for the preliminary assessment of existing railway bridges for high-speed traffic*. Eng Struct 58(1):25-35, 2014.
- [7] M.D. Martínez-Rodrigo, A. Andersson, C. Pacoste, R. Karoumi. *Resonance and cancellation phenomena in two-span continuous beams and its application to railway bridges*. Eng Struct 222-111103, 2020.

## TRACK-BRIDGE INTERACTION IN RAILWAY BRIDGES COMPOSED BY SINGLE-TRACK ADJACENT DECKS USING 3D FE MODELS

J.C. Sánchez-Quesada\*, E. Moliner\*, A. Romero†, P. Galvín† and M.D. Martínez  
Rodrigo\*

\* Dpto. Ingeniería Mecánica y Construcción,  
Universitat Jaume I  
12071 Castellón, Spain  
e-mail: jquesada@uji.es  
ORCID: 0000-000-1-6268-6202

† Escuela Técnica Superior de Ingeniería  
Universidad de Sevilla  
41092 Sevilla, Spain

**Abstract.** A significant number of railway bridges composed by simply-supported (SS) spans are present in existing railway lines. Special attention must be paid to short to medium span length structures, as they are prone to experience high vertical acceleration levels at the deck due to their low weight and damping, compromising the travelling comfort and the structural integrity. The accurate prediction of the dynamic response of these bridges is a complex issue since it is affected by uncertain factors such as structural damping and complex interaction mechanisms such as vehicle-bridge, soil-structure or track-bridge interaction. Concerning track-bridge interaction, experimental evidences of a dynamic coupling exerted by the ballasted track between subsequent SS spans and also between structurally independent single-track twin adjacent decks have been reported in the literature. Nevertheless, this phenomenon is frequently disregarded due to the computational cost that involves the introduction of the track in the numerical models and the uncertainties in the mechanical parameters that define the track system.

The present work contributes to the study of the coupling effect exerted by the continuity of the ballasted track in railway bridges composed by SS spans and structurally independent decks at each span. With this purpose a 3D finite element (FE) track-bridge interaction model is implemented, which-includes a continuous representation of the track components meshing the sleepers, ballast and sub-ballast with solid FE. The numerical model is updated with experimental measurements performed on an existing railway bridge in a view to evaluate (i) the influence of the track continuity on the bridge modal parameters and on the train-induced vibrations; (ii) the adequacy of the implemented numerical model and (iii) the importance of the track-bridge interaction for an accurate prediction of the vertical acceleration levels under operating conditions.

**Key words:** railway bridges, vertical acceleration, track-bridge interaction, ballasted track, resonance.

## 1 INTRODUCTION

The dynamic behaviour of railway bridges has been a matter of concern for scientists and engineers during the past decades. The periodic nature of the railway excitation, associated to the succession of identical passenger coaches and track components travelling at constant speed, may cause important vibration levels in the infrastructure. Moreover, particular combinations of the structure natural periods and the train repetitive distances may induce resonance on the bridges, leading to a progressive increase of the vertical acceleration at the platform only bounded by the system damping. Bridges composed by simply supported spans are common in countries like Germany or China, as they may be constructed with rather systematic procedures, allowing prefabrication and partial replacement of the decks. In short-to-medium spans such structures are prone to experience resonance and important vertical vibrations due to their usually associated low mass and structural damping [1]-[4]. According to European Standards (EC) [5], the maximum vertical acceleration in railway bridges is limited to  $3.5\text{m/s}^2$  for ballasted tracks, which constitutes a considerably restrictive requirement for the design of new structures.

In an attempt to predict accurately the bridge dynamic response under operating conditions several numerical models of different complexities have been proposed over the years. For practical purposes one major concern is to meet a compromise between accuracy, computational cost and the assumption of simplifications aligned with current regulations. The structural geometry and scheme of train loads are obvious and rather certain factors that affect the dynamic response significantly. In engineering consultancies it is common to assume a beam or plate-type behaviour for the bridge deck and

to represent the railway excitation as constant moving loads, which is in accordance with the current standards and extensively used in the scientific literature [6]-[10]. However, other factors such as train-track-bridge and soil-structure interaction mechanisms are generally disregarded for practical applications, due to their uncertain nature and the computational effort usually required. The influence of such mechanisms on the bridge dynamics is the subject of study of a number of current investigations, and the work presented herein is specifically devoted to the coupling effect exerted by the ballasted track on bridges composed by SS spans under operating conditions.

In the present work, the authors analyse the properties and coupling effect of the ballasted track taking as starting point Old Guadiana Bridge, a representative railway bridge from a conventional railway line in Spain. The bridge is composed by two identical SS spans and two structurally independent but adjacent single-track decks. A clear dynamic coupling between the spans attributable to the track continuity, and also between the adjacent decks through the shared ballast layer was detected during experimental tests [11]. This work aims to assess the extent of track-bridge interaction effects in such bridges and the key parameters affecting the dynamic coupling between structurally independent parts. With this purpose a 3D FE model is implemented. A degraded type of ballast with elastic anisotropic behaviour is assumed at the regions between subsequent spans or adjacent decks to consider the potential degradation of this layer due to the relative vertical movements over these areas. The model is updated applying optimisation procedures to reproduce the modal properties identified experimentally. Finally the bridge response under the passage of railway traffic is predicted and compared with experimental measurements in a view to assess the adequacy of the proposed numerical

model.

## 2 BRIDGE DESCRIPTION

The structure under study is a double-track bridge that belongs to the conventional railway line Madrid-Alcázar de San Juan-Jaén in Spain. It is composed by two identical SS spans of 11.93m length between supports centres. The horizontal structure is formed by two adjacent but structurally independent single-track decks. Each deck is made of a reinforced concrete slab resting on five pre-stressed concrete girders. The decks are weakly connected along their longitudinal border through the ballast. Each track is conformed by Iberian gauge UIC60 rails and mono-block concrete sleepers separated 0.60m. The bridge substructure consists of two external abutments and one central support. The girders rest on them through laminated rubber bearings.

On May 2019 the response of the bridge was measured to characterise the modal parameters and the dynamic response under operating conditions. 18 accelerometers were installed underneath the girders and the vertical response was measured under ambient vibration and several train passages. The accelerometers were installed at points 1 to 18

indicated in Figure 1. For details of the experimental campaign the reader is referred to Reference [11].

In Figure 2 the first five experimental natural frequencies ( $f_i^{exp}$ ), mode shapes and modal damping ratios ( $\xi_i^{exp}$ ) identified from the ambient vibration response are included. Notice that the number of sensors installed was limited, especially in the second span. The lowest mode in frequency order corresponds to the first longitudinal bending mode of each span where the two adjacent decks vibrate in phase. In the second mode the two decks deform jointly creating a combined first torsion mode in each span. In the third mode, the two adjacent decks deform under independent torsion but out of phase conforming a first transverse bending mode. In the aforementioned modes, the coupling exerted by the ballast layer over the adjacent decks is evident. The fourth and fifth modes correspond to an in-phase torsional deformation and to the transverse bending of each deck, respectively.

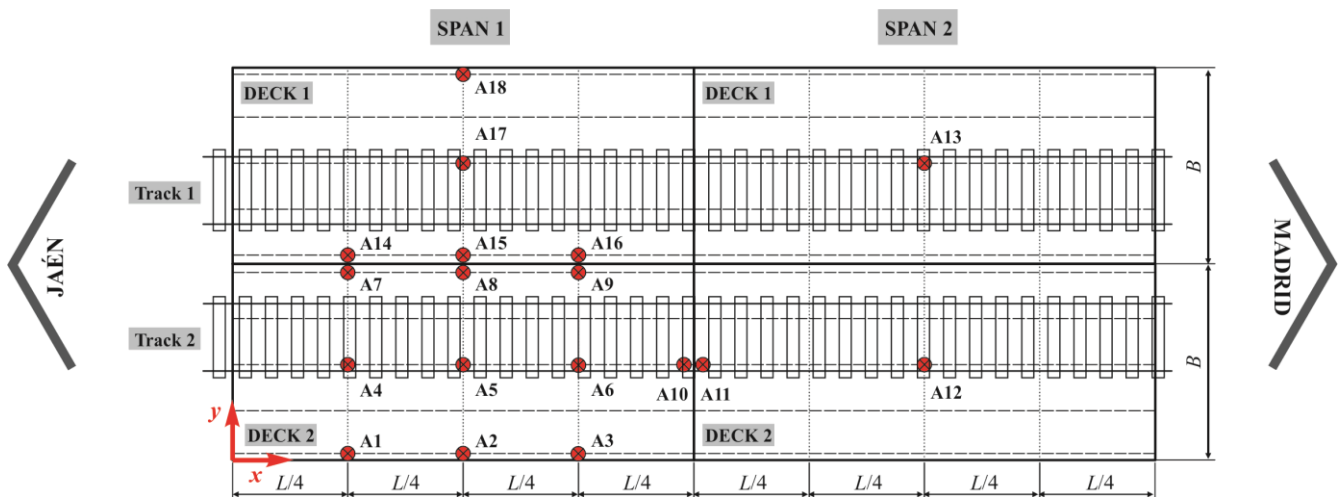
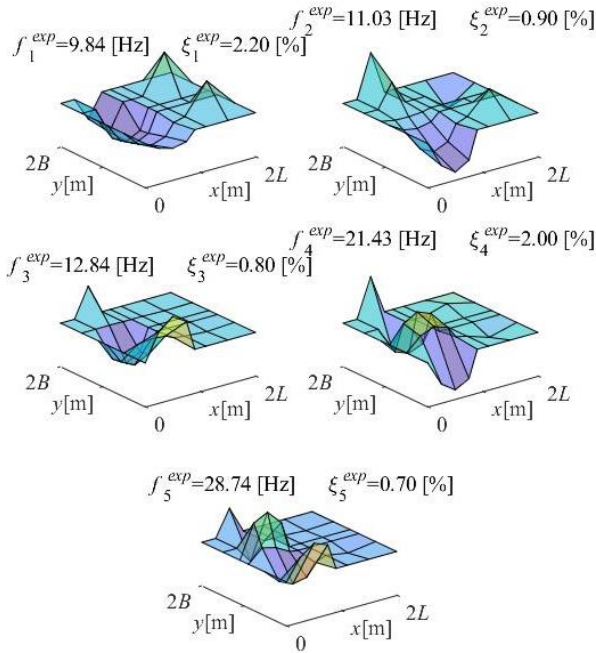


Figure 1: Sensors layout.



**Figure 2:** First five experimental modes, natural frequencies and modal damping ratios identified from ambient vibration.

### 3 NUMERICAL MODEL

A 3D continuous track-bridge interaction model of the complete bridge is implemented in ANSYS. The model includes the two spans and 15m of the track over the embankment before and after the bridge (Figure 3).

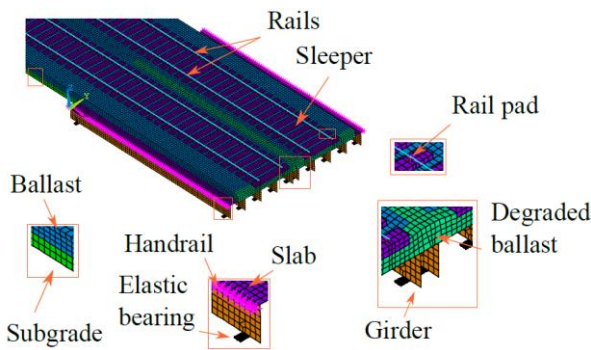


**Figure 3:** 3D track-bridge numerical model. In the view: detail of one span and track extension.

The main features of the model are:

- The slabs and longitudinal girders are meshed with shell FE (SHELL181)

with 6 degrees of freedom (DOF) per node.

- For the laminated rubber bearings located at the girders supports solid FE (SOLID185) of isotropic material are used, considering their real dimensions. The elastic modulus of the material is estimated in order to reproduce the experimental static deflection measured during the proof load test in 2005 before the bridge opening [12]. Kinematic constraints are applied at each girder end for the connection with the elastic bearing through a massless infinitely rigid plate defined at the bearing top surface. In the bottom surface, classical fixed boundary conditions are used.
- Timoshenko beam elements with 6 degree of freedom (DOF) per node (BEAM188) are used for the rails, while the sleepers are discretised using solid elements (SOLID185) with 3 DOF per node. The rails are connected to the sleepers through discrete spring-damper elements (COMBIN14) representing the rail pads.
- The ballast layer, meshed with solid elements (SOLID185), is divided into (i) a non degraded region of isotropic elastic behaviour; and (ii) a degraded region, placed in the vicinity of the longitudinal joint between the decks and along the transverse border between the two spans, of transversely isotropic material behaviour. With this approach different interlocking mechanisms of the ballast granules in the out-of-plane (vertical) and in the in-plane directions can be considered.
- The subgrade layer at the embankment, also meshed with solid elements (SOLID185), is restrained in

its bottom surface.

- Finally, the handrails are included in the model as lumped masses (MASS21) uniformly distributed along the two external borders of the bridge decks.

The numerical model contains 231940 elements and 260210 nodes, which correspond to 769801 degrees of freedom.

#### 4 MODEL CALIBRATION

The numerical model of the bridge is calibrated based on the modal parameters (natural frequencies and mode shapes) identified from ambient vibration in the experimental test performed in Guadiana bridge. The agreement between the experimental and numerical mode shapes is quantified through the Modal Assurance Criterion (MAC) [13] and the relative difference between the numerical and experimental frequencies of the paired modes, as per

$$MAC = \frac{(\phi_i^{exp,T} \cdot \phi_j^{num})^2}{(\phi_i^{exp,T} \cdot \phi_i^{exp}) \cdot (\phi_i^{num,T} \cdot \phi_j^{num})} \quad (1)$$

$$e_{\%1} = \frac{f_i^{exp} - f_j^{num}}{f_i^{exp}} \cdot 1$$

$$i = \{1, 2, 3, 4, 5\} ; j = \{1, 2, \dots, n\}$$

In the previous equations,  $\phi_i^{exp}$  and  $\phi_j^{num}$  are the  $i^{\text{th}}$  and  $j^{\text{th}}$  experimental and numerical mode vectors, respectively,  $f_i^{exp}$  and  $f_j^{num}$  the corresponding natural frequencies,  $T$  implies transpose and  $n$  maximum numerical mode.

An optimisation iterative procedure implemented in ANSYS-MATLAB is performed based on the minimisation of an objective function involving the difference in natural frequencies and MAC residuals, under variations of seven model parameters that are chosen according to (i) a preliminary

sensitivity analysis; and (ii) the level of knowledge and certainty on the particular track-bridge system properties. Successive model samples are generated from variations of the selected model parameters within reasonable limits with respect to nominal values extracted from the project information, scientific literature and current standards.

Table 2 shows the model parameters used in the numerical idealisation of Old Guadiana bridge, in which the following nomenclature is used:  $E$ ,  $\nu$  and  $\rho$  stand for the elastic modulus, Poisson's ratio, and mass density, respectively. Also,  $X$ ,  $Y$  and  $Z$  refer to the longitudinal direction (parallel to the track), transverse and vertical directions, respectively. In the rail,  $I_{yr}$  refers to the moment of inertia of the cross-section with respect to  $Y$ , and  $m$  denotes linear distributed mass. Concerning the track components, the spring-dashpot discrete properties of the rail pads ( $K_p$  and  $C_p$ ) are provided, and the sleepers dimensions (length, width and height) and total mass are designated as  $l_{sl}$ ,  $w_{sl}$ ,  $h_{sl}$  and  $M_{sl}$ , respectively. In the ballast properties,  $h_b$  is the total height of the layer, which is assumed constant and uniform over the platform. Underneath the sleepers, the ballast thickness is  $h_b - h_{sl}/2$ . A ballast thickness of  $h_b = 45\text{cm}$  is considered based on in situ inspection, leading to a total ballast thickness underneath the sleepers of  $34\text{cm}$ , in accordance with Spanish regulations [14].

Notice that the main ballast presents isotropic elastic properties  $E_b$  and  $\nu_b$  identical in the three directions, and that the degraded ballast elastic constants are expressed as  $E_{bI}$ ,  $G_{bIJ}$  for the shear modulus, and  $\nu_{bIJ}$ , where  $I$  and  $J$  refer to the spatial directions  $X$ ,  $Y$  and  $Z$ . The degraded ballast behaviour is considered transversely isotropic, therefore unequivocally defined by five independent elastic constants:

$$\begin{aligned} E_{bX} = E_{bY} ; E_{bZ} ; G_{bXZ} = G_{bYZ} \\ \nu_{bXY} ; \nu_{bXZ} = \nu_{bYZ} \end{aligned} \quad (2)$$

In equation (2),  $E_{bX} = E_{bY}$  are the in-plane elastic moduli,  $E_{bZ}$  and  $G_{bXZ} = G_{bYZ}$  the out-of-plane elastic and shear moduli, respectively, and  $\nu_{bXY}$  and  $\nu_{bXZ} = \nu_{bYZ}$  the Poisson's ratios.

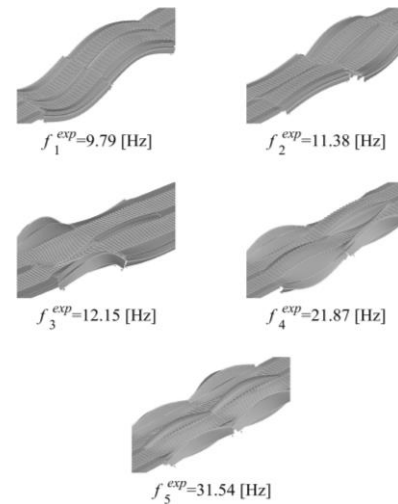
The seven optimisation parameters are those for which optimization ranges are provided in Table 2. Concerning the ballast, three properties are chosen ( $\rho_b$  and the degraded ballast elastic properties  $E$  and  $G$ ), as their influence is found much more significant than the remaining ballast parameters. The preliminary sensitivity analysis revealed the importance of considering degraded ballast regions with transversely isotropic material properties, since a better correspondence with the experimental modal parameters is achieved when the in-plane elastic constants  $E_{bX} = E_{bY}$  are much lower than  $E_{bZ}$ . Therefore, the elastic constants in the degraded regions were initially set to  $E_{bX} = E_{bY} = E_{bZ}$  (isotropic material) and successively reduced up to  $0.1 \cdot E_{bZ}$  during the optimization procedure. In a similar way, the constants  $G_{bXZ} = G_{bYZ}$  were initially set to  $E_{bZ}/(2 \cdot (1 + \nu_{bXZ}))$  (isotropic material) and reduced up to 90% during the calibration. The final updated values for the optimisation parameters are also given in Table 2.

Table 1 shows the results of the model calibration in terms of numerical frequencies ( $f_j^{num}$ ), frequency differences  $e_{100\%}$ , and MAC numbers of the paired numerical modes. In Figure 4 the first five numerical mode shapes and natural frequencies of the updated model are included. All the modes identified experimentally with natural frequencies below 30Hz are finally reproduced numerically with reasonably good accuracy in terms of frequency differences and MAC numbers. The second and third modes, which are more affected by the continuity of the ballasted track between adjacent decks, are predicted with frequency differences lower than 5.5%. Also their MAC numbers exhibit a satisfactory

correlation with the measurements, with values close to 0.90 or even above. As can be seen the correspondence of the fifth numerical mode with the experimental measurements is less accurate, though very reasonable considering the limited number of sensors available in the experimental campaign for the identification of higher frequency modes.

Mode	1	2	3	4	5
$f_i^{exp}$ [Hz]	9.84	11.03	12.84	21.43	28.74
$f_j^{exp}$ [Hz]	9.79	11.38	12.15	21.87	31.54
MAC	0.94	0.89	0.97	0.93	0.75
$e_{100\%}$	0.47	-3.17	5.37	-2.05	-9.75

**Table 1:** Experimental and numerical frequencies for modes under 30Hz. Frequency differences and MAC numbers of the paired modes after calibration.



**Figure 4:** Paired numerical modes and natural frequencies of the calibrated 3d model.

## 5 BRIDGE RESPONSE UNDER TRAIN PASSAGES

During the experimental campaign performed by the authors in 2019 [11] the acceleration response of Old Gadiana Bridge was also recorded under several train circulations. In this section a comparison between the experimental and numerical prediction of the vertical acceleration levels at

Bridge component	Parameter	Initial value	Lower	Upper	Final value	Unit
Girder	$E_g$	$3.60 \cdot 10^{10}$	$2.52 \cdot 10^{10}$	$5.22 \cdot 10^{10}$	$4.82 \cdot 10^{10}$	Pa
	$\nu_g$	0.3	-	-	0.3	-
	$\rho_g$	2500	1750	3250	2504	kg/m <sup>3</sup>
Slab	$E_s$	$3.60 \cdot 10^{10}$	$2.52 \cdot 10^{10}$	$4.86 \cdot 10^{10}$	$3.10 \cdot 10^{10}$	Pa
	$\nu_s$	0.3	-	-	0.3	-
	$\rho_s$	2500	1500	4000	2480	kg/m <sup>3</sup>
Elastic bearings	$E_{eb}$	$2.39 \cdot 10^8$	-	-	$2.39 \cdot 10^8$	Pa
	$\nu_{eb}$	0.2	-	-	18.20	-
	$\rho_{eb}$	1230	-	-	1230	kg/m <sup>3</sup>
Rail UIC60	$E_r$	$2.1 \cdot 10^{11}$	-	-	$2.1 \cdot 10^{11}$	Pa
	$I_{yr}$	$3038 \cdot 10^8$	-	-	$3038 \cdot 10^8$	m <sup>4</sup>
	$\rho_g$	60.34	-	-	60.34	kg/m
Rail pad	$K_p$	$1.00 \cdot 10^8$	-	-	$1.00 \cdot 10^8$	N/m
	$C_p$	$7.5 \cdot 10^4$	-	-	$7.5 \cdot 10^4$	Ns/m
Sleeper	$E_{sl}$	$3.60 \cdot 10^{10}$	-	-	$3.60 \cdot 10^{10}$	Pa
	$\nu_{sl}$	0.3	-	-	0.3	-
	$w_{sl}$	0.30	-	-	0.30	m
	$l_{sl}$	2.60	-	-	2.60	m
	$h_{sl}$	0.22	-	-	0.22	m
	$M_{sl}$	300	-	-	300	kg
Ballast	$h_b$	0.45	-	-	0.45	m
	$E_b$	$1.10 \cdot 10^8$	-	-	$1.10 \cdot 10^8$	Pa
	$\nu_b$	0.3	-	-	0.3	-
	$\rho_b$	1800	1260	2340	1584	kg/m <sup>3</sup>
Degraded Ballast	$E_{bX} = E_{bY}$	$1.10 \cdot 10^8$	$1.21 \cdot 10^7$	$1.10 \cdot 10^8$	$12.10 \cdot 10^6$	Pa
	$E_{bZ}$	$1.10 \cdot 10^8$	-	-	$1.10 \cdot 10^8$	-
	$G_{bYZ} = G_{bXZ}$	$4.58 \cdot 10^7$	$2.29 \cdot 10^7$	$4.58 \cdot 10^7$	$2.29 \cdot 10^7$	-
	$\nu_{bXY} = \nu_{bYX}$	0.2	-	-	0.2	-
	$\nu_{bXZ} = \nu_{bYZ}$	0.2	-	-	0.2	-
	$\rho_b$	1800	1260	2340	1584	kg/m <sup>3</sup>
Subgrade	$E_f$	$9.00 \cdot 10^7$	-	-	$9.00 \cdot 10^7$	Pa
	$\nu_f$	0.3	-	-	0.3	-
	$\rho_f$	1800	-	-	1800	kg/m <sup>3</sup>
Handrail	$m_h$	50	-	-	50	kg/m

**Table 2:** Model parameters: initial values, ranges of variations and final values.

different sensors locations under the passage of one train composition is presented.

The chosen circulation corresponds to the passage of S449 train from Jaén to Madrid along track 2 (Figure 1) at 154.8 km/h. S449 is a train with distributed traction and five cars: driver and passenger integrated cars at each end and three additional passenger coaches. The distance between shared bogies is  $d=17.75\text{m}$  and each axle load attains 161 kN.

According to the characteristic distance  $d$  of the train, the circulating speed is relatively

close to the theoretical fourth resonant speed of the fundamental mode of Old Guediana Bridge,  $v_{1,4} = f_1 \cdot d/4 = 9.84 \cdot 17.75 \cdot 3.6/4 = 157.2 \text{ km/h}$ . Furthermore,  $L/d = 0.67$  for this particular train (with  $L$  being the span length, measured between supports centres). This ratio approaches the theoretical second cancellation of the cited resonance order in SS plates [10]. Even though the real bridge behaviour is not completely explained by the train axles scheme and the theoretical resonance and cancellation conditions, these

ratios are helpful estimates for the interpretation of the results, and justify that the amplification at resonance of the fundamental mode excited by the S449 train should not be relevant.

Each row of Figure 5 shows the vertical acceleration response under the circulation of S449 at the sensors installed at the centre of the second span (A12 and A13), outer and inner borders of the loaded deck (A2, A8) and inner border of the unloaded deck at the first span (A15), according to the sensor location of Figure 1. The response at each sensor and for each train is plotted in the time domain (first column), frequency domain (second column) and in one-third octave frequency bands (third column). In the upper left corner of the third column graphs, letters (L) and (U) differentiate sensors installed under the loaded or unloaded track, respectively. This allows a good comparison of the effects of the traffic direction and type of train in the response at equivalent positions.

The experimental responses, represented in black trace, have been filtered applying two third-order Chebyshev filters with high-pass and low-pass frequencies of 1 Hz and 30 Hz, respectively. The numerical acceleration response, in red trace, is computed by Modal Superposition, considering a constant moving load model for the train excitation and therefore neglecting vehicle-bridge interaction (VBI) effects. The dynamic equations of motion of the full FE model are transformed to modal space and numerically integrated by the Newmark-Linear Acceleration algorithm. The time-step is defined as 1/50 times the smallest period used in the analysis, accounting for mode contributions up to 30 Hz as per European Standards [15]. Twenty modes are included in the numerical analyses. Modal damping values identified during the experimental campaign under ambient vibration (Figure 2) are assigned to the paired numerical modes. For the rest of the modes EC

recommended damping values are used.

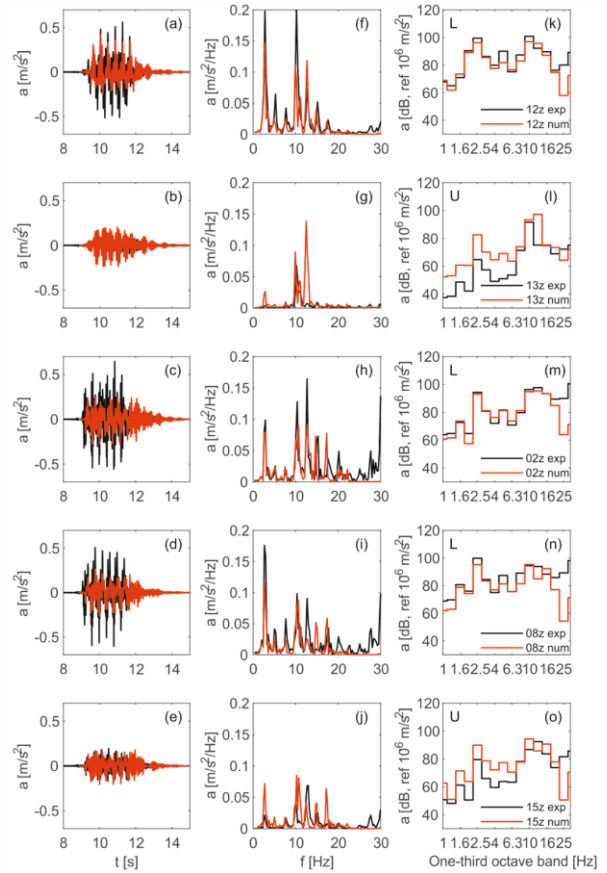


**Figure 5:** Time history (a-e), frequency content of the acceleration (f-j) one-third octave band content of the acceleration (k-o) at points A12 A13 A2 A8 and A15, induced by S449 on track 2 J-M at speed  $v=154.8$  [km/h]. Experimental results (black line) vs numerical prediction (red line).

The experimental acceleration responses reveal a noticeable coupling between the two decks that conform each span, which exhibit significant acceleration levels at points A13 and A15 when compared to the measurements at the same locations of the loaded deck (points A12 and A8, respectively), meaning that the transmission of vibrations between the loaded and unloaded decks through the ballast layer is substantial. The evident vibration transmission between the twin decks and the coupling detected in the lowest frequency modes justifies the need of a numerical model

accounting for the continuity of the ballast in order to reproduce the real bridge response under passing trains.

The proposed numerical model is reasonably accurate, especially for frequency contents below 20 Hz. The frequency domain plots exhibit clear peaks at frequencies below 9 Hz associated to the excitation (i.e. axle or bogie passing frequency, calculated as  $v/d$ ) and their corresponding multiples, which are much more perceptible at the loaded sensors. Additional peaks appear in the range 10-20 Hz in the frequency domain plots which could be associated to structural modes and also multiples of the bogie passing frequency. The peak amplitudes are overestimated at the unloaded deck and underestimated at the loaded deck.

The time-history responses show certain underestimation of the amplitude levels in the loaded decks during the forced vibration phase. Conversely, at the unloaded decks the predicted time history response during the forced vibration is overestimated. The correspondence with the measurements improves during the free vibration phase. It is well known that VBI effects, not considered in this study, tend to reduce the vibration levels on the structure and may become significant at resonance for train compositions with a high number of coaches [16]. For the S449, VBI should not be of importance either as clear resonance of the first bending mode is not induced.

As general conclusions, it can be said that (i) taking into account the ballasted track coupling between the decks is relevant in order to capture the contribution of modes higher than the first bending or first torsion modes under train passages; (ii) in this type of structures where the ballasted track coupling may be of importance, identifying the structure properties experimentally becomes essential; (iii) the model presented herein reproduces with acceptable accuracy the bridge response

both at the loaded and unloaded decks, but the correspondence is better in the former case; (iv) the solution of the dynamic problem is performed in reasonable time with a personal computer once the modal analysis has been performed.

## 6 CONCLUSIONS

In this work the dynamic response of railway bridges composed by SS spans and adjacent single-track decks weakly connected through the ballasted track is investigated. The main aim is to assess the extent of track-bridge interaction effects in such bridges and the key parameters affecting the dynamic coupling between structurally independent parts. With this purpose a 3D FE model is implemented. A degraded type of ballast with elastic anisotropic behaviour is assumed at the regions between subsequent spans or adjacent decks to consider the potential degradation of the ballast due to the relative vertical movements under train passages. The model is updated with experimental results and the main ballast properties affecting the decks coupling are identified and evaluated by means of sensitivity analyses. Finally the bridge response under the passage of a crossing the bridge is predicted and compared with experimental measurements, in a view to assess the adequacy of the proposed numerical model.

The updated numerical model is able to reproduce the first five natural frequencies and mode-shapes identified experimentally with an average error in the frequencies close to 4% and an average MAC of 0.9, and with a remarkably good correspondence in the particular case of the first longitudinal bending, third transverse bending and fourth second torsion modes. In order for the model to reproduce experimental modes higher than the second one, it is essential to consider the coupling effect of the ballast layer, especially

between the adjacent decks. Also, in order to be able to reproduce with reasonable accuracy the first five modes of the structure, considering the ballast along the shared borders as an elastic isotropic material does not provide satisfactory results. For this reason, in those areas the ballast elastic behaviour is assumed transversely isotropic, with elastic moduli in the horizontal directions of approximately 10% of the vertical elastic modulus.

The bridge response under the passage of a train is compared with the numerical predictions. The numerical response is obtained by Modal Superposition. Experimental modal damping values obtained from ambient vibration are used in the analysis. From the experimental-numerical comparison the following may be concluded:

- The bridge exhibits a noticeable dynamic coupling between adjacent decks under operating conditions which can be attributed to the continuity of the ballasted track. Therefore, for an accurate assessment of the vertical acceleration levels in bridges formed by structurally independent SS decks, the implementation of weak connections between the parts may be a good practice. The results presented herein may be useful for the definition of alternative discrete track models for this same purpose.
- The experimental-numerical comparison reveals that the dynamic behaviour of these type of bridges under railway traffic is complex and difficult to predict, since it is affected by a number of interaction mechanisms highly uncertain. Despite the good correspondence of the calibrated model with the first five identified modes in terms of both natural frequencies and MAC values,

the predicted vertical acceleration levels are reasonable but less accurate for frequency contents above 20 Hz. The assumption of a classically-damped structure and the amplitude dependent mechanisms associated to the shared ballast layer can play an important role and deserve further studies.

- In general terms, the numerical model predicts the vertical acceleration levels with more accuracy at the sensors located at the loaded decks. In the unloaded decks the amplitudes associated to the excitation frequencies and to the lowest natural frequencies of the bridge are sometimes overestimated.
- In this type of structures where the ballasted track coupling may be of importance, identifying the structure properties experimentally becomes essential.

## 7 ANKNOLEDGEMENTS

The authors would like to acknowledge the financial support provided by the Spanish Ministry of Science and Innovation under research project PID2019-109622RB; FEDER Andalucía 2014-2020 Operational Program for project US-126491; Generalitat Valenciana and Universitat Jaume I under research projects AICO2019/175 and UJI/A2008/06; and the Andalusian Scientific Computing Centre (CICA).

## REFERENCES

- [1] ERRI-D-214/RP9. *Rail bridges for speeds > than 200km/h, Final report. Part A. Synthesis of the results of D214 research.* International Union of Railways, 1999.
- [2] L. Fryba. Dynamic behaviour of bridges due to high-speed trains. *Workshop*

- Bridges for High-Speed Railways*, Porto: 137-158, June 2004.
- [3] W. Hoopah. Dynamic calculations of high-speed railway bridges in France some case studies. *Dynamics of High-Speed Railway Bridges*.:133-145, January 2008.
- [4] M. Zacher, M. Baeßler. Dynamic behaviour of ballast on railway bridges. *Dynamics of High-Speed Railway Bridges*: 99-112, 2008.
- [5] UNE-EN 1991-2:2019. *Eurocode 1: Actions on Structures - Part 2: Traffic loads on bridges*. European Committee for Standardization, Brussels, 2003.
- [6] Y.B. Yang, J.D. Yau. L.C. Hsu, Vibration of simple beams due to trains moving at high speeds. *Engineering Structures*. 19(11):936-944, 1997.
- [7] L. Frýba. A rough assessment of railway bridges for high speed trains. *Engineering Structures*. 23(5):548-556, 2001.
- [8] J.D. Yau, Y.B. Yang. Vertical accelerations of simple beams due to successive loads traveling at resonant speeds. *Journal Of Sound and Vibration*. **289**(1-2):210-228, 2006.
- [9] X.Q. Zhu, S.S. Law. Dynamic behavior of orthotropic rectangular plates under moving loads. *Journal of Engineering Mechanics*. 129(1):79-87, 2003.
- [10] M.D. Martínez-Rodrigo, E. Moliner, A. Romero, G. De Roeck, P. Galvín. Maximum resonance and cancellation phenomena in orthotropic plates traversed by moving loads: Application to railway bridges. *International Journal of Mechanical Sciences*. 169.
- [11] P. Galvín, A. Romero, E. Moliner, G. De Roeck, M.D. Martínez-Rodrigo. On the dynamic characterisation of railway bridges through experimental testing. *Engineering Structures*. 226, 111261.
- [12] CITEF, *Informe sobre resultado de registros en puente sobre Río Guadiana P.K. 160.000. Línea Madrid-Cádiz, tramo Alcázar de San Juan-Manzanares*.
- [13] R.J. Allemang. The modal assurance criterion - twenty years of use and abuse. *Journal of Sound and Vibration*. 37:14-21, 2003.
- [14] IF3. *Instrucción para el proyecto y construcción de obras ferroviarias*. Ministerio de Fomento, Gobierno de España, 2015.
- [15] CEN/TC250. *Eurocode: Basis of structural design. Annex A2: Application for bridges. Final version*. European Committee for Standardization, Brussels, 2005.
- [16] A. Doménech, P. Museros, M.D. Martínez-Rodrigo. Influence of the vehicle model on the prediction of the maximum bending response of simply-supported bridges under high-speed railway traffic. *Engineering Structures*. 72:123-139, 2014.

## BALLAST TRACK-BRIDGE INTERACTION IN SINGLE-TRACK RAILWAY BRIDGES OF DIFFERENT TYPOLOGIES

J. Chordà-Monsonís\*, M.D. Martínez-Rodrigo\*, P. Galvín†, A. Romero† and E.  
Moliner\*

\* Departamento de Ingeniería Mecánica y Construcción,  
Universitat Jaume I  
12006 Castelló, Spain  
e-mail: chordaj@uji.es  
ORCID: 0000-0002-2544-2951

† Departamento de Mecánica de Medios Continuos y Teoría de Estructuras  
Universidad de Sevilla  
41092 Sevilla, Spain

**Abstract.** Short-to-medium span simply-supported (SS) railway bridges are prone to experience high levels of vertical acceleration due to train passage. The necessity of predicting accurately their dynamic behaviour, for design, safety and maintenance reasons, requires a deep understanding of the train induced vibrations in these structures. A key factor of this phenomenon is the influence exerted by the ballasted track on their dynamic response. This paper provides a detailed sensitivity analysis over a single-track bridge catalogue covering lengths of interest from 10 to 25 m considering two different typologies, (i) girder-deck bridges and (ii) slab-deck bridges. The effect of the vertical flexibility of elastic bearings is also analysed. A 2D Finite-Element (FE) track-bridge interaction model is implemented with the aim to evaluate the influence of the track parameters on the modal properties, the harmonic response and also the dynamic response due to train passage of the bridges. The obtained results reveal the influence of the ballast shear stiffness and damping in the dynamic behaviour of the structures, especially in the case of the girder bridges.

**Key words:** Railway Induced Vibrations, Bridges, Track-Bridge Interaction, Resonance, Vertical Acceleration, Ballast Track.

### 1 INTRODUCTION

In a context of an increasing demand of personal and freight mobility around the world, railway systems have experienced a sustained development that projects them as a reliable and sustainable way of transportation for the time to come.

For this reason, dynamic effects on railway bridges are considered of major interest and concern for scientists and engineers, especially since the appearance of High Speed (HS) [1]. In this regard, short-to-medium span (10 – 25

m) SS railway bridges are particularly prone to experience an excessive level of vertical acceleration at the deck during train passage, due to its usually associated low mass and structural damping, especially at resonance [2]. This could cause discomfort for the passengers, flaws in the ballast layer, a rise in the maintenance service cost of the track and an increased risk of derailment in the worst-case scenario.

Train induced vibrations in railway bridges is a rather complex interaction problem, which is affected by several factors. Apart from the

mechanical and geometrical properties of the bridge and the characteristics of the train, interaction mechanisms regarding the vehicle, the track and the soil may also affect the response of the structure, which are currently under investigation [3]. In addition, the computational cost of including these mechanisms is considerable, thus, simplified models that usually disregard them are commonly used in engineering consultancies.

This work is dedicated to the investigation of the effect exerted by the ballast track on the vertical dynamic response of SS railway bridges. To this aim, the influence of the main parameters of the ballast track on the bridge modal properties, harmonic response and also the dynamic response due to train passage, is evaluated. With this purpose, a 2D FE track-bridge interaction model is implemented, where the track is represented using a three-layer discrete model, based on the work by Zhai et al. [4]. The model is employed to perform a sensitivity analysis over a bridge catalogue covering bridges of two different deck typologies and for a selected range of lengths of interest from 10 to 25 m. In sections 2 and 3, the bridge catalogue is presented, and the numerical model is described. In section 4, the results of the dynamic are included. Finally, in section 5, the main conclusions are summarized.

## 2 BRIDGE CATALOGUE

The catalogue contemplates single-track railway bridges of span lengths that range from 10 to 25 m in 2.5 m intervals. For each length, two common deck typologies are considered: (i) pre-stressed concrete girder decks; and (ii) voided or solid concrete slabs, or pre-stressed filler beams encased in a concrete pseudo-slab (see Fig. 1). As for the vertical support of the decks, infinitely rigid supports and elastic supports accounting for the vertical flexibility of neoprene bearings are differentiated.

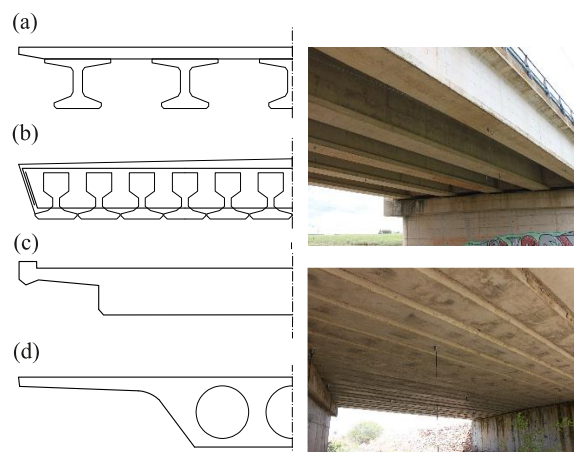


**Figure 1:** Left: (a) pre-stressed concrete girder deck; (b) concrete filler beam pseudo-slab; (c) solid concrete slab; (d) voided concrete slab. Right: girder deck (up) and pseudo-slab (down) of two bridges in Madrid-Sevilla HS line.

The main characteristics regarding the mass and the fundamental frequency of the bridges are calculated according to the work presented by Doménech et al. [5], where an ensemble of existing bridges of the considered typologies were studied. Fig. 2 shows for the 28 bridges of the catalogue the total mass per bridge span and the fundamental frequency. For the girder decks, the mass of the reported single-track existing bridges approaches the inferior limit. Additionally, this corresponds to the worst-case scenario for the vertical acceleration criterion. The fundamental frequency is selected as 50% of the difference between the Eurocode 1 (EC1) simplified method limits for each length [6]. For the slab decks, the mass value is selected as 25% of the difference between the upper and the lower limits for each length. This corresponds to an average value for the mass of existing single-track slab bridges. For the fundamental frequency, the same criterion is applied, and the frequency is calculated as 25% of the difference between the limits for each length. In addition, an ES version for each bridge is also defined admitting that the ratio  $\kappa$  between the bridge

bending stiffness and the vertical stiffness of the bearings is approximately equal to 0.05, which leads to a reduction of the fundamental frequency of 3-4% with respect to the SS case [7], as indicated in Eq. 1. This equation shows the relation between the cross-section flexural rigidity of each section ( $E_{bi}I_{ybi}$ ) and the product of the vertical dynamic stiffness of the elastic bearings ( $K_{bi,dyn}^n$ ) by the span length ( $L_{bi}$ ).

$$\kappa = \frac{E_{bi} I_{ybi} \pi^3}{\overline{K}_{bi,dyn}^n L_b^3} \approx 0.05 \quad (1)$$

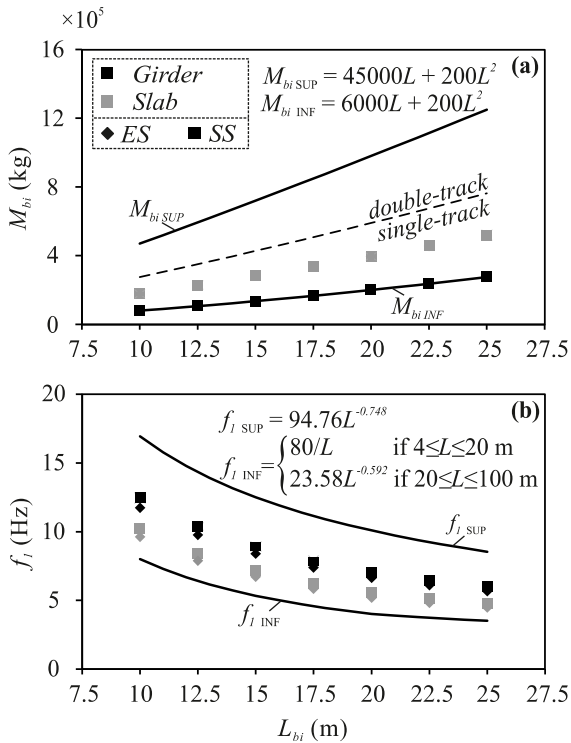


**Figure 2:** (a) Mass per span and (b) fundamental frequency of the bridges under study.

The mechanical properties of the bridges of the catalogue are shown in Tables 1 and 2, where the data are expressed per bridge span. The first column (ID) stands for the identification code for each bridge, which contains the typology, the type of support and the span length (e.g. GD-ES-10 stands for girder-deck bridge, elastically-supported with

10 m of span length). The next columns include the fundamental frequency,  $f_l$ , total mass,  $M_{bi}$ , cross-section flexural rigidity of the span section,  $E_{bi}I_{ybi}$ , and the vertical dynamic stiffness of the elastic bearings ( $K_{bi,dyn}^n$ ).

ID	$f_l$ [Hz]	$M_{bi}$ [t]	$E_{bi}I_{ybi}$ [MN/m <sup>2</sup> ]	$K_{bi,dyn}^n$ [MN/m]
GD-SS-10	12.46	80.0	$3.56 \cdot 10^3$	$\infty$
GD-ES-10	11.72	80.0	$3.12 \cdot 10^3$	$3.12 \cdot 10^3$
GD-SS-12.5	10.36	106.3	$6.45 \cdot 10^3$	$\infty$
GD-ES-12.5	9.75	106.3	$5.81 \cdot 10^3$	$2.87 \cdot 10^3$
GD-SS-15	8.92	135.0	$1.06 \cdot 10^4$	$\infty$
GD-ES-15	8.39	135.0	$9.63 \cdot 10^3$	$2.70 \cdot 10^3$
GD-SS-17.5	7.86	166.3	$1.64 \cdot 10^4$	$\infty$
GD-ES-17.5	7.39	166.3	$1.50 \cdot 10^4$	$2.58 \cdot 10^3$
GD-SS-20	7.04	200.0	$2.41 \cdot 10^4$	$\infty$
GD-ES-20	6.62	200.0	$2.20 \cdot 10^4$	$2.49 \cdot 10^3$
GD-SS-22.5	6.48	236.3	$3.51 \cdot 10^4$	$\infty$
GD-ES-22.5	6.09	236.3	$3.20 \cdot 10^4$	$2.49 \cdot 10^3$
GD-SS-25	6.02	275.0	$4.93 \cdot 10^4$	$\infty$
GD-ES-25	5.66	275.0	$4.51 \cdot 10^4$	$2.50 \cdot 10^3$

**Table 1:** Mechanical properties of the girder bridges.

ID	$f_l$ [Hz]	$M_{bi}$ [t]	$E_{bi}I_{ybi}$ [MN/m <sup>2</sup> ]	$K_{bi,dyn}^n$ [MN/m]
SD-SS-10	10.22	177.5	$6.63 \cdot 10^3$	$\infty$
SD-ES-10	9.62	177.5	$6.06 \cdot 10^3$	$4.67 \cdot 10^3$
SD-SS-12.5	8.38	228.1	$1.09 \cdot 10^4$	$\infty$
SD-ES-12.5	7.88	228.1	$9.97 \cdot 10^3$	$4.03 \cdot 10^3$
SD-SS-15	7.12	281.3	$1.66 \cdot 10^4$	$\infty$
SD-ES-15	6.70	281.3	$1.53 \cdot 10^4$	$3.59 \cdot 10^3$
SD-SS-17.5	6.22	336.9	$2.40 \cdot 10^4$	$\infty$
SD-ES-17.5	5.84	336.9	$2.21 \cdot 10^4$	$3.32 \cdot 10^3$
SD-SS-20	5.52	395.0	$3.32 \cdot 10^4$	$\infty$
SD-ES-20	5.19	395.0	$3.05 \cdot 10^4$	$3.03 \cdot 10^3$
SD-SS-22.5	5.11	455.6	$4.69 \cdot 10^4$	$\infty$
SD-ES-22.5	4.80	455.6	$4.32 \cdot 10^4$	$2.99 \cdot 10^3$
SD-SS-25	4.76	518.8	$6.41 \cdot 10^4$	$\infty$
SD-ES-25	4.48	518.8	$5.95 \cdot 10^4$	$2.96 \cdot 10^3$

**Table 2:** Mechanical properties of the slab bridges.

### 3 TRACK-BRIDGE INTERACTION MODEL

For the subsequent analysis, a discrete FE 2D track-bridge interaction model, shown in Fig. 3, is implemented. A three-layer discrete

model for the track is configured, based on that proposed by Zhai et al. [4], which couples a series of elastically or simply-supported bridge spans. The track admits Ahlbeck hypothesis, so it can be assumed that the load transmitted from each sleeper to the ballast coincides with a cone distribution.

In the proposed model, the rail is represented with a Bernoulli-Euler (B-E) beam, where  $E_r$ ,  $I_{yr}$ , and  $m_r$  stand for the rail Young Modulus, cross-section moment of inertia with respect to the Y axis and linear mass, respectively. Below, the vertical damping and stiffness of the rail pads ( $C_p$ ,  $K_p$ ), of the mobilized ballast ( $C_b$ ,  $K_b$ ) and of the subgrade ( $C_f$ ,  $K_f$ ) are included in the location of the sleepers. The continuity and coupling effect of the interlocking ballast granules is also considered in the model by means of spring-damper elements ( $C_w$ ,  $K_w$ ) that link relative vertical displacements between adjacent ballast masses. Then,  $M_{sl}$  and  $M_b$  stand for the mass of each sleeper and the vibrating ballast mass under each support, respectively. Damping and stiffness on the bridge deck ( $C_f^b$ ,  $K_f^b$ ) are set to 0 and  $100 \cdot K_f$ , respectively, assuming that the ballast rests directly on the bridge deck. The longitudinal interaction

between the rails and the deck through the ballast layer is disregarded in a first approach due to the high flexural stiffness of the bridges. As shown in Fig. 3, rail and track parameters are multiplied by a factor of two, as only one rail is explicitly included in the model.

The bridge is represented by means of  $N_{sp}$  simply or elastically-supported B-E beams representing each span of the bridge. In the present paper,  $N_{sp}$  is set to a value of 2, as two identical spans are considered for each bridge. The vertical stiffness of the neoprene bearings is introduced by the constant equivalent vertical stiffness  $\bar{K}_{bi,dyn}^n$  at each end section of the  $i$ -th bridge span. The parameters  $L_{bi}$ ,  $E_{bi}$ ,  $I_{bi}$  and  $m_{bi}$  stand for the length, Young Modulus, cross-section moment of inertia with respect to the Y axis and linear mass of the  $i$ -th bridge span, respectively.

With this configuration, the interaction between successive spans is only allowed by the continuous ballasted track. In the simulations, a track length of  $L_{r,prev} = 20$  m is included before and after the bridge, which is considered according to previous publications [8]. The rail is discretized into two beam elements between consecutive sleepers, and so are the bridges.

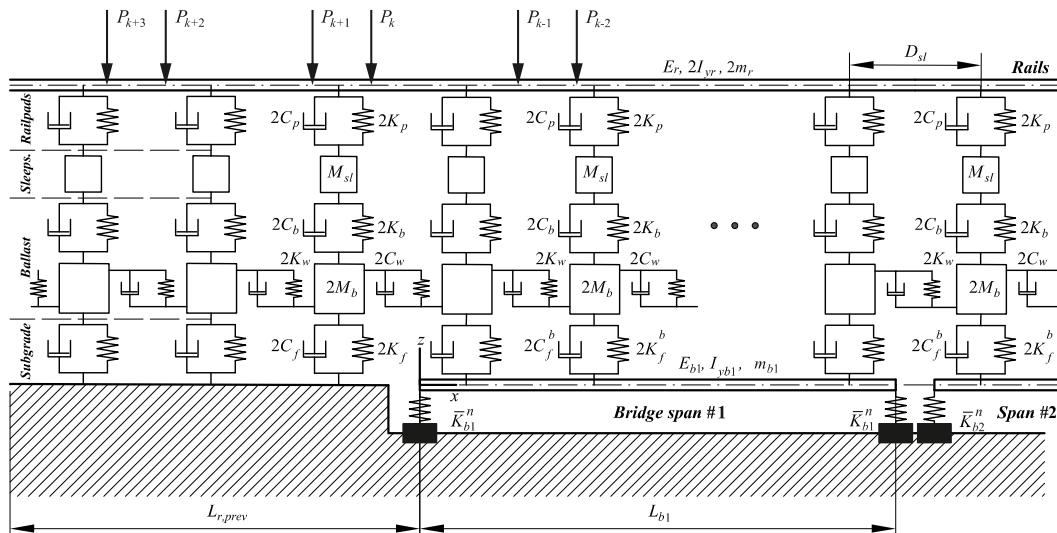


Figure 3: Track-bridge interaction model.

The train excitation is represented by means of a constant moving load model, which implies that vehicle-structure interaction effects are neglected. In this way, it is expected to isolate the effect of the track components affecting the dynamic behaviour of the bridge to investigate their influence separately.

For the track parameters, an important dispersion has been found among different publications. Based on a review presented by the authors in [9], the values selected are shown in Table 3, expressed per rail seat.  $M_b$ ,  $K_b$  and  $K_f$  are calculated with the equations given in [4]. Data from the European and Spanish Standards are adopted for the rail, rail pads and sleepers properties. In the case of the ballast shear stiffness and damping, the authors have found that most of the times these parameters are not considered in track models. In the few cases where included, the majority of them adopted those proposed in [4]. For this reason, in this work, these same values are employed, and its influence investigated.

The model is implemented in ANSYS. For the computation of the bridges response under passing trains (see section 4), mass, stiffness and damping matrices are exported to MATLAB, and the equations of motion equations of the full model are integrated in the time domain applying the Newmark-beta constant acceleration algorithm. The time step for the numerical integration is set as the minimum between 1/50 times the smaller period of interest and 1/20 times the load travelling time between two consecutive sleepers.

## 4 SENSITIVITY ANALYSIS: MODAL PROPERTIES, HARMONIC RESPONSE AND VERTICAL ACCELERATION

### 4.1 Reference case and adopted approach

This section presents the results for the sensitivity analysis regarding the influence of the track properties on the dynamic behaviour

of the bridges. To this aim, individual variations for the track parameters are considered to evaluate how this impacts the modal properties, the harmonic response and the vertical acceleration on the bridge deck under train passage. It is also intended to determine what bridges are the most affected by these variations.

Not.	Parameter	Value	Unit	Ref.
$E_r$	Rail UIC 60 elastic modulus	$2.1 \cdot 10^{11}$	Pa	[10]
$I_{yr}$	Rail UIC 60 moment of inertia	$3038.3 \cdot 10^{-8}$	$m^4$	[10]
$m_r$	Rail UIC 60 mass per unit length	60.21	kg/m	[10]
$K_p$	Rail pad vertical stiffness	$1 \cdot 10^8$	N/m	[11]
$C_p$	Rail pad damping	$7.5 \cdot 10^4$	Ns/m	[4]
$M_{sl}$	Sleeper mass	300	kg	[12]
$D_{sl}$	Sleeper distance	0.6	m	[12]
$l_e$	1/2 Sleeper effect. support length	0.95	m	[4]
$l_b$	Sleeper width	0.3	m	[12]
$\alpha$	Ballast stress distr. angle	35	°	[4]
$h_b$	Ballast thickness	0.3	m	[12]
$\rho_b$	Ballast density	1800	$kg/m^3$	[4]
$M_b$	Ballast vibrating mass	317.91	kg	[4]
$E_b$	Ballast elastic modulus	$1.1 \cdot 10^8$	Pa	[4]
$K_b$	Ballast vertical stiffness	$1.933 \cdot 10^8$	N/m	[4]
$C_b$	Ballast damping	$5.88 \cdot 10^4$	Ns/m	[4]
$E_f$	Subgrade $K_{30}$ modulus	$9 \cdot 10^7$	Pa/m	[4]
$K_f$	Subgrade vertical stiffness	$7.399 \cdot 10^7$	N/m	[4]
$C_f$	Subgrade damping	$3.115 \cdot 10^4$	Ns/m	[4]
$K_w$	Ballast shear stiffness	$7.84 \cdot 10^7$	N/m	[4]
$C_w$	Ballast shear damping	$8 \cdot 10^4$	Ns/m	[4]

**Table 3:** Nominal parameters for the whole model.

For the sake of simplicity, GD-ES-10 bridge is set as a reference case in order to show the main assumptions considered in the analysis. Fig. 4 shows some of the natural frequencies and shapes obtained for this particular bridge. The first six global deformation modes are represented on the left (a-f), whereas (g-l) on the right side correspond to higher frequency modes with a predominant participation of the track. The mode shapes are similar for all considered bridges. Track modes, which appear in symmetrical pairs, start at frequencies higher than 150 Hz. The mode shown in Fig. 4 (l) is included due to its participation in the harmonic analysis presented in the next subsection.

To evaluate the influence of the track parameters in a first approach, Table 4 shows the frequency variation in the GD-ES-10 bridge for the first and second modes with respect to the nominal case under individual variations for  $K_p$ ,  $K_b$ ,  $K_f$  and  $K_w$  between 0.5 and 2 times their nominal values. These results show that the only parameter that affects significantly these frequencies is the ballast shear stiffness ( $K_w$ ). This same trend has been observed for higher modes and for the remaining bridges. In this sense, Zhai et al. [4] pointed out too the great influence of the ballast shear stiffness and damping on the dynamic behaviour of the track, since neglecting their effect could lead to an overestimation of the computed ballast vibration level. In view of this, the following analyses focus on the influence of these parameters ( $K_w$ ,  $C_w$ ) on the dynamic behaviour of the bridges.

#### 4.2 Influence of $K_w$ on the bridge modal parameters

In this section the influence of the ballast shear stiffness on the bridge modal parameters is evaluated. To this aim, the first, third and fifth longitudinal bending modal frequencies

are calculated under individual variations of  $K_w$ . Fig. 5 shows the results for all the bridges in the catalogue, grouped per bridge length. Each plot shows the ratio between the natural frequency  $f_i$  for  $i = 1, 3, 5$  when factors [0.0, 0.5, 1.0, 1.5, 2.0] multiply the nominal value of  $K_w$  (Table 3) and that in the nominal case.

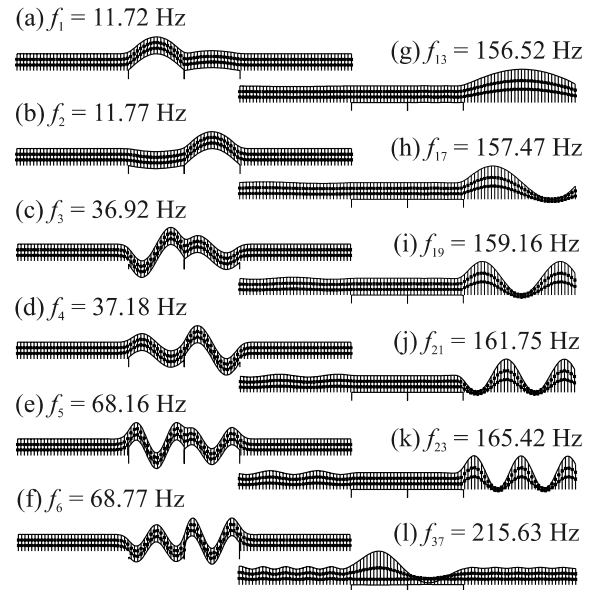


**Figure 4:** Modes of the GD-ES-10 track-bridge system.

Parameter	$f_1$ [Hz]	Var. [%]	$f_2$ [Hz]	Var. [%]
$K_p \cdot 0.5$	11.714	-0.05	36.916	-0.05
$K_p \cdot 2$	11.725	0.04	36.931	0.02
$K_b \cdot 0.5$	11.718	-0.03	36.920	-0.01
$K_b \cdot 2$	11.722	0.02	36.928	0.01
$K_f \cdot 0.5$	11.705	-0.13	36.899	-0.07
$K_f \cdot 2$	11.734	0.12	36.952	0.07
$K_w \cdot 0.5$	11.118	-5.14	36.33	-1.54
$K_w \cdot 2$	12.858	9.71	38.008	2.93

**Table 4:**  $f_1$  and  $f_2$  variations for the GD-ES-10 bridge due to the modification of  $K_p$ ,  $K_b$ ,  $K_f$  and  $K_w$ .

From the obtained results, the following is observed.

- Natural frequencies increase with  $K_w$ . Bridges with shorter spans in a certain typology are more affected with the variation of this parameter.
- The fundamental frequency  $f_1$

corresponding to the first longitudinal bending mode is significantly more affected than higher frequencies. The effect of  $K_w$  reduces with the frequency number.

- Regarding the typology, girder bridges, with lower longitudinal bending stiffness, are affected to a higher extent than slab bridges.
- As per the bridge supports, bridges on elastic supports are slightly more affected by  $K_w$  variations than rigidly supported bridges. Nevertheless, the difference is not significant, especially for modes higher than the fundamental one.

These results are consistent in all the considered bridges. From the sensitivity analysis it is concluded that regarding the modal parameters, short-span elastically-supported girder bridges are the most sensitive ones to the value of  $K_w$ . On this matter, the maximum variations for the frequency obtained for the first, third and fifth modes are 20%, 6% and 3%, respectively, for the shortest bridge considered (GD-ES-10), and 10%, 3% and 1.5% for the longest one (GD-ES-25).

### 4.3 Influence of $K_w$ and $C_w$ on the bridge harmonic response

Next, the influence of the ballast shear stiffness and damping in the harmonic response of the bridges is evaluated. A vertical harmonic force with amplitude  $F_0 = 210$  kN is applied on the rail at mid-span location of the first span. The maximum absolute vertical displacement at the same section is determined for forcing frequencies in the range  $f_f \in [1,600]$  Hz in steps of  $\Delta f_f = 0.1$  Hz. This analysis is repeated for individual variations of the ballast shear stiffness and damping of  $[0.0, 0.5, 1.0, 1.5, 2.0] \cdot K_w$  and  $[0.5, 1.0, 1.5, 2.0] \cdot C_w$ , respectively, being  $K_w$  and  $C_w$  the nominal values of these parameters.

In Fig. 6 results from the harmonic response analysis are represented for four bridge lengths. Individual variations of  $K_w$  and  $C_w$  are applied in Fig. 6 (a-d) and in Fig. 6 (e-h), respectively. For the sake of brevity, only the results for the ES girder bridges are presented in this section for  $L_{bi} = 10, 15, 20$  and 25 m, as no significant differences were detected in the trends between typologies or supporting conditions. From the computed solution, the following observations can be made:

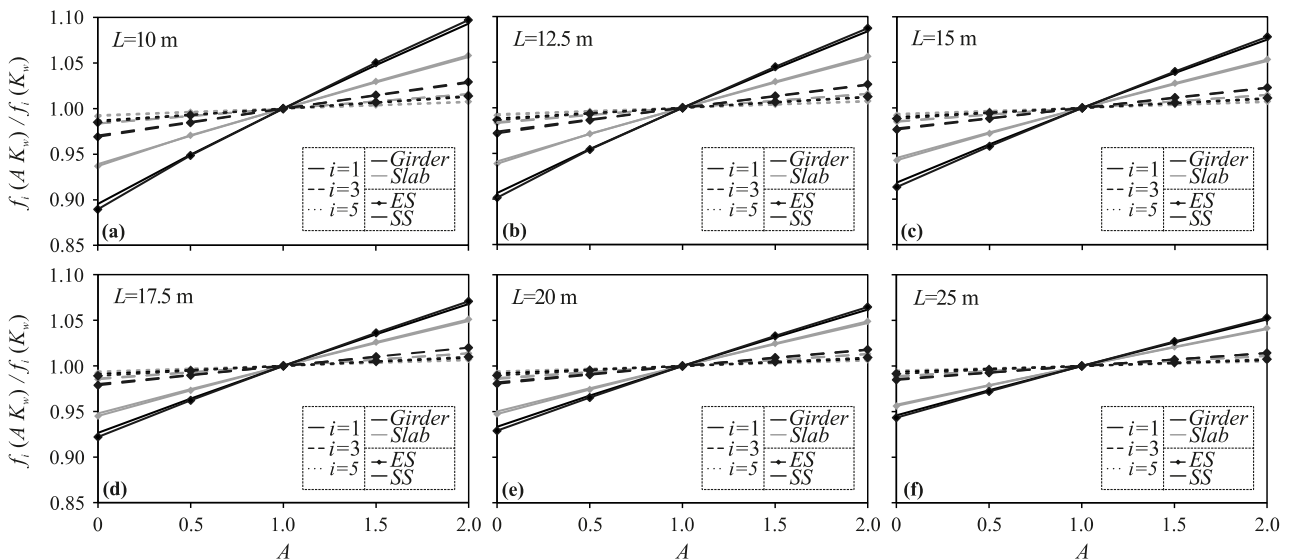
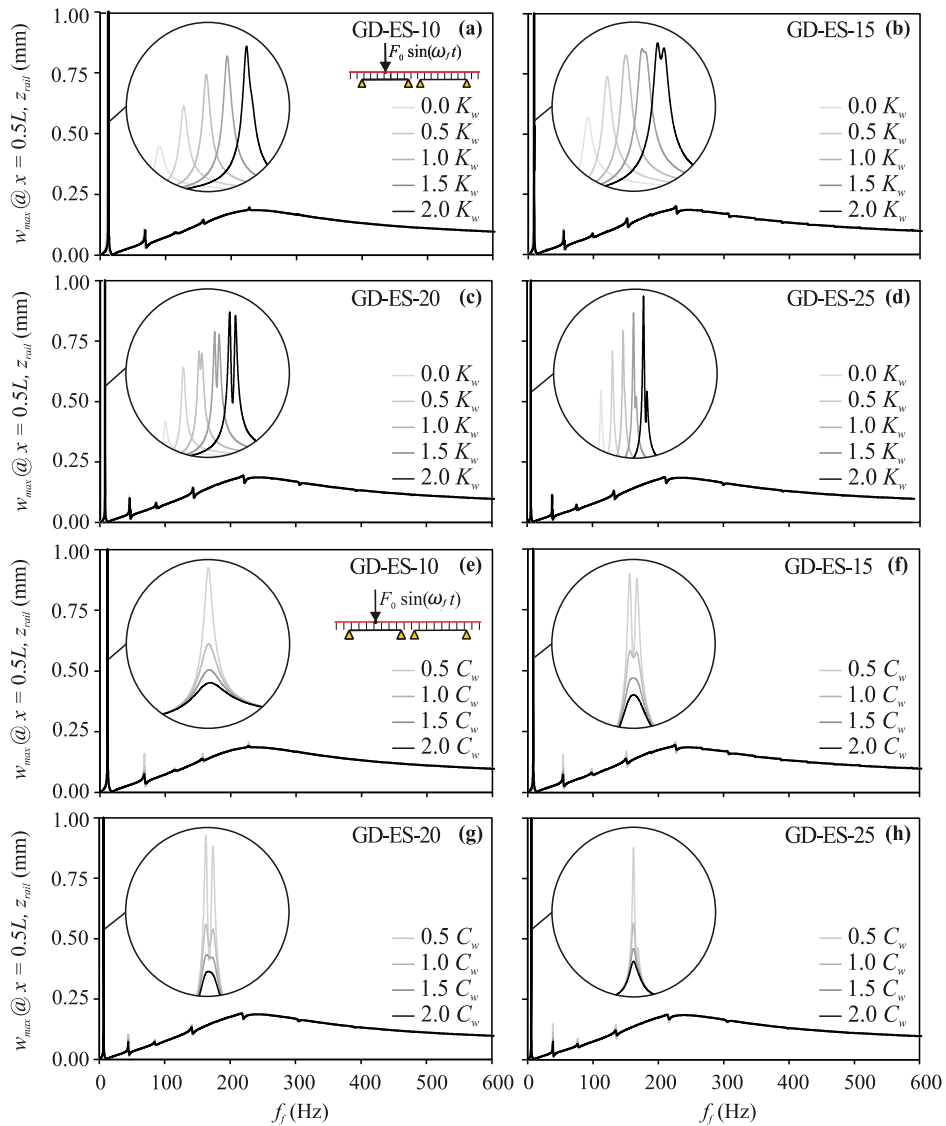


Figure 5: Influence of the variation of  $K_w$  in  $f_1, f_3$  and  $f_5$  with respect to the frequency in the nominal case.

- A maximum narrow peak occurs in the vicinity of the fundamental frequency. Because of a greater difference between the first and the second frequency modes, for the cases when  $L_{bi} = 15$  and 20 m, two peaks appear instead of one. A wider maximum is also perceptible close to 215 Hz coinciding with the track mode included in Fig. 4(1). Smaller peaks appear along the

curve coinciding with higher modes of the bridges with not-zero amplitude at mid-span of the first span.

- As  $K_w$  increases so does the resonant frequency associated to the fundamental mode, consistently with the variations observed in the natural frequencies.
- The response at resonance of the



**Figure 6:** Influence of  $K_w$  and  $C_w$  in the harmonic response of elastically-supported girder bridges.

fundamental mode reduces with  $C_w$ . The effect of this parameter at higher frequencies is not significant.

#### 4.4 Influence of $K_w$ and $C_w$ on the deck vertical acceleration due to train passage

The influence of  $K_w$  and  $C_w$  on the vertical acceleration at the bridge deck under train passages is investigated in this section. To this aim, several dynamic analyses are carried out on the GD-ES-10 bridge under the circulation of HSLM-A1 Universal Train presented in the EC1 [6]. Only this bridge is selected for the sake of conciseness and for being the most influenced one by the ballast shear stiffness and damping properties.

The acceleration response is calculated for the HSLM-A1 train in the range of velocities [40, 117] m/s (e.g. [144, 420] km/h) every 1 m/s at a quarter, mid-span and three quarters of both spans. A Chebyshev order 3 filter is applied to the response in order to filter contributions below 1 Hz and above 60 Hz. Then, maximum response envelopes are obtained for each speed. The following individual variations of track parameters are imposed:  $[0.0, 0.5, 1.0, 1.5, 2.0] \cdot K_w$  and  $[0.5, 1.0, 1.5, 2.0] \cdot C_w$ . Also, Rayleigh damping is assumed according to EC1 [6] for pre-stressed concrete bridges as 1.7% for the GD-ES-10 bridge. This ratio is applied on the first and fifth natural frequencies.

In Fig. 7 (a-b), an envelope of the maximum acceleration response at the bridge deck is represented at the most critical section which corresponds to the center of the second span. Also, and in order to visualize how the variation of  $K_w$  and  $C_w$  affects the bridge response in different situations, the acceleration time-history at the same section is represented in for three different velocities: second resonance speed of the first mode (e.g.  $n = 1, j = 2$  in Eq. 2 [13]), which is equals to 380 km/h (see Fig. 7 (c-d)).

$$V_{nj}^r = \frac{d_k}{jT_{nbi}} = \frac{\omega_{nbi}}{2\pi j}, \quad n, j \geq 1 \quad (2)$$

In the previous equation,  $d_k$  stands for the characteristic distance of the HSLM-A1 train (18 m),  $T_{nbi}$  is the  $n$ -th natural period of the bridge and  $j$  the resonant order. Following that, the response is computed at 324 km/h, far both from resonance and from cancellation of resonance (see Fig. 7 (e-f)). Finally, it is determined for a speed near a cancellation of resonance condition, given by Eq. 3[13]:

$$\left(\frac{L_{bi}}{d_k}\right)_{nji}^c = \left(\frac{\lambda_n}{n\pi}\right)^2 \frac{n}{2jK_{ni}^c}, \quad n, j, i \geq 1 \quad (3)$$

In this way, when the relation  $L_{bi}/d_k$  between the length of each span and the characteristic distance of the train approaches the  $i$ -th cancellation ratio  $(L_{bi}/d_k)^c$  given by Eq. 3, the cancellation of the resonance is produced, and the vibration level gets significantly attenuated [13]. For the case of the GD-ES-10 bridge associated to the circulation of the HSLM-A1 train, the third resonance speed, equals to 253 km/h approaches the  $(L_{bi}/d_k)^c$  theoretical condition of cancellation for this resonance (e.g.  $j = 3, n = 1, i = 1$ , respectively, although is not coincident (the difference is approximately 15%). Nevertheless, the phenomenon is visible, leading to a quite reduced resonant peak. These results are shown in Fig. 7 (g-h). In summary, the subsequent observations can be made.

- An increase in  $K_w$  leads to a rise in the resonant velocities, in the same proportion that the resonant frequency is modified by this parameter (in this particular case, neglecting or doubling  $K_w$  entails variations of -17.4% to +9.3% of the resonant velocity for the nominal case). This affects similarly different order resonances.

- For the range of  $K_w$  values considered, resonance at a certain speed may or may not take place depending on  $K_w$  (see Fig. 7(c-e)).
- Regarding the effect of the ballast shear damping, it is only relevant at resonance, leading to a pronounced

reduction of the acceleration response. In this particular case, if  $C_w$  is doubled with respect to its nominal value, the vertical acceleration reduces by a 26%. The effect of this parameter on the second peak is much higher than the effect on the third resonant peak.

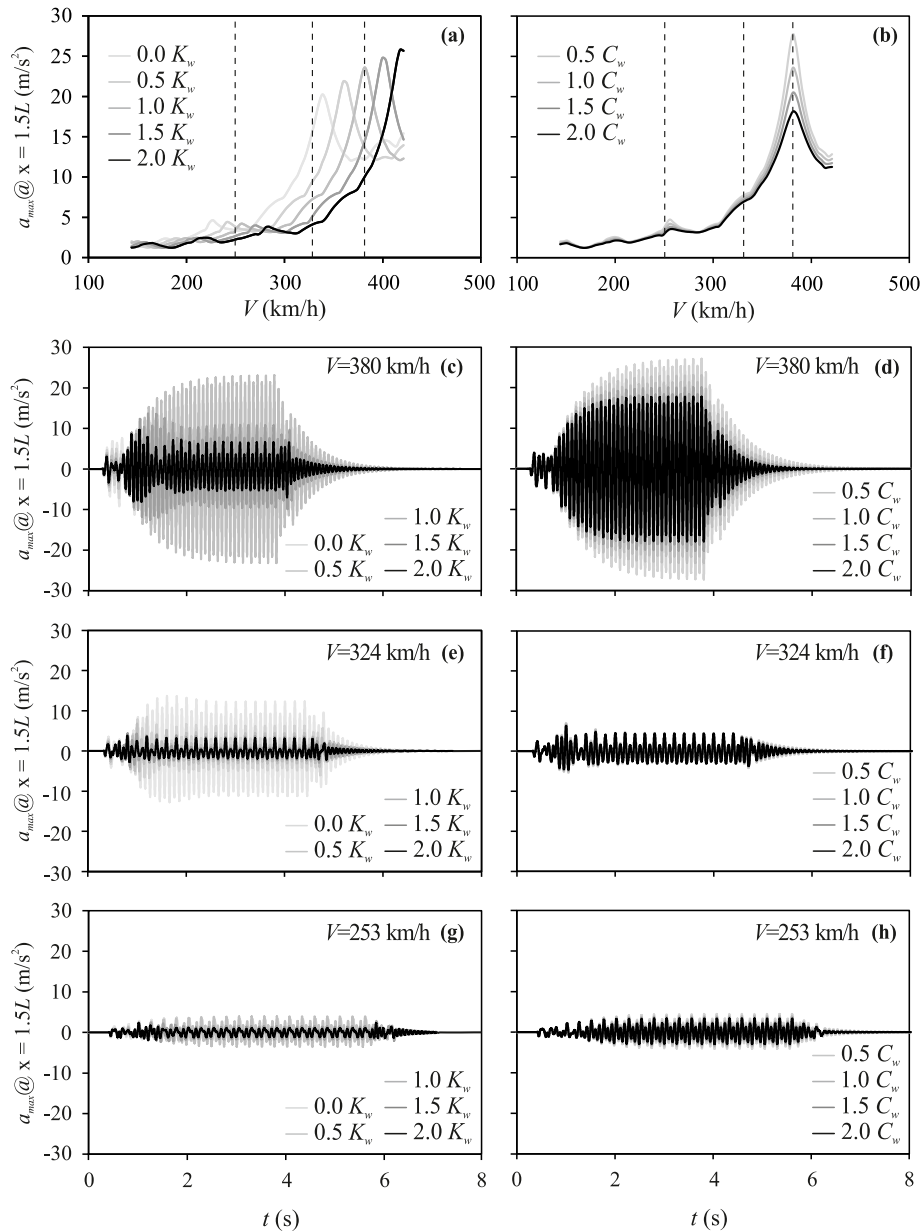


**Figure 7:** GD-ES-10 bridge. Maximum acceleration response for each velocity (a-b), and acceleration time-history at different speeds (c-h).

Nevertheless, this last peak is close to cancellation and no conclusions can be extracted in this regard.

- Finally, for the resonance speed approaching the cancellation conditions, a very significant attenuation of the acceleration level is observed.

## 5 CONCLUSIONS

The longitudinal coupling effect exerted by the continuity of the ballasted track in single-track railway bridges composed by several isostatic consecutive spans is evaluated in this work. Specifically, the influence of the ballast shear stiffness and damping in the modal parameters, harmonic response and vertical acceleration under train passages is investigated.

In the first place, a comprehensive bridge catalogue considering short-to-medium span lengths and two common bridge deck typologies has been prepared. Then, a sensitivity analysis has been performed by means of a 2D FE track-bridge interaction model, in which individual variations of the track parameters have been imposed, in order to study their influence on the dynamic behaviour of the bridges. The main conclusions for this work are summarized as follows:

- In the discrete track model presented, the ballast shear stiffness and damping are the parameters that affect the most the bridge response in the frequency range of interest. The influence of the remaining parameters is negligible compared to these two.
- Regarding the modal parameters of the bridges,  $K_w$  exerts a notable influence on them, which is stronger in shorter bridges. When it comes to the typology, girder-deck bridges

are the most affected due to their initially lower bending stiffness. The correlation with the flexibility of elastic supports is minor.

- The influence of  $K_w$  and  $C_w$  in the harmonic response is significant only at low frequencies. An increase of  $K_w$  leads to a rise in the resonant frequency for the first mode.  $C_w$  produces a pronounced reduction of the corresponding amplitude, as expected. Higher frequencies related with track deformation modes are not especially affected by these parameters.
  - With respect to the vertical acceleration level caused by the passage of a train, it is found that the effect of  $K_w$  and  $C_w$  is significant, especially at resonance. In particular, an increment of  $K_w$  leads to an important rise in resonant velocity, while an increment of  $C_w$  results into a reduction of the resonant acceleration amplitude. The effect of  $C_w$  far from resonance is negligible. These results are consistent, since, higher  $K_w$  values lead to an increase on the natural frequencies, especially of the fundamental one and in the case of short flexible structures.
- Future investigations are required in order to understand completely the influence of these shear parameters. It is also needed to find clear ways to determine their value, since their influence on the dynamic behaviour of railway bridges is significant and the information about it found in the literature is scarce. Experimentally appraised values for these parameters could be quite useful in the case of using discrete track models, which is a reasonable

solution permitting solving the dynamic equations of motion in the time domain performing a full analysis in a reasonable amount of time.

## 6 ACKNOWLEDGEMENTS

The authors would like to acknowledge the financial support provided by the Spanish Ministry of Science and Innovation under research project PID2019-109622RB and Generalitat Valenciana under research project AICO2019/175.

## REFERENCES

- [1] L. Frýba. *Dynamic behaviour of bridges due to high-speed trains*, Bridges for High-Speed railways, CR, Press, pp.137-158, 2008.
- [2] M. Zacher, M. Baeßler. *Dynamic behaviour of ballast in railway bridges*, Dynamics of High-Speed Railway Bridges, 2008.
- [3] J. Rocha, A. Henriques, R. Calçada. *Probabilistic safety assessment of a short span high-speed railway bridge*, Engineering structures 71, pp. 99-111, 2014.
- [4] W. Zhai, K. Wang, J. Lin. *Modelling and experiment of railway ballast vibrations*, Journal of Sound and Vibration 270, pp. 673-683, 2004.
- [5] A. Doménech, P. Museros, M. Martínez-Rodrigo. *Influence of the vehicle model on the prediction of the maximum bending response of simply-supported bridges under high-speed traffic*, Engineering Structures 72, pp. 123-139, 2014.
- [6] CEN, EN 1991-2. *Eurocode 1: Actions on Structures - Part 2: Traffic loads on bridges*, European Committee for Standardization, Brussels, 2003.
- [7] M. Martínez-Rodrigo, E. Moliner, A. Romero, P. Galvín. *Maximum resonance and cancellation phenomena in orthotropic plates traversed by moving loads: Application to railway bridges*, International Journal of Mechanical Sciences 169 105316, 2020.
- [8] P. Lou. *A vehicle-track bridge interaction element considering vehicle's pitching effect*, Finite Elements in Analysis and Design 41, pp. 397-427, 2005.
- [9] P. Galvín, A. Romero, E. Moliner, G. De Roeck, M. Martínez-Rodrigo. *On the dynamic characterisation of railway bridges through experimental testing*, Engineering Structures 226 (1) 111261, 2020.
- [10] CEN/TC256, EN 13674-1:2011+A1:2017 *Railway applications – Track – Rail – Part 1: Vignole railway rails 46 kg/m and above*, European Committee for Standardization, Brussels, 2017.
- [11] K. Nguyen, J. Goicolea, F. Gabaldón. *Comparison of dynamic effects of high-speed traffic load on ballasted track using simplified two-dimensional and full three-dimensional model*, Journal of Rail and Rapid Transit 228 (2) pp. 128-142, 2012.
- [12] Ministerio de Fomento, Gobierno de España. *Instrucción de acciones a considerar en puentes de ferrocarril, Actions in railway bridges (in spanish)*, 2010.
- [13] P. Museros, E. Moliner, M.D. Martínez-Rodrigo. *Free vibrations of simply-supported beam bridges under moving loads: Maximum resonance, cancellation and resonant vertical acceleration*, Journal of Sound and Vibration 332, pp. 326-345, 2013.

# DYNAMIC ANALYSIS OF A RAILWAY BRIDGE WITH TUNED VIBRATIONS ABSORBERS SUBJECTED TO HIGH SPEED TRAIN LOAD MODELS

Javier Naranjo-Pérez\*, Christian Gallegos-Calderón\*, José María Goicolea\* and Iván M. Díaz\*

\* ETS Ingenieros de Caminos, Canales y Puertos  
Universidad Politécnica de Madrid  
28040 Madrid, Spain  
e-mail: javier.naranjo@upm.es  
ORCID: 0000-0001-3-2239-7048

**Abstract.** Dynamic behaviour of railway bridges is highly influenced by the speed of the train. This makes high speed trains an important conditioning feature for the design and maintenance of this type of structures. In case that vertical accelerations do not fulfil the requirements, two alternatives may be followed: a) oversizing the structure or b) mitigating the excessive vibrations via the installation of damper devices. The second option is considered hereby through the inclusion of a tuned vibration absorber, usually known as Tuned Mass Damper (TMD). The analysis accounts for an interacting coupled TMD-structure system. The structure is modelled as a beam and its dynamic behaviour is assumed to be characterised by its modal properties, and the TMD is modelled as a single degree of freedom system. This method is implemented in the software CALDINTAV, allowing the user to consider several scenarios and perform parametric analysis in a simple manner. The results obtained for high-speed trains running on a typical railway bridge are compared with those obtained by a 3D FE model. The outcomes prove that the assessment of the controlled bridge response through the simplified interaction model becomes easier and less time-consuming than the detailed FE models without losing the precision.

**Key words:** Railway bridges, High-speed trains, Dynamic response, Vibration control, TMD.

## 1 INTRODUCTION

It is well known that the dynamic response of railway bridges induced by high-speed trains is an important issue for their design, as it is included in standards [1]. The magnitude of the dynamic response varies with the speed of the train, which can lead to resonance phenomena. Thus, a parametric calculation, including several trains and velocities, becomes essential.

To control high train-induced vertical accelerations, greater than  $3.5 \text{ m/s}^2$  for ballast track and  $5 \text{ m/s}^2$  for slab track, passive inertial devices may be installed. Among the available

dampers, the fairly simple but usually effective Tuned Mass Damper (TMD) is considered herein.

Since the first theoretical approach [2], TMDs have proven to be feasible solutions to control vertical or lateral excessive vibrations in bridges. The principal advantage of these passive inertial devices is that their functioning is purely mechanical, so no power supply is necessary in contrast to semi-active or active control strategies. By selecting adequate parameters of a TMD (mass, stiffness and damping), a significant reduction in the dynamic response of the structure under the

action of earthquakes, wind, or humans/vehicles/trains, can be achieved. Successful applications can be found in references [4] and [5]. To the best of the author's knowledge, no real applications for railway bridges have been developed yet. However, there are numerical studies, such as the work of Pisal and Jangid, who developed a procedure for vibration control of railway bridge subjected to multi-axle loads using multiple TMDs [6].

In this study, a TMD is designed and implemented to control the excessive vertical vibrations of a railway bridge subjected to high-speed train loads. Moreover, it is implemented in the GUI-based software CALDINTAV, developed by the Computational Mechanics group of the Technical University of Madrid [7]. For this purpose, a modal analysis of the bridge using beam-type models is carried out, which allows fast assessment of several scenarios providing the critical cases that should be evaluated in detail. The results obtained under this approach will be compared with those obtained through a 3D FE model, which often leads to a more time-consuming analysis when a direct time integration method is performed.

## 2 THEORETICAL BACKGROUND IN CALDINTAV

CALDINTAV is a software developed by the Computational Mechanics group of the Technical University of Madrid. Herein, the dynamic calculation for railway bridge vibrations is addressed employing a simplified beam model of the structure. The forces produced by the train are implemented as a set of moving loads which are determined by the weights per axle of the bogies.

The governing equation of motion under this set of moving loads is:

$$\rho \ddot{u} + c \dot{u} + EI \frac{\partial^4 u}{\partial x^4} = p(x, t) \quad (1)$$

with  $\rho$  being the mass per unit length,  $c$  the damping coefficient,  $EI$  the bending stiffness,  $u$  the transverse deflection and  $p(x, t)$  the loads at distance  $x$  and at instant  $t$ .

This equation is solved applying the modal superposition technique. Under this method, the train excites several vibration modes simultaneously and the dynamic response may be obtained via the contribution of modal responses. The response, considering  $n$  vibration modes is:

$$u(x, t) = \sum_{i=1}^n q_i(t) \phi_i(x) \quad (2)$$

where  $q_i(t)$  are the modal generalised coordinates and  $\phi_i(x)$  the mode shape of the vibration mode  $i$  which, in case of simply supported beam, is calculated as:  $\phi_i(x) = \sin(i\pi x/L)$ , being  $L$  the length of the beam.

By substituting Equation (2) into Equation (1), taking into account the orthogonality relationship between mode shapes and integrating the resulting equation, yields the following:

$$\begin{aligned} \ddot{q}_i(t) + 2\xi\omega_i\dot{q}_i(t) + \omega_i^2q_i(t) &= \\ &= \frac{2}{\rho L} \int_0^L p(x, t)\phi_i(x)dx \end{aligned} \quad (3)$$

being  $\xi$  the damping factor and  $\omega_i$  the angular natural frequency.

As it was mentioned, the load induced by the train is assumed to be a point moving load. However, the above expression is different depending on whether there is only one moving load or a set of moving loads. Figure 1 shows both configurations. Although the set of moving loads is a superposition of single moving loads, the results are very different since resonance phenomena may occur due to the simultaneous action of the loads.

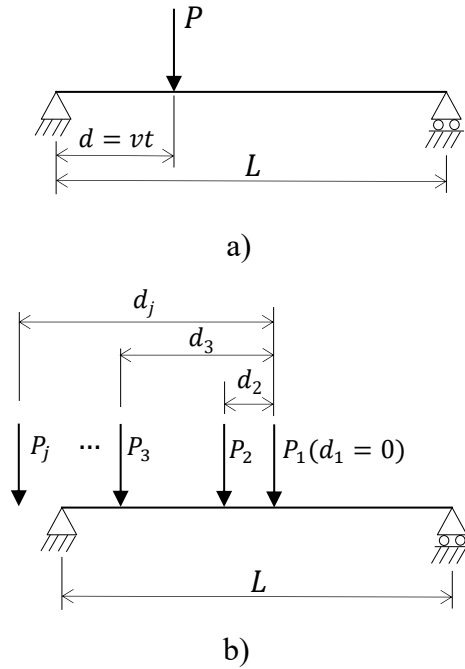


**Figure 1:** Moving load at velocity  $v$ : a) single moving load and b) set of moving loads.

The last term of Equation (3), in case of a single moving load is:

$$-\frac{2}{\rho L} P \phi_i(vt) \quad (4)$$

Otherwise:

$$-\frac{2}{\rho L} \sum_{j=1}^{N_p} P_j \phi_i(x_k) = -\frac{2}{\rho L} \sum_{j=1}^{N_p} P_j \phi_i(vt - d_k) \quad (5)$$

being  $N_p$  the number of loads.

In order to solve Equation (3), CALDINTAV performs the integration based on the interpolation of the excitation [8].

Next section details the formulation of the TMD-structure interaction system which is implemented in the software.

### 3 TMD-STRUCTURE INTERACTION MODEL

The TMD-bridge interaction model is formulated applying the principle of dynamic equilibrium to the balance of the two sub-models. This interaction model, depicted in Figure 2, is formed by the TMD sub-model and the structure sub-model. This interaction model is defined at the control point.

The TMD is modelled as a single degree of freedom system which is defined by three following parameters: its mass,  $m_{tmd}$ ; its damping,  $c_{tmd}$  and its stiffness,  $k_{tmd}$ .

On the other hand, the dynamic behaviour of the structure is assumed to be simulated through its modal decomposition, hence, it is modelled by the three following modal parameters: modal mass,  $m_s$ ; modal damping,  $c_s$  and modal stiffness,  $k_s$ . For the sake of simplicity, the structure is represented by one vibration mode.

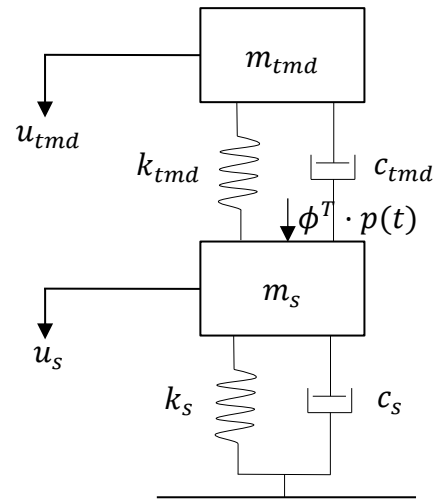


**Figure 2:** Structure-TMD interaction model.

From the dynamic equilibrium on both masses, the interaction model formulation is represented by the following coupled system of differential equations:

$$\begin{aligned}
 m_s \ddot{u}_s + c_s \dot{u}_s + c_{tmd}(\dot{u}_s - \dot{u}_{tmd}) + \\
 + k_s u_s + k_{tmd}(u_s - u_{tmd}) &= \phi^T \cdot p(t) \quad (6)
 \end{aligned}$$

$$\begin{aligned}
 m_{tmd} \ddot{u}_{tmd} + c_{tmd}(\dot{u}_{tmd} - \dot{u}_s) \\
 + k_{tmd}(u_{tmd} - u_s) &= 0
 \end{aligned}$$

being  $u_s$ ,  $\dot{u}_s$  and  $\ddot{u}_s$  the vertical displacement, velocity and acceleration of the vibration modes of the structure, respectively, and  $u_{tmd}$ ,  $\dot{u}_{tmd}$  and  $\ddot{u}_{tmd}$  the vertical displacement, velocity and acceleration of the TMD. Finally,  $p(t)$  denotes the applied force.

The equations system (6) can be rewritten as follows:

$$\begin{aligned}
 m_s \ddot{u}_s + \dot{u}_s(c_s + c_{tmd}) - \dot{u}_{tmd}c_{tmd} \\
 + u_s(k_s + k_{tmd}) - u_{tmd}k_{tmd} &= \phi^T \cdot p(t) \quad (7)
 \end{aligned}$$

$$\begin{aligned}
 m_{tmd} \ddot{u}_{tmd} - \dot{u}_s c_{tmd} + \dot{u}_{tmd} c_{tmd} \\
 - u_s k_{tmd} + u_{tmd} k_{tmd} &= 0
 \end{aligned}$$

It can be noticed that this equations system may be reorganized in a matrix form:

$$\mathbf{M} \ddot{\mathbf{u}} + \mathbf{C} \dot{\mathbf{u}} + \mathbf{K} \mathbf{u} = \mathbf{F}(t) \quad (8)$$

where:

$$\mathbf{M} = \begin{bmatrix} m_s & 0 \\ 0 & m_{tmd} \end{bmatrix}$$

$$\mathbf{C} = \begin{bmatrix} c_s + c_{tmd} & -c_{tmd} \\ -c_{tmd} & c_{tmd} \end{bmatrix} \quad (9)$$

$$\mathbf{K} = \begin{bmatrix} k_s + k_{tmd} & -k_{tmd} \\ -k_{tmd} & k_{tmd} \end{bmatrix}$$

$$\ddot{\mathbf{u}} = \begin{bmatrix} \ddot{u}_s \\ \ddot{u}_{tmd} \end{bmatrix}; \dot{\mathbf{u}} = \begin{bmatrix} \dot{u}_s \\ \dot{u}_{tmd} \end{bmatrix}; \mathbf{u} = \begin{bmatrix} u_s \\ u_{tmd} \end{bmatrix}$$

$$\mathbf{F}(t) = \begin{bmatrix} \phi^T p(x, t) \\ 0 \end{bmatrix}$$

The vector  $\mathbf{F}$  is defined from Equations (4) or (5) according to the case under study. Equation (8) is solved in time domain using the  $\beta$ -Newmark algorithm setting  $\beta = 1/4$  and  $\gamma = 1/2$  to obtain an unconditionally stable solution [8].

### 3.1 Design of the TMD

The passive device, TMD, is designed to control the resonant vibrations associated to a dominant vibration mode. Therefore, the frequency of the TMD is adjusted to the natural frequency of the structure. For the optimum design of the TMD, the  $H_\infty$  criterion proposed by Den Hartog [2, 3] is considered. This method calculates the parameters of the TMD that minimize the dynamic response of the structure under a harmonic excitation. Next, the steps are summarized.

First, from the modal mass of the structure, mass ratio is chosen:

$$\mu = \frac{m_{tmd}}{m_s} \quad (10)$$

The mass of the TMD is usually chosen in such a way that  $\mu$  equals [0.01-0.05] (1%-5% of the modal mass), approximately. Anyway, this value should be chosen to achieve a vibration reduction objective.

Then, the frequency ratio,  $\delta$ , and the damping ratio,  $\xi_{tmd}$ , are derived from the mass ratio:

$$\begin{aligned}
 \delta &= \frac{1}{1 + \mu} = \frac{f_{tmd}}{f_s} \\
 \xi_{tmd} &= \sqrt{\frac{3\mu}{8(1 + \mu)}} \quad (11)
 \end{aligned}$$

Once the frequency of the TMD has been calculated, the parameters that characterize the TMD are established:

$$\begin{aligned} k_{tmd} &= m_{tmd}(2\pi f_{tmd})^2 \\ c_{tmd} &= 2m_{tmd}\xi_{tmd}(2\pi f_{tmd}) \end{aligned} \quad (12)$$

#### 4 CASE STUDY

The TMD design method and its implementation described above is applied to a typical box-slab bridge. It is a single track bridge where the loads have no eccentricity respect the longitudinal axis of the deck.

The dynamic parameters to perform the calculation in CALDINTAV are as follows:

- Span length:  $L = 28$  m.
- Bending stiffness:  
 $EI = 76.619E9$  Nm<sup>2</sup>.
- Damping ratio:  $\xi = 2\%$ .
- Linear density:  $\rho = 14439$  kg/m.

The fundamental natural frequency of the bridge results in:  $f_0 = 4.62$  Hz.

The results will be compared with those obtained through a FE model of the bridge, built in Abaqus software [9].

The FE model, shown in Figure 3, consists of shell elements to model the deck and beam elements for the box girder. The bridge is assumed to be simply supported at the abutments. After a modal analysis is conducted, a natural frequency for the first vertical bending mode of 4.65 Hz is obtained. This vibration mode is the second as the first one (3.46 Hz) is a torsional mode.

The results are obtained applying modal superposition. When the TMD is implemented, a direct time integration using the Hilber-Hughes-Taylor (HHT- $\alpha$ ) method is performed for this purpose. Moreover, the Rayleigh damping is employed to model the damping of

the structure.

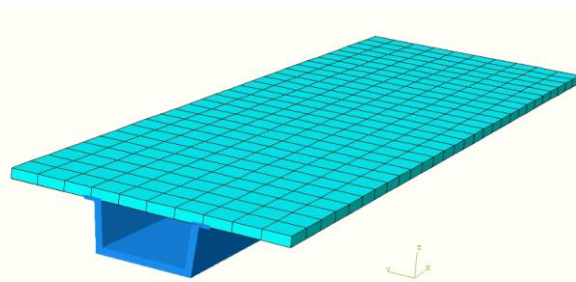


Figure 3: FE shell model of the railway bridge.

#### 4.2 Dynamic response of the bridge

The loading corresponds to the ten virtual train load models (HSLM-A) [1, 10].

In CALDINTAV, a time step of  $\Delta t = 0.001$ s and 3 vibration modes are considered. This number is higher in the FE model since it has more degrees of freedom.

Figure 4 shows, for instance, the acceleration envelope produced by the HSLM-A1 load model running from 125 to 400 km/h in increments of 5 km/h. It can be seen that both curves are similar although a clear difference is obtained when the velocity is greater than 310 km/h. Nevertheless, the maximum vertical acceleration is about 1.8 m/s<sup>2</sup> in both models when  $v = 295$  km/h.

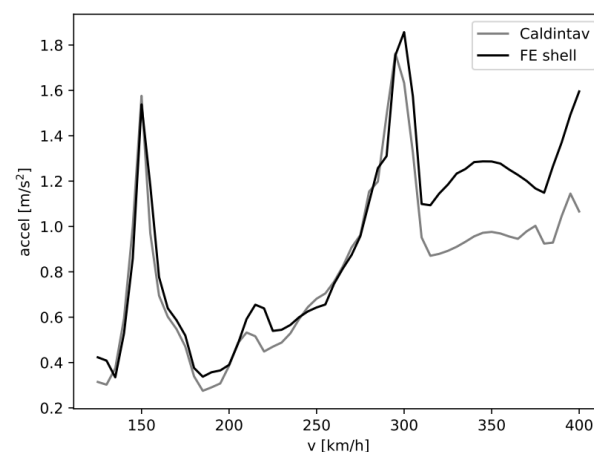
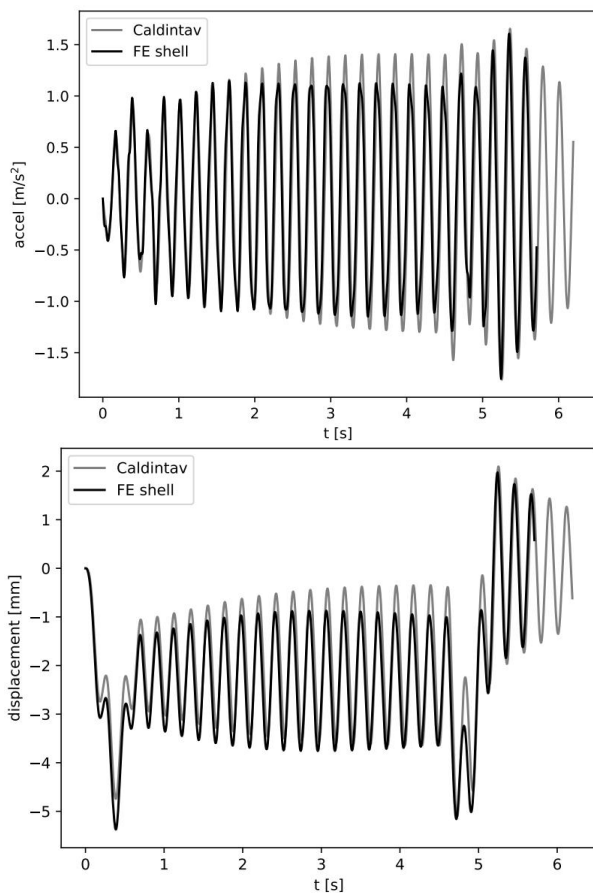


Figure 4: Acceleration envelope produced by the HSLM-A1 load model running at different velocities obtained in Caldintav and in the FE model.

Taking the velocity when resonance effects occur ( $v = 295 \text{ km/h}$ ), the dynamic responses are given in Figure 5, showing a very close approximation between the two models. The maximum vertical acceleration, as indicated before, is about  $1.8 \text{ m/s}^2$ . The large amplification of the response due to resonance is clearly observable. The maximum vertical displacement at mid-span is  $5.5 \text{ mm}$ .



**Figure 5:** Dynamic response of the railway bridge under HSLM-A1 running at  $295 \text{ km/h}$ : a) vertical acceleration at mid-span and b) vertical displacement at mid-span.

This calculation may be performed for all the HSLM-A load models. The acceleration envelope obtained in the FE shell model is depicted in Figure 6 and the envelope of all these load models in Figure 7. As it was expected, since the peaks between the FE shell

model and the beam model of CALDINTAV were the same, both envelopes are in good agreement.

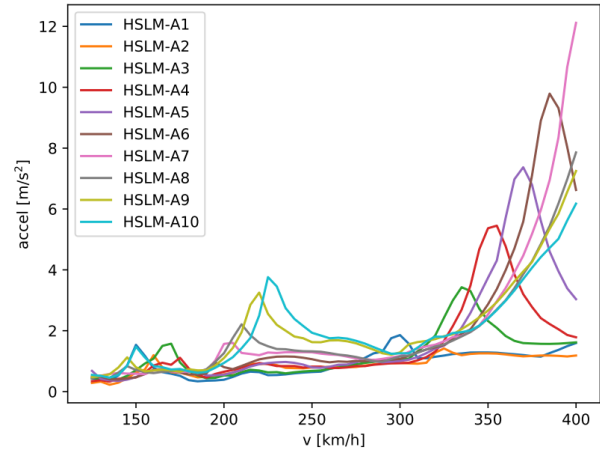


**Figure 6:** Acceleration envelopes produced by all the HSLM-A load models running at different velocities.

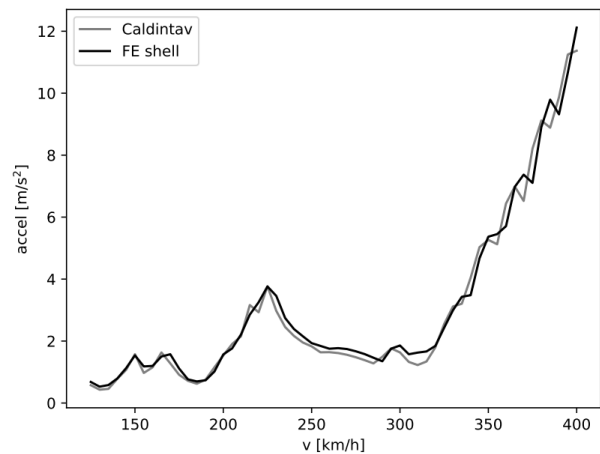


**Figure 7:** Acceleration envelope produced by all the HSLM-A running at different velocities.

#### 4.1 Implementation of the TMD

Once the beam model employed in CALDINTAV has been demonstrated to be a good approximation to the bridge, the TMD is designed and implemented according to previous sections.

The TMD mass is adopted following the recommendations of 1-5% of the generalised mass. In this problem, the modal mass of the

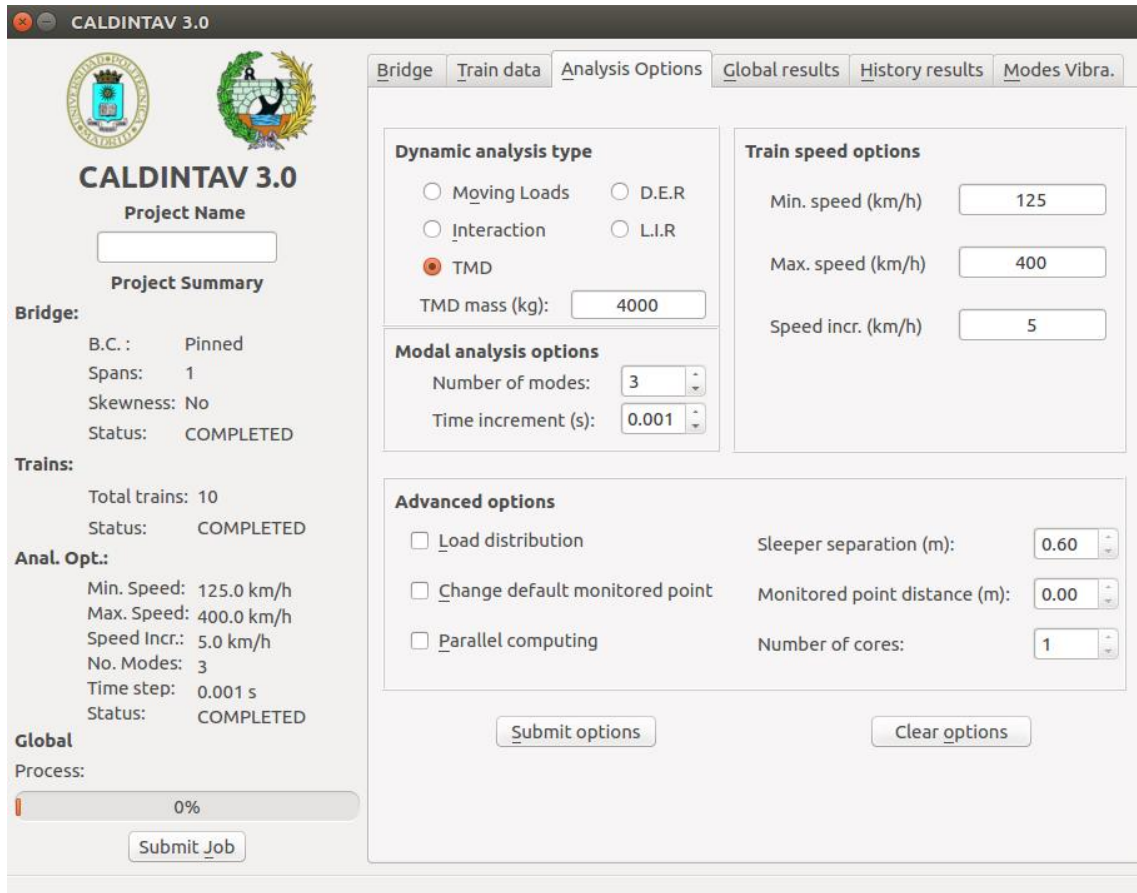


**Figure 8:** GUI of CALDINTAV.

first bending vibration mode is 200E3 kg, hence, considering a 2% of this mass, the TMD mass results in 4000 kg. Applying Equations (10)-(12), the stiffness and the damping coefficient of the TMD are the followings:

$$k_{tmd} = 3.22568E06 \text{ N/m} \quad (12)$$

$$c_{tmd} = 19480.5 \text{ Ns/m}$$

Regarding the software CALDINTAV, the user is asked to enter the mass of the TMD and the rest of parameters are calculated (Figure 8). The time step and number of modes are the same as before.

In Abaqus, the TMD is modelled as an inertial mass connected via a wire to the mid-span of the bridge. This wire is characterised by the stiffness and damping given in Equation

(12).

The dynamic response of the bridge with a TMD placed at the mid-span is shown in Figure 9 and Figure 10 for the FE shell model and the beam model of CALDINTAV, respectively. To check the performance of the TMD, the results computed previously without the TMD are also drawn. From these two figures, two conclusions may be extracted. First, the vibration level of the bridge is reduced significantly due to the action of the device. The maximum acceleration is now around  $0.95 \text{ m/s}^2$ , what implies a reduction of the 50% with respect to the initial configuration without the TMD. By comparing the root-mean square (RMS) acceleration, a global estimator of the dynamic response, between both configurations, the reduction given in Table 1 is achieved.

Software	Without TMD	With TMD	Reduction [%]
Caldintav	0.85	0.34	60.00
Abaqus	0.81	0.34	58.02

**Table 1:** RMS acceleration and reduction achieved with the TMD.

Second, the simplified model leads to accurate results as it is demonstrated in Figure 11.

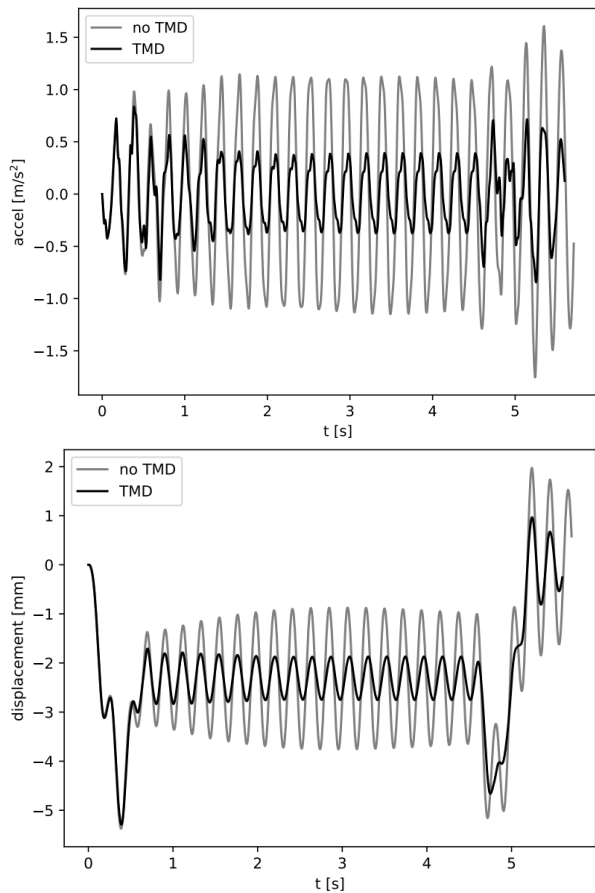


**Figure 9:** Dynamic response of the railway bridge under HSLM-A1 running at 295 km/h with a TMD implemented (FE model in Abaqus): a) vertical acceleration at mid-span and b) vertical displacement at mid-span.

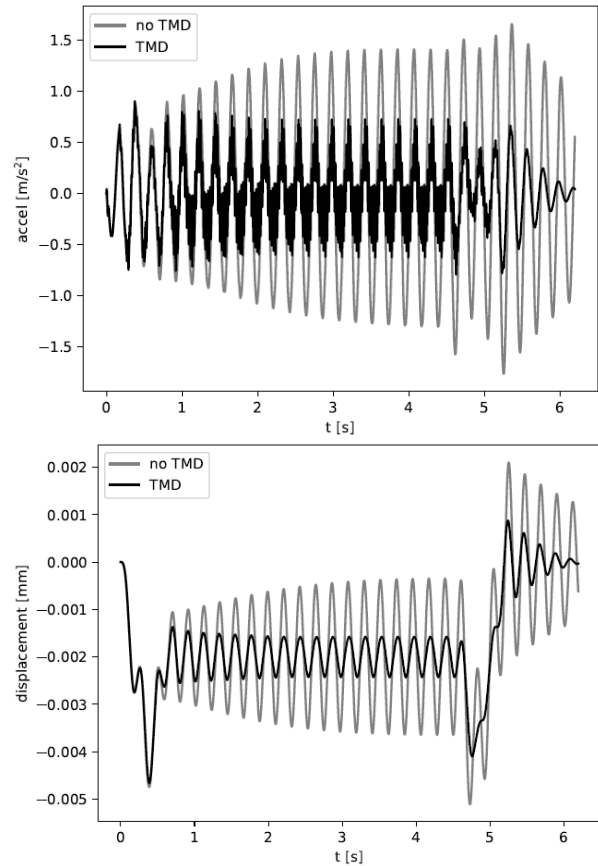


**Figure 10:** Dynamic response of the railway bridge under HSLM-A1 running at 295 km/h when a TMD is implemented (CALDINTAV): a) vertical acceleration at mid-span and b) vertical displacement at mid-span.

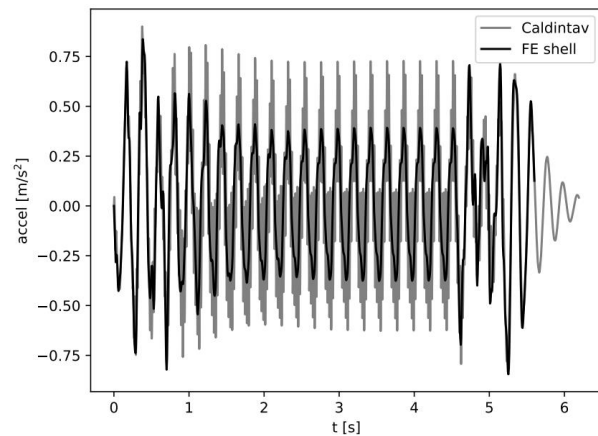


**Figure 11:** Dynamic response of the railway bridge under HSLM-A1 running at 295 km/h with a TMD implemented: Caldintav and FE shell model comparison.

When all the HSLM-A train load models are

considered in the study, the envelope of all the dynamic response represented in Figure 12 is achieved. The TMD leads to a reduction of the railway bridge vibrations for all velocities. Finally, the behaviour of both models is compared in Figure 13 where it is observed the good agreement between them is.

These results allow concluding that the coupled TMD-structure interaction model used in this study is valid for this type of box-slab railway bridge.

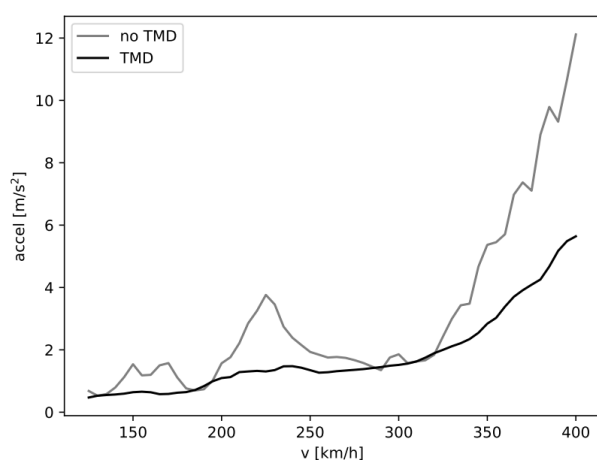


**Figure 12:** Acceleration envelope produced by all the HSLM-A running at different velocities when a TMD is implemented.

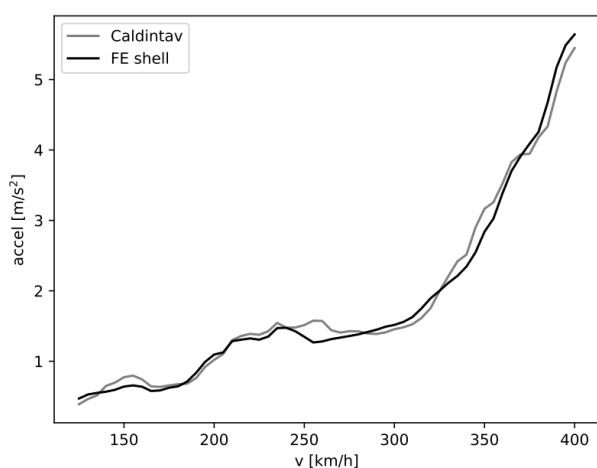


**Figure 13:** Acceleration envelope produced by all the HSLM-A running at different velocities when a TMD is implemented.

To close this section, some remarks are

drawn. The mass of the TMD seems to be quite high, however, a steel box with dimensions  $1 \times 1 \times 0.5 \text{ m}^3$  would be enough to get the mass the of the device. The second option may be to divide the TMD into two TMDs placed at mid-span above the deck at the lateral ends.

In case the TMD is installed inside the box girder, it must be checked that the stroke is less than the height of the box.

For this case study, when the HSLM-A1 runs at  $v = 225 \text{ km/h}$ , the maximum displacement of the TMD is 8 mm. The HSLM-A10 running at  $v = 225 \text{ km/h}$  (its resonant peak) causes a maximum displacement equals to 17 mm. In both cases, the result is much smaller than the inner depth of the box girder. Therefore, there is enough space for installation and movement of the inertial device.

Although it is not discussed here, the requirements of the Ultimate Limit State (ULS) must be verified again once the TMD is installed.

Finally, the computational cost of both methods is compared. A 64 Gb of RAM computer with a 3.40 GHz processor has been used for both calculations. The simplified model of CALDINTAV lasts about 10 minutes whilst the FE shell model in ABAQUS has a duration of 5 hours for all trains and velocity range.

## 5 CONCLUSIONS

A simplified TMD-railway bridge interaction model has been presented and implemented in this paper. It consists of two sub-models, one accounting for the structure and other for the passive inertial device. The first one has been defined through its modal properties and the second one modelled as a single degree of freedom system defined by its mass, stiffness and damping coefficient.

The performance of this simplified interaction model has been validated through

its application to a railway bridge subjected to a series of high-speed load models. A clear reduction of the vertical acceleration of the bridge has been calculated. In addition, the results have been compared with those obtained by modelling the structure through a 3D FE model, giving as conclusion that the simplified model represent a good approximation to the problem with less computational cost.

Further research may be undertaken focusing on skew bridges or with eccentric loads where torsion arises, and more than one device should be installed.

### ACKNOWLEDGEMENTS

The authors acknowledge the financial support provided by the Ministry of Science, Innovation and Universities of Spain through the project SEED-SD RTI2018-099639-B-I00. Christian Gallegos-Calderón thanks the Secretariat of Higher Education, Science, Technology and Innovation of Ecuador (SENESCYT) for the PhD scholarship CZ02-000167-2018.

### REFERENCES

- [1] EN 1991-2:2003: *Actions on Structures – Part 2: Traffic Loads on Bridges*. Brussels: CEN, 2003
- [2] J.P. Den Hartog. *Mechanical vibrations*. Courier Corporation, 1956.
- [3] F. Weber, G. Feltrin and H. Olaf. *Samco final report—F05 guidelines for structural control*. Structural engineering research laboratory, Swiss federal laboratories for materials testing and research. 2006
- [4] C. Heinemeyer, C. Butz, A. Keil et al. *Design of Lightweight Footbridges for Human Induced Vibrations*. JRC European Commission, 2009.
- [5] S. Elias and V. Matsagar. *Research developments in vibration control of structures using passive tuned mass dampers*. Annual Reviews in Control, 44, 129-156, 2017.
- [6] A.Y. Pisal and R.S. Jangid. *Vibration control of bridge subjected to multi-axle vehicle using multiple tuned mass friction dampers*. Int J Adv Struct Eng 8, 213–227, 2016.
- [7] J.M. Goicolea and K. Nguyen. *CALDINTAV v3.0 User's Manual*, 2018.
- [8] R.W. Clough and J. Penzien. *Dynamics of Structures*. New York: McGraw-Hill, 1993.
- [9] SIMULIA. *Abaqus Analysis User's Manual, v6.14*. Dassalt Systèmes SIMULIA Corp, Vélizy-Villacoublay, France (2014).
- [10] Committee ERRI D214. ERRI D214/RP 9. *Rail bridges for speeds > 200 km/h – Final Report Part A: Synthesis of the results of D214 research*. European Research Institute, 1999.

## EXPERIMENTAL MEASUREMENTS ON RAILWAY BRIDGES BELONGING TO SPANISH LINES

**P. Galvín\***, **E. Moliner†**, **A. Romero\***, **M.D. Martínez-Rodrigo†**

\*Escuela Técnica Superior de Ingeniería, Universidad de Sevilla, Camino de los Descubrimientos s/n,  
41092 Sevilla, Spain

e-mail: pedrogalvin@us.es

ORCID: 0000-0001-8981-1413

† Universitat Jaume I, Department of Mechanical Engineering and Construction, Avda. Sos Baynat s/n,  
12071 Castellón, Spain

**Abstract.** The authors have carried out an extensive experimental campaign in several railway bridges in Spain with the purpose of characterising the structures including the soil properties and the bridge dynamic responses under railway traffic. The response of isostatic steel and concrete bridges located in high-speed and conventional lines have been measured and analysed. Six bridges have been experimentally studied: i) Bracea: is an isostatic concrete double-track bridge composed by two identical S-S bays of 15.25 m equal spans; ii) Algodor: is an isostatic double-track concrete bridge composed by three S-S bays of 10 m equal spans; iii) Guadiana: is an isostatic single-track concrete bridge composed by two S-S bays of 12 m equal spans; iv) Jabalón I: is an isostatic double-track concrete HST bridge composed by three S-S bays of 20 m equal spans and v) Jabalón II is a steel truss single-track bridge composed by three of 25 m equal spans. The study includes: bridge modal parameters and dynamic soil properties identification, vibration levels corresponding to actual railway traffic, differences between the structural behaviour of structures for the same traffic and estimation of the response associated to the train speed.

**Key words:** railway traffic; bridge; experimental results; dynamic response; vibrations.

### 1 INTRODUCTION

The construction of the trans-European network (RTE-T), based on the interconnection and interoperability of the corresponding national systems, including the railway network, is of paramount importance

for the economic competitiveness of the European Union (EU) and its balanced and sustainable development. The European Commission [1], in 2010, in the context of establishing a single European railway space, defines the railway transport mode as “an environmentally friendly mode of transport

which can contribute to establishing new forms of mobility that are energy-efficient and limit the risks of aggravating pollution, congestion and climate change”. Therefore, developing a sustainable transport system has become a strategic priority in the long-term, to meet future requirements and challenges in mobility. The European Commission [1] adopts a strategy with the aim of “promoting the development of an effective EU rail infrastructure, establishing an attractive and truly open rail market, removing administrative and technical barriers, and ensuring a level playing field with other transport modes”. Thus, it is intended to increase by 30 to 50 percent the passenger transport by 2050 [2].

Despite the growth indices in the railway sector and despite of the clear advantages that a single European railway area would entail, the researchers of this work detect uncertainties in relation to the changes in the operating conditions of the railway lines, that will require an adequate maintenance of the infrastructure to ensure the levels of quality, safety, and reliability of rail transport. Therefore, expanding the capacity of the lines will require a much more detailed study and characterization of the dynamic effects that occur in the infrastructure. Specifically, the Spanish railway network currently has a total of 135 km of track that runs over more than 6000 bridges. Yearly, infrastructure maintenance includes the auscultation of 250 bridges and conducting 25 to 30 load tests. This situation may also be perfectly applicable to other EU countries.

The dynamic response of a bridge under the circulation of a railway convoy is complex and it is affected by several factors. The most obvious ones are the bridge properties, the

geometric scheme of train axles and the speed of circulation, being also those that less uncertainty entails its determination [3]. Additionally, there are other factors which determination is much more uncertain that significantly affect the response of the bridge such as structural damping and various interaction mechanisms which modelling is not trivial and is currently under investigation, being the most relevant vehicle-structure, rail-structure and soil-structure interaction effects [4]. In engineering consultancies, simplified numerical models that generally disregard these mechanisms are usually used, given the uncertainties that their modelling entail and the considerable computational cost involved.

Several works showed the importance of having available experimental measurements on bridges. Although there is a significant number of papers on this topic, researchers do not always find available experimental measurements for their own purpose. Therefore, the need for such studies justifies the work presented in this paper. A comprehensive experimental campaign in several railway bridges in Spain is presented in this work. The tests include the identification of the modal parameters of the structures, the characterization of the soil surrounding the bridge and the bridge dynamic responses under railway traffic. Five bridges were tested: i) Old Guadiana Bridge: a double-track simply-supported bridge with two 12 m equal spans composed by two adjacent single-track decks with continuous ballast; ii) Jabalón High-Speed Bridge (Jabalón HSL from now on): an isostatic bridge of three S-S bays of 20 m equal spans composed by a double-track pre-stressed concrete girders deck; iii) Algodor Bridge: an isostatic double-track bridge with three S-S bays of 10 m equal spans and a pseudo-slab

concrete deck; iv) Jabalón conventional Line Bridge (Jabalón from now on): a steel truss single-track structure composed by three 25 m equal spans; and v) Tinajas Bridge: a steel-concrete composite single-track bridge with three bays of 25, 35 and 22 m spans, respectively.

## 2 EXPERIMENTAL SET-UP

In April and May 2019 the authors performed an experimental campaign on several railway bridges with the purpose of characterizing the structure and soil dynamic properties along with the bridge dynamic response under railway traffic. As per the acquisition equipment, a portable acquisition system LAN-XI of Brüel & Kjaer was used. The acquisition system fed the sensors (accelerometers) and an instrumented impact hammer in the case of the soil tests. It also performed the Analog/Digital conversion (A/D). The A/D was carried out at a high sampling frequency that avoided aliasing effects using a low-pass filter with a constant cut-off frequency. The sampling frequency was  $f_s = 4096$  Hz. The acquisition equipment was connected to a laptop for data storage. Endevco model 86 piezoelectric accelerometers were used with a nominal sensitivity of 10 V/g and a lower frequency limit of approximately 0.1 Hz. The acquisition system was configured to avoid the sensors' overload. Nevertheless, in some cases, the signals were overloaded. In the case of Tinajas Bridge, Etna stations of Kinematics with internal triaxial accelerometers with a nominal sensitivity of 1.25 V/g were used. Here, the sampling frequency was  $f_s = 250$  Hz.

The modal parameters of the bridges were identified from ambient vibration data by the stochastic subspace identification technique

[5]. The ambient vibration response was acquired during the tests while the trains were not crossing the bridges. Data were decimated to carry out data analysis in the frequency range of interest (0 to 30 Hz). The signals were filtered applying two third-order Chebyshev filters with high-pass and low-pass frequencies of 1 Hz and 30 Hz, respectively.

The dynamic characterisation of the soil was carried out by the seismic refraction and the Spectral Analysis of Surface Waves (SASW) tests. The seismic refraction test allowed the identification of the P-wave velocity ( $C_p$ ) of the soil layers. The SASW test was used to determine the S-wave velocity ( $C_s$ ) and the material damping ratio of the soil layers ( $\beta$ ) [6]. 100 hammer impacts were applied to a 50 cm x 50 cm x 8 cm aluminum foundation anchored to the soil surface. The instrumented hammer included a PCB 086D50 force sensor. The vertical free field response was recorded by means of accelerometers anchored to the soil surface every 2 m (2 m to 72 m). Steel stakes of cruciform section and 30 cm of length were driven into the ground surface and each of the accelerometers was screwed to a stake. After each impact, a time signal of 16348 samples (4 s) was stored. The force channel was used as a trigger, a pre-trigger of 1 s, and a post-trigger of 3 s. The signals were decimated (order 4), filtered with a third-order Chebyshev filter with a high-pass frequency of 1 Hz and a low-pass frequency of 100 Hz.

## 3 RAILWAY BRIDGES

In Dinest 2021 conference, the specificities of the experimental set-ups and the experimental measurements recorded in Old Guadiana, Jabalón HSL, Jabalón, Algodor and Tinajas bridges will be outlined. Here, the first

case is presented in detail.

### 3.1 Old Guadiana Bridge

#### 3.1.1 Description of the structure

This first bridge under study crosses Old Guadiana River in the conventional railway line Madrid-Alcazar de San Juan-Jaén, in the Alcázar de San Juan-Manzanares section (see Figure 1). It is a double track concrete bridge composed by two identical simply-supported bays. The horizontal structure is formed by two structurally independent although adjacent decks, one for each track, sharing the ballast layer. Each deck is composed by a concrete slab resting on five pre-stressed concrete 0.75 m 0.3 m rectangular girders with no transverse stiffening elements. The longitudinal girders rest on the two abutments and on a central support through neoprene bearings. Each deck accommodates a ballasted eccentric track with Iberian gauge (1668 mm), UIC60 rails and mono-block concrete sleepers separated 0.60 m.



**Figure 1:** Old Guadiana Bridge (39°17'37.8"N 3°12'22.5"W).

The vertical acceleration response was measured at 18 points of the lower flange lower horizontal face of the pre-stressed concrete girders. The accelerometers were attached to the girders using circular aluminum plates with 9 cm of diameter and 6 mm of

thickness fixed with epoxy resin to the concrete surface which was previously treated for proper adherence. The response at points of the two decks in both spans was recorded.

#### 3.1.2 Modal parameters identification

Ten modes have been identified from the ambient vibration recorded during 3600 s corresponding to the vertical bending and torsion of the decks. The lowest one in frequency order correspond to the first bending mode. The second one is a torsional mode that involves both decks because the tracks components cause the deck coupling. Nevertheless, the third mode corresponds to the torsion of each deck independently. Bending and torsional behaviours can be observed in the rest of the mode shapes. The identified damping for the fundamental mode reaches 2.3%, higher value than that prescribed by standards for design purposes for this length and bridge typology (1.5% as per [7]).

The damping ratio estimation was deeply analysed. The damping ratios were obtained using the response to the wind load and also from 10 s of free vibration after the train passages. The amplitude of the oscillations is rather higher in the later case. The damping ratio estimations are presented in Figure 2. The obtained results for the same vehicle crossing the bridge for the same track are consistent. As a general conclusion, it can be mentioned that the damping ratios from the response to train loads were higher than those obtained from the ambient response. Notwithstanding the uncertainties, the estimations from the railway traffic were done under operational conditions of the bridge and can represent better the actual behaviour of the structure.

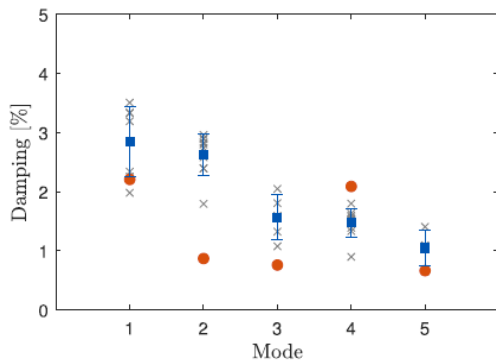


**Figure 2:** Old Guadiana bridge: estimated damping ratios from (red circle) ambient vibration and (grey crosses) train passages. The (blue square) mean value and (blue line) the mean value the standard deviation are also presented.

### 3.1.3 Response due to train passages

The circulations took place on the 6th of May between 12:18 and 17:38 hours. The structural response to different vehicles at around 160 km/h has been measured.

Figure 3 shows the bridge response at points 5, 17, 8 and 15 due to a Renfe Altaría train on tracks 1 and 2 at  $v=160$  km/h and  $v=155$  km/h, respectively. It should be mentioned that the resonant speeds for mode 1 and resonance

order 3 is  $v_{1,3} = 9.8 \times 13.1/3 \times 3.6 = 154$  km/h, very close to the actual speeds. The damping ratios for mode 1 obtained from the free response after the trains left the structure were 2.5% and 5.0%, respectively for the two train passages. The response at points 5 and 17 present a similar behaviour when the trains cross the bridge along the tracks 1 and 2. The response at point 5 when the train was on track 2 is like the response at point 17 when the train was on track 1. The contribution of modes 1 and 3 is clearly observed in the responses. Moreover, the characteristic vehicle frequency  $v/d = 160/3.6/13.1 = 3.4$  Hz and its second harmonic can be also observed in the observation points close to the track which the train was travelling. The train crossing the bridge along the track 2 induces a higher level in the deck 2, although the deck 1 is also excited. The maximum amplitude in the deck 1 is about the 45% of the highest value in deck 2. The response at point 8, at the edge of the deck 2, presents the highest level for the train on the track 2. The mode 4 also contributes to this response. The decks responses are clearly coupled through the ballast track.

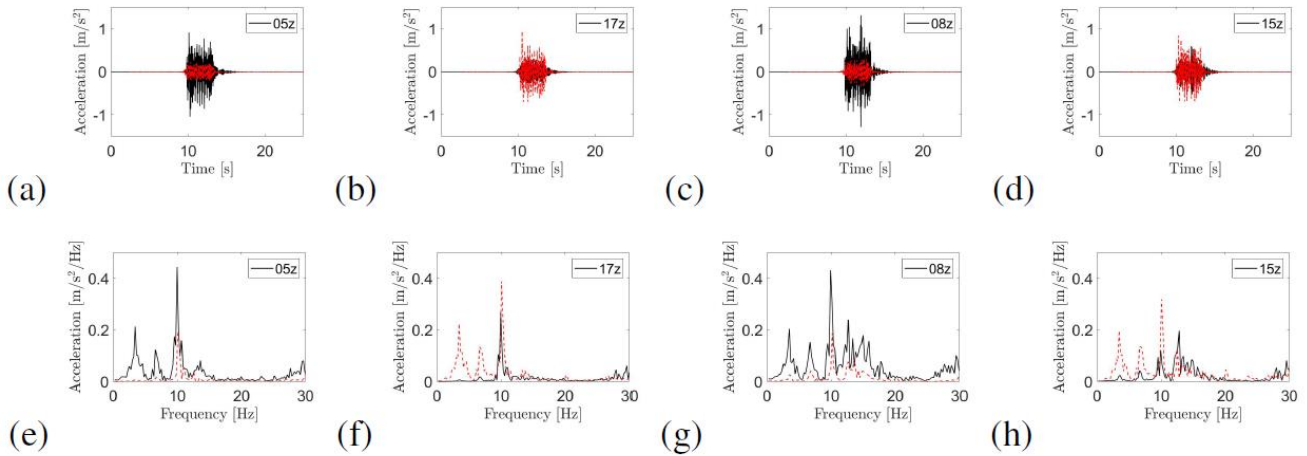


**Figure 3:** Old Gadiana Bridge: (a-d) time history and (e-h) frequency content of the acceleration at points 5, 17, 8 and 15 induced by Renfe Altaria train with 9 coaches (black line) at  $v = 160$  km/h circulating on track 2 and (red line) at  $v = 155$  km/h circulating on track

#### 4. CONCLUSIONS

An experimental campaign was performed at several railway lines in Spain in order to characterize the soil and the bridge dynamic behaviour induced by train passages. The results allow a better understanding of the structural performance of these short bridges, which can be helpful for the development and updating of numerical models useful for practical applications.

#### ACKNOWLEDGEMENTS

The authors would like to acknowledge the financial support provided by the Spanish Ministries of Economy and Competitiveness, Science and Innovation under research projects BIA2016-75042-C2 and PID2019-109622RB; US-126491 funded by the FEDER Andalucía 2014–2020 Operational Program; Generalitat

Valenciana under research project [AICO2019/175] and the Andalusian Scientific Computing Centre (CICA).

#### REFERENCES

- [1] European Commission, Communication from the commission concerning the development of a Single European Railway Area, Tech. rep. (2010).
- [2] European Commission, Transport in the European Union. Current Trends and Issues, Tech. rep. (March 2019).
- [3] J. Rocha, A. Henriques, R. Calcada, Safety assessment of a short span railway bridge for high-speed traffic using simulation techniques, *Engineering Structures* 40 (2012) 141 – 154. doi:http://doi.org/10.1016/j.engstruct.2012.02.024.
- [4] J. Rocha, A. Henriques, R. Calcada,

Probabilistic safety assessment of a short span high-speed railway bridge, *Engineering Structures* 71 (2014) 99–111.

- [5] E. Reynders, System identification methods for (operational) modal analysis: Review and comparison, *Archives of Computational Methods in Engineering* 19 (1) (2012) 51–124. doi:10.1007/s11831-012-9069-x.
- [6] S. A. Badsar, M. Schevenels, W. Haegeman, G. Degrande, Determination of the material damping ratio in the soil from SASW tests using the half-power bandwidth method, *Geophysical Journal International* 182 (3) (2010) 1493–1508. doi:10.1111/j.1365-246X.2010.04690.x.
- [7] CEN/TC250, Eurocode: Basis of structural design. Annex A2: Application for bridges. Final version, European Committee for Standardization, Brussels, 2005.

## **Section 4: Marine structures**

---

## DYNAMIC ANALYSIS OF FLOATING BREAKWATERS: A CASE STUDY

Cebada-Relea, A. J.\*, López M.†, Aenlle M. ‡ and Claus, R.†

\* DyMAST Research Group, Escuela Politécnica de Mieres  
Universidad de Oviedo  
33600 Asturias, Spain  
e-mail: cebadaalejandro@uniovi.es  
ORCID: 0000-0001-7479-0533

† DyMAST Research Group, Escuela Politécnica de Mieres,  
Universidad de Oviedo  
33600 Asturias, Spain

‡ DyMAST Research Group, Escuela Politécnica de Ingeniería de Gijón,  
Universidad de Oviedo  
33206, Asturias, Spain

**Abstract.** Fixed structures are commonly used to shelter port basins and vessels from extreme wave conditions. Nonetheless, in port basins and harbours with mild wave conditions, floating solutions represent an interesting alternative due to their lower cost and impact on the seabed. Numerical modelling of wave-structure interaction is of paramount importance since the dynamic behaviour of any floating structure determines key issues such as the mooring arrangement and the module connection system. This work deals with the numerical modelling of a modular breakwater in Asturias (Spain), which has suffered frequent structural failures in the module connection elements after extreme wind-sea wave conditions. The dynamics of the floating structure are analysed by means of a panel model that applies the boundary element method (BEM) to solve the linear radiation-diffraction problem. The hydrodynamic coefficients of the modular pontoon are used to define the response amplitude operators and, subsequently, identify the natural modes of oscillation.

**Key words:** Pontoon breakwater, marine structures, numerical simulation, BEM.

### 1 INTRODUCTION

Wave dissipating structures are needed to shelter the vessels at port from the oncoming waves. Although most of these structures are fixed to the seabed, floating breakwaters are commonly used in locations with mild environmental conditions. The latter are a low-cost environmentally friendlier alternative

since they reduce current affection and its associated sediment transport [1].

The modular concrete floating breakwater of the Port of Figueras is a prime example of these structures (Figure 1). This port is located within the Ria of Eo, an estuary that separates the coastlines Galicia and Asturias, two northern regions of Spain.



**Figure 1.** Location of the Port of Figueras (left) and panoramic view of the floating breakwater (right).

Over the last years, this breakwater has frequently suffered the breakage of the connections between the concrete modules and the corresponding cascade of structural failures (Figure 2). Once the connection elements are broken, incoming waves induce large relative motions on the unrestrained modules, which tend to hit each other. This situation leads not only to structural failures (including concrete cracking), but also to losses of the breakwater's wave dissipation efficiency that reduce port operability.



**Figure 2.** Breaking of the connectors and damage on the concrete modules.

These structural failures are associated to harsh environmental conditions dominated by strong southern winds. Given the considerable fetch length in the South-North direction, strong wind seas are frequently generated within the estuary (Figure 1). These wave conditions are particularly adverse during high tides and cause violent strokes of the

breakwater and docks. The failure of the connections is presumed to occur under these conditions due to the excessive forces they must withstand, but it requires confirmation by a comprehensive analysis.

Advanced engineering techniques are required to properly estimate the forces acting on these floating structures. A usual approach is to conduct the experimental testing of these structures in wave flumes or basins, where scaled models are tested [2]. Although these results are difficult to extrapolate to full-size structure, they can be used to calibrate numerical models [3].

As for today, numerical models are a feasible approach to address the dynamics of a floating structure under complex environmental actions. The first numerical studies regarding floating breakwaters applied the potential flow theory to simplified 2D geometries [4]. Recent studies applied models that solve the Navier-Stokes equations, both from an eulerian [5] and lagrangian [6] perspective. The most innovative methods entail high computational costs, making them unsuitable for a comprehensive analysis of a structure as complex as the dynamics of a floating breakwater. The 3D panel models, based on the potential flow theory, are a compromise between accuracy and computational cost [7].

The purpose of this work is to present a first approximation of the dynamic behaviour of one of the modules of the breakwater of the Port of Figueras. It is achieved through advanced simulation techniques that feature a 3D panel numerical model. This analysis

provides an estimation of the hydrodynamic coefficients that govern the dynamic response of the structure. These coefficients could be used in a further, more complex, analysis of these structures.

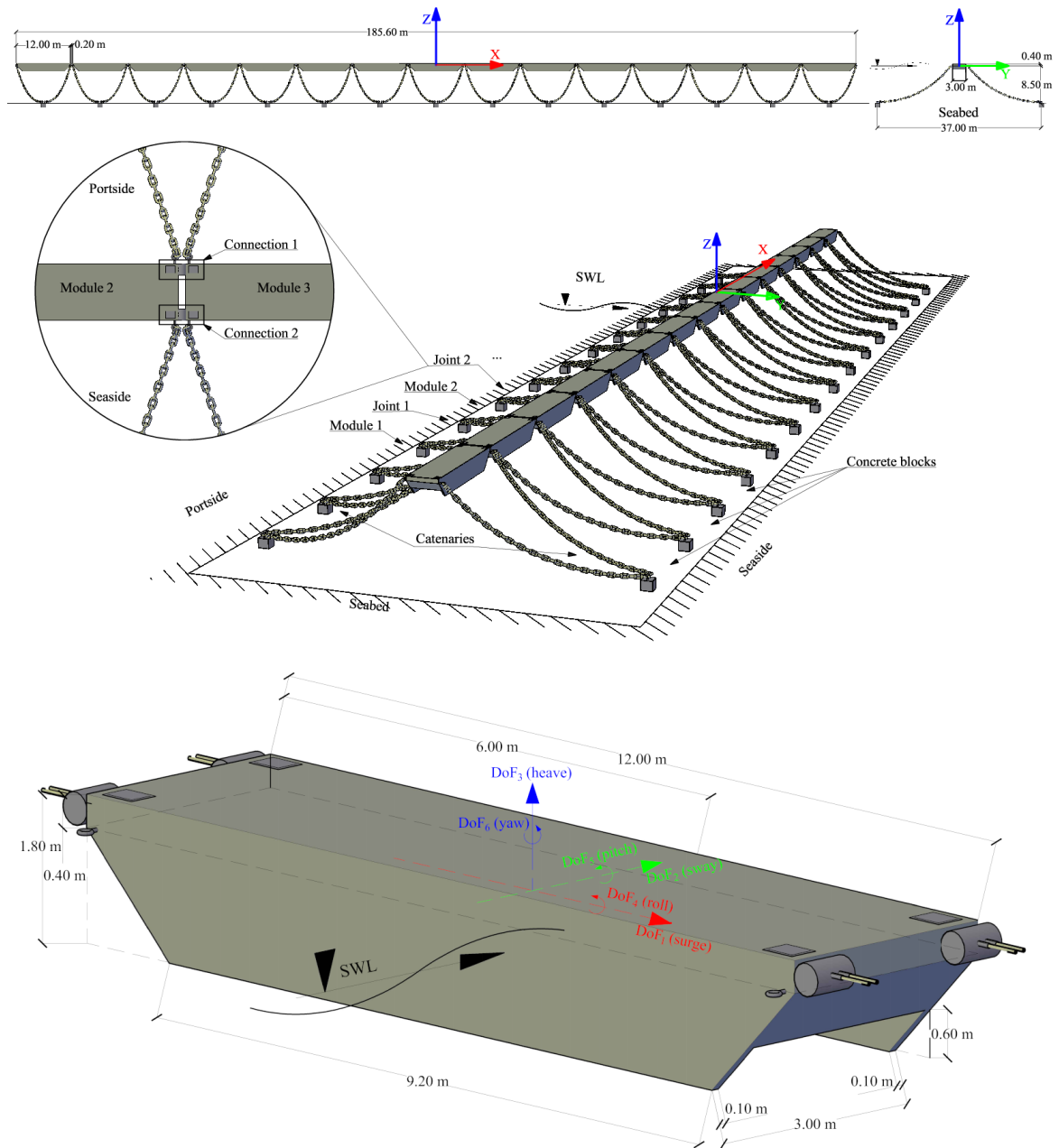


**Figure 3.** General schematics of the floating breakwater (upper panel) and dimensions of a single modules (lower panel).

## 2 FLOATING BREAKWATER DESCRIPTION

The complete structure of the Figueras breakwater has a 198.45 m length and consists of 15 prefabricated concrete modules (Figure 3). Each module is a SF BW-300 model, manufactured by SF Marina. These modules are connected by two connections, each consisting of two steel braid cables. This arrangement provides enough stiffness to make the complete breakwater function as a whole. Each module is also moored to the seabed by 4 steel chains that are anchored by concrete blocks.

The modules are pontoon-type hollow structures, with the following dimensions: a 12.00 m length ( $X$  direction), a 3.00 m beam ( $Y$  direction), a 1.80 m height ( $Z$  direction), a 0.40 m freeboard and a 24 t displacement tonnage.

## 2 FREQUENCY DOMAIN NUMERICAL MODELLING

The wave forces acting on a floating structure are dependent on its characteristic dimensions ( $D$ ) as well as the wavelength ( $\lambda$ ) and wave height ( $H$ ) (Figure 4). According to the on-site wave conditions ( $H_s = 0.76$  m and  $T_p = 3.41$  s) [8], the water depth ( $d = 8.50$  m) and the characteristic dimension of the modules ( $D = 3.00$  m), this case study corresponds to a region II wave force regime, in which diffraction forces are dominant.

ANSYS Aqwa was used to analyse the fluid-structure dynamic interaction between a single module and the oncoming waves. A diffracting behaviour of the modules of the breakwater was assumed.

This simulation environment has been already applied to other marine structures, such as floating drilling platforms [10], Mid Water Arch submarine structures [11] or wave energy converters [12]. It has also been employed in floating breakwaters [13].

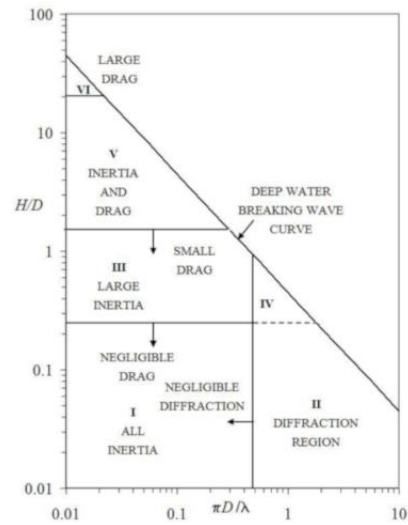


Figure 4. Regions of dominant wave forces [9].

Aqwa Line applies the potential flow theory; thus, the fluid is considered to be ideal and the flow irrotational. The floating body is assumed to be rigid, with no forward speed and small enough motions so that the boundary conditions are met around the equilibrium position. Under these hypotheses and the cartesian coordinate system  $\mathbf{X} = (X, Y, Z)$ , the flow around the floating body is defined through the velocity potential,

$$\phi(\mathbf{X}, t) = \text{Re}[\varphi(\mathbf{X})e^{-i\omega t}], \quad (1)$$

where:  $t$  is the time,  $\omega$  is the angular frequency,  $\text{Re}$  implies “the real part of”, and  $\varphi$  is the velocity potential in terms of the spatial coordinate. This potential satisfies the Laplace continuity condition,

$$\nabla^2 \varphi(\mathbf{X}) = \frac{\partial^2 \varphi}{\partial X^2} + \frac{\partial^2 \varphi}{\partial Y^2} + \frac{\partial^2 \varphi}{\partial Z^2} = 0, \quad (2)$$

through which the linearity of the solution is guaranteed for all the fluid domain. For convenience’s sake, the potential can be expressed through three different terms: the incident potential ( $\varphi_i$ ), the diffracted potential ( $\varphi_d$ ) and the radiated potential ( $\varphi_{rm}$ ). This last term is radiated by the  $m$  structure, due to its movements in the  $j$  degree of freedom (DoF),

for all  $M$  interacting structures. This velocity potential can be therefore expressed as follows

$$\varphi e^{-i\omega t} = \left[ \varphi_l + \varphi_d + \sum_{m=1}^M \sum_{j=1}^6 \varphi_{rm} x_{jm} \right] e^{-i\omega t}, \quad (3)$$

where  $x_j$  is the motion for the  $j$  DoF.

Several methods can be used to solve the velocity potential, being the Boundary Element method (BEM) one of the most used. This method transforms this problem into partial derivatives in integrable surfaces, where loads are applied through the pulsating Green's function in finite depth water [14]. The following conditions must be met:

- Free surface ( $Z = 0$ ) condition,

$$-\omega^2 \varphi + g \frac{\partial \varphi}{\partial Z} = 0, \quad (4)$$

where  $g$  is the gravitational acceleration.

- The rigid body is impermeable and therefore the velocities of the flow particles that are in contact with the surface of the body are equal to the velocity of the body ( $\mathbf{u}$ ),

$$\partial \varphi / \partial n = \mathbf{u} \cdot \mathbf{n}, \quad (5)$$

where  $\partial / \partial n$  is the derivation throughout the direction normal to the body, and  $\mathbf{n}$  is a unit vector normal to the body surface.

- Seabed surface condition at a depth of  $Z = d$ ,

$$\frac{\partial \varphi}{\partial Z} = 0. \quad (6)$$

- Far apart from the floating body, the perturbation on the fluid is dissipated, meaning that the potential becomes zero,

$$\lim_{R \rightarrow \infty} (\varphi) = 0, \quad (7)$$

for  $R = (X^2 + Y^2)^{0.5}$ .

A computational mesh was used to determine the velocity potentials over a floating module. The mean wet surface ( $S_0$ ) was discretized in similarly sized quadrilaterals (Figure 5).

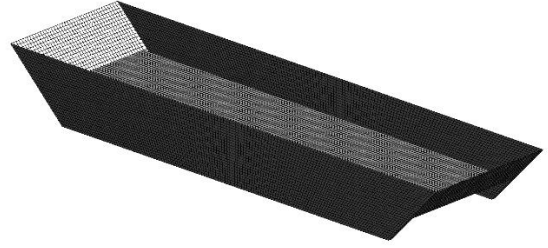


**Figure 5.** Mesh of diffracting panels over the mean wet surface ( $S_0$ ).

Once the velocity potentials are obtained, the dynamics of a free-floating body under the action of waves can be analysed as a mass-spring system.

The equation of motion of the floating body in the frequency domain is

$$\left[ -\omega^2 (\mathbf{M} + \mathbf{A}) - i\omega \mathbf{B} + \mathbf{C} \right] \cdot \boldsymbol{\chi} = \mathbf{f}(\omega), \quad (8)$$

where:  $\mathbf{M}$  is the structural mass matrix;  $\mathbf{A}$  is the added mass matrix;  $\mathbf{B}$  is the damping matrix;  $\mathbf{C}$  is the hydrostatic stiffness matrix;  $\boldsymbol{\chi}$  is the amplitude of motion of the rigid body in its 6 DoF's; and  $\mathbf{f}(\omega)$  are the frequency dependent unitary forces and moments. Each of these terms will be described at length hereunder.

When a floating body is in motion, it induces accelerations to its surrounding fluid particles. This effect may be represented considering that said floating body has an added mass ( $\mathbf{A}$ ) in every one of its DoF's.

A free-floating body also generates waves due to its very own motions. The phenomenon where energy is dissipated through radiation is known as hydrodynamic damping. The matrix  $\mathbf{B}$  represents this phenomenon for every DoF.

Both matrices can be obtained through the radiation forces of the body as

$$\mathbf{A} = \frac{\rho}{\omega} \int_{S_0} \text{Im}[\varphi_r] \mathbf{n} dS \quad (9)$$

and

$$\mathbf{B} = -\rho \int_{S_0} \text{Re}[\varphi_r] \mathbf{n}_j dS, \quad (10)$$

where  $\rho = 1027 \text{ kg/m}^3$ , a typical seawater density. The values of  $\mathbf{A}$  and  $\mathbf{B}$  are not only dependent on the geometry, but also on water depth, as it influences the wave fronts that ultimately interact with the structure. Both  $\mathbf{A}$  and  $\mathbf{B}$  are symmetrical if there is no forward speed and in absence of water currents [15]. The hydrostatic stiffness matrix ( $\mathbf{C}$ ) is only dependent on the geometry (due to the position of the centre of gravity and  $S_0$ ) and the fluid density.

The term  $\mathbf{f}(\omega)$  stands for the forces and moments vector that acts over the mean wetted surface of the body. This vector encompasses different force types. These are the incident or Froude-Krylov forces  $\mathbf{f}_i(\omega)$ , the diffraction forces  $\mathbf{f}_d(\omega)$  and the radiation forces  $\mathbf{f}_r(\omega)$ . The first two are considered exciting forces whereas the last one exists due to the motions of the body in all of its 6 DoF's. All these forces may be expressed as functions of the velocity potentials of the fluid

$$\mathbf{f}_i(\omega) = -i\omega\rho \int_{S_0} \varphi_i \mathbf{n} dS, \quad (11)$$

$$\mathbf{f}_d(\omega) = -i\omega\rho \int_{S_0} \varphi_d \mathbf{n} dS, \quad (12)$$

$$\mathbf{f}_r(\omega) = -i\omega\rho \int_{S_0} \varphi_m \mathbf{n}_m dS. \quad (13)$$

Once the harmonic response of a floating body is solved, it can be expressed by means on its Response Amplitude Operators (RAO). These are defined as the response amplitude of a floating body for a certain DoF  $j$  divided by a wave height ( $H$ ), that is

$$\text{RAO}_j = 2 \frac{\chi_j}{H}. \quad (14)$$

The RAO may be used to identify the natural oscillation modes of the floating body, for which the response amplitude will be maximum. The natural periods of a free-floating module will tend to infinity for all DoF's in the horizontal plane (surge, sway and

yaw), as the restoring forces are negligible [16].

Even if the moorings were considered, the natural periods would still be very high, far away from the periods that should be expected from a wind sea state. Therefore, only low period oscillations or long waves could be able to excite these structures [17]. As for the DoF contained in the vertical plane, the natural periods will be low, similar to those of the waves, with or without the contribution of the mooring system. This is because gravity will always act as a restoring force.

### 3 RESULTS

One of the main outputs of the frequency domain analysis was the obtention of  $\mathbf{A}(\omega)$  and  $\mathbf{B}(\omega)$ , both 6x6 matrices. Since the modules are symmetric with respect to the vertical planes  $XZ$  and  $YZ$ , the terms outside the main diagonal are zeroes. The resulting added mass and damping matrices are

$$\mathbf{A} = \begin{pmatrix} A_{11} & 0 & 0 & 0 & A_{15} & 0 \\ 0 & A_{22} & 0 & A_{24} & 0 & 0 \\ 0 & 0 & A_{33} & 0 & 0 & 0 \\ 0 & A_{42} & 0 & A_{44} & 0 & 0 \\ A_{51} & 0 & 0 & 0 & A_{55} & 0 \\ 0 & 0 & 0 & 0 & 0 & A_{66} \end{pmatrix} \quad (15)$$

and

$$\mathbf{B} = \begin{pmatrix} B_{11} & 0 & 0 & 0 & B_{15} & 0 \\ 0 & B_{22} & 0 & B_{24} & 0 & 0 \\ 0 & 0 & B_{33} & 0 & 0 & 0 \\ 0 & B_{42} & 0 & B_{44} & 0 & 0 \\ B_{51} & 0 & 0 & 0 & B_{55} & 0 \\ 0 & 0 & 0 & 0 & 0 & B_{66} \end{pmatrix}. \quad (16)$$

Figure 6 shows the variation of the terms in the added mass matrices for different values of angular frequency. The first three terms in the

main diagonal relate translations in the directions of the coordinate axis with forces in the same direction. Regarding these terms, the highest added mass corresponds to the vertical mode or heave ( $A_{33}$ ).

For this mode, the virtual mass is kept constant at 50.00 t for angular frequencies above 2.00 rad/s. For frequencies below this value, the virtual mass increases its value inversely proportional to the frequency until it reaches a maximum value of 111.56 t.

The term corresponding to the sway motions of the body ( $A_{22}$ ) shows a maximum value of 58.81 t for  $\omega \approx 1.54$  rad/s. Above this frequency, the added mass is drastically diminished while under it, the added mass is reduced to 40.14 t. The added mass for surge motions ( $A_{11}$ ) presents the lowest values, being always below 1.00 t for any of the analysed frequencies. This is because the module has a smaller exposed surface in this particular direction.

As for the rotation terms of the main diagonal, the highest value of added mass was found for the pitch motion ( $A_{55}$ ), with  $626.89 \text{ t}\cdot\text{m}^2/\text{rad}$  around the  $\omega = 1.25$  rad/s frequency. This result is explained by the inertias of the module. The yaw term ( $A_{66}$ ) shows a  $454.35 \text{ t}\cdot\text{m}^2/\text{rad}$  maximum value, around the  $\omega = 2.00$  rad/s frequency. In both cases, the added mass drastically plummets for higher frequencies. Finally, the added mass for the roll motions ( $A_{44}$ ) presents a value somewhat constant throughout the analysed range of frequencies. This value slightly varies around  $30.00 \text{ t}\cdot\text{m}^2/\text{rad}$ .

Figure 6 also shows the translational added mass in each of the horizontal axis. These are induced by the rotations around the horizontal axis perpendicular to them and are represented by the terms  $A_{15}$  and  $A_{24}$ . Since the body has no forward speed and no currents were defined, the matrix is symmetrical for these components, meaning that:  $A_{15} = A_{51}$  and

$A_{24} = A_{42}$ . The rotational added mass  $A_{15}$

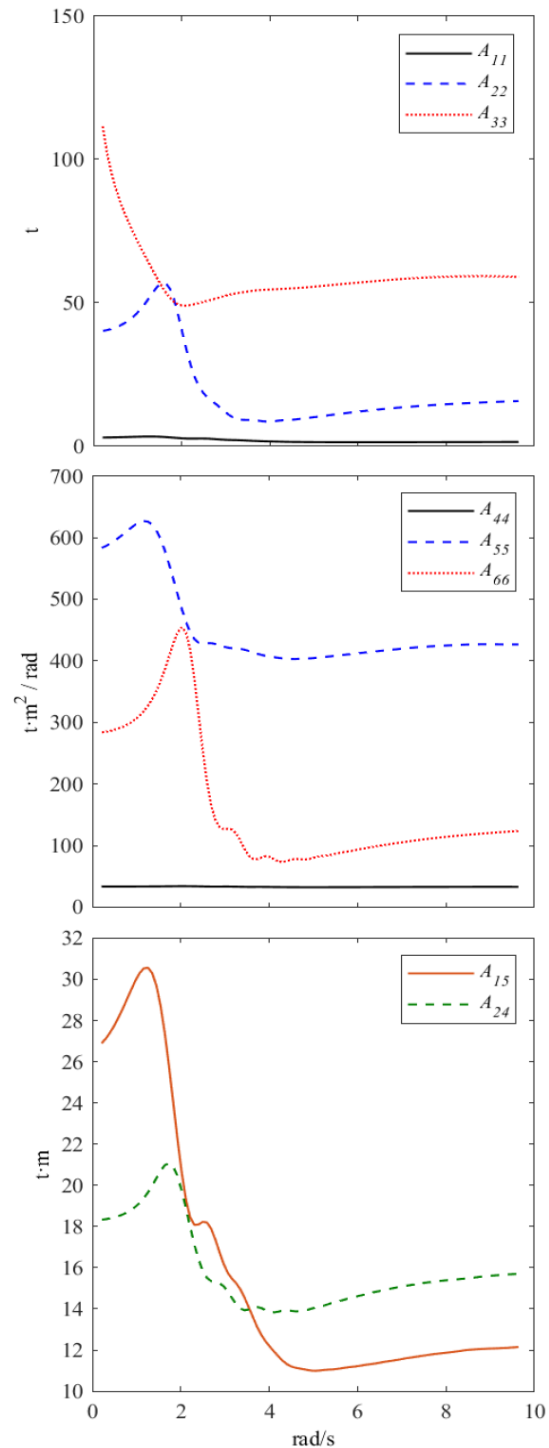


**Figure 6.** Terms of the added mass matrix in the frequency domain: components of the main diagonal (upper and middle panel) and components outside the main diagonal (lower panel).

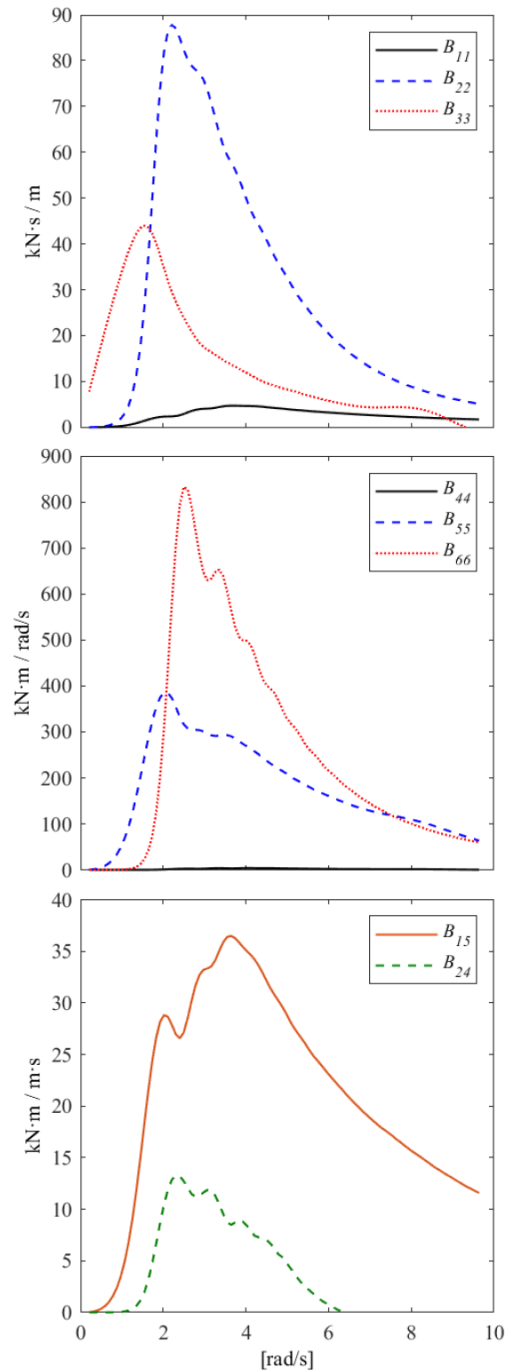
reaches a peak value of 30.56 t·m for  $\omega = 1.26$  rad/s. This value rapidly decreases for lower frequencies until reaching a value of 12.00 t·m. As for the  $A_{24}$  term, its maximum values are significantly lower than those of the previous term, reaching a value of 21.08 t·m around 1.73 rad/s. For  $\omega > 2.00$  rad/s, both parameters tend to align and for frequencies above  $\omega = 3.54$  rad/s,  $A_{24}$  yields the higher values.

Figure 7 shows the terms of the hydrodynamic damping matrix ( $\mathbf{B}$ ) in the frequency domain. The pontoon-type shape of the analysed module is designed to amplify the damping in sway motions. These designs are meant to attenuate waves and have a high wave transmission coefficient to protect the sheltered docks and vessels. The highest values obtained in the hydrodynamic damping matrix were associated to the sway terms ( $B_{22}$ ), reaching a value of 87.87 kN·s/m for  $\omega = 2.00$  rad/s. A remarkable damping was also found associated to the yaw motions ( $B_{66}$ ), for similar angular frequencies, with a maximum value of 833.18 kN·m/s/rad.

As seen in Figure 7, two other modes show significant hydrodynamic damping: the heave and pitch modes. Both present a similar pattern, with maximum values of  $B_{33} = 43.98$  kN·s/m and  $B_{55} = 385.56$  kN·m/s/rad around  $\omega \approx 1.50$  rad/s.

As for the surge and roll modes, their damping is comparatively inferior for the whole frequency domain, being almost negligible in the roll modes. Roll damping is usually underestimated in potential theory codes, so additional damping is introduced to reproduce the motions realistically. This additional damping is achieved through a linear stiffness matrix with a single value of 20.00 kN·m/rad·s in the corresponding roll term. This value is based on an average added mass of 30.00 t $m^2$ /rad, the inertia around the  $X$

axis, and considering 15% of the critical damping.



**Figure 7.** Terms of the hydrodynamic matrix in the frequency domain: components of the main diagonal (upper and middle panel) and components outside the main diagonal (lower panel).

The variation of the components outside the main diagonal can be seen in the lower panel of Figure 7. The rotational damping in the longitudinal axis due to pitch motions shows a maximum value of  $B_{15} = 36.50 \text{ kN}\cdot\text{m}$  for  $\omega \approx 3.64 \text{ rad/s}$ . In this mode, lower frequencies while for higher frequencies, the value stabilizes at  $B_{15} \approx 15.00 \text{ kN}\cdot\text{m}$ .

The rotational damping in the transversal axis due to roll motions reaches a maximum value of  $B_{24} = 13.28 \text{ kN}\cdot\text{m}$  for  $\omega \approx 2.20 \text{ rad/s}$ .

Finally, the hydrostatic stiffness matrix was obtained

$$\mathbf{C} = \begin{pmatrix} 0 & 0 & 0 & 0 & 0 & 0 \\ 0 & 0 & 0 & 0 & 0 & 0 \\ 0 & 0 & C_{33} & 0 & 0 & 0 \\ 0 & 0 & 0 & C_{44} & 0 & 0 \\ 0 & 0 & 0 & 0 & C_{55} & 0 \\ 0 & 0 & 0 & 0 & 0 & 0 \end{pmatrix} \quad (17)$$

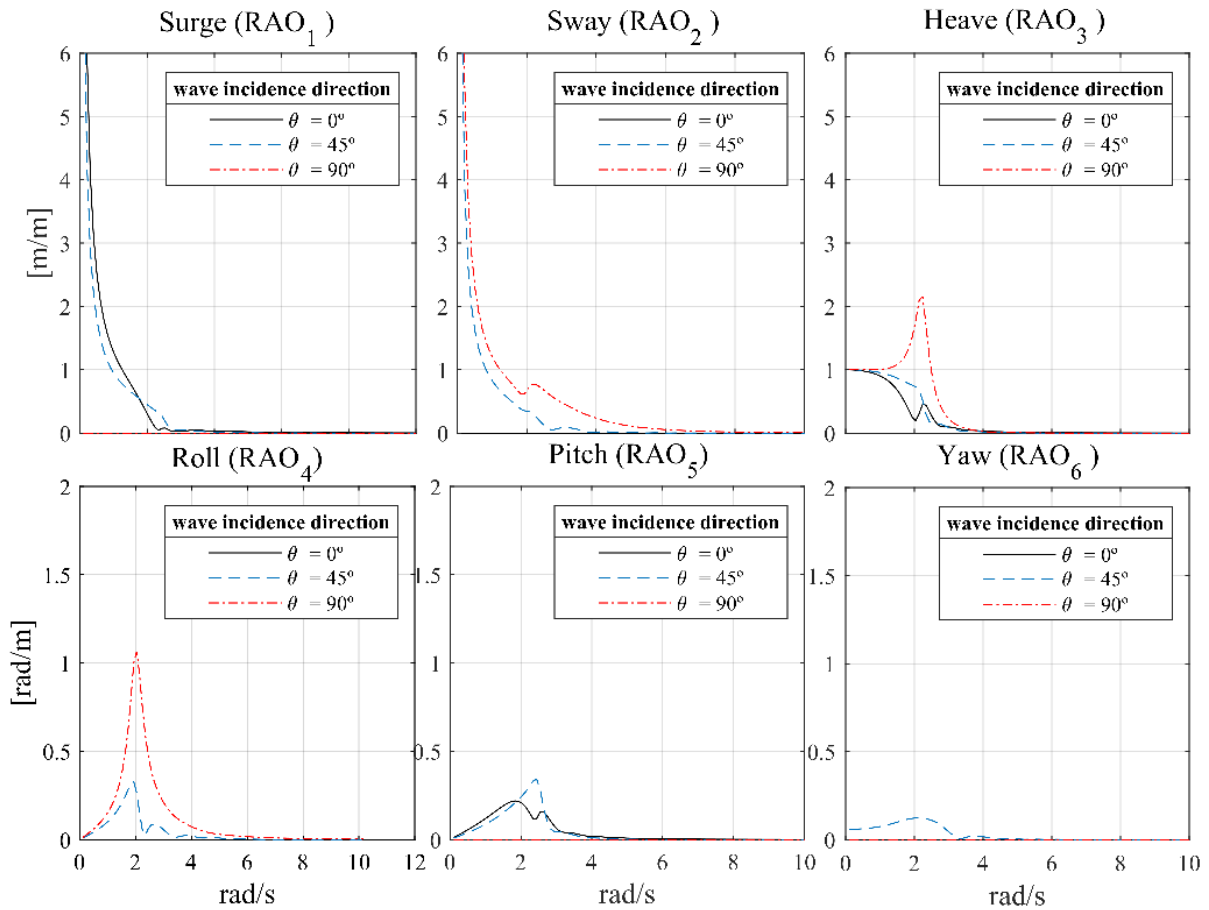


Figure 8. RAO vs angular frequency ( $\omega$ ) for the analysed floating module.

where  $C_{33} = 361.86$  kN/m;  $C_{44} = 212.11$  kN·m/rad; and  $C_{55} = 4283.11$  kN·m/rad. Since the centre of gravity is vertically aligned with the centre of floatation,  $\mathbf{C} = \mathbf{C}^T$ . Moreover, given the symmetry of the floating modules with respect to both vertical planes, all  $\mathbf{C}$  terms are zero except for those corresponding to motions in the vertical planes of the main diagonal.

Once the values of  $\mathbf{A}$ ,  $\mathbf{B}$  and  $\mathbf{C}$  were known, the modal response of the free-floating pontoon was computed. Figure 8 shows the RAO obtained for each DoF and each of the defined wave directions. These directions ( $\theta$ ) are  $0^\circ$ ,  $45^\circ$  and  $90^\circ$  with respect to the  $X$  horizontal axis. These outcomes can be used to estimate the natural frequencies of the floating module, as a first approach to assess the hydrodynamic behaviour of this structure.

For the heave and roll motions, the natural frequencies are around  $\omega = 2.00$  rad/s. In both cases, the RAO quickly diminish outside this frequency. For low frequencies, the vertical motions of the structure (heave) are paired with the oncoming waves since the RAO match the wave amplitudes. For both heave and roll motions, the RAO is greater for the  $\theta = 90^\circ$  wave direction.

As for the pitch motions, the natural frequency has a slightly higher value of  $\omega \approx 2.50$  rad/s, where a damped oscillation mode of 0.50 rad/m appears. Furthermore, the values of the RAO are higher for the  $\theta = 45^\circ$  wave direction, lower for  $\theta = 0^\circ$  and zero for the  $\theta = 90^\circ$  wave direction. This is explained due to the symmetry of the module with respect to its transversal plane.

On the other hand, no natural frequencies of oscillation were identified for the surge, sway, and yaw motions. This is due to the free-floating nature of the body. Since no moorings were considered in this stage of the analysis, the RAO corresponding to surge and sway tend to infinity as frequencies tend to zero. Greater

values are obtained, for a given frequency, when the wave front is aligned with each of these motions.

#### 4 CONCLUSIONS

A linear hydrodynamic model of single pontoon floating breakwater placed in the Port of Figueras (Spain) was carried out. The model applies the potential theory throughout the Boundary Element Method. The hydrodynamic coefficients and the harmonic response were solved in the frequency domain. The conclusions of the analysis are summarized below:

- For translations and rotations about  $X$  axis (surge and roll) the added mass can be neglected. In other DoF's the highest value of the added mass appears at low frequencies ( $\omega < 2.0$  rad/s), and for upper frequencies added mass tends to stabilize.
- The hydrodynamic damping of the translations and rotations about  $X$  axis also can be neglected, but at least its necessary introduce an additional linear damping. In this case is remarkable the damping of the translations about  $Y$  axis, in which the highest values appear over  $2.0 \leq \omega \leq 4.0$  rad/s.
- Three natural modes of the pontoon were identified throughout the Response Amplitude Operator on each DoF. The modes relative to the heave and roll appear around 2.00 rad/s, especially when the wave incidence angle is transverse to the pontoon. In oblique wave conditions another damped mode also appears in pitch rotation near the frequency of 2.50 rad/s.
- To get a more realistic approximation of the behaviour of the set of pontoons, an exhaustive analysis in the time

domain is required, considering the mooring and anchoring forces and the representative wave conditions of the site.

## REFERENCES

- [1] B. L. McCartney, "Floating breakwater design," *J. Waterw. Port, Coast. Ocean Eng.*, vol. I, no. 2, pp. 304–318, 1985.
- [2] J. Ferreras, E. Peña, A. López, and F. López, "Structural performance of a floating breakwater for different mooring line typologies," *J. Waterw. Port, Coast. Ocean Eng.*, vol. 140, no. 3, pp. 1–11, 2014.
- [3] P. Rosa-Santos, M. López-Gallego, F. Taveira-Pinto, D. Perdigão, and J. Pinho-Ribeiro, "Numerical simulation and validation of CECO wave energy converter," in *Sustainable Hydraulics in the Era of Global Change - Proceedings of the 4th European Congress of the International Association of Hydroenvironment engineering and Research, IAHR 2016*, 2016, pp. 254–260.
- [4] R. W. Yeung, "Added mass and damping of a vertical cylinder in finite-depth waters," *Appl. Ocean Res.*, vol. 3, no. 3, pp. 119–133, 1981.
- [5] H. Zhang, B. Zhou, C. Vogel, R. Willden, J. Zang, and J. Geng, "Hydrodynamic performance of a dual-floater hybrid system combining a floating breakwater and an oscillating-buoy type wave energy converter," *Appl. Energy*, vol. 259, p. 114212, 2020.
- [6] Z. Liu and Y. Wang, "Numerical investigations and optimizations of typical submerged box-type floating breakwaters using SPH," *Ocean Eng.*, vol. 209, p. 107475, 2020.
- [7] I. Diamantoulaki and D. C. Angelides, "Analysis of performance of hinged floating breakwaters," *Eng. Struct.*, vol. 32, no. 8, pp. 2407–2423, 2010.
- [8] Centro de Estudios y Experimentación de Obras Públicas (CEDEX), "Estudio del canal de Figueras de la Ría del Eo (Castropol, Asturias)." Madrid, 2006.
- [9] DNV GL, "DNVGL-RP-C205: Environmental Conditions and Environmental Loads," *DNV GL Recomm. Pract.*, no. August, pp. 1–259, 2017.
- [10] T. Wang and Y. Liu, "Dynamic response of platform-riser coupling system with hydro-pneumatic tensioner," *Ocean Eng.*, vol. 166, no. May, pp. 172–181, 2018.
- [11] J. Hill, S. Laycock, S. Chai, C. Balash, and H. Morand, "Hydrodynamic loads and response of a Mid Water Arch structure," *Ocean Eng.*, vol. 83, pp. 76–86, 2014.
- [12] M. López, F. Taveira-Pinto, and P. Rosa-Santos, "Numerical modelling of the CECO wave energy converter," *Renew. Energy*, vol. 113, pp. 202–210, Dec. 2017.
- [13] X. Chen, Y. Miao, X. Tang, and J. Liu, "Numerical and experimental analysis of a moored pontoon under regular wave in water of finite depth," vol. 5302, no. June, 2016.
- [14] G. Green, "An Essay on the Application of Mathematical Analysis to the Theories of Electricity and Magnetism," *Proc. Cambridge Philos. Soc.*, vol. 7, 2008.
- [15] D. T. Sen and T. C. Vinh, "Determination of Added Mass and Inertia Moment of Marine Ships Moving in 6 Degrees of Freedom," *Int. J. Transp. Eng. Technol.*, vol. 2, no. 1, pp. 8–14, 2016.
- [16] O. Faltinsen, *Sea loads on ships and offshore structures*, vol. 1. Cambridge

university press, 1993.

- [17] M. López, G. Iglesias, and N. Kobayashi, “Long period oscillations and tidal level in the Port of Ferrol,” *Appl. Ocean Res.*, vol. 38, pp. 126–134, 2012.

# MOTION AND DYNAMIC RESPONSE APPROACH FOR FLOATING PHOTOVOLTAIC STRUCTURES UNDER MARINE LOADS

R. Claus<sup>†,\*</sup>, M. López<sup>†</sup>, Z. A. Hernández<sup>†</sup>, O. Simancas<sup>‡</sup>

<sup>†</sup> Dpto. de Construcción e Ing. de Fabricación, Escuela Politécnica de Mieres,  
Universidad de Oviedo  
33600 Mieres, Spain

\*e-mail: clausruben@uniovi.es  
ORCID: 0000-0002-7547-883X

<sup>‡</sup> ASTURMADI RENEERGY S.L.  
Avilés, Asturias, Spain

**Abstract.** Floating photovoltaic (FPV) systems raise as a promising alternative to ground mounted. Nonetheless, due to the absence of a standardized calculation procedure for this technology, the industry has focussed on simple designs for continental sheltered waters. In this work, a verification procedure for marine FPV structures is proposed and applied to a novel concept that consists of a top-of-pole solar panel mount attached to a tension leg platform (TLP). The procedure comprises the definition of test cases, the dynamic response analysis of the floating structure and the verification of its main components. Key guidelines regarding the design of similar structures, as well as future research lines are presented.

**Key words:** FPV, rigid body dynamics, numerical simulation, marine structures, Aqwa, TLP.

## 1 INTRODUCTION

Floating photovoltaic (FPV) systems have been installed on freshwater bodies over the last decade with a growing rate of 133 % [1]. This growth was possible due to the advantages that FPVs pose over ground-mounted photovoltaic systems. These have been analysed by many authors [2]–[4]. Some of them are:

- the cooling effect of the water [5],
- water availability for cleaning [6],
- absence of shadowing effects due to the presence of obstacles [7],
- evaporation prevention [8],
- algae reduction [9]
- synergies with hydropower plants [10].

The main components of a FPV system are the photovoltaic (PV) modules, the floating system, the supporting structure, the mooring system, and the anchoring (Figure 1).

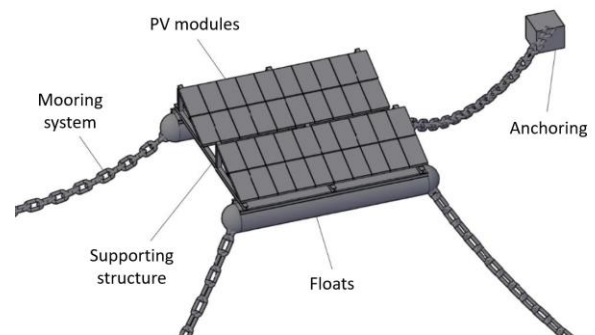


**Figure 1:** Main components of a generic FPV system.

There are different designs when it comes to FPV structures. A classification based on materials, floatation systems, configuration and moorings was proposed by [11]. A classification based on the most deployed designs, from a structural point of view, was done by [12]. However, despite the large number of proposed concepts, the FPV industry has committed to the simplest designs

and the safest locations. The vast majority of FPV projects are cheap, simple solutions deployed in freshwater bodies [13]. The risk associated with these projects is still high and the lack of standards, as well as the maturity of the technique, hinder the expansion of this technology. This is specially the case when environmental actions gain relevance, since they compromise the structural reliability of FPVs. The offshore environment represents a vast untapped source of renewable energy [14], but to make it fully accessible for the FPV technology, further research is needed. Some marine FPV projects were recently launched with that objective [15]–[17], but the fully commercial deployment of these designs is yet to be developed.

Very few publications regard the structural analysis of FPVs. Some authors have applied analytic static approaches to analyse these structures [18], [19]. However, this approach ignores the dynamic response of the structure as well as non-linear behaviours. Other authors have applied a complex fluid-structure interaction approach to analyse FPV structures [20]. This approach considers the dynamic response of the structure but is computationally very expensive and unsuitable for a comprehensive analysis. Some authors have applied the finite element method (FEM) to these structures [21], but have greatly simplified the environmental loading on the structure. To properly address the analysis of a FPV structure, the implemented approach must be both sufficiently realistic and computationally reasonable. A rigid body dynamics analysis meets both requirements.

The purpose of this work is to present a structural verification procedure for FPV systems and to implement it to a novel concept designed to harvest solar energy in semi-sheltered coastal waters. The dynamic response analysis of the structure is carried out for generic environmental conditions of waves, wind, and water levels.

The remainder of this paper is structured as follows: Section 2 details the calculation procedure, describes the analysed device and discloses the environmental conditions considered. Section 3 presents and discusses the main outputs of the implementation of this procedure, namely the motions and loads on the structure and the structural verification of its main components. Finally, key conclusions of this work are summarized in Section 4 and some future research lines are presented.

## 2 MATERIALS AND METHODS

### 2.1 Proposed procedure

In this work, a procedure to assess the environmental and site conditions for the design of FPV systems is presented. This method is suitable to evaluate the main environmental actions (namely wind, waves, and tides) and their effects on these floating structures. There are four general approaches regarding the estimation of marine environmental loads:

- the static/quasi-static approach [18],
- the rigid body dynamics approach, solved through the Boundary Element Method (BEM) [22],
- the hydroelastic approach [23],
- the Computational Fluid Dynamics approach (CFD) [24].

Due to the stochastic nature of the environmental actions and the complex interactions between the water, the floating structure, and the mooring system, FPVs are structures with a significant dynamic response. This discards static and quasi-static approaches or at least it limits them to preliminary analysis. Most FPV structures can be properly modelled by connected rigid bodies. Unless structural deformation was a paramount feature of the analysed FPV design, hydroelastic approaches can also be discarded due to computational costs. CFD techniques are only suitable if viscous flow separation,

wave breaking, and wave overtopping are relevant phenomena since they would otherwise be unreasonably expensive. Since these non-linear phenomena are comparatively not relevant, this procedure will be based on rigid body dynamics.

The proposed calculation and optimization procedure goes as follows. First, the geometry is modelled by means of either diffracting elements or Morison elements, depending on the relative size of the bodies. Then, a fluid-structure interaction analysis is undertaken. If the model has diffracting elements, a frequency domain dynamic analysis followed by a time domain dynamic analysis is performed through the potential flow theory and the BEM. If the structure was modelled without any diffracting elements, the frequency domain analysis can be disregarded. In any case, movements, forces, and moments can be obtained in each time step of this analysis. Subsequently, structural verifications of the elements of the FPV can be performed through standard methods. Elements can be structurally optimized but note that, since this implies changes in the geometry, the complete analysis must be overtaken in an iterative process.

## 2.2 Description of the device

The described procedure has been applied to a novel design of marine FPV system intended for harnessing solar energy in semi-sheltered coastal waters, such as port basins, bays, and estuaries (Figure 2).

The concept is at an early development stage (TRL 1-2), requiring basic technology research. The proposed concept consists on attaching a top-of-pole solar panel mount to a tension leg platform (TLP). Given that large structure motions due to environmental loads can impact reliability as well as production, the structure has its vertical motions partially restrained with taut mooring lines.

The key and differentiating feature of this device is that the PV modules are installed at a height that prevents their undesired interaction with waves. Another interesting feature is the built-in double-axis tracking system that both maximizes the energy harvest and can be used as a defence mechanism against violent wind conditions. This design can be divided into two separate parts:

- a superstructure, consisting of all the structural members that hold the PV modules, and
- a substructure, a TLP consisting of a post, four legs and the mooring system.

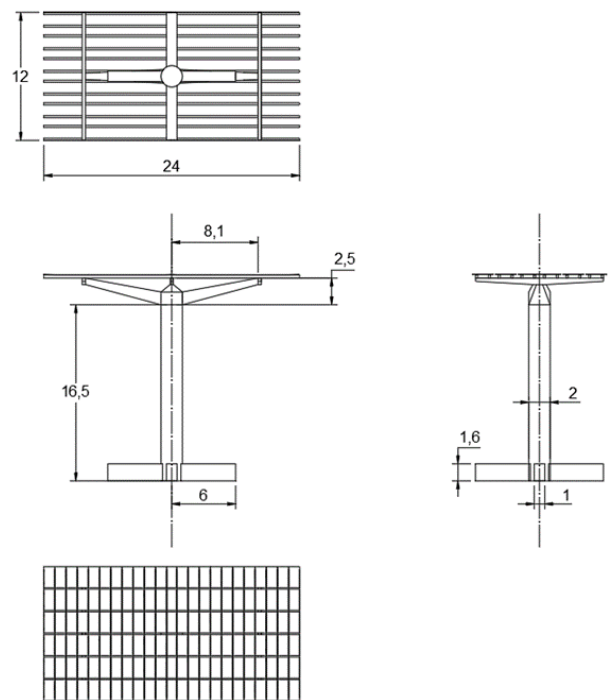


**Figure 2:** Schematics and main dimensions of the device (units in m).

The superstructure holds the PV modules and accommodates the tracking systems. It is based on a top-of-pole solar panel design. It consists of a V shaped element that holds the main beams, in which the secondary beams are laid out to support the PV modules. The vertical and horizontal trackers are installed

immediately below and above the V shaped element, respectively. This allows the rotation of the full superstructure around the vertical axis and the inclination of the array of PV modules. The design holds up to 138 typical industrial use panels ( $196 \times 99 \text{ cm}^2$ ) in 6 rows of 23 PV modules each. The total weight of the superstructure is 11.6 t, where 4.8 t corresponds to the V structure and the remaining 6.8 t to the beams and modules. The main material for the device was structural steel (properties in Table 1), but it is prone to be changed after the full optimization process.

Structural steel mechanical properties	
Density	7850 kg/m <sup>3</sup>
Young's module	210000 MPa
Poisson's ratio	0.30
Tensile strength	250 MPa
Tensile ultimate strength	460 MPa
Compressive strength	250 MPa

**Table 1:** Mechanical properties of the structural steel. Data extracted from the ANSYS engineering library.

The purpose of the substructure is to keep the superstructure afloat and safe. The substructure consists of a post and a TLP. The post is a 16.5 m long hollow cylinder made of structural steel. Its purpose is to maintain the panels at a safe height from the waterline, even during spring tide events. It has a 2 m diameter and a 1 cm thickness. The four legs are 6 m long hollow beams, also made of structural steel. They have a  $1 \times 1.6 \text{ m}^2$  rectangular cross section and a 1 cm thickness. The mooring lines are 23.5 m long vertical taut steel cables that connect each leg end to the seabed. They are made of AISI316 stainless steel, and their mechanical properties are summarized in Table 2. The weight of the substructure is 18.1 t, where 9.7 t corresponds to the legs, 8.1 t to the post and 0.3 to the mooring system.

The device has been tested for offshore conditions of wind and waves. The forces and moments acting on the structure were obtained

and used as input data for the subsequent structural verification. The main components of the substructure have been analysed, and some iterations of the optimization process were performed.

Stainless steel AISI316 mechanical properties	
Elastic modulus	130 GPa
Nominal diameter	26 mm
Weight	3.30 Kg/m
Section	399 mm <sup>2</sup>
Breaking load	533.66 kN
Maximum tension	1570 MPa

**Table 2:** Mechanical properties of the stainless steel AISI316 wire rope [25].

### 2.3 Modelling of the geometry

To adapt the real geometry to a hydrodynamic model, the whole structure must be divided into elements. Then, said elements must be simplified into 1D or 2D geometries. This comprises line bodies and surface bodies, that can also be 3D hollow objects. To properly model these elements, the Chakrabarti's [26], Morison's [27] or the DNV's [28] method may be used to determine the most suitable wave regimen for wave force estimation. The relationship between the wave height ( $H$ ), the wavelength ( $L$ ) and the characteristic dimension ( $D$ ) determine whether the element is in a diffracting, a Froude-Krilov or a Morison regime. Diffracting regimes ( $D/L > 0.2$ ) are dominated by diffraction and radiation forces and are typical for large structures with a small variation of their wet surface. Slender elements and small structures usually fall in a Morison regime ( $D/L < 0.1$ ), where inertia and drag forces are dominant. Intermediate elements could fall in a Froude-Krilov regime ( $0.1 > D/L > 0.2$ ), where neither diffraction forces nor the wet surface variation can be neglected.

Elements that will not interact with the water may be synthesized through their mass points, buoyancy points and aerodynamic

coefficients. The mass, inertial and aerodynamic properties can be therefore associated to an interacting structure to minimize computational costs.

In the analysed design, the post was modelled as a Morison slender element since its characteristic dimension was small with respect to the waves it interacted with. The legs were also modelled as Morison slender elements for the same reasons. Finally, since the superstructure does not interact with the waves, it was modelled through its aerodynamic coefficients and mass points. Aerodynamic coefficients were extracted from Eurocode 1 (wind force coefficient method).

## 2.4 Load estimation

The approach to analyse the fluid-structure interactions that define the load estimations is dependent on the nature of the modelled elements. If a structure has diffracting elements, a harmonic response analysis is performed, followed by a time domain dynamic analysis. If the whole structure was modelled using only Morison elements, the frequency domain analysis can be omitted. The frequency domain analysis provides interesting results, such as the natural frequencies of the structure and the response amplitude operators as well as the hydrodynamic coefficients for the subsequent time domain analysis. In the time domain analysis, loads on the structure are estimated for each time step of the simulation. In this case, the time response dynamic analysis is enough to properly assess the loading on the structure. The Aqwa Naut code was used to perform the analysis of this novel device.

The time domain analysis provides the forces and moments on the structure for each time step of the simulation. In this analysis, all connections and moorings are considered, and the wet surface is recalculated at each time step. This allows for the Morison and the

hydrostatic forces to be accurately computed in every time step. Specific wave, wind and current actions may be defined in this analysis through the definition of their magnitude and spatial and temporal distribution. Note that the wave theory to be used must also be defined at this point. The airy or linear theory is the most used in technical standards [29]. However, this theory is not usually the most suitable. An appropriate theory can be selected through the Le Méhauté abacus [30]. This method was applied to the studied case and the Second Order Stokes wave theory was found to be the most suitable approach.

The time dependent motions of a general floating structure are governed by the following function

$$\mathbf{M}\ddot{\mathbf{x}}(t) = \mathbf{f}_h(t) + \mathbf{f}_I(t) + \mathbf{f}_d(t) + \mathbf{f}_r(t) + \mathbf{f}_j(t) + \mathbf{f}_m(t) + \mathbf{f}_w(t) + \mathbf{f}_c(t), \quad (1)$$

where:  $\mathbf{M}$  is the mass matrix,  $\mathbf{x}(t)$  is the position of the structure,  $\mathbf{f}_h(t)$  is the non-linear hydrostatic force,  $\mathbf{f}_I(t)$  are the forces due to the incident waves,  $\mathbf{f}_d(t)$  are the diffraction forces,  $\mathbf{f}_r(t)$  are the radiation forces,  $\mathbf{f}_j(t)$  are the forces on joints,  $\mathbf{f}_m(t)$  are the forces on the structure due to the mooring system,  $\mathbf{f}_w(t)$  are wind induced forces and  $\mathbf{f}_c(t)$  are current induced forces.

However, since the analysed design is fully non-diffracting, the loading due to waves can be obtained through the semi-empirical Morison equation

$$\mathbf{F}_M = \rho V \dot{u} + \rho C_a V (\dot{u} - \dot{v}) + \frac{1}{2} \rho C_d A (u - v) |u - v|, \quad (2)$$

where:  $\rho$  is the fluid density,  $V$  is the volume of the body,  $u$  is the flow velocity,  $C_a$  is the added mass coefficient,  $v$  is the velocity of the moving body,  $C_d$  is the drag coefficient and  $A$  is the reference area (*e.g.* the cross-sectional area of the body perpendicular to the flow direction). The inertia coefficient, directly

related to the added mass coefficient, and the drag coefficient are estimated empirically and are influenced by several parameters, including the Reynolds number and the Keulegan-Carpenter number. In this case, standard values provided by [31] are used, but experimental analysis could be performed to obtain these parameters.

Once the acting forces on the structure have been defined, the dynamic response is solved through the integration of the time motion equation. This can be performed by means of a predictor-corrector algorithm. The first stage of this algorithm is to obtain the total forces acting on the structure at a given time step. Newton's second law is applied to obtain the accelerations, which are used to predict the velocity and position of the structure. The second stage recalculates the forces for the next time step based on these predictions, thus obtaining the accelerations. Then, the velocity and position are corrected using Taylor's theorem. The structure is moved to its new position and the algorithm reiterates.

## 2.5 Structural analysis

The outputs from the previous stage are the 6 degree of freedom (DOF) time-dependent rigid body motions of the structure and the forces and moments acting on it. The structural verification of the FPV may be performed for each time step of the simulations through analytic methods, such as the classic mechanics of materials approach or the FEM approach. The first approach may be applied through a spreadsheet or a programming code. The FEM approach is a numerical method for solving differential equations generated by theories of mechanics and can be used to assess complex geometries, dynamic responses, stability, and non-linear behaviour.

Regardless of the adopted approach, the results of this analysis can be used to perform a structural verification. These outputs are the

input for the optimization process, where the geometry is adapted to endure more efficiently the loads acting on it. Note that significant changes on the geometry will affect critical parameters such as buoyancy or wave exposure, modifying the hydrodynamic model. This means that the iterative process also encompasses the redefinition of the model and the rigid body dynamic analysis. Iterations are performed until a satisfactory design is achieved.

The post, legs, and moorings of the analysed device were structurally verified using the mechanical properties of these components. The classic mechanics of materials approach was applied, and the structural verification was performed through an *ad-hoc* Matlab code. This code applied the Euler-Bernoulli beam theory, as well as the formulation provided by the Eurocode 3 to the components of interest. These were structurally verified for each time step of each of the performed simulations.

## 2.6 Test cases

The device was tested for 108 test cases with a 100 s duration and a 0.01 s time-step. This duration allowed the stabilization of the dynamic response, so results could be retrieved once the motion was harmonic. These test cases resulted from combining the following parameters (summarized in Table 3):

- Horizontal tracker ( $\alpha$ ): The device was tested for 3 positions of the horizontal tracker ( $0^\circ$ ,  $20^\circ$  and  $40^\circ$ ). Each position implied a different set of aerodynamic coefficients.
- Leg position ( $\beta$ ): The device was tested for 2 leg positions (Figure 3): aligned with the main and secondary beams ( $0^\circ$ ) and oblique to them ( $45^\circ$ ).
- Water depth ( $d$ ): To replicate the effect of tides, two different water depths were studied: 35 and 30 m (Figure 4).
- Wind speed ( $U$ ): The device was tested

for constant wind speeds of: 30, 15, 10 and 0 m/s. Each one corresponds to the maximum wind speed that the system should endure for each position of the horizontal tracker.

- Wind direction ( $\theta$ ): The device was tested for the 2 wind directions with greater wind force coefficients (Figure 3). These are  $\theta = 0^\circ$  and  $\theta = 180^\circ$ .
- Wave height ( $H$ ): The device was tested for regular waves with a 2 m wave height and for no waves at all.
- Wave period ( $T$ ): The wave period associated to the waves with a 2 m wave height was 7 s.
- Wave direction ( $\delta$ ): The device was tested for 4 wave directions. The wave front could be aligned with the wind front or perpendicular to it.

Parameter	Test values	Units
Horizontal tracker ( $\alpha$ )	0, 20, 40	deg
Leg position ( $\beta$ )	0, 45	deg
Water depth ( $d$ )	30, 35	m
Wind speed ( $U$ )	0, 10, 15, 30	m/s
Wind direction ( $\theta$ )	0, 180	deg
Wave height ( $H$ )	0, 2	m
Wave period ( $T$ )	7	s
Wave direction ( $\delta$ )	0, 90, 180	deg

**Table 3:** Values of the parameters for the simulations.

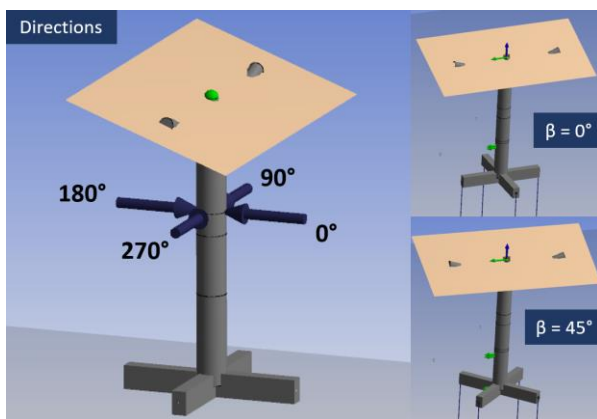


**Figure 3:** Wind/wave directions (left) and positions of the vertical tracker (right), on the hydrodynamic model.

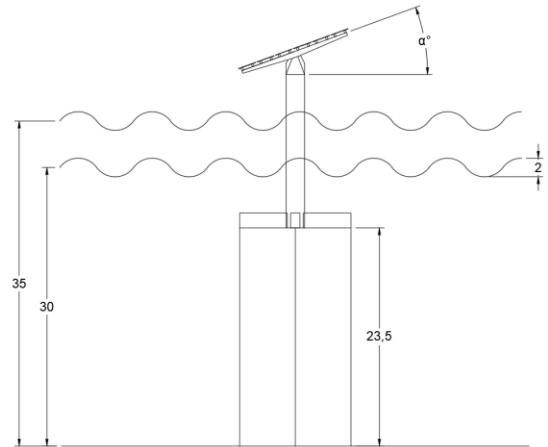


**Figure 4:** Mooring lines, water depths ( $d$ ), wave height ( $H$ ) and position of the horizontal tracker ( $\alpha$ ).

### 3 RESULTS AND DISCUSSION

The main outcomes of the implementation of the proposed procedure to the TLP device are the 6-DOF rigid body motions, the loads on the structure and the structural verification of its main components, namely the post, legs and mooring system. These values were retrieved once the motions of the device were stationary.

#### 3.1 Motions of the floating structure

The motions of the device were registered for all test cases. As an example, Figure 5 shows the motions of the device for a certain test case. In this case, wind forces are responsible for surge motions and waves forces are responsible for sway motions. Heave motions are proportional to the horizontal displacements but are overall restrained. In the first instants of the simulation, the surge motion peaks, inducing a maximum value for the heave value as well. Surge stabilizes to a constant value while sway oscillates harmonically, due to the nature of the forces responsible for these motions. As for rotational motions, yaw is clearly the most relevant. It peaks in the first instances of the test due to an insufficient ramping process but stabilizes into a harmonic oscillation. This motion is governed by the forces acting on the device and the restoring moment of the mooring system.

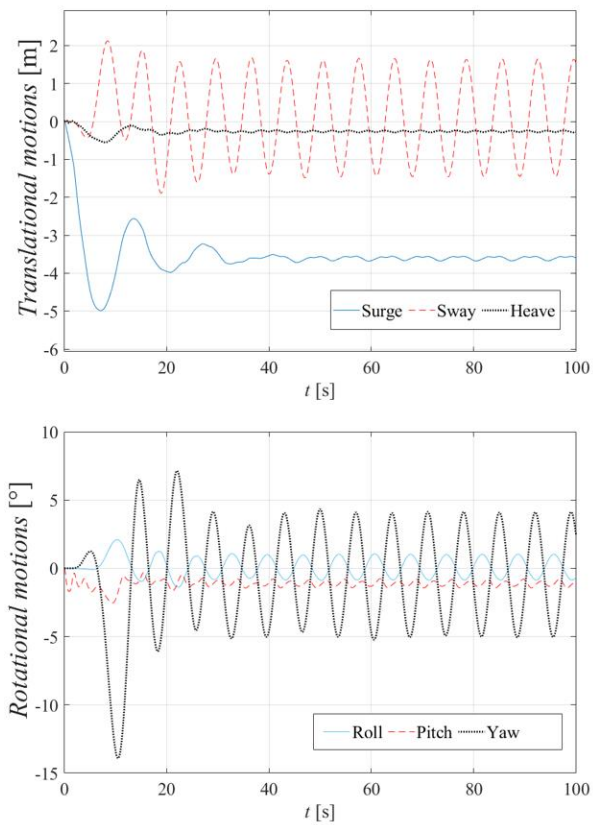


**Figure 5:** Motions for  $\alpha = 20^\circ$ ,  $\beta = 0^\circ$ ,  $d = 30$  m,  $U = 15$  m/s,  $\theta = 180^\circ$ ,  $H = 2$  m,  $T = 7$  s, and  $\delta = 90^\circ$ .

The maximum 6-DOF motion amplitudes of the device, as well as the test case that led to them, are presented in Table 4. Some conclusions may be drawn from these results. The maximum surge motion was registered with the horizontal tracker tilted at the most

exposed position ( $45^\circ$ ), even though the wind speed was inferior to the defined for any other inclinations. This 5.8 m value was registered for  $\theta = 180^\circ$ , due to the higher aerodynamic coefficients of the structure for this wind direction. The maximum surge motion also required the evaluated actions to be aligned, although wind is still responsible for the main component of this motion. An interesting conclusion is that the maximum surge was registered for a low water depth. This is because the TLP resists surge and sway motions through overbuoyancy, and low tides diminish the buoyancy of the floating structure. The maximum sway motion was comparatively smaller due to the reduced wind exposure, reaching a value of 1.7 m. The main contribution to this displacement were the wave loads. Again, a low tide scenario was required, for the same reasons. Note that the position of both trackers as well as the influence of the wind loads was of little relevance since all cases with the same wave direction and water depth showed similar maximum sway values. As for heave, the maximum value was registered for the exact same scenario that led to the maximum surge, where it sank 0.7 m with respect to its equilibrium position. This is due to the very nature of the TLP. To move the structure away without stretching the mooring lines implies to slightly sink the structure.

Motion	Value	Test conditions						
		$\alpha$	$\beta$	$d$	$U$	$\theta$	$H$	$\delta$
Surge	5.8 m	$40^\circ$	$45^\circ$	30 m	10 m/s	$180^\circ$	2 m	$180^\circ$
Sway	1.7 m	$20^\circ$	$45^\circ$	30 m	15 m/s	$180^\circ$	2 m	$90^\circ$
Heave	-0.7 m	$40^\circ$	$45^\circ$	30 m	10 m/s	$180^\circ$	2 m	$180^\circ$
Roll	$1.4^\circ$	$20^\circ$	$45^\circ$	35 m	15 m/s	$180^\circ$	2 m	$90^\circ$
Pitch	$7.8^\circ$	$40^\circ$	$0^\circ$	30 m	10 m/s	$180^\circ$	2 m	$180^\circ$
Yaw	$12.5^\circ$	$20^\circ$	$0^\circ$	35 m	15 m/s	$180^\circ$	2 m	$90^\circ$

**Table 4:** Maximum motion amplitudes of the device.

However, the heave motions are heavily restricted, as expected in a TLP design. An interesting aspect regarding the position of the legs is that it barely has any influence on the maximum displacements of the floating structure. This is beneficial since it provides alternative positions without compromising the station-keeping function of this design.

As for the rotational motions, roll is irrelevant when compared to pitch. The maximum pitch reached a value of  $7.8^\circ$ . Higher values could compromise the stability of this system, and this aspect should be carefully studied in the optimization process. Wind forces are the main reason for this phenomenon and that is why the most limiting test conditions are similar to those responsible for the maximum surge. Limiting wind exposure can significantly reduce the maximum pitch. The position of the legs also plays a significant role on this motion, since the alternative position yielded a smaller result. The low tide scenario was also required to reach the maximum pitch value, since it greatly reduces stability.

Yaw motions are barely relevant for most test cases, but they reached an unusually high value for a particular combination of wind and wave directions. This value is not dependent on the position of the tracking systems, but it did require a high tide scenario. These yaw

motions could affect productivity, but they hardly reduce structural safety. Since their occurrence is very circumstantial, they are not considered a mayor issue. If they were, they could be limited by designing longer legs.

### 3.2 Loads and structural verification

The structural verification of the main components, as well as the test cases that led to them, are presented in Table 5.

The maximum tension on the post (75 MPa) was achieved due to the combination of axial and flexural tension. This tension increases from the upper cross-sections to the lower ones. This maximum tension was registered for the position of the horizontal tracker that resulted in the maximum wind exposure. The wind direction that implied the highest force coefficient was also required. Wind loads are the main contribution for these maximum tensions. A low tide scenario was also required for these values since this contributes to a higher bending moment. Although the wave loads alone did not procure high tensions, the alignment of wave and wind loads resulted on tensions 50 % greater than those generated by the wind loads alone. The position of the legs had a smaller influence, being the  $45^\circ$  position slightly more restrictive. The shear and torsion forces on the post are negligible.

Component	Verification	Maximum value	Safety factor	Test conditions						
				$\alpha$	$\beta$	$d$	$U$	$\theta$	$H$	$\delta$
Post	Flexion - axial (tension)	75 MPa	3.3	$40^\circ$	$45^\circ$	30 m	10 m/s	$180^\circ$	2 m	$180^\circ$
Post	Shear - torsion (force)	119 kN	48.4	$40^\circ$	$45^\circ$	30 m	10 m/s	$180^\circ$	2 m	$180^\circ$
Leg	Flexion - axial (tension)	65 MPa	3.9	$40^\circ$	$0^\circ$	35 m	10 m/s	$180^\circ$	2 m	$180^\circ$
Leg	Shear - torsion (force)	219 kN	21.1	$40^\circ$	$0^\circ$	35 m	10 m/s	$180^\circ$	2 m	$180^\circ$
Moorings	Maximum load (force)	322 kN	1.7	$40^\circ$	$0^\circ$	30 m	10 m/s	$180^\circ$	2 m	$180^\circ$

**Table 5:** Structural verification of the main components of the device.

The maximum tension on the legs was also achieved due to the combination of axial and flexural tensions. These values were higher near the joint that connected the legs with the post. The leg position was very relevant in this analysis since the highest tensions (65 MPa) were registered when the legs were aligned with the wind and wave actions ( $0^\circ$  position). Again, the alignment of wind and wave loads was required even if wind loads were the main contribution to this tension. Wind and wave directions were therefore the same as the ones responsible for the higher tension values in the post. However, the water level had a reduced relevance. Again, the shear and torsion forces on the legs are comparatively negligible.

The mooring system endured the loads with a safety factor of 1.7. Before running this analysis, the overbuoyancy of the structure was assumed to be the main issue concerning the mooring system. This overbuoyancy was to be countered by the mooring lines alone and it greatly increased with high tides events. However, the highest cable loading (322 kN) was registered during a low water level test case. The fact that the mooring lines need to endure higher loads in the high tide scenarios holds true under no external actions. However, with wind and wave forces acting on the structure, the excess of buoyancy can aid the mooring system by limiting horizontal motions. This contribution overcomes the additional tension transmitted to the mooring lines due to overbuoyancy. This happens because, in this case, environmental forces are more impactful on the mooring system than overbuoyancy. The maximum values of the mooring line loading were registered under the same conditions that yielded the maximum tension values on the post. The  $0^\circ$  legs position registered higher values due to its alignment with wind and wave loads.

#### 4 CONCLUSIONS

On account of the lack of publications that address the structural verification of FPV systems, a procedure based on rigid body dynamics was presented and applied to a novel FPV technology. The motions, moments and forces acting on the structure were obtained for a total of 108 different combinations of environmental and site conditions. These outcomes were used to structurally verify the main components of this device. The main conclusions of this work are summarized:

- The procedure was fully applicable to the device, allowing the analysis of its dynamic response.
- The device structurally withstood all the test cases.
- The maximum motions of the structure did not compromise its stability.
- Wind induced forces were dominant over wave induced forces, given the geometry of the device.
- The overbuoyancy of this design does not compromise the mooring system. In fact, the additional stability prevents excessive loading.
- The position of the legs hardly affects the structural response of the device.

Future research lines are presented., both for the applied procedure and the analysed device:

- This approach could be applied to other FPV technologies to prove its feasibility.
- Given the lack of specific standards, a full methodology for the structural analysis and optimization of FPV structures could be proposed.
- This device should be structurally optimized in its further development.
- This research could benefit from experimental analysis to validate the numerical models.

## ACKNOWLEDGEMENTS

This research was funded by the Ports Towards Energy Self-Sufficiency (PORTOS) project, co-financed by the Interreg Atlantic Area Programme through the European Regional Development Fund, grant number EAPA\_784/2018.

## REFERENCES

- [1] M. Rosa-Clot and G. M. Tina, "Current Status of FPV and Trends," in *Floating PV Plants*, Academic Press, 2020, pp. 9–18.
- [2] P. Ranjbaran, H. Yousefi, G. B. Gharehpetian, and F. R. Astarai, "A review on floating photovoltaic (FPV) power generation units," *Renew. Sustain. Energy Rev.*, vol. 110, no. May, pp. 332–347, 2019.
- [3] P. S. Sujay, W. M. M., and S. N. N., "A Review on Floating Solar Photovoltaic Power Plants," *Int. J. Sci. Eng. Res.*, vol. 8, no. 6, pp. 789–794, 2017.
- [4] V. Kumar, R. L. Shrivastava, and S. P. Untawale, "Solar Energy: Review of Potential Green & Clean Energy for Coastal and Offshore Applications," *Aquat. Procedia*, vol. 4, no. Icwrcoc, pp. 473–480, 2015.
- [5] W. C. L. Kamuyu, J. R. Lim, C. S. Won, and H. K. Ahn, "Prediction model of photovoltaic module temperature for power performance of floating PVs," *Energies*, vol. 11, no. 2, 2018.
- [6] R. Cazzaniga, M. Rosa-Clot, P. Rosa-Clot, and G. M. Tina, "Floating tracking cooling concentrating (FTCC) systems," *Conf. Rec. IEEE Photovolt. Spec. Conf.*, pp. 514–519, 2012.
- [7] A. Goswami, P. Sadhu, U. Goswami, and P. K. Sadhu, "Floating solar power plant for sustainable development: A techno-economic analysis," *Environ. Prog. Sustain. Energy*, 2019.
- [8] M. Redón Santafé, J. B. Torregrosa Soler, F. J. Sánchez Romero, P. S. Ferrer Gisbert, J. J. Ferrán Gozávez, and C. M. Ferrer Gisbert, "Theoretical and experimental analysis of a floating photovoltaic cover for water irrigation reservoirs," *Energy*, vol. 67, pp. 246–255, 2014.
- [9] M. Z. B. Alam and S. Ohgaki, "Evaluation of UV-radiation and its residual effect for algal growth control," in *Advances in water and wastewater treatment technology*, Elsevier, 2001, pp. 109–117.
- [10] J. Farfan and C. Breyer, "Combining floating solar photovoltaic power plants and hydropower reservoirs: A virtual battery of great global potential," *Energy Procedia*, vol. 155, pp. 403–411, 2018.
- [11] D. Friel, M. Karimirad, T. Whittaker, W. J. Doran, and E. Howlin, "A review of floating photovoltaic design concepts and installed variations," *4th Int. Conf. Offshore Renew. Energy CORE 2019*, pp. 1–10, 2019.
- [12] R. Cazzaniga, "Chapter 4 - Floating PV Structures," in *Floating PV Plants*, M. Rosa-Clot and G. Marco Tina, Eds. Academic Press, 2020, pp. 33–45.
- [13] World Bank Group, ESMAP, and SERIS, "Where Sun Meets Water: Floating Solar Handbook for Practitioners." 2019.
- [14] S. Oliveira-Pinto and J. Stokkermans, "Marine floating solar plants: An overview of potential, challenges and feasibility," *Proc. Inst. Civ. Eng. Marit. Eng.*, vol. 173, no. 4, pp. 120–135, 2020.
- [15] Oceans of Energy, "Offshore floating solar farm installed and operational at the Dutch North Sea System survived several storms, including the 'Ciara'

- storm (February 2020),” *Oceans of Energy*, 2020. [Online]. Available: <https://oceansofenergy.blue/north-sea-1-offshore-solar-project/>. [Accessed: 07-May-2020].
- [16] D. Snieckus, “Offshore oil industry giants Equinor and Saipem tie up for floating solar,” *RECHARGE*, 2020. [Online]. Available: <https://www.rechargenews.com/transiti on/offshore-oil-industry-giants-equinor-and-saipem-tie-up-for-floating-solar/2-1-778151>. [Accessed: 25-May-2020].
- [17] Ocean Sun, “A unique solution to floating solar.” [Online]. Available: <https://oceansun.no/>. [Accessed: 22-Feb-2021].
- [18] M. Ikhennicheu, B. Danglade, R. Pascal, V. Arramounet, Q. Trébaol, and F. Gorintin, “Analytical method for loads determination on floating solar farms in three typical environments,” *Sol. Energy*, 2021.
- [19] A. M. Al-Yacoub, E. R. B. A. Halim, and M. S. Liew, “Hydrodynamic Analysis of Floating Offshore Solar Farms Subjected to Regular Waves,” in *Advances in Manufacturing Engineering*, Springer, 2020, pp. 375–390.
- [20] Y. G. Lee, H. J. Joo, and S. J. Yoon, “Design and installation of floating type photovoltaic energy generation system using FRP members,” *Sol. Energy*, vol. 108, pp. 13–27, 2014.
- [21] S. H. Kim, S. C. Baek, K. B. Choi, and S. J. Park, “Design and installation of 500-kW floating photovoltaic structures using high-durability steel,” *Energies*, vol. 13, no. 18, 2020.
- [22] M. López, F. Taveira-Pinto, and P. Rosa-Santos, “Numerical modelling of the CECO wave energy converter,” *Renew. Energy*, vol. 113, pp. 202–210, 2017.
- [23] W. G. Price and W. Yousheng, “Hydroelasticity of marine structures,” in *Theoretical and applied mechanics*, Elsevier, 1985, pp. 311–337.
- [24] A. Elhanafi, G. Macfarlane, and D. Ning, “Hydrodynamic performance of single--chamber and dual--chamber offshore--stationary Oscillating Water Column devices using CFD,” *Appl. Energy*, vol. 228, pp. 82–96, 2018.
- [25] Cables Estructurales, “Catalogs.” [Online]. Available: <https://www.cablesestructurales.com/latinoamerica-catalogos/>. [Accessed: 03-Apr-2021].
- [26] S. K. Chakrabarti, *Hydrodynamics of offshore structures*. WIT press, 1987.
- [27] J. R. Morison, J. W. Johnson, S. A. Schaaf, and others, “The force exerted by surface waves on piles,” *J. Pet. Technol.*, vol. 2, no. 05, pp. 149–154, 1950.
- [28] G. L. DNV, “DNV-OS-J101--Design of offshore wind turbine structures,” *DNV GL Oslo, Norw.*, 2014.
- [29] M. Dolores Esteban, J.-S. López-Gutiérrez, V. Negro, C. Matutano, F. M. García-Flores, and M. Á. Millán, “Offshore wind foundation design: some key issues,” *J. Energy Resour. Technol.*, vol. 137, no. 5, 2015.
- [30] B. Le Méhauté, *An introduction to hydrodynamics and water waves*. Springer Science & Business Media, 2013.
- [31] ANSYS, “Aqwa Theory Manual,” *Ansys*, no. November. 2015.



## COMPOSITE FLOOR BEAMS WITH CONSTRAINED LAYER DAMPING: EXPERIMENTAL TESTS ON REDUCED SCALE MODELS

Carlos M. C. Renedo\*, Wilson P. Ortega\*, Iván M. Díaz\* and Jaime H. G. Palacios†

\* Department of Continuous Mechanics and Theory of Structures. ETSI Caminos, Canales y Puertos  
Universidad Politécnica de Madrid  
28040 Madrid, Spain  
e-mail : carlos.martindelaconcha@upm.es  
ORCID : 0000-0003-1014-0878

† Department of Hydraulics, Energy and Environmental Engineering. ETSI Caminos, Canales y Puertos  
Universidad Politécnica de Madrid  
28040 Madrid, Spain

**Abstract.** Vibration Serviceability Limit State due to human-induced vibrations is an important requirement that increasingly influences the sizing of current long-span floors. Usually, structural designers tend to overcome this issue by stiffening the floor to avoid any low-frequency response in resonance with human footfalls. An alternative solution to this one consist of increasing the floor's damping to enhance its dynamic performance.

This paper experimentally studies the effectiveness of a Constrained Layer Damping (CLD) treatment applied along the whole length of a typical composite floor beam. The aim of the paper is to quantify the additional damping ratio provided by this damping technique. To reduce the economical and time effort involved in a Full-scale experimental campaign, two reduced-scale models (RSMs) were developed with and without any CLD treatment. Those models were designed to exhibit the same amount of extra damping ratio when treated with the same CLD configuration to be used in Full-scale specimens. Once the RSMs were designed and built, free-response tests were performed to derive their natural frequencies and the relation between their damping ratio and the vibration amplitude.

**Key words:** Constrained Layer Damping, Floor vibration, Viscoelastic materials, Experimentation, Composite structures.

### 1 INTRODUCTION

Nowadays, architectural trends in office buildings demand open-plan spaces that minimize the presence of non-structural elements (avoiding vertical partitions, heavy furniture, paper cabinets, etc.) [1]. In this context, steel-concrete composite floor systems have become a common structural solution for these spaces. The use of stronger steel beams reduces the floor's weight and increases its strength, which enables it to be a competitive solution especially for long spans

between 8 and 15 m [2]. Typically, the structural design of floor structures has been governed by the Deformation Serviceability Limit State, however, since these modern and long-span floors became a widespread solution, their dynamic performance begun to worry structural designers [3].

As a result of all mentioned, current open-plan office floors have less self-weight, less dead loads, and less inherent damping, and therefore, their performance against dynamic

loads (such as those induced by humans at walking) has deteriorated. Modern floors are “livelier” than in the past. Furthermore, the tolerance vibration levels related to offices are quite restrictive (around  $0.04 \text{ m/s}^2$ ), as they are classified as calm spaces. All this has led to consider the Vibration Serviceability Limit State (VSLS) as an important requirement that these floors must fulfil to be functional [4].

Most of the guidelines focused on assessing the VSLS of floors [4],[5],[6] usually classify them into two types according to their fundamental natural frequency: low frequency floors (LFFs) and high-frequency floors (HFFs) by setting the limit at 10 Hz. This approach is based on floors’ dynamic response to human-induced vibration. LFF tend to develop remarkable resonant responses with higher harmonics of the human load (between 5 and 8 Hz), whereas HFF responses are predominantly non-resonant presenting a peak in the transient regime. Currently, many long-span composite floors tend to be LFF and thus, VSLS check is even more crucial at the design stage [7].

When facing the design of a “lively” LFF, structural engineers usually tend to overcome the VSLS through enlarging the steel members, and thus, increasing the system stiffness until the dynamic response predicted by a footfall analysis is below the required tolerance limit [8]. This implies to oversize the floor in terms of strength, decreasing a lot its section utilization. This approach is not beneficial in terms of  $\text{CO}_2$  credentials, even less so when considering that floors may represent up to the 30% of the embodied carbon footprint of a steel framed building [9].

The dynamic performance of a LFF may

also be considerably improved through increasing its damping, as this parameter is inversely proportional to the steady-state response of the system. There are different technologies that can be implemented for that, such as for example inertial dampers [10] (commonly known as Tuned Mass Dampers or TMDs), viscous dampers or active solutions that mitigate the vibration in real time [11]. In addition to these, in 2006 ARUP came up with a new damping solution called “Resotec” that integrated Constrained Layer Damping (CLD) into composite floors. This system is based on the use of a thin layer of high-damping viscoelastic (VE) material (around 1 mm thick) comprised between two thin steel sheets. This 3-layer element is integrated between the concrete slab and the steel member of a composite beam for a certain proportion of its length near the support. Along this portion, the steel beam and the concrete slab are disconnected to shear as depicted in Figure 1. When the floor vibrates in a bending mode, the slab slips with respect to the steel beam and the intermediate VE layer develops a shear hysteretic behaviour in which mechanical energy is dissipated [12].

Willford et al. provided the description, a brief analysis and a full-scale experimentation of “Resotec” for a composite beam specimen of 12 m span. They reported a 2% damping ratio increase for a “Resotec” application along the 50% of the specimen length (50%-CLD). The authors consider that despite the results obtained by Willford et al. are encouraging, the research community has not focused enough attention on this topic. As a consequence, the results provided in [12] are considered to be limited and insufficiently contrasted.

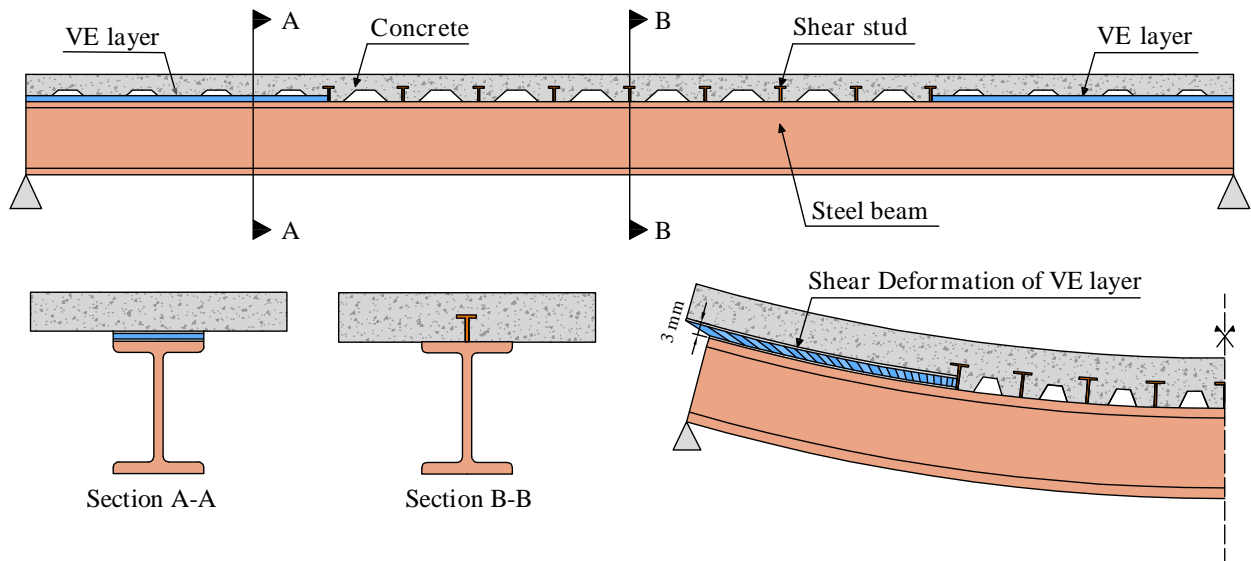


**Figure 1** CLD treatment integrated into a composite floor beam for 50 % of its length.

This paper is focused on the development of experimental tests to validate the use of CLD systems in LFFs. Since the construction of a full-scale long-span composite floor prototype is costly and difficult, reduced scale models have been developed by means of scaling laws. The study is based on two reduced-scale composite specimens of 3,60 m long. The first one called 0%-CLD does not incorporate any damping treatment, so the concrete slab and the steel beam are connected by means of studs. The second one called 100%-CLD incorporates CLD treatment along its entire length.

The remainder of this paper is organized as follows: In Section 2 the mechanical behaviour of a VE material is described. Section 3 explains the different techniques to increase the damping through integrating VE materials within a structural matrix. Section 4 exposes the development of the reduced scales models employed in the paper. Section 5 describes the experimental test performed and Section 6 provides the results obtained. Finally, Section 7 outlines some conclusions.

## 2 MECHANICAL PROPERTIES OF VE MATERIALS

The mechanical properties of VE materials are time-dependent. These properties are mainly characterized by two rheological phenomena: relaxation and creep [13]. Indeed, this fact enables to analyze the VE mechanical behavior in the frequency domain thanks to the Fourier transform. This means to study the response of a VE material to harmonic excitations (such as a cyclic stress or a harmonic imposed strain). This approach results in a stress-strain relation defined by a Frequency Response Function (FRF) in the  $j\omega$  domain. When performing this study for shear stresses and strains this FRF is defined as follows:

$$\frac{\tau(j\omega)}{\gamma(j\omega)} = G^*(j\omega) = G'(\omega)(1 + j\eta(\omega)) \quad (1)$$

$$G^*(j\omega) = G'(\omega) + jG''(\omega) \quad (2)$$

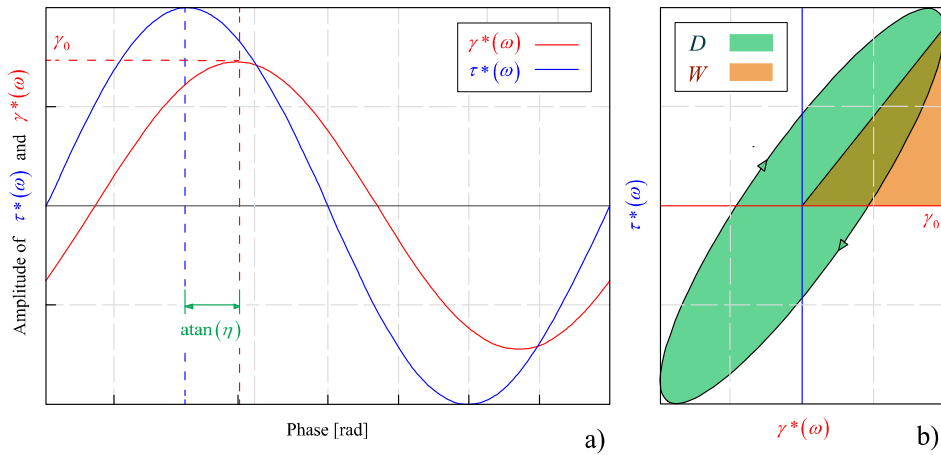


**Figure 2** Shear stress and shear strain relation for a certain frequency

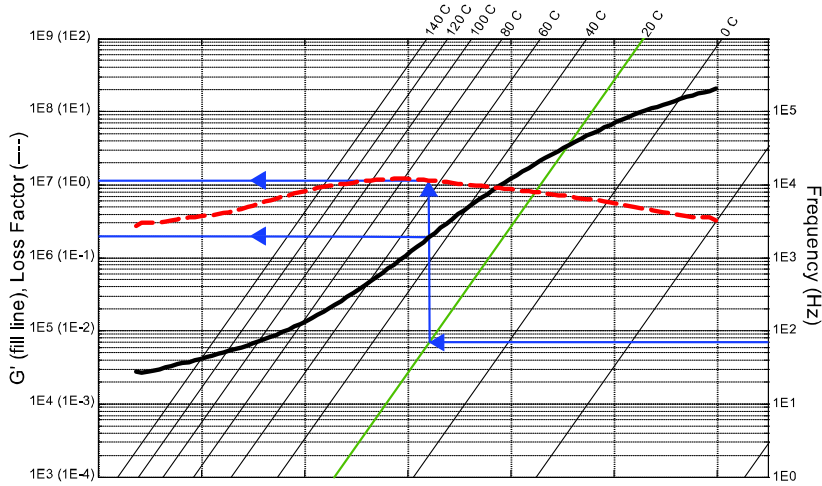


**Figure 3** Nomogram of HIP2, the VE material used for the experimental tests presented in the paper [15].

where  $G^*(j\omega)$  corresponds to the complex FRF usually called complex shear modulus.  $G'(\omega)$  is its real part referred as the ‘storage modulus’ due to it represents the elastic component of the VE behavior.  $G''(\omega)$  is the so called ‘dissipation modulus’ as it plays the role of the viscous component. Additionally,  $\eta(\omega)$  represents the phase of this FRF and it is named ‘loss factor’. The higher the phase between strain and stress the higher the energy dissipated per vibration cycle as depicted in Figure 2. The amplitude or gain of this FRF may be computed as follows:

$$|G^*(\omega)| = \sqrt{(G'(\omega))^2 + (G''(\omega))^2} \quad (3)$$

Additionally, VE mechanical behavior is also influenced by temperature. In fact, an analogy can be established between temperature and frequency dependent properties, the so called ‘Time-Temperature equivalence’. This enables to sum up the mechanical properties of a certain VE material in a single abacus called ‘Nomogram’ [14]. Figure 3 depicts the correct way of reading a Nomogram for a given temperature and frequency, the provided is from the HIP2 from (Heathcote

Industrial Plastics) material used in this paper [15].

### DAMPING INCREASE WITH LAYERS OF VE MATERIAL

VE materials have been mainly used in aircraft and mechanical engineering to mitigate undesired vibrations. Their use was then extended to civil engineering in the form of the well-known VE dampers. These devices concentrated their action into a single structural point, where the VE material was located acquiring a great shear strain. They have been widely used for cancelling seismic and wind-induced vibrations as Figure 4

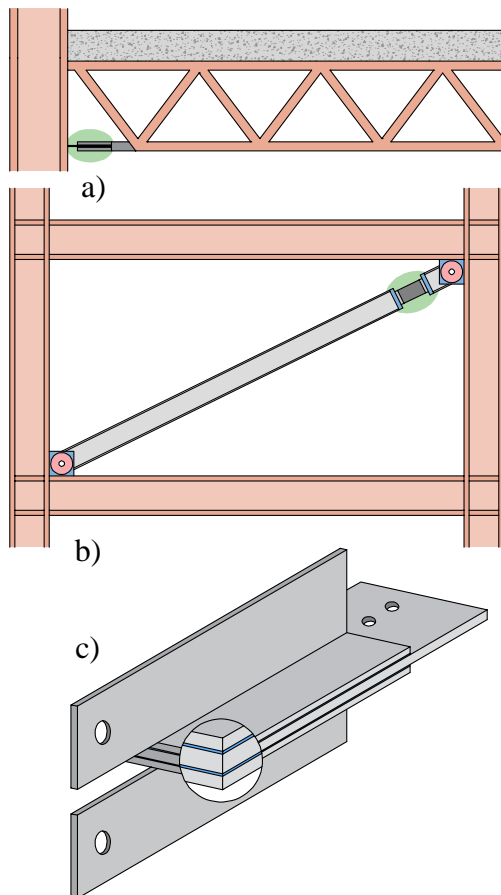


**Figure 4** VE Dampers (c) applied in high rise buildings to mitigate wind-induced (a) and seismic vibrations (b) [16].

depicts [16].

In addition to this damping technology, VE materials have been successfully applied as thin layers or ‘tapes’ glued to a bending-vibrant surface on a wide variety of mechanical systems [17]. In these cases, they are intended to dissipate energy through normal or shear stress loading cycles. Hence, two types of treatments may be differentiated:

**Unconstrained Layer Damping (ULD):** consists in attaching a VE layer to an eccentric surface of the structural element to be treated. ULD enables additional energy dissipation through extensional hysteresis of the VE tape. The additional damping achieved with this technique is usually small (Figure 5.a).

**Constrained Layer Damping (CLD):** consists in constraining a layer of VE material between two bending elements. In this case the layer must be located as closer as possible to the sectional centroid of the element to be treated, as the energy dissipation is achieved through a shear hysteresis. This treatment usually provides greater damping improvements than the ULD. It is important to note that in CLD treatments there exists an optimum geometry (thickness and width) of the VE layer that provides a maximum damping increase (Figure 5.b).

Both damping treatments are depicted in Figure 5 which also includes the rules of thumb for efficiently designing them. As mentioned before, this paper is about the integration of a CLD treatment into composite floor systems.

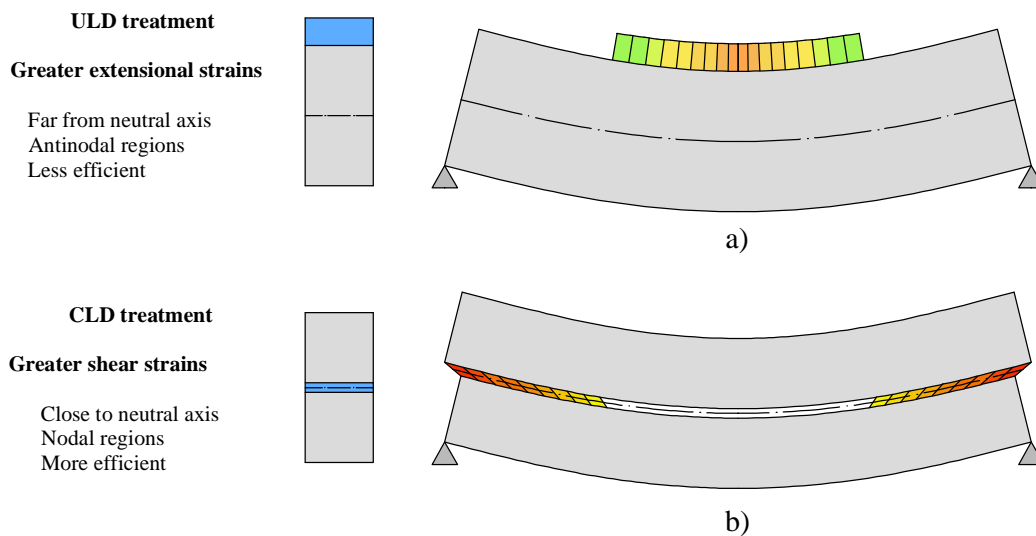


Figure 5 ULD (a) and CLD (b) damping treatments [17].

#### 4 DEVELOPMENT OF REDUCED SCALE MODELS

From now on, the text will refer to two different concepts, "Full-scale model" (FSM) which refers to the system for which predictions have been made, and "Reduced-Scale model" (RSM) which refers to the model itself that has been used to reproduce the first one.

The FSM studied is a long-span composite floor beam of 12 m span. The objective of the paper is to know the additional damping ratio provided by a 100%-CLD treatment applied along the whole length of the studied beam. Thus, ideally, two FSMs would be tested with and without CLD. The beam without any damping treatment would be expected to be stiffer, hence its fundamental natural frequency would be higher, as the concrete slab would be connected to the steel profile through shear studs, however, its damping ratio would be considerably lower.

The RSM proposed has been intended to provide the same amount of additional damping ratio when treating it with the same CLD configuration that would be applied to the FSM. This has enabled to perform the same experimental test as those that would have been performed in the FSM but without so much time, economical and facility resources.

The conceptual design of the RSM was the same as the FSM's one: a composite beam consisting in a concrete slab and a steel profile beam. This decision was adopted for the RSM to be representative, thus, for preserving certain realism. Both concrete and steel mechanical properties were considered identical for FSM and RSM.

The following subsection describes the methodology used to obtain the final geometry of the equivalent RSM.

#### 4.1 Methodology adopted to compute the RSM adequate dimensions

The following methodology is based on an analytical solution developed by Mead for the study of simply-supported beams with 100%-CLD treatment [17]. This solution enables knowing the extra damping ratio provided by the CLD treatment and it is based on two dimensionless parameters. These can be computed from the beam's mechanical and geometrical properties (outlined in Figure 6.a).

The 'geometric parameter'  $Y$  which represents the loss of beam's bending resistance when the 100%-CLD treatment is applied,

$$Y = \frac{d_{321}^2}{(EI_t)} \left[ \frac{E_1 A_1 E_3 A_3}{E_1 A_1 + E_3 A_3} \right], \quad (4)$$

and the 'modified shear parameter'  $g_i$  that indicates the shear stiffness of the constrained VE layer for a given vibration mode of the beam,

$$g_i = \frac{G'_2 b_2 L_b^2}{i^2 \pi^2 h_2} \left[ \frac{1}{E_1 A_1} + \frac{1}{E_3 A_3} \right], \quad (5)$$

where,  $E_1$ ,  $A_1$  and  $I_1$  are the Young modulus, the area and the moment of inertia of the steel profile and  $E_3$ ,  $A_3$  and  $I_3$  are the same for the concrete slab,  $d_{321}$  is the distance between the sectional centroids of the concrete slab and steel beam,  $EI_t$  is the beam's bending stiffness when the slab and the profile are disconnected to shear and bend as independent elements,  $G'_2$  is the 'storage modulus' of the VE material,  $b_2$  and  $h_2$  are the width and the height of the VE layer,

respectively,  $i$  indicates the vibration mode to be analyzed and  $L_b$  the length of the beam.

Mead's solution allows computing the additional modal damping ratio of the treated beam as a function of  $Y$ ,  $g_i$  and  $\eta_2$  (the loss factor of the VE material used) as follows:

$$\xi_i \approx \frac{g_i \eta_2 Y}{2 \left( 1 + g_i (2 + Y) + g_i^2 (1 + \eta_2^2) (1 + Y) \right)} \quad (6)$$

As the formulation provided by Mead is dimensionless, it can be used to develop some scaling laws for obtaining the adequate geometry of the RSM. Those scaling equations need to be intended to achieve a reasonable similarity between the FSM and the RSM. Therefore, since the damping increment provided by the CLD treatment is the fundamental parameter to be studied in this paper, the first scaling equation used was the following one:

$$\xi_{1FS} = \xi_{1RS} \quad (7)$$

where  $\xi_{1RS}$  and  $\xi_{1FS}$  are the extra damping ratio of the RSM and of the FSM respectively, and they need to be equal.

To achieve a higher degree of similarity, a second scaling equation was imposed. The aim of this second condition was to make a RSM with the same loss of bending resistance when the CLD would be applied. Thus, it was expressed as follows:

$$Y_{RS} = Y_{FS} \quad (8)$$

where  $Y_{RS}$  and  $Y_{FS}$  are the 'geometric parameter' for the RSM and FSM, respectively.

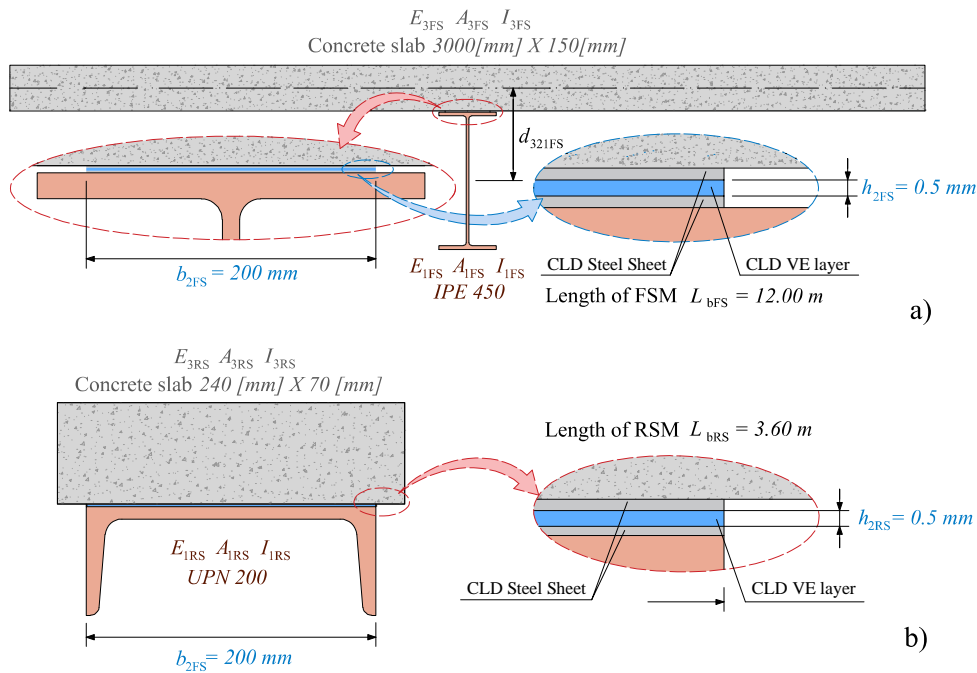


**Figure 6** FSM (a) and RSM (b) geometry and CLD details.

Finally, the following equations were imposed to achieve that the CLD configuration and the mechanical properties of the materials used were the same for RSM and FSM.

$$h_{2RS} = h_{2FS}, \quad (9)$$

$$b_{2RS} = b_{2FS}, \quad (10)$$

$$E_{1RS} = E_{1FS}, \quad (11)$$

$$E_{3RS} = E_{3FS}. \quad (12)$$

Some additional constraints were imposed on the RSM design. First, its length ( $L_{bRS}$ ) should be lower than 4 m, to minimize its impact on the laboratory,

$$L_{bRS} < 4m. \quad (13)$$

Second, the fundamental natural frequency of the RSM with 0% CLD ( $f_{1RS-0\%}$ ) should be

lower than 20 Hz, to ease its testing with an electrodynamic shaker:

$$f_{1RS-0\%} < 20Hz. \quad (14)$$

Additionally, the mechanical properties of the VE layer need to be considered in the design. These depend on frequency and on temperature. Hence, a certain temperature should be chosen for computing the equivalent RSM. The temperature at which RSM and FSM are equivalent was decided to be 20° C. For the experimental test, this value was assured by means of a thermostat. In addition, the VE mechanical properties also rely on frequency. The fundamental natural frequency of the specimen must be used to compute them as the additional modal damping ratio to be studied corresponds to a fundamental bending mode. It should be noted that none scaling condition was imposed with respect to  $f_{1RS-100\%}$ .

Consequently, the resulting  $f_{1RS-100\%}$  is considerably higher than  $f_{1FS-100\%}$ . This means that the VE properties of the RSM ( $G'_{2RS}$  and  $\eta_{2RS}$ ) are different to those of the FSM ( $G'_{2FS}$  and  $\eta_{2FS}$ ). This fact could not be avoided as  $L_{bRS}$  needed to achieve a frequency value identical to  $f_{1FS-100\%}$  would have been much higher than 4 m.

Mead also provided an approximated way of computing the natural frequency of a 100%-CLD beam according to the following equation:

$$f_{i-100\%} = \sqrt{\frac{i^4 \pi^2 (EI_t)}{4m_t L_b^4} \left[ 1 + \frac{g^* Y}{\left(\frac{i\pi}{L_b}\right)^2 + g^*} \right]}, \quad (15)$$

where  $m_t$  is the mass per unit of length of the beam and  $g^*$  is the so called ‘shear parameter’ computed as follows:

$$g^* = \frac{G_2' b_2}{h_2} \left[ \frac{1}{E_1 A_1} + \frac{1}{E_3 A_3} \right] \quad (16)$$

The determination of the natural frequency of a VE damped structure is a convergent iterative process in which the properties of the VE material vary and at the same time modify the natural frequency of the overall system. This iterative procedure is shown in Figure 7 and it is used in this paper.

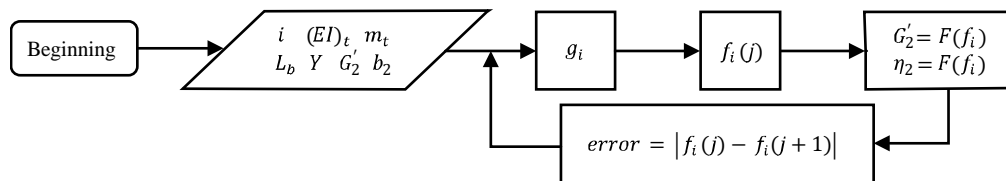


**Figure 7** Convergent iterative process for determining the natural frequency of a VE damped structure.

## 4.2 FSM to be reproduced, geometry and mechanical properties

The FSM chosen is intended to be a typical composite floor beam used for long-spans. It consists in a 12 m span beam composed by an IPE 450 S355 steel profile and a concrete slab of 3 m width by 0.15 m height as the one shown in Figure 6.a. The concrete Young modulus chosen is 30 GPa and the steel modulus is 210 GPa. The width of the integrated CLD is 200 mm and the height of its VE layer is 0.5 mm. Furthermore, the thickness of the constraining steel plates belonging to the CLD is also 0.5 mm.

The VE material used is the HIP2, a polymer manufactured by Heathcote Industrial Plastics whose properties are defined in the nomogram depicted Figure 3. The predicted natural frequencies and additional damping of the FSM are the following ones:

**Table 1** Dynamic properties of the FSM.

$f_{1FS-0\%}$ [Hz]	$f_{1FS-100\%}$ [Hz]	$\xi_{1FS}$ [%]
4.86	4.34	7.30

## 4.3 RSM designed, geometry and mechanical properties

To design the RSM, the following strategy was adopted. First, four varying geometrical parameters were defined for combining them and achieve an adequate design: a steel profile ranging between the UPN 140 and the

**Table 2** Detailed dynamic properties estimated for the RSMs developed.

Beam [Prof]	$bc_{RS} \times hc_{RS}$ [mm <sup>2</sup> ]	$L_{bRS}$ [m]	$Y_{RS}$ [-]	$g_{1RS}$ [-]	$G'_{2RS}$ [Mpa]	$\eta_{2RS}$ [-]	$f_{1RS-0\%}$ [Hz]	$f_{1RS-100\%}$ [Hz]	$\xi_{1RS}$ [%]
UPN 200	240 X 70	3.60	1.64	1.38	0.80	1.01	18.04	15.10	7.30

UPN 240, the width of the concrete slab ( $bc_{RS}$ ) defined between 0.2 and 0.4 m, the slab height ( $hc_{RS}$ ) limited between 0.05 m and 0.15 m due to constructive reasons, and the beam span ( $L_{bRS}$ ) ranged from 1 to 4 m. Those combinations of UPN,  $bc_{RS}$ ,  $hc_{RS}$  and  $L_{bRS}$  complying with the scaling laws exposed from Equations (7) to (12) were obtained by performing an iterative computation. The mechanical properties of the steel and the concrete were assumed to be identical to those used in the FSM. Finally, those successful geometrical layouts were filtered according to the natural frequency constrain exposed in Equations (14). From among the finalist equivalent geometries the authors chose the one with a lower natural frequency and a feasible concrete height from a constructive point of view.

The final RSM obtained by means of the described procedure is presented in Figure 6 and its estimated dynamic properties are outlined in Table 2. It consists in a 3.60 m span composite beam with an UPN 200 steel profile and a small concrete slab of 0.24 m width by 0.07 m height. The geometry of the CLD treatment used for the RMS is identical to the one assumed in the FSM (Figure 6.b).

## 5 EXPERIMENTAL TESTS

### 5.1 Experimental tests performed

In the present study, free vibration response tests of the RSMs against an impulsive load provided using an elastic-tip hammer were performed. Impulsive loads were located next to the mid-span section. An accelerometer was placed at mid span to obtain the beam's free response in terms of acceleration. The transducer used was a PCB 393B12 accelerometer with a sensitivity of 1V/m/s<sup>2</sup> and a measurement range of  $\pm 5$  m/s<sup>2</sup>. The measurements were acquired using a NI CompactRIO 9066 with a NI 9234 acquisition module for reading IEPE Voltage signals. A sampling frequency of 1000 Hz was used.

Three experimental tests were developed, one for 0%-CLD beam, and two tests for the 100%-CLD mode (a first one at 10° C and a second one at 20 °C). These free vibration tests were performed hitting the models with the hammer several times during a single measurement that lasted 200 seconds. After each hit the beam was left vibrating freely until the vibration was completely damped. Once recorded, the signal was divided into several free-decay 'subtests' which were analyzed independently.

### 5.2 Experimental data processing

Two types of data processing were performed for each free-decaying 'subtest'. First, the damping ratio of the studied

specimen was computed as a function of the vibration amplitude. For that, the damping ratio was estimated from the logarithmic decrement at each vibration cycle for a given number of subsequent vibration cycles, as follows:

$$\xi \approx \frac{1}{2\pi N} \ln \left[ \frac{u_i}{u_{i+N}} \right], \quad (17)$$

where  $N$  is the number of vibration cycles chosen to compute the logarithmic decrement (3 in this paper),  $u_i$  is the amplitude of vibration the first vibration cycle and  $u_{i+N}$  the amplitude of the last cycle.

Secondly, the frequency spectrum for each ‘subtest’ was derived by means of a Fast Fourier Transform. The peak-picking method was used to determine the natural frequency of the studied specimen. Finally, all the computed values were averaged to determine the final value of the fundamental natural frequency.

## 6 RESULTS

The results of the experimental natural frequencies for the RSMs are given in Table 3. Figure 8 provides the results related to the damping ratio of the models. Polynomial tendencies have been included in this Figure.

In terms of natural frequencies, the experimental results are quite similar to those predicted. The lower natural frequency of the 0%-CLD specimen is probably due to the concrete-steel shear connection which is not perfectly rigid as it was assumed. In addition, for the 100%-CLD beam it can be observed a decrease in the natural frequency as the temperature increases, which seems to be logical as the shear modulus of a VE material tend decrease with temperature.

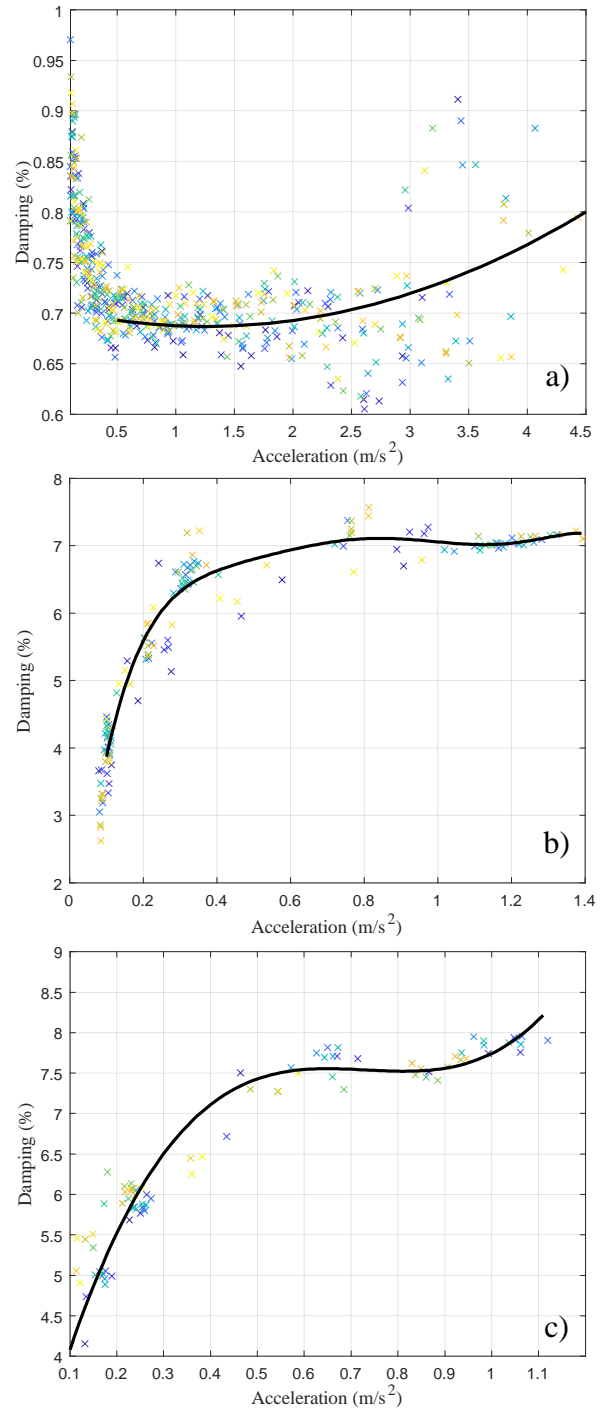


**Figure 8** Damping ratio against acceleration for the three studied RSMs. a) 0%-CLD b) 100%-CLD at 10°C and c) 100%-CLD at 20°C.

Results provided in Figure 8 provide clear information about the RSM behavior in relation to damping ratio. First, for the 100%-CLD model, the higher the amplitude of vibration the higher the damping ratio as usually happens. For the 0%-CLD beam the relation between damping and amplitude is not so clear.

For higher accelerations (above  $0.2 \text{ m/s}^2$ ), the VE layer seems to be ‘switched on’ and consequently dissipates additional energy through shear hysteresis. For lower amplitudes, this dissipating mechanism does not seem to be activated, and thus the damping ratio decreases. This might suggest that HIP2 mechanical properties could also depend on the amplitude of the excitation. Further characterization of this material would be needed to confirm this. For higher amplitudes, the experimental results match well with the additional damping ratio predicted (around 7%).

**Table 3** Experimental frequencies of the RSMs tested.

$f_{1RS-0\%}$ [Hz]	$f_{1RS-100\%}$ at $10^\circ\text{C}$ [Hz]	$f_{1RS-100\%}$ at $20^\circ\text{C}$ [Hz]
16.70	15.43	15.00

## 7 CONCLUSIONS

This paper has presented an experimental study related to composite floor beams with integrated CLD. The damping treatment studied is like the one proposed by Willford et al. in 2006, in which a thin VE layer is constrained between the concrete slab and the steel profile of a composite beam. The paper aims to experimentally quantify the additional damping ratio provided by a CLD treatment applied along the whole length of a floor

beam (100%-CLD).

To reduce the amount of economical, time and facility resources to be involved in the experimental campaign, the authors decided to develop two RSMs with and without CLD treatment. These models reproduce the dynamic behavior of a Full-Scale composite beam (named as FSM) of 12 m span. They were designed to achieve the same amount of additional damping ratio as the FSM with the same CLD configuration. The proposed scaling laws to design the RSM geometry are based on a dimensionless analytical solution provided by Mead for 100%-CLD beams.

Free-decay test have been performed by means of hammer impacts and the measured acceleration responses have been analyzed. The fundamental natural frequencies of the RSMs and the relation between their damping ratios and the amplitude of vibration have been derived. Finally, as a conclusion, it can be said that the results obtained corroborate the validity of Mead’s dimensionless solution and thus, the scaling procedure developed in the paper. Therefore, it can be concluded that a 100%-CLD treatment applied to a composite floor beam (like the one proposed in this paper) may provide a remarkable increase in the damping ratio.

## 8 AWKNOWLEDGEMENTS

The authors acknowledge the Spanish Ministry of Science, Innovation and Universities through the project SEED-SD (RTI2018-099639-B-I00). Carlos M. C. Renedo would like to thank Universidad Politécnica de Madrid for the financial support through a PhD research grant.

## REFERENCES

- [1] A. Ebrahimpour and R. L. Sack, “A review of vibration serviceability criteria for floor structures,” *Comput. Struct.*, vol. 83, no. 28-30 SPEC. ISS., pp. 2488–2494, 2005, doi: 10.1016/j.compstruc.2005.03.023.
- [2] Ove Arup and Partners, “Structural Scheme Design Guide,” 2006.
- [3] W. I. Simms and A. F. Hughes, *Composite design of steel framed buildings*, 1st ed. Ascot: Steel Concrete Institute, 2011.
- [4] T. M. Murray, D. E. Allen, E. E. Ungar, and D. B. Davis, *AISC Steel Design Guide 11. Vibrations of Steel-Framed Structural Systems Due to Human Activity*, Second. AISC, 2016.
- [5] A. L. Smith, S. J. Hicks, and P. J. Devine, *Design of Floors for Vibration: ( Revised Edition , February 2009 )*, Second. Ascot: SCI, 2009.
- [6] M. R. Willford and P. Young, *A Design Guide for Footfall Induced Vibration of Structures*. Surrey: The Concrete Society, 2006.
- [7] Z. O. Muhammad and P. Reynolds, “Vibration Serviceability of Building Floors: Performance Evaluation of Contemporary Design Guidelines,” *J. Perform. Constr. Facil.*, vol. 33, no. 2, pp. 1–17, 2019, doi: 10.1061/(ASCE)CF.1943-5509.0001280.
- [8] J. J. Connor, *Introduction To Structural Motion Control*, First. Boston: Prentice Hall, 2002.
- [9] V. J. L. Gan, C. M. Chan, K. T. Tse, I. M. C. Lo, and J. C. P. Cheng, “A comparative analysis of embodied carbon in high-rise buildings regarding different design parameters,” *J. Clean. Prod.*, vol. 161, pp. 663–675, 2017, doi: 10.1016/j.jclepro.2017.05.156.
- [10] T. H. Nguyen, I. Saidi, E. F. Gad, J. L. Wilson, and N. Haritos, “Performance of distributed multiple viscoelastic tuned mass dampers for floor vibration applications,” *Adv. Struct. Eng.*, vol. 15, no. 3, pp. 547–562, 2012, doi: 10.1260/1369-4332.15.3.547.
- [11] C. Camacho-Gómez, X. Wang, E. Pereira, I. M. Díaz, and S. Salcedo-Sanz, “Active vibration control design using the Coral Reefs Optimization with Substrate Layer algorithm,” *Eng. Struct.*, vol. 157, no. November 2017, pp. 14–26, 2018, doi: 10.1016/j.engstruct.2017.12.002.
- [12] M. Willford, P. Young, and W. H. Algaard, “A constrained layer damping system for composite floors,” *Struct. Eng.*, vol. 84, no. 4, pp. 31–38, 2006.
- [13] A. M. Baz, “Active and Passive Vibration Damping,” in *Active and Passive Vibration Damping*, Wiley, Ed. Chichester, West Sussex, England: John Wiley and Sons, 2019.
- [14] D. I. G. Jones, “Shock and Vibration Handbook,” in *Shock and Vibration Handbook*, Fifth Edit., McGRAWHILL, Ed. New York: McGRAWHILL, 2002.
- [15] H. I. Plastics, “HIP2 Material Properties,” Staffordshire, 2020.
- [16] B. Samali and K. C. S. Kwok, “Use of viscoelastic dampers in reducing wind- and earthquake-induced motion of building structures,” *Eng. Struct.*, vol. 17, no. 9, pp. 639–654, 1995, doi: 10.1016/0141-0296(95)00034-5.
- [17] D. J. Mead, “Passive Vibration Control,” in *Passive Vibration Control*, John Wiley & Sons, Ed. Southampton: John Wiley & Sons, 2000, p. 591.

# SEMI-ACTIVE TUNED MASS DAMPER: MAGNETORHEOLOGICAL DAMPER IDENTIFICATION AND PERFORMANCE EVALUATION

Christian A. Barrera-Vargas\*, Iván M. Diaz\*, Jaime H. Garcia-Palacios\*  
and José M. Soria†

\* Department of Continuum Mechanics and Theory of Structures, ETSI Caminos, Canales y Puertos.  
Universidad Politécnica de Madrid  
28040 Madrid, Spain  
e-mail: christian.barrera.vargas@alumnos.upm.es  
ORCID: 0000-0003-3281-7595

† Escuela Politécnica Superior  
Universidad de Alcalá de Henares  
28805 Alcalá de Henares, Spain

**Abstract.** A tuned vibration absorber, usually known as tuned mass damper (TMD), is an effective solution for control vibration in civil structures. When they are perfectly tuning, the relative movement of the inertial mass with regarding the structure movement is  $90^\circ$ , as a result, the inertial control force opposes harmonic excitations at the tuning frequency. For slender structures, in which human activities may excite several modes simultaneously, the TMD loses efficiency. When dealing with vibration control of lightweight structures subjected to human-induced vibrations, several modes can be excited, and modal parameters of the human-structure system may change over time. Thus, TMDs suffer detuning issues and do not perform well. Then, semi-active TMD (STMD) may alleviate this problem. However, a smart damper properly controlled should be employed. A magnetorheological (MR) damper can be used for this purpose. In this paper, firstly an MR damper is identified and secondly, a STMD is applied to a lightweight structure model considering an ideal semi-active damper and a “real” one, i.e., the identification model is considered. The identification of the MR Damper uses a genetic algorithm for fitting a Bingham and a Kelvin-Voigt model. Each configuration of the TMD and the STMD are analyzed through a sensitivity analysis and for excitation forces induced by human actions.

**Key words:** Tuned vibration absorber, Semi-active vibration control, Magnetorheological Damper, Genetic Algorithms.

## 1 INTRODUCTION

The new tendencies forward sustainable structures make the use of lightweight structures common. Thus, these structures are susceptible to suffer excessive vibrations.

A lot of research has been developed about vibration control devices in structures, where the most popular is known as tuned vibration

absorber also known as tuned mass damper (TMD) [1-2], which is a passive control device. TMDs can control the harmonic vibration responses associated with a specific frequency. In structures where the natural frequencies are variable or unpredictable, the TMD tends to be detuned, losing effectiveness.

The addition of smart dampers in the design of a TMD allows increasing the range of

controlled frequencies. Thus, developing a new generation of TMDs is known as Semi-Active Tuned Mass Dampers (STMD) [3]. STMDs are usually implemented using Magneto-Rheological (MR) dampers, which show the advantage of low current consumption, high force response, and rapid transient response.

An appropriate control law must be defined to achieve the correct working of the STMD. Koo et al [4], proposed a control method for Semi-active tuned vibration absorbers, using the “groundhook” concept, also known as phase control (ON-OFF). In this case, the damping force depends on the velocity or displacement of the structure and the relative velocity between the inertial mass and the structure. Moutinho [5] modified this control law, substituting the parameter of the displacement of the structure by the acceleration of the structure, and neglecting the structure velocity with respect to the TMD velocity, which leads to practical implementation for control in structures. The phase control has been studied in some experimental and numerical research, in STMD [6], and in base isolation seismic devices [7].

When an ideal viscous damping model for the smart damper is assumed, the STMD performs really well when canceling harmonic vibrations. However, unfortunately, the model that represents the constitutive equation of the MR is highly non-linear. Thus, in order to carry out the realistic and reliable simulation, the real MR model should be identified previously. Amongst the MR models found in the literature, phenomenological models are preferred if one wants to look for optimal properties for the damper. Spencer et al [8] studied the Bingham and Bouc-Wen models among others, to represent a numerical approximation for the behavior of this device. Varela [9] considered a constitutive model for shear yield stress of the magnetorheological

fluid. Weiss [10] has examined the viscoelastic behavior in Magneto and Electro-Rheological fluids, remarking that the magneto-rheological fluids exhibited the pre-yield properties within the range exhibited by common viscoelastic solids. Kwok et al [11] studied the identification of the parameters of an MR fluid damper using genetic algorithmic, Marzuki [12] used dynamic neural networks for the identification of the nonlinear parameters of the MR damper, among other researches.

This paper analyzes the performance of a footbridge recently constructed in the laboratory with a TMD and a STMD implemented. The STMD is studied under two configurations i) considering an ideal behavior for the damping parameter (I-STMD), and ii) using a numerical model that represents an approximation for a real magnetorheological damper (MR-STMD). The experimental test carried out on the MR damper (RD-8041-1 of Lord Corporation) is fully explained in Section 3. Then, the device is identified considering two phenomenological models: Bingham and Kelvin-Voigt models. Afterward, a sensitivity analysis is developed for each studied configuration considering the phase control for the I-STMD and MR-STMD. Finally, some concluding remarks are pointed out.

## 2 PASSIVE AND SEMI-ACTIVE TUNED MASS DAMPERS

The passive version of the TMD is described in section 2.1, In section 2.2 the STMD is presented together with the control law.

### 2.1 Tuned Mass Damper

The TMD is composed of an inertial mass, a spring, and a viscous damper, which is incorporated into a structure that has a vibration mode to be controlled. The inertial mass movement of the TMD, when perfectly

tuned, should present a delay of 90 degrees with respect to the structure movement.

A structure with a TMD can be simplified as a system of two degrees of freedom as shown in Figure 1, in which  $m$ ,  $c$  and  $k$  are the mass, damping coefficient and stiffness respectively, and the sub-indexes “s” and “t” indicated the structure and the TMD.

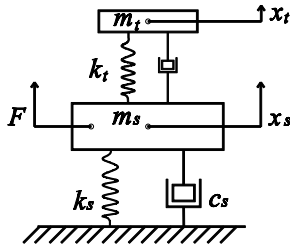


**Figure 1:** Representation of a Structure with a TMD.

The equation of motion of a structure with a TMD is:

$$\begin{aligned} m_s \ddot{x}_s + c_s \dot{x}_s + k_s x_s - c_t (\dot{x}_t - \dot{x}_s) \\ - k_t (x_t - x_s) = F, \end{aligned} \quad (1)$$

where  $\ddot{x}$ ,  $\dot{x}$  and  $x$  are acceleration, velocity and displacement, respectively, and  $F$  is the external force, while the equation of motion for the degree associated with the TMD is as follows:

$$m_t \ddot{x}_t + c_t (\dot{x}_t - \dot{x}_s) + k_t (x_t - x_s) = 0, \quad (2)$$

## 2.2 Semi-active Tuned Mass Damper

The STMD is a passive TMD with a real-time damping variation (see Figure 2). The response of the MR damper is controlled through a control law, which analyzes the structure and inertial mass movement at each time instant.

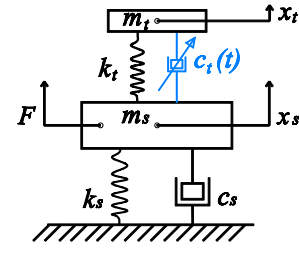


**Figure 2 :** Representation of a structure with a STMD.

The equation of motion of the structure with a STMD is similar to the equation (1), changing the parameter  $c_t$  by  $c_t(t)$ , it happens similarly with the equation of motion of the STMD, as presented in the next equation:

$$m_t \ddot{x}_t + c_t(t) (\dot{x}_t - \dot{x}_s) + k_t (x_t - x_s) = 0, \quad (3)$$

where  $c_t(t) (\dot{x}_t - \dot{x}_s)$  is the damping force ( $F_d$ ) for the I-STMD. For the MR-STMD,  $F_d$  corresponds with the force obtained from the phenomenological model studied, and a new equation should be added to set the value of  $c_t(t)$  with respect to the system kinematic.

## 2.3 Semi-active Tuned Mass Damper

The semi-active ON-OFF control law proposed by Koo [4], has been analyzed, considering each step of movement for the system of two degrees of freedom as shown in Figure 3.

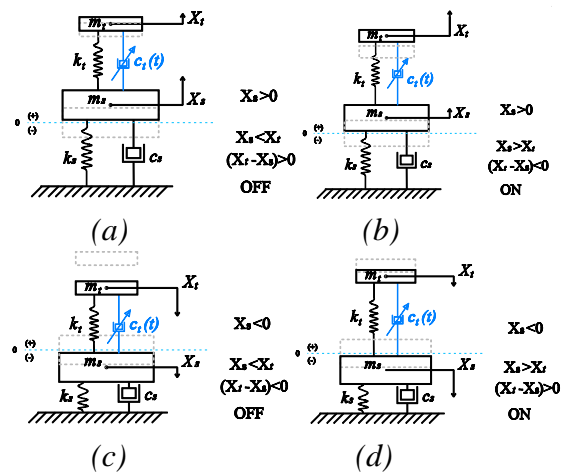


**Figure 3 :** Illustration of the phase control logic.

According to Moutinho [5], the phase control can be rewritten, substituting the displacement of the structure by the acceleration of the structure, the modified equation that represents the control law becomes:

$$\begin{cases} \ddot{x}_s \cdot (\dot{x}_t - \dot{x}_s) \leq 0 \rightarrow c_t(t) = c_{min} \\ \ddot{x}_s \cdot (\dot{x}_t - \dot{x}_s) > 0 \rightarrow c_t(t) = c_{max} \end{cases} \quad (4)$$

where  $c_{min}$  and  $c_{max}$  are the minimum and maximum damping coefficients achieved by the semi-active device in the case of the I-STMD. For the MR-STMD these parameters change to  $V_{min}$  and  $V_{max}$  respectively. The minimum value corresponds with the normal functioning while the maximum value is the blocking functioning. In equation (4),  $\dot{x}_s$  may be neglected if the movement of the structure is much smaller than the one of the inertial mass.

Although ON-OFF control laws are recommendable when dealing with non-linear smart damper, one should account for this nonlinear control law that may introduce chattering problems once implemented.

### 3 IDENTIFICATION EXPERIMENTAL TEST

The MR Damper studied is an RD-8041-1 of Lord Corporation. The piston was attached to a concrete block and the cylinder to a hydraulic jack as shown in Figure 4. This hydraulic jack has the characteristic of generating displacement at a given frequency initially defined. To achieve this, the jack applied the necessary force to get the desired displacement. Different combinations of frequency and displacement can be defined within the range of the jack capacity.

The MR damper is characterized by modified its viscosity with the presence of voltage. Thus, front low and high voltage values, the MR damper develops normal functioning and blocking functioning respectively.



**Figure 4** : View of the MR Damper, joining to the concrete block and the hydraulic jack.

#### 3.1 Configuration of the Experimental Test

The experimental test carried out to identify the MR damper consisted in applying a series of sinusoidal displacement-controlled tests, associated with frequencies of [0.5, 1, 2, 3, and 5 Hz]. Each frequency has been combined with sinusoidal amplitudes of  $\pm 1\text{mm}$ ,  $\pm 2\text{mm}$ , and  $\pm 10\text{mm}$  making a total of 15 tests. These 15 configurations were repeated for voltages of 0.5, 1, 2, 3, 4, and 5 V applied to the MR damper covering the voltage range of the MR. Figure 5 shows the first configuration studied.

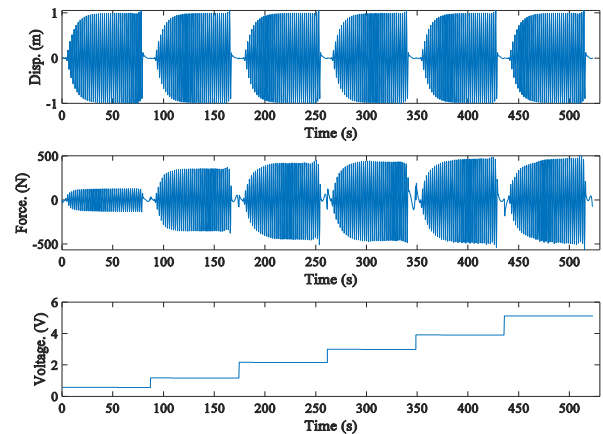


**Figure 5** : Experimental test for the frequency of 0.5 Hz, with  $\pm 1\text{mm}$  displacement and variable voltages.

### 3.2 Identification process

Once the 15 tests are carried out, the model parameters are identified, minimizing the mean square error between the estimated ( $\hat{F}$ ) and measure ( $F_{exp}$ ) damper force, as follows:

$$J(\underline{z}, V, x) = \frac{1}{N} \sum_{i=1}^N (\hat{F} - F_{exp})^2, N=1 \dots 15 \quad (5)$$

$$\min_{\underline{z}} J(\underline{z}, V, x),$$

in which  $\underline{z}$  is the vector of the model parameters,  $V$  is the voltage applied, and  $x$  is the rod displacement measured by the testing machine.

All experimental tests are summary in Figure 6, where the value for the maximum force produced by the MR damper depending on the voltage applied, the frequency of the movement applied, and the amplitude of displacement is show for each test.

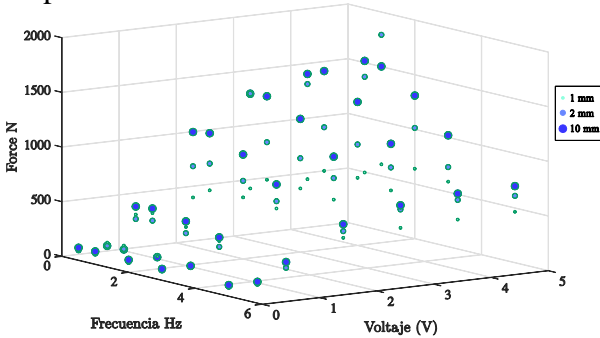


**Figure 6** : Summary experimental test: The sizes of the points indicate the test to 10mm, 2mm, and 1mm.

Figure 6 shows that the reaction force produced by the MR damper depends on the three variables described (displacement amplitude, the frequency content of the displacement, and input voltage). As a first approach to the identification process, it is only considered the voltage variable as an independent variable.

The optimization process (5) has been solved using a metaheuristic algorithm (Mono-objective genetic algorithm) to assure that the

global minimum is achieved. It is assumed that have a polynomial depending on voltage  $\underline{z} = \underline{z}(v)$ . Thus, two phenomenological models are identified: *i*) the Bingham model, and *ii*) the Kelvin-Voigt model, which is described in equations (6) and (7) respectively.

$$F - f_0 = F_c \cdot \text{sgn}(\dot{x}) + c_o \cdot \dot{x}, \quad (6)$$

$$F - f_0 = k \cdot x + c \cdot \dot{x}, \quad (7)$$

where  $F$  and  $f_0$ , are the total force of the MR damper and the force due to the preload introduced by the pressurized gas, respectively. For the Bingham model,  $f_c$  and  $c_o$  are the friction force and the damping coefficient, while the Kelvin-Voigt model,  $k$  and  $c$  are the stiffness and the damping coefficients respectively.

The following dependencies on the voltage have been assumed: the parameters  $f_c$ ,  $c_o$ ,  $k$ , and  $c$  are defined with a voltage-dependent polynomial function:

$$F_c = a_0(V) \cdot V + a_1(V) \cdot V^2 + a_2(V) \cdot V^3, \quad (8)$$

$$c_o = b_0(V) + b_1(V) \cdot V, \quad (9)$$

$$k = c_0(V) + c_1(V) \cdot V + c_2(V) \cdot V^2 + c_3(V) \cdot V^3, \quad (10)$$

$$c = d_0(v) + d_1(v) \cdot v + d_2(v) \cdot v^2 + d_3(v) \cdot v^3. \quad (11)$$

Thus,  $\underline{z} = [a_i, b_i, c_i, d_i]$  is finally the vector of parameters that are obtained the minimum of the function  $J(\underline{z}, V, x)$ .

The optimization process is carried in two steps: *i*) For each of the 15 tests, the optimization process is running, and a vector of parameters  $\underline{z}$  is obtained. and *ii*) for all parameters obtained for each test, a second optimization process is carried out, assuming each parameter as a polynomial voltage-dependent, as follows:

$$a_0(V) = a_{0,0} + a_{0,1} \cdot V + a_{0,2} \cdot V^2 \quad (12)$$

$$+ a_{0,2} \cdot V^2 + a_{0,4} \cdot V^4 + a_{0,5} \cdot V^5,$$

This step is repeated for all the parameters of  $z$ . Table 1 summarizes the values obtained after step 2 is carried out.

	(v) <sup>5</sup>	(v) <sup>4</sup>	(v) <sup>3</sup>	(v) <sup>2</sup>	(v)	const.
a <sub>0</sub>	-0.27	3.81	-19.54	43.59	-39.83	12.72
a <sub>1</sub>	0.16	-2.39	13.45	-33.64	35.34	-9.97
a <sub>2</sub>	-	-	-0.15	1.57	-5.23	5.57
b <sub>1</sub>	0.18	-2.20	10.96	-24.44	23.11	-6.78
b <sub>2</sub>	-	-0.19	2.31	-9.79	16.05	-7.28

**Table 1** Summary of coefficients for the parameters of the polynomial adjusted with the Bingham model.

The mean relative error obtained for the Bingham and Kelvin-Voigt model is, 46% and 139% respectively.

#### 4 DESIGN OF TUNED MASS DAMPERS SYSTEMS

The design of the TMD consider three types of configurations, *i*) a TMD designed under the criteria proposed by Den Hartog [1], *ii*) an I-STMD with a phase control law, and *iii*) the MR-STMD with a phase control. The effectivity for these configurations is analyzed using a sensitivity analysis.

##### 4.1 Excitation

To carry out the design of the structure with a TMD or an STMD, two excitation forces are considered.

- The first excitation corresponds to a chirp signal with an amplitude of 770 N, and with linear frequency variation from 0.1 Hz to 10 Hz.
- The second excitation is a sinusoidal signal that corresponds with the second harmonic of the walking effect, as defined in [13], with a frequency of 2.5 Hz acting in the second mode ( $nf = 5$  hz,  $\alpha_{n,v} = 0.10$  and  $G = 700$  N).

##### 4.2 Sensitivity Analysis

In this section, the pedestrian bridge presented in [14] is analyzed, considering that has a TMD, an I-STMD, and a MR-STMD

(using the identified Bingham model). In table 2, the modal parameters of the structure and each TMD is defined.

Modal Parameters			
Structure		Value	
$m_s$	Mass	838	kg
$f_s$	Range frequency	[3.50 to 6.50]	Hz
$\zeta_s$	Damping ratio	2	%
$k_s$	Stiffness	$8.27 \times 10^5$	N/m
$c_s$	Damping	1053.1	kg/s
$\eta$	$f_s/f_i$	[0.70 to 1.30]	-
TMD		Value	
$\mu$	Mass ratio	1	%
$m_t$	Mass	8.38	kg
$f_t$	Frequency	5.15	Hz
$k_t$	Stiffness	8789.1	N/m
$\zeta_t$	Damping ratio	[0.1 to 25]	%
$c_t$	Damping	[0.54 to 135.7]	kg/s
I-STMD		Value	
$c_{min}$	Damping OFF	$c_t$	kg/s
$c_{max}$	Damping ON	$200 \cdot c_t$	kg/s
MR-STMD		Value	
$v_{min}$	Voltage	[0.50-2.50]	V
$v_{max}$	Voltage	5	V

**Table 2:** Parameters for the sensitivity analysis

The different systems are analyzed considering variation in the damping coefficient of the TMD and the I-STMD, also the variation in the frequency of the structure is taking into account, keeping fixed the tuned frequency of the TMD. This relation is represented by the symbol  $\eta = f_s/f_t$ . Figure 7 to 9 shows the behavior for maximum acceleration of the structure and maximum displacement of the TMD for each configuration.

Figure 7 shows that the optimal performance is obtained when the TMD has a damping coefficient between 5% and 10%, with a frequency of the structure close to the tuned frequency of the TMD. If the frequency of the structure change, the system presents detuning.

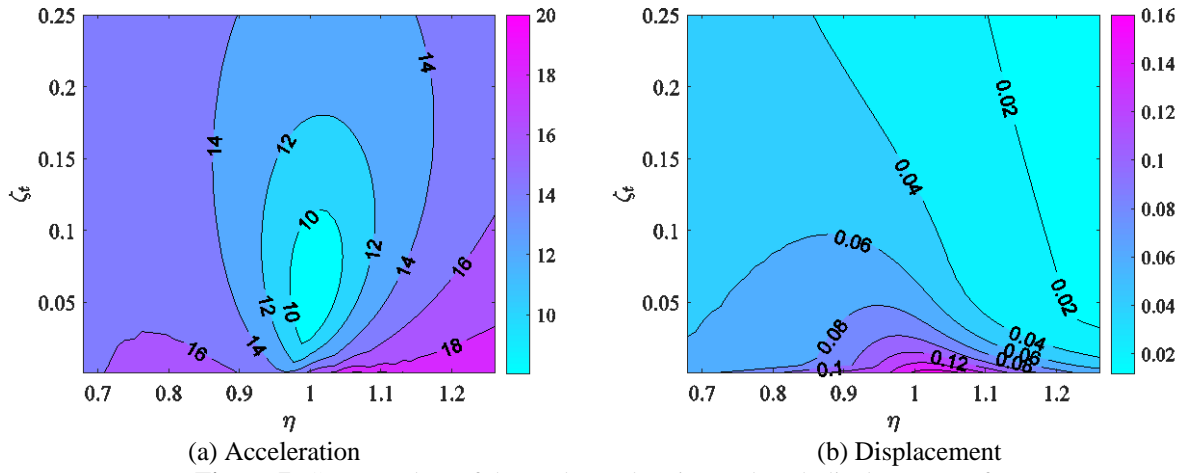


**Figure 7:** Contour plots of the peak acceleration and peak displacement of TMD.

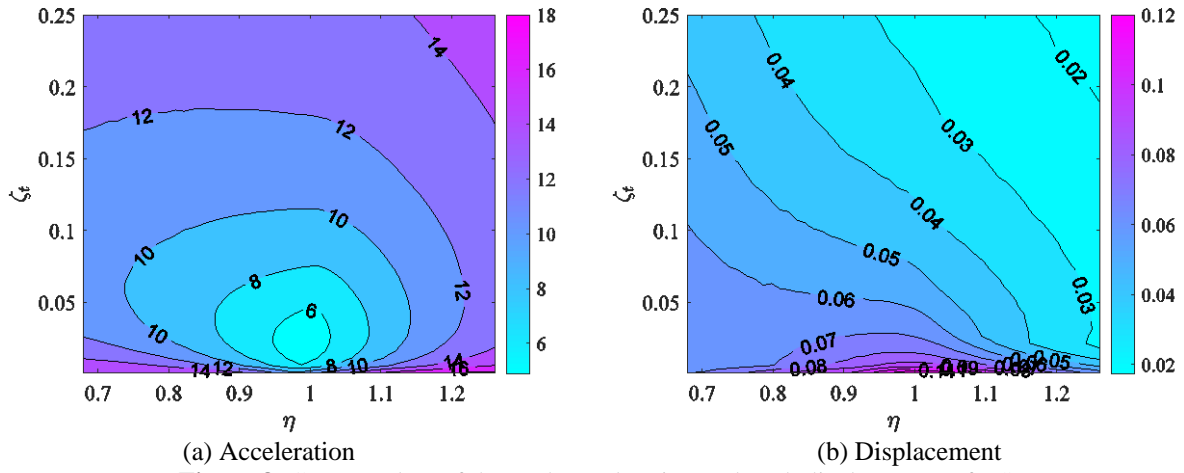


**Figure 8:** Contour plots of the peak acceleration and peak displacement of I-STMD.

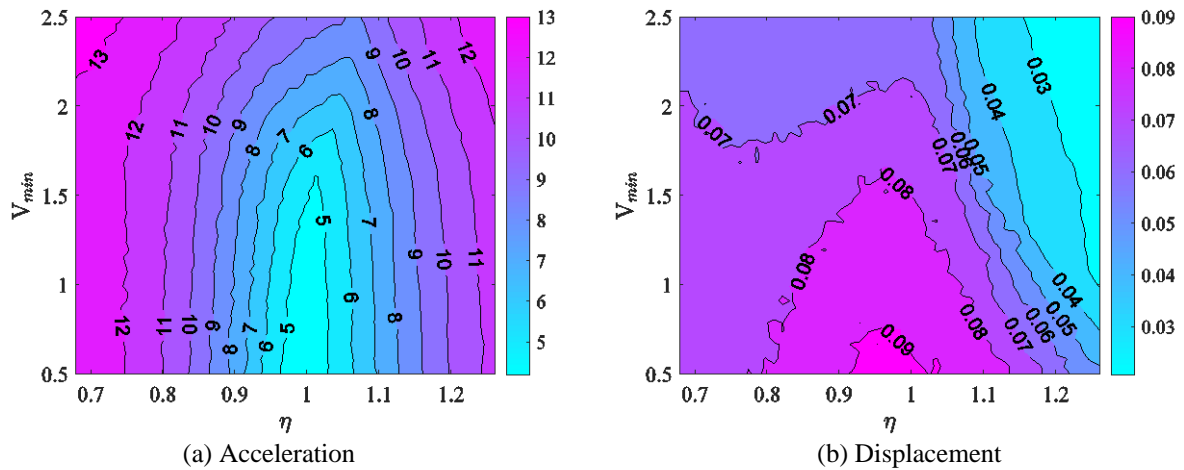


**Figure 9:** Contour plots of the peak acceleration and peak displacement of MR-STMD.

Figure 8 shows the behavior with an I-STMD. In this case, the semi-active damper generates a robust control with a lower damping coefficient. Furthermore, the I-STMD has developed better performance than the passive TMD, but with a range width of 0.9 to 1.1 of  $\eta$

The addition of the MR damper in the STMD is analyzed with the same phase control used in the I-STMD but varying the value for the minimum voltage ( $V_{min}$ ). The response in the acceleration of the structure and the displacement of the MR-STMD are shown in Figure 9, where it is exhibited that the optimum response is obtained for low values of voltage.

## 5 RESULTS AND ANALYSIS

The optimal parameters obtained in the sensitivity analysis are presented in Table 3. Besides, the peak acceleration for each system is presented in two situations, *i*) considering a forcing frequency of 2.5 Hz, exciting the structure with the second harmonic, and the TMD or the STMD tuned for the frequency of the structure, and *ii*) changing the frequency of the structure to 4 and 6 Hz, with a forcing frequency of 2 and 3 Hz, exciting the structure with the second harmonic. The second situation has considered the case when the TMD or STMD could be detuning regarding the frequency vibration of the structure, below or above.

Optimal Parameters				$f_s$ (4 Hz)	$f_s$ (5 Hz)	$f_s$ (6 Hz)
System	$f_t$ (Hz)	$\zeta$ (%)	$V_{min}$	max  Acc	max  Acc	max  Acc
Structure	-	2	-	2.07	2.07	2.07
TMD	5.15	7.21	-	1.75	0.95	1.60
I-STMD	5.15	2.13	-	1.02	0.97	1.05
MR-STMD	5.15	-	0.58	1.73	0.97	0.90

**Table 3** : Optimum results obtained from the sensitivity analysis.

The vibration dose value (VDV) is also considered to understand the response of each system. The VDV is a parameter that considers the accumulated magnitude of the vibration along time and is given by the next equation:

$$VDV = \left( \int_0^t \ddot{x}_s^4(t) dt \right)^{1/4} \quad (13)$$

Figures 10 and 11 represent the acceleration and VDV respectively for the first situation. These figures show that the TMD passive, the I-STMD, and MR-STMD, have similar behavior under a tuned control.

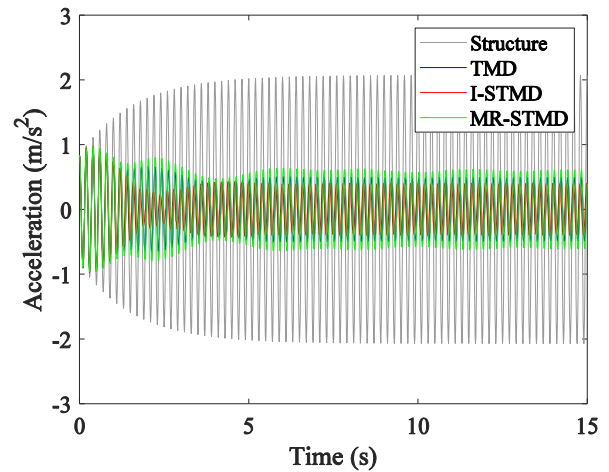


**Figure 10** : Acceleration response of the systems tuned to 5Hz.

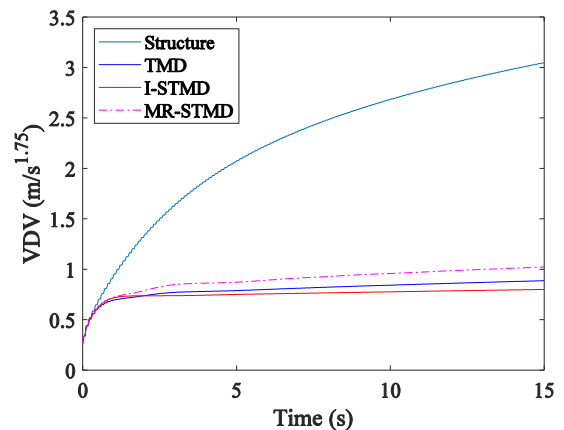


**Figure 11** : VDV of acceleration response for each system tuned to 5Hz.

Figures 12 to 15 show the acceleration and VDV respectively under a detuned control (second situation).

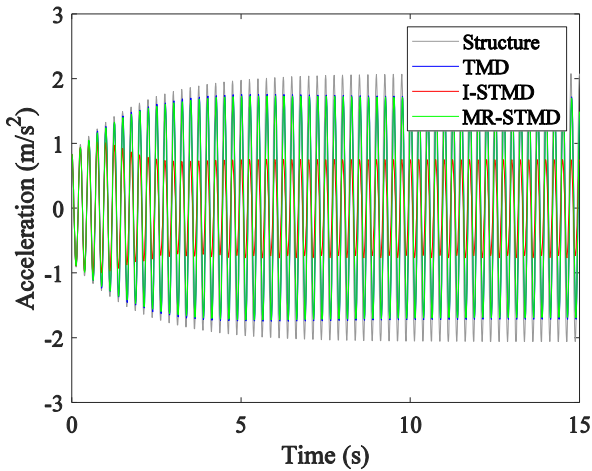


**Figure 12** : Acceleration response of the systems detuned to 4Hz

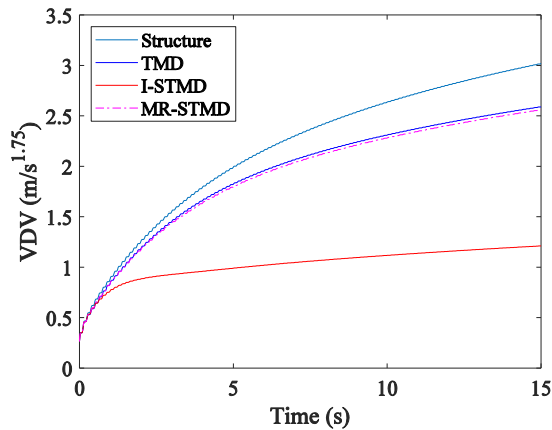


**Figure 13** : VDV of acceleration response for each system detuned to 4Hz.

Figures 12 and 13 show that the three configurations lose effectiveness. However, the I-STMD keeps better behavior regarding the TMD or the MR-STMD, and the structure without control.

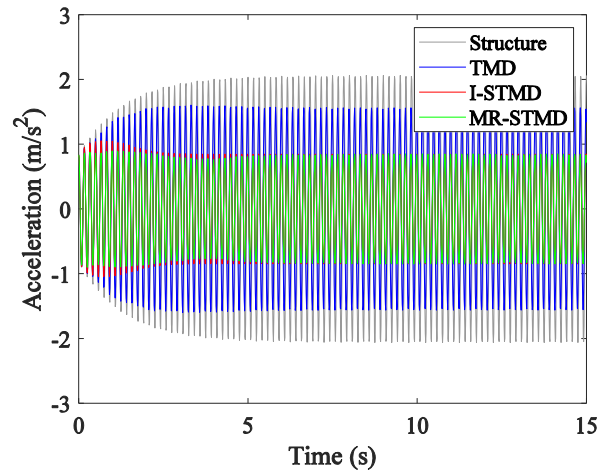


**Figure 14** : Acceleration response of the systems detuned to 6Hz

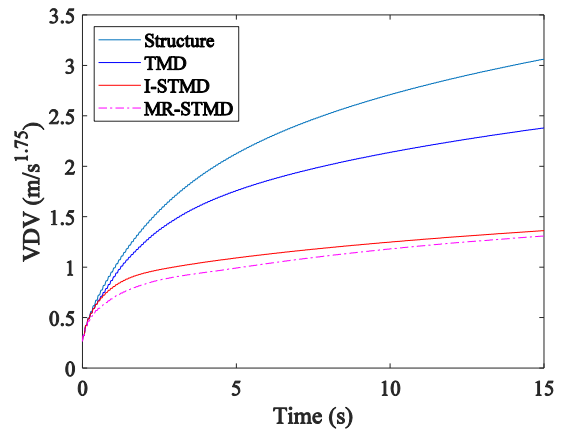


**Figure 15** : VDV of acceleration response for each system detuned to 6Hz.

Figures 14 and 15 show as the MR-STMD develop a better behavior when the is detuned below the frequency vibration of the structure, matching the behavior of the I-STMD.

Figure 16 shows the same results represented previously, but in root mean square (RMS) value, for the two situations, tuned and detuned.

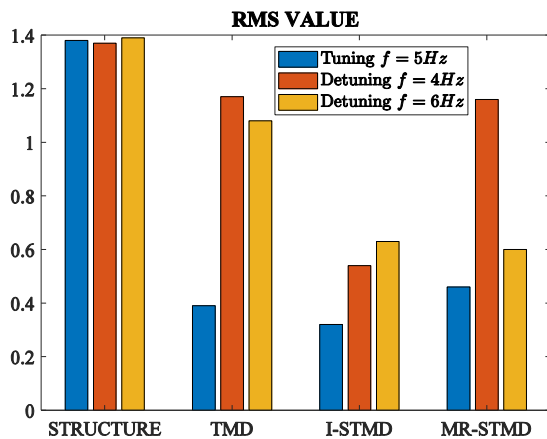


Figure 16 : RMS values for each system studied.

## 6 CONCLUSIONS

This paper studied the design of a structure with a vibration control based on tuned vibration absorbers type TMD or STMD, considering the semi-active device in two-states, *i*) with an ideal damping behavior, and *ii*) analyzing the numerical model behavior of a MR damper.

An experimental setup has carried out to calibrate the MR damper, using genetic algorithms to obtain a numerical model, which represents an approximation of the results obtained in laboratory. The following remarks can be extracted.

- The MR Damper RD-8041-1 of Lord Corporation presents a behavior that depends primarily on the induced voltage, but the displacement and frequency of excitation could be also considered in the process of the identification. Thus, the Bingham model must be modified considering the incorporation of these parameters.
- The TMD under a tuned excitation or response of the structure generates an excellent control, even better to the studied MR-STMD. However, in the situation where the frequency of the structure is detuned, the STMD device has better response behavior.

- The phase control (ON-OFF) used in the I-STMD has the capacity to control the vibration for the two studied excitations. On the contrary, this control law couldn't be the most proper for the case of the MR-STMD.
- The implementation of a continuous control law to govern the behavior of the MR-STMD could be a great solution, allowing change between different values of voltage as required at each time interval.

Future works will focus in improving the identification model for the MR Damper and the development of the continuous control law.

## FUNDING:

This research was funded by Ministry of Science, Innovation and Universities grant number RTI2018-099639-B-I00.

## REFERENCES

- [1] J.P. Den Hartog. *Mechanical vibrations*. Courier Corporation, 1985.
- [2] SAMCO “*Final Report 2006 F05 Guidelines for Structural Control*”
- [3] Hrovat D, Barak P, Rabins M. *Semi-Active versus Passive or Active Tuned Mass Dampers for Structural Control*. 1983,109(3): 691-705.
- [4] Koo, J.H.; Ahmadian, M.; Setareh, M.; Murray, T.M. *In Search of Suitable Control Methods for Semi-Active Tuned Vibration Absorbers*. J. Vib. Control 2004, 10, 163–174.
- [5] Moutinho C. *Testing a Simple Control Law to Reduce Broadband Frequency harmonic vibrations using Semi-Active Tuned Mass dampers*. Smart Mater. Struct. 2015,24(5):964-1726
- [6] Soria J.M, Díaz I.M., García-Placios J.H. *Further Steps Towards the Tuning of Inertial Controllers for Broadband-*

- Frequency-Varying Structures*. Struct control Health Monit. 2019:e2461.
- [7] Barrera-Vargas Christian A., Díaz Iván M., Soría José M and García-Palacios Jaime H. *Enhancing Friction Pendulum Isolation Systems Using Passive and Semi-Active Dampers* Appl. Sci 2020, 10, 5621
- [8] Spencer B.F., Dyke S.J., Sain M.K., and Carlson J.D. *Phenomenological Model of a Magnetorheological Damper* 1997 Engineering Mechanics
- [9] Varela-Jiménez M., Vargas Luna J., Cortés-Ramírez J. and Song G. *Constitutive model for shear yield stress of magnetorheological fluid based on the concept of state transition*. Smart Mater. Struct 24 (2015) 045039
- [10] Weiss Keith D, Carlson J. David and Nixon Donald A. *Viscoelastic Properties of Magneto- and Electro-Rheological Fluid*. 1994 Journal of Intelligent Material Systems and Structures.
- [11] Kwok N. M., Ha Q.P., Nguyen M. T., Li J., Samali B. *Bouc-Wen model parameter identification for a MR fluid damper using computationally efficient GA*. ISA Transactions 46 (2007) 167-179.
- [12] Marzuki Khalid, Rubiyah Yusof, Majid Joshani and Hazlina Selamat *Nonlinear Identification of a Magneto-Rheological Damper Based on Dynamic Neural Networks* Computer-Aided Civil and Infrastructure Engineering 29 (2014) 221-233.
- [13] ISO 10137. *Bases for Design of Structures Serviceability of Buildings and Walkways against Vibrations*, international organization for standardization edition, 2007.
- [14] Díaz I.M, Gallegos CA, Ramirez Senent J and Renedo CMC. *Interaction Phenomena to Be Accounted for Human-Induced Vibration Control of Lightweight Structures* (2021) Front. Build Environ 7:658529

# DESIGN, IMPLEMENTATION AND EXPERIMENTAL VALIDATION OF AN ACTIVE MASS DAMPER FOR VIBRATION MITIGATION IN SLENDER STRUCTURES USING A LOW-COST PROCESSOR.

César Peláez\*, Álvaro Magdaleno† and Antolín Lorenzana‡

Escuela de Ingenierías Industriales,  
Universidad de Valladolid  
47011 Valladolid, Spain

e-mail: \*cesar.pelaez@uva.es, †alvaro.magdaleno@uva.es, ‡ali@eii.uva.es

ORCID: \*0000-0003-1260-8112, †0000-002-5606-1545, ‡0000-0003-2562-0532

**Abstract.** The purpose of this work is the design and implementation of an active mass damper (AMD) for vibration mitigation in slender structures using a standard actuator (APS 400) commanded by a low-cost processor (NI myRIO-1900). The control law is experimentally validated on a 13.5-meter lively footbridge and has been formulated assuming a reduced mechanical model of the structure (just considering its first mode).

As it is known, problems related to vibrations produced by human locomotion in slender, lightweight and low damped structures could require systems to mitigate the movement of the structure, which can be large around its natural frequencies. In those conditions, the AMD must guarantee the comfort and fulfil the serviceability conditions for the pedestrian use according to some design guides.

After the dynamic identification of the actuator, the procedure consisted in the experimental characterization and identification of the modal properties of the structure (natural frequency and damping ratio) associated to its first mode. Once the equivalent state space system of the structure is obtained, the design of the control law is developed, based on state feedback, which was deployed in the low-cost controller. Finally, experimental adjustments (filters, gains, ...) were implemented and the validation test carried out.

The system performance has been evaluated using different indicators both in the frequency and time domain and under different loads scenarios, including pedestrian transits to demonstrate the feasibility and robustness of the proposed system.

**Key words:** Active control, Vibration mitigation, Active Mass Damper, Low-Cost processor, Footbridge

## 1 INTRODUCTION

Recent advances in structural technologies, including new construction materials and more innovative design technologies, promote the trend toward designing lighter and slenderer structures with fewer nonstructural elements, giving them a more cost-effective and architecturally attractive approach.

However, these structures exhibit much lower inherent damping and lower natural frequencies than in past constructions, making them more susceptible to be excited by pedestrians walking on them [1].

Induced vibrations may cause a service problem in terms of discomfort to users, although they will rarely affect the service life

or the safety of the structures.

Regarding pedestrian walkways, the trend has been toward increased spans and the use of high-performance materials and sophisticated design techniques. Consequently, stiffness and mass have decreased, resulting in smaller natural frequencies and a greater propensity to dynamic loading.

One of the usual approaches in footbridges for the mitigation of these pedestrian-induced vibrations are passive control systems, namely TMD (Tuned Mass Dampers). These consist of a mass-spring-damper device whose natural frequency is tuned to "match" with the frequency of the footbridge. This system has the advantage of having a minimum cost, due to its small size (its mass ranges between 0.15 and 2 % of the structure mass) and its easy implementation in the existing structure. However, despite reducing the response of the footbridge to excitations close to its natural frequency, it still allows a relatively large response to impulsive actions.

When high performance is required, it is more convenient to use an active control device. These systems are able to adapt the response of the structure during dynamic loads, applying control actions at each instant in response to the load, reaching high levels of efficiency in vibration mitigation. In addition, active systems enable the simultaneous control of several vibration modes with a single device, which makes this system an interesting solution for reducing the response of low damping flexible structures characterized by several modes of vibration modes that contribute significantly to the overall dynamics. Furthermore, active systems are versatile, have no tuning problems and can be unconditionally stable by adopting a properly designed control system [2]. However, active control may not be an attractive solution in terms of cost because it requires a higher level of technology and maintenance than other control systems.

Also, it often requires expensive devices as well as power supply systems, and may have reliability problems under certain circumstances.

For the design of an active control system, two critical issues need to be considered. The first is that it will be necessary to create a structural control algorithm that is sufficiently robust to compute the control force to be applied on the structure in real time, since instabilities may result in fatal damage to the structure itself. The second issue relates to the need for an actuator capable of applying the desired control force on the structure with an admissible error in real time.

With regard to the control strategy, two radically different approaches may be considered: feedback and feedforward [3]. The principle of feedback control is depicted in Figure 1; system output is compared with the reference signal, obtaining the error signal ( $\text{Error} = \text{Output} - \text{Reference}$ ). This signal is transmitted to a compensator and its result is applied to the system. The design problem in these control systems is to find the right compensator so that the closed-loop system is stable and behaves optimally. On the other hand, the principle of feed-forward control is shown in Figure 2. This method is based on the availability of a reference signal correlative to the main disturbance, this signal is passed through an adaptive filter, whose output is applied to the system by secondary sources. The main limitation of this control strategy lies in the need of requiring a signal related to the system perturbation, which is not always feasible.

In relation to the second question, one of the commonly used actuators to apply forces to mechanical systems are the Active Mass Damper (AMD), since they can be placed in the most favorable positions regarding the most significant vibration modes and can be and can be easily concealed within the structure.

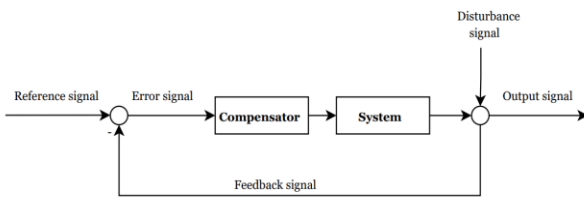


**Figure 1:** Structure of feedback control

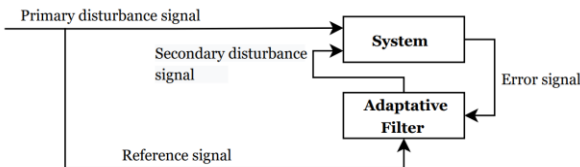


**Figure 2:** Structure of feedforward control

This paper presents the design and practical implementation of an inertial mass-based active damping device, in order to cancel excessive vertical vibrations on a footbridge. Experimental validation of this system was performed on a 13.5 m long wooden platform at laboratory scale, whose first natural frequency is around 2 Hz, so that it can be excited by walking. The developed system is focused on the vibrations mitigation in a range close to the first natural frequency, considering the structure as a single degree of freedom system. The control law of the feedback control system has been designed using genetic algorithms to minimize the response of the closed-loop system, using as AMD a commercial electrodynamic inertial actuator (APS 400 ELECTRO-SEIS with a moving mass of 31.2 kg) controlled by a low-cost processor (NI myRIO 1900).

This document continues with the description of the test structure, the identification of its modal parameters and the creation of the associated model. The dynamics of the actuator used and the creation of its model are described in section 3. The design and development of the AMD are presented in section 4. The experimental results conducted to assess the performance of

the closed-loop system is presented in section 5, where several loading scenarios, in order to validate the damping device both in time and frequency domain were used. Finally, some discussions and conclusions, together with suggestions for future work, are given in section 6.

## 2 STRUCTURE DYNAMICS AND GENERATION OF THE SDOF MODEL

This section describes the test structure and the identification of its modal parameters. This identification consisted in performing an experimental modal analysis (EMA) for obtaining the experimental frequency response function (FRF) at the point of maximum amplitude of the first bending mode. Afterwards, the modal parameters of the first mode of the structure (frequency, damping and generalized mass) were extracted from these FRFs. Finally, these modal properties were used to obtain the state-space representation of the system.

### 2.1 Description of the structure

The structure to be used is a wooden platform (GLULAM 24h) of 13.5 m long and 1 m wide. It is made from ten independent beams of  $13.5 \times 0.1 \times 0.14$  m connected by thirteen threaded rods located every 1.11 m. The platform is placed on two fixed supports at the at the ends. In the central section 6 springs (3 on each side of the platform, with a stiffness constant of 6600 m) are arranged in order to increase the stiffness of the structure. A picture of the footbridge is shown in Figure 3.

The system itself is very flexible and with low damping, which means that the response of the structure to disturbances close to its natural frequencies remains high. Figure 4 shows the theoretical bending modes of the footbridge, which have been extracted from the model of the structure in the finite element

software SAP 2000.



**Figure 3:** Picture of the test structure

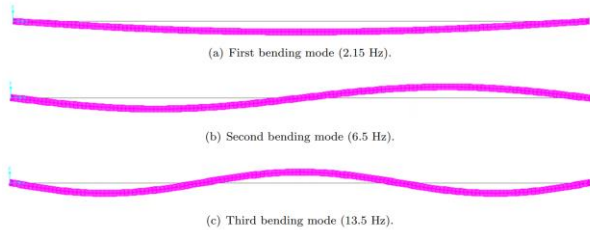


**Figure 4:** Theoretical bending modes of the structure obtained via SAP 2000 model.

## 2.2 Experimental modal analysis

In order to carry out the process of obtaining the experimental frequency response function (FRF) of the structure, the inertial mass actuator was used to induce forces on the structure placing a piezoelectric accelerometer on its moving mass so that the applied force is known ( $F = M \cdot A$ ). A second accelerometer has also been placed on the footbridge to measure its response. Figure 5 shows the experimental set-up implemented.

The exciter has been controlled by feeding it with a white noise signal with an amplitude of  $\pm 2$  volts in a frequency range between 0 and 30 Hz commanded through the software implemented in the myRio. Data acquisition was carried out using a Dewesoft data acquisition card, with a sampling frequency of

1 KHz.

The acquired data have been postprocessed using Matlab software to estimate the experimental FRFs by executing the *tfestimate* function, selecting a Blackman window with a size of 150,000 points. Figure 6 shows the FRF obtained, representing the system acceleration between 0 and 25 Hz.

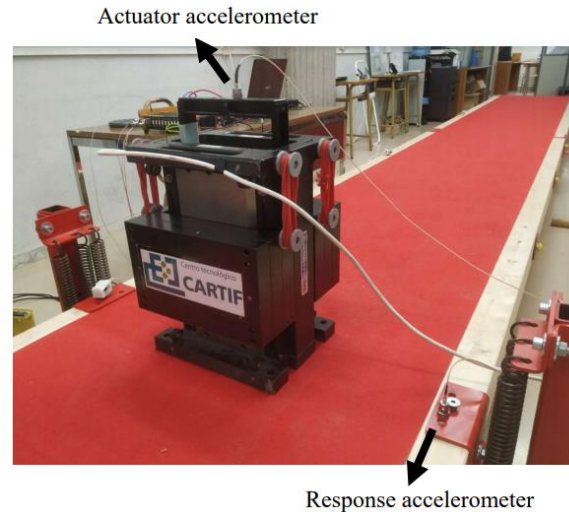


**Figure 5:** Experimental set-up used for structure identification.

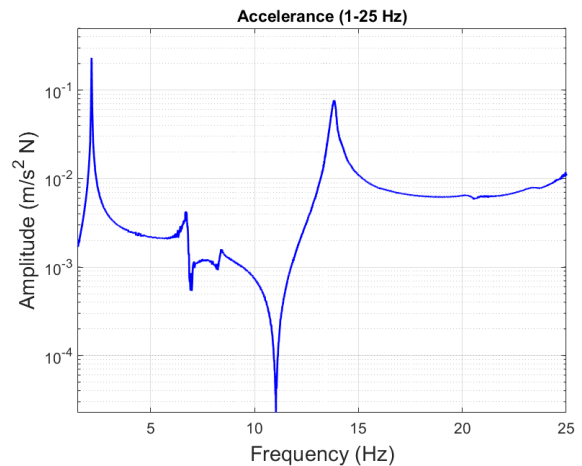


**Figure 6:** Accelerance of the structure between 0 and 25 Hz.

## 2.3 Modal properties extraction and model generation

A curve fitting optimization algorithm has been used to extract the modal properties of the first mode of the structure, in such a way that

the error between the experimental and analytical FRF in the frequency range close to the first mode (1.5-4 Hz) is minimized.

With the aim of determining the analytical frequency response functions of the system, its state space representation was used (Eq. 1), where the input of the system ( $f(t)$ ) correspond with the force applied on the structure, and the output ( $y(t)$ ) with the response acceleration that the structure will experience at its midpoint,  $x(t)$  denotes the vector formed by the state variables of the system, selected to correlate with the position and velocity of the structure's midpoint (Eq. 2).

$$\dot{x}(t) = A_{ss}x(t) + B_{ss}f(t) \quad (1)$$

$$y(t) = C_{ss}x(t) + D_{ss}f(t)$$

$$x_1(t) = u(t) \quad (2)$$

$$x_2(t) = \dot{u}(t)$$

The matrices  $A_{ss}$ ,  $B_{ss}$ ,  $C_{ss}$  and  $D_{ss}$  are chosen to satisfy the equation of motion of the structure according to its modal properties (Eq. 3). Hence, they are expressed according to the equations presented in (Eq. 4).

$$\ddot{u} + 2\xi_0\omega_0\dot{u} + \omega_0^2u = \frac{1}{m}f(t) \quad (3)$$

$$A_{ss} = \begin{bmatrix} 0 & 1 \\ -\omega_0^2 & -2\xi_0\omega_0 \end{bmatrix} \quad (4)$$

$$B_{ss} = \begin{bmatrix} 0 \\ \frac{1}{m} \end{bmatrix}$$

$$C_{ss} = [-\omega_0^2 \quad -2\xi_0\omega_0]$$

$$D_{ss} = \begin{bmatrix} \frac{1}{m} \end{bmatrix}$$

For obtaining the analytical FRFs, the Matlab function *ss* is used to create the state space model, introducing the parameters of the matrices of the state space representation, and

the *freqresp* function is then applied on the model created, indicating the desired frequency range. Following this process, the three modal parameters were optimized by applying a genetic optimization algorithm whose fitness function consisted in minimizing the error between the FRF of the experimental system and the one obtained with the modal parameters of each iteration.

The modal parameters obtained are expressed in (Eq. 5), in addition, Figure 7 shows the comparison between both experimental and analytical frequency response functions for the first mode of the structure.

$$\omega_0 = 2.147 \text{ Hz} \quad (5)$$

$$\xi_0 = 0.406 \%$$

$$m = 520.879 \text{ kg}$$

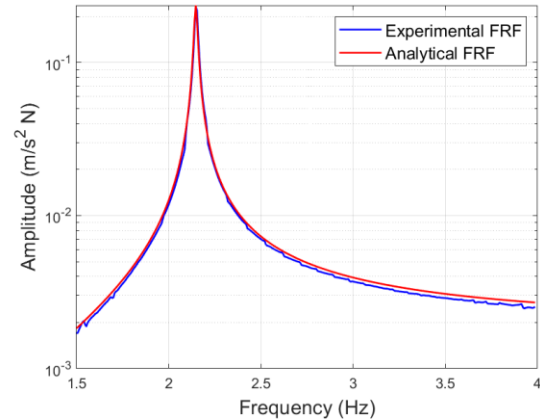


Figure 7: Comparison between simulated and experimental FRF of the sdof system.

### 3 INERTIAL-MASS ACTUATOR DYNAMICS

For developing an AMD system that operates optimally, it is essential to obtain a model that describes the behavior and dynamics of the inertial mass actuator that will be used to feedback forces into the system, allowing to accurately predict how it will

behave according to the signal it is fed with.

The actuator used will be the same as the one shown in Figure 5 that was applied for the experimental FRF extraction of the structure. It consists of an inertial actuator, which works by generating inertial forces on the structure on which it is placed without the need for a fixed reference. The actuator consists of a mobile reaction mass (31.2 kg) attached to a current coil that moves in a magnetic field created by an array of permanent magnets. The moving mass is connected to the frame by a suspension system. This exciter is powered by an electrical signal that varies in voltage between  $\pm 2$  V, it also has an amplifier that allows to change the gain that reaches the system by a manual control.

The dynamics of an inertial mass actuator can be described [4] according to the third order transfer function given in (Eq. 6), where  $K_A$  corresponds with the transducer constant (in N/A),  $\omega_A$  is the natural frequency associated with the suspended moving mass system,  $\xi_A$  represents the damping coefficient and the pole at  $\varepsilon$  accounts for the low-pass filtering property of these instruments, absorbing frequencies higher than the cut-off frequency  $\varepsilon$  (in rad/s),

$$G_A(s) = \left( \frac{K_A s^2}{s^2 + 2\xi_A \omega_A s + \omega_A^2} \right) \cdot \left( \frac{1}{1 + \varepsilon} \right) \quad (6)$$

The process of obtaining the model consisted in optimizing the parameters of the transfer function applying a genetic algorithm so that the experimental and simulated FRFs had a minimum error. Eq. 7 displays the obtained transfer function, where the values determined for each parameter are ( $K_A = 9348.52$  N/A,  $\omega_A = 13.69$  rad/s,  $\xi_A = 0.26$  and  $\varepsilon = 78.23$  rad/s. Figure 8 shows the comparison between the experimental and the modelled FRF.

$$G_A(s) = \frac{9348.52s^2}{s^3 + 85.44s^2 + 751.8s + 14660} \quad (7)$$

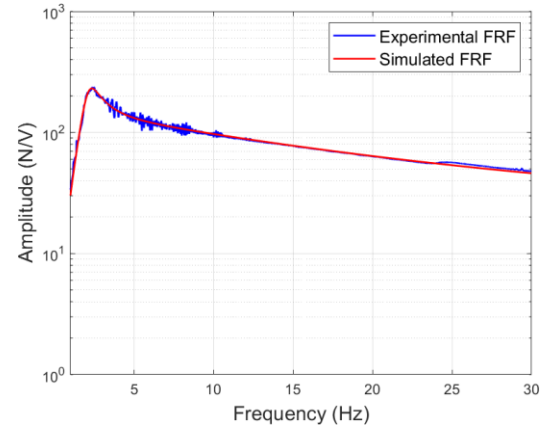


**Figure 8:** Comparison between simulated and experimental FRF of the sdf system.

## 4 CONTROLLER DESIGN

This section will describe the design of the developed controller. A state feedback control structure will be used, whose basic scheme of operation is shown in Figure 9. This control structure consists of multiplying the state variable vector by the feedback gain, obtaining the signal in volts to be applied on the actuator. The design of the control law will consist in selecting the feedback gain  $K_r$  so that the closed-loop system performs as efficiently as possible, this will be done by applying genetic algorithms to optimize this behavior.

Nevertheless, in the experimental system no devices are available to measure the position and velocity of the structure (state variables), only accelerometers are at disposal, so it will be necessary to implement a state estimator (Figure 10).

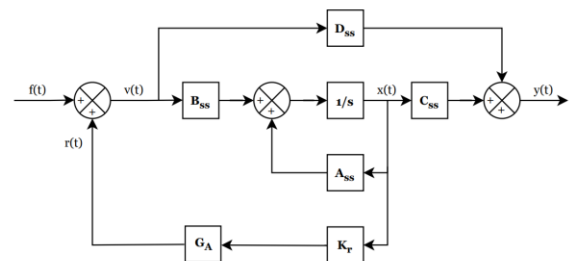


**Figure 9:** Block diagram of the state feedback control system.

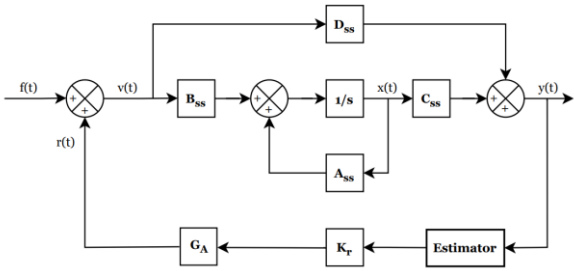


**Figure 10:** Block diagram of the state feedback control with the state estimator.

#### 4.1 State Estimator

The estimator development process has consisted of two phases: design and implementation.

Parting from a block diagram as shown in Figure 11, where the matrices  $A_{ss}$ ,  $B_{ss}$ ,  $C_{ss}$  and  $D_{ss}$  represent the state space matrices of the open-loop system (Eq. 4),  $x_{est}$  represent the estimation of the space state variables (position and velocity),  $y_{est}$  is the estimate acceleration and  $K_e$  and  $K_c$  are constant matrices of dimensions  $[n_{ss} \times p_{ss}]$  and  $[m_{ss} \times n_{ss}]$ , respectively, where  $n_{ss}$  represents the number of state variables of the open-loop system,  $m_{ss}$  the number of inputs, and  $p_{ss}$  the number of outputs. So  $K_e$  is a  $[2 \times 1]$  matrix that multiplies the error signal between the measured and estimated acceleration and  $K_c$  is a  $[1 \times 2]$  matrix that multiplies the estimated state variables converting them to force units.

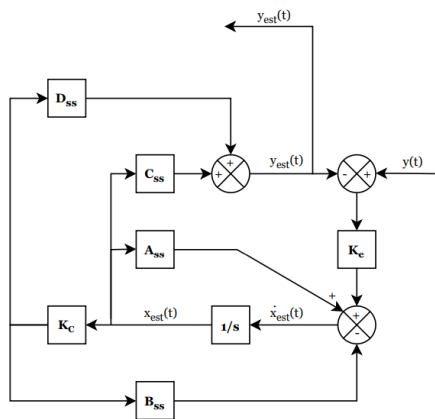


**Figure 11:** Block diagram representation of the state space estimator.

In this design phase, the objective will be to establish the values of  $K_e$  and  $K_c$  so that, in the second implementation phase, the estimator may work as desired. For this purpose, the estimator can be represented as a state space system, where the input would be the measured acceleration ( $y$ ), the output would be the estimated acceleration ( $y_{est}$ ), and the state variables would be ( $x_{est}$ ).

According to the block diagram shown in Figure 11 the state equation for this system can be obtained (Eq. 8), as well as the coefficients of the space state matrices of the system, that can be denoted as  $A_{est}$ ,  $B_{est}$ ,  $C_{est}$  and  $D_{est}$  (Eq. 9), and the output equation (Eq. 10).

$$\dot{x}_{est} = A_{ss}x_{est} - B_{ss}K_c x_{est} - K_e C_{ss}x_{est} - K_e D_{ss}K_c x_{est} + K_e y(t) \quad (8)$$

$$A_{est} = (A_{ss} - B_{ss}K_c - K_e C_{ss} - K_e D_{ss}K_c) \quad (9)$$

$$B_{est} = K_e$$

$$C_{est} = A_{est}(2, :)$$

$$D_{est} = 0$$

$$y_{est} = C_{est}x_{est} + D_{est}x_{est} \quad (10)$$

Then the optimization algorithm was applied so that the error between the measured acceleration (system input) and the estimated acceleration (system output) is minimized, for this,  $K_e$  and  $K_c$  were optimized so that the FRF of the system is as close as possible to a line of constant unit value in the frequency range corresponding to the first mode of the structure (1.5-4 Hz). The optimized values obtained are represented in Ec. 11, Figure 12 shows the frequency response function of the estimator space state system and Figure 13 shows the validation of the estimator in the temporal domain, confirming that the error between measured and estimated acceleration is minimal.

$$K_c = [0.0001 \quad 10.7464] \quad (11)$$

$$K_e = \begin{bmatrix} -8.8555 \\ -0.0001 \end{bmatrix}$$

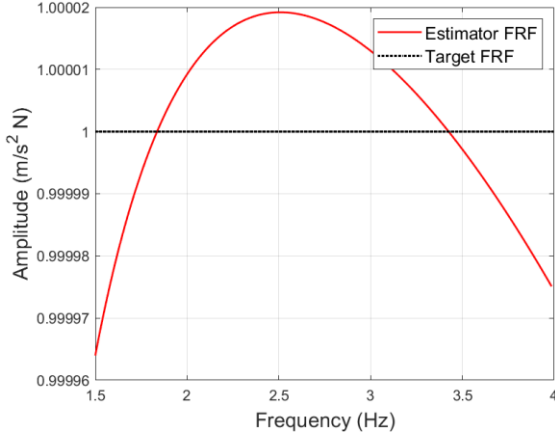


Figure 12: Estimator FRF compared to the target FRF

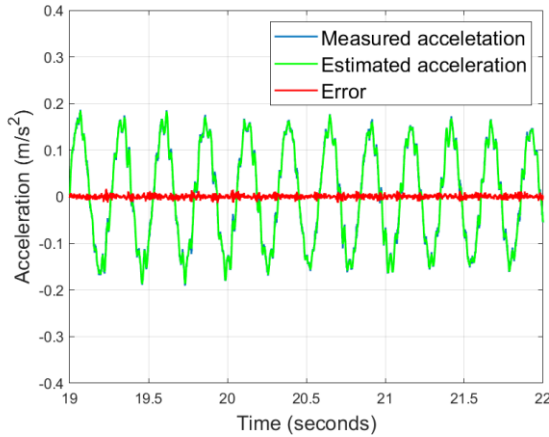


Figure 13: Validation of the estimator on the temporal domain

Once the estimator has been designed and the matrices  $K_e$  and  $K_c$  have been determined, the implementation process consists of changing the system output to be the estimated state variables of the structure (Figure 14) rather than the estimated acceleration, modifying the system output equation in the state space representation of the estimator, thus changing the matrices  $C_{est}$  and  $D_{est}$  (Eq. 12).

$$C_{est} = \begin{bmatrix} 1 & 0 \\ 0 & 1 \end{bmatrix} \quad (12)$$

$$D_{est} = 0$$

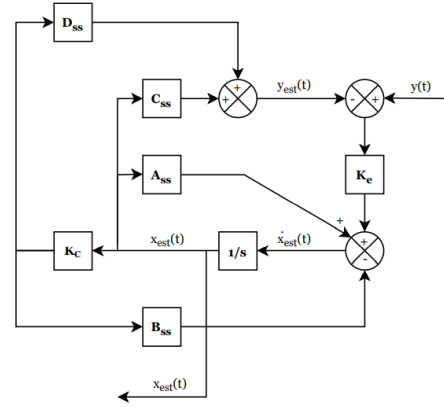


Figure 14: Block diagram representation of the state space estimator.

## 4.2 Control law design

The controller feedback gain has been designed using a genetic optimization algorithm, so that the criteria defined below are used as the fitness function, including the additional requirement that the closed loop system poles must be located in the negative semi-plane of the real axis, in order to guarantee the stability of the system.

1. Minimization of the maximum value of the FRF of the closed-loop system.
2. Minimization of the area below the FRF of the closed-loop system.
3. Minimization of the real part of the closed-loop system pole of higher value.
4. Minimization of the product of the absolute values of the poles of the closed-loop system.
5. Minimization of the temporal response of the closed-loop system to a chirp input oscillating between 1.5 and 4 Hz.
6. Weighted combination of criteria 1 and 2.

The values for the gain obtained after executing the algorithm are as shown in Eq. 13. Subsequently, the closed-loop performance of the system is tested for the different calculated values. Figure 15 displays the FRFs obtained for these systems. The appearance of two

peaks instead of one may be observed, this can be explained by the coupling between the dynamics of the first mode of the structure with those of the exciter itself, since both systems exhibit very close natural frequencies (2.15 vs. 2.17 Hz).

The performance of these systems has also been evaluated for a step input of amplitude 1 N. The settling times are shown in Table 1, where the maximum value of FRFs as well as its value at the resonance frequency of the structure for the different criteria are also displayed.

Finally, the gain obtained by criterion 5 has been chosen since it presents a fairly fast settling time, besides a stable behavior in the whole frequency range.

$$K_1 = [-213.14 \quad -5.02] \quad (13)$$

$$K_2 = [-634.41 \quad -25.12]$$

$$K_3 = [-227.10 \quad -14.40]$$

$$K_4 = [-52.44 \quad 0.77]$$

$$K_5 = [-277.91 \quad -4.57]$$

$$K_6 = [-421.05 \quad -16.75]$$

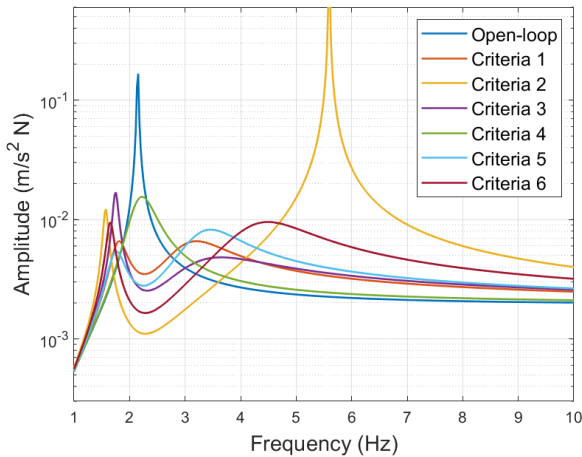


**Figure 15:** Closed-loop FRF for different feedback gain values.

Criteria	Settling time [s]	Maximum amplitude [m/s <sup>2</sup> N]	Amplitude at structure resonance [m/s <sup>2</sup> N]
Open-loop	96.96	0.17	0.17
1	5.02	0.0066	0.0035
2	114400	1.61	0.0011
3	15.73	0.017	0.0025
4	4.18	0.015	0.016
5	4.52	0.0082	0.0028
6	9.64	0.0094	0.0016

**Table 2:** Evaluated performance for the different closed-loop systems considered.

### 4.3 System deployment in the controller

For the implementation of the system in the myRIO 1900 low-cost controller, a transfer function has been used to generate the voltage signal sent to the actuator according to the acceleration measurement provided by a MEMS digital accelerometer ADXL355, as shown in Figure 16.

This transfer function (Eq. 14) has been calculated as the product of the feedback gain and the state estimator, and has been discretized using a first order hold method with a sampling time of 0.001 s.

The system has been deployed in the controller using Labview 2019 software. In addition, a low pass filter has been included to avoid instabilities due to the dynamics of the structure associated with high frequencies, since the control system does not take into account these dynamics when modeling only its first mode. A point-by-point finite impulse response filter has been used, applying a Welsch window with a cut-off frequency of 24 Hz and 50 taps.

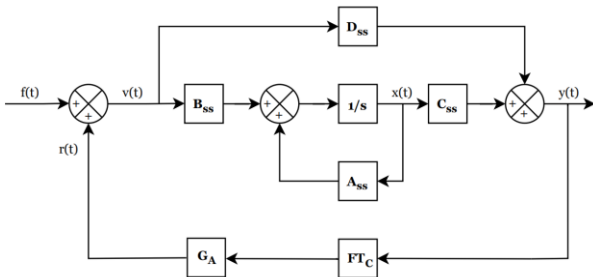


**Figure 16:** Block diagram representation of the closed loop system.

$$FT_C(s) = \frac{2461s^3 + 3.947 \cdot 10^6 s^2 - 1.074 \cdot 10^7 s - 1.75 \cdot 10^6}{s^4 + 3222s^3 + 2.596 \cdot 10^6 s^2 + 8.005 \cdot 10^5 s + 6.171 \cdot 10^4} \quad (14)$$

$$FT_C(z) = \frac{0.7679z^4 - 1.238z^3 + 0.07964z^2 + 0.4815z - 0.09068}{z^4 - 2.399z^3 + 1.838z^2 - 0.479z + 0.03986}$$

## 5 SYSTEM VALIDATION

The efficacy of the active control system developed will be assessed in this section.

For this purpose, the behavior of the open and closed loop systems was compared both in the frequency domain, calculating their respective frequency response functions, and in the temporal domain, measuring the time taken for both systems to return to the initial stationary position starting from the same initial conditions. Finally, both systems have been evaluated under load, carrying out walking tests on the structure at its resonance frequency.

### 5.1 Frequency domain validation

The frequency response functions were experimentally performed via impact, measuring the induced force with a Mutronic load cell with a capacity of up to 500 kg and with a sensitivity of 2 mV/V.

Figure 17 and 18 shows the comparison of open-loop and closed-loop systems, both in the whole frequency domain and in the frequency range around the first natural frequency of the structure, for which the control system has been designed.

It can be appreciated that at the structure's

natural frequency, the system response is reduced from 0.662 to 0.006055 m/s<sup>2</sup>N when applying the control system, representing a decrease of 99.09%. Furthermore, the maximum value of the controlled system presents an amplitude of 0.02207 m/s<sup>2</sup>N at a frequency of 2.95 Hz, which also represents a reduction of 96.67 % with the maximum value of the uncontrolled system.

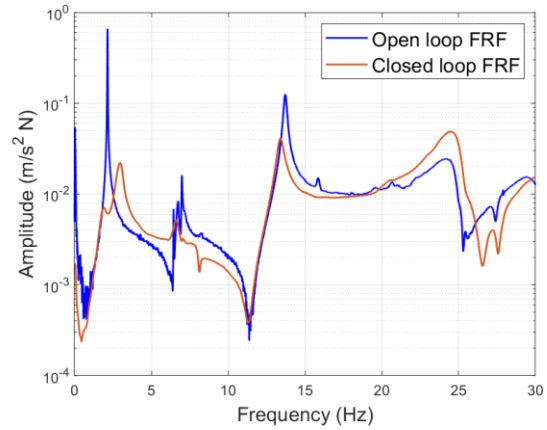


**Figure 17:** Uncontrolled and controlled system frequency response functions between 0 and 30 Hz.

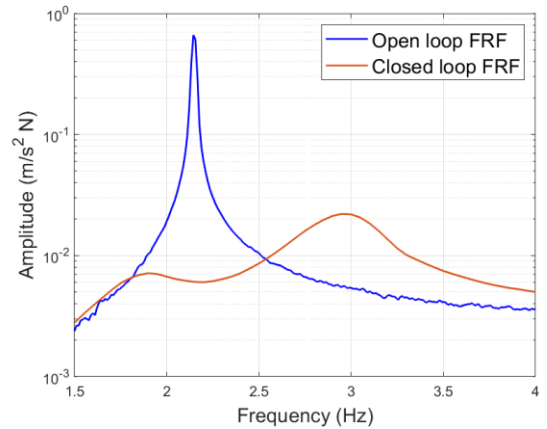


**Figure 18:** Uncontrolled and controlled system frequency response functions between 1.5 and 4 Hz.

### 5.2 Temporal domain validation

Further, the performance of the feedback system in the time domain is studied compared to the uncontrolled system. The response of the systems to a step input is analyzed. The same initial conditions are used to compare the time taken for the two systems to return to rest

position. The maximum displacement of the platform at its midpoint has been limited, so that when a person jumps off the structure, the system starts from a position of constant displacement and zero velocity, making the experiment repeatable for both systems.

Figures 19 and 20 shows the results of this experiment, it is observed that the initial excitation of both systems is practically the same, however, the controlled system stops significantly earlier than the uncontrolled system, specifically, the uncontrolled system takes 121.4 s to reach an acceleration of less than 2% of the initial impulse, while the controlled system takes 4.2 s, which means a reduction of 96.54 %.

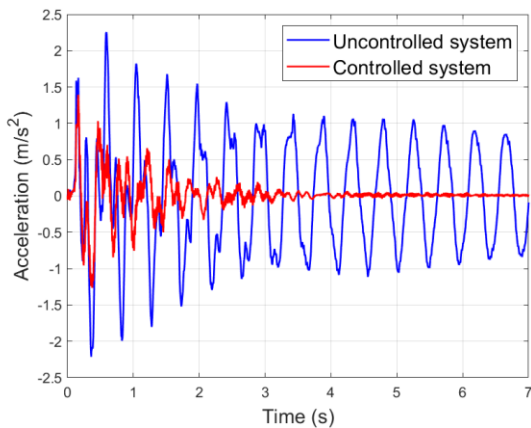


Figure 19: Time response to a step input.

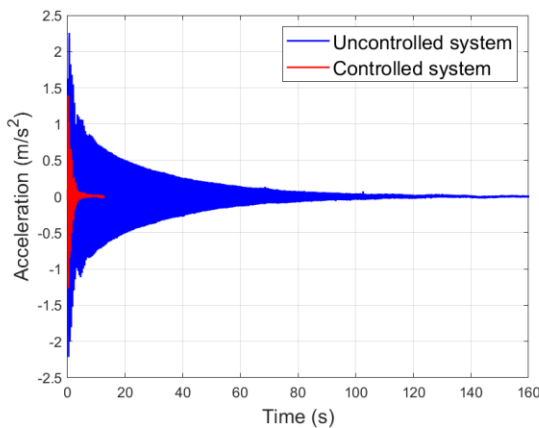


Figure 20: Time response to a step input.

### 5.3 In-transit validation

A walking test was carried out to assess the efficacy of the control device designed. It consisted of walking from one extreme to the other of the footbridge at 2.15 Hz, matching it first vibration mode. The pacing frequency was controlled using a metronome set to 129 beats per minute (bpm). Test was repeated four times, waiting until the platform had completely decelerated between each trial. All the tests were carried out by a person of approximately 700 N.

The results are compared by means of the maximum peak acceleration and the maximum transient vibration value (MTVV) computed from the 1-s running root mean square (RMS) acceleration [5], and they are displayed in Figures 21 and 22. A reduction of 66.07% (from 2.412 to 0.8183  $\text{m/s}^2$ ) when applying the control system may be observed.

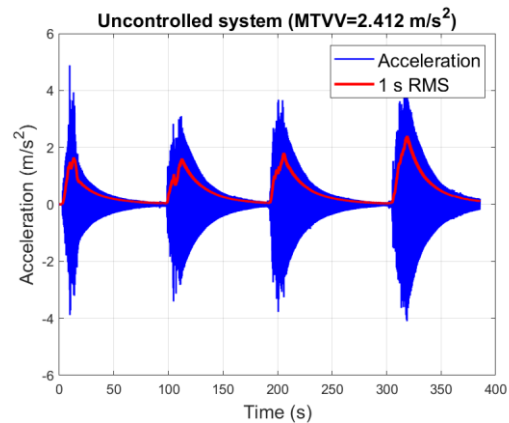


Figure 21: Walking response at 2.15 Hz.

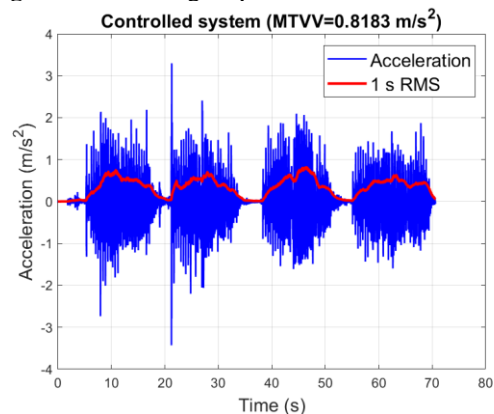


Figure 22: Walking response at 2.15 Hz.

## 6 DISCUSSION, LIMITATION AND CONCLUSIONS

Throughout this paper the mitigation of human-induced vibrations on a lab-scale footbridge using an active control system has been addressed. Once the dynamic properties of both the structure and the actuator were identified after performing an experimental modal analysis, the design and implementation of an active control system were carried out based on a state feedback strategy.

The reduction made of considering the structure as a sdof system limits the control system designed to only mitigate the vibrations associated with the structure's first mode, achieving a 99.09 % reduction in the amplitude response at the first resonant frequency, as well as a 66.07 % MTVV reduction when walking at this frequency. The efficiency of the system has also been validated by evaluating the settling time for a step input, obtaining a 96.54% reduction with respect to the uncontrolled system.

As a consequence of just modeling the structure performance in a frequency range around its first mode, it has been necessary to implement a low pass filter in the controller in order to avoid instabilities due to the dynamics associated to the high frequencies that are beyond the designed model.

This filter restricts the controller's processing time, which limits the cycle time chosen in the system. Lowering this cycle time (currently it is fixed in 1 ms) will make the system act faster, resulting in better performance. Future work in this direction will be to model the structure as a multi-degree-of-freedom system, in order to remove the signal filter, as well as to make the control system able to mitigate several modes simultaneously.

Furthermore, this work has focused on using low-cost means, employing a NI MyRIO 1900 controller, whose cost is 83% lower than other traditional systems of the same brand,

such as the Compact RiO-9030 (608€ vs. 3677€). The accelerometers used (MEMS ADXL355BEZ also represent an important saving of 87% with respect to piezoelectric accelerometers KS76C10 (44€ vs 360€). However, the exciter used is a high-cost commercial device (around 25000€), so that another future line of work is the development of a low cost inertial mass exciter.

**Acknowledgments:** This research was partially funded by the Ministerio de Economía y Competitividad, Spanish Government, through the research project number RTI2018-098425

## REFERENCES

- [1] H. Bachmann. *Case studies of structures with man-induced vibrations*. Journal of Structural, 1992.
- [2] C. Moutiño *Implementation of active and passive control systems in laboratorial and real structures*. Repositório Alberto da Universidade do Porto, 2010.
- [3] *Vibration Control of Active Structures*. Springe (1999).
- [4] C. Casado et al. *Implementation of passive and active vibration control on an in-service footbridge*. Structural Control and health monitoring, 2013.
- [5] ISO 2631-1. *Mechanical Vibration and Shock—Evaluation of Human Exposure to Whole-body Vibration, Part 1, General Requirement*, International Organization for Standardization, 2008.

# PARAMETRIZATION OF A TELESCOPE MOUNT WITH PYANSYS FOR INITIAL MODAL PERFORMANCE EXPLORATION

César Rodríguez Pereira\*, Javier Gracia Rodríguez\*, Ali Ranjbar† and Fernando  
Sánchez Lasheras\*‡

\* Institute of Space Sciences and Technologies of Asturias (ICTEA)  
University of Oviedo 33004 Oviedo, Spain  
e-mail: rodriguezcesar.fuo@uniovi.es  
ORCID: 0000-0001-5523-1381

† Astrophysics Research Institute  
Liverpool John Moores University  
146 Brownlow Hill, Liverpool L3 5RF, UK

‡ Department of Mathematics, Faculty of Sciences  
University of Oviedo, 33007 Oviedo, Spain

**Abstract.** The New Robotic Telescope is designed to be a 4-meter class telescope allowing rapid follow up of transient events, having a pointing time of 30 seconds or less. To achieve this, the structure needs to settle quickly after moving, thus requiring it to be sufficiently rigid. At the same time, it is useful to keep the overall weight low, to lower costs and minimize drive requirements. In this study we present a parametric model of the NRT mount made with PyMAPDL, a new wrapping of the Ansys Mechanical APDL interface, and discuss de advantages of using such tools.

**Key words:** Telescope mount, New robotic telescope (NRT), Finite element Analysis (FEA), PyAnsys.

## 1 INTRODUCTION

The exploration of transient astronomic events such as Supernovae or Gamma Ray Bursts (GRBs) is reaching a new age due to the construction of large-scale survey telescopes (eg. Vera Rubin Observatory LSST) and the observation of new phenomena, such as the gravitational waves detected by LIGO.

These transient events will require quick follow up, as many of them are faint and fade quickly. The NRT is posed to be a 4-meter autonomous telescope, allowing quick response to these rapidly fading transients and other explosive phenomena [1]. The NRT will be located at Roque de los Muchachos on La Palma, Canary Islands.

The telescope consists of a Ritchey-Chrétien design with a 4.18 m of diameter primary mirror, consisting of 18 hexagonal segments and a focal ratio of f/7.5. These 18 segments and their sub-assemblies will have a weight of approximately 150 kg each, amounting to a weight of approximately 2700kg.

The Optical Support System (OSS) comprises this primary mirror (M1), a secondary mirror (M2), the tube that separates both mirrors, the assemblies that support them, an acquisition and guidance box, and the telescope instruments. While some details are yet to be defined, for the purposes of this study, the weight of the OSS will be of 20 tonnes.

This OSS will be mounted on an altitude-

azimuth mount, following a conventional fork configuration that most telescopes of this size use. This configuration consists of a base mounted on top of an Azimuth ring, which allows rotation on the azimuth plane; and two yokes coming up from the base, which attach through the elevation motors and bearings to the OSS, allowing rotation on the altitude plane.

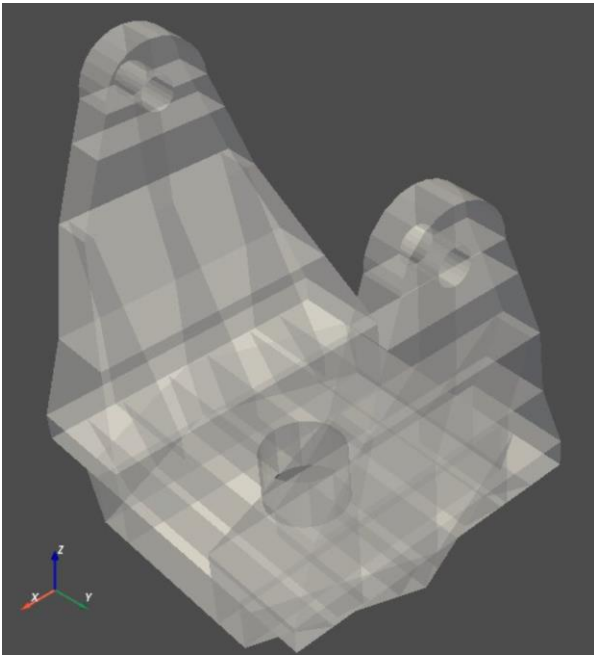


**Figure 1:** 3D model of the mount.

The telescope is required to be able to respond to ultra-rapid events, which require that the pointing operations occur within 30 seconds. A key structural aspect to achieve this pointing time is the Locked rotor resonance frequency of the telescope. In order to improve the design of the mount, this paper focuses on the first few modes that the mount exhibits, as an indicator of overall behaviour and stiffness. A common goal for telescopes of this size is to achieve a first mode greater than 10 Hz.

This mount is parametrized with PyMAPDL. The following sections will delve deeper into PyMAPDL, its advantages respect

other parametrization tools and plain Mechanical APDL scripting. Finally, some initial results derived from the models are presented, although the design and optimization of this mount is an ongoing work.

## 2 MATERIALS AND METHODS

### 2.1 PyMAPDL

All the geometries, meshes and simulation results presented in this article have been made with the use of the PyMAPDL library, which has been used in terms of parametrize every aspect of the model.

It is important to note that Ansys already provides a Python interface through Ansys ACT. The possibility of using this interface for the NRT design was discarded due to ACT being based on IronPython 2.7, which is based on an old implementation of Python that is not compatible with most current libraries.

In terms of parametrization, Ansys Mechanical already offers many capabilities with the added benefit of offering a GUI, but with the downside of having less interoperability with external tools.

PyMAPDL is part of the larger PyAnsys effort to facilitate the use of Ansys directly from Python [2]. It is based around the package `ansys-mapdl-core`, which provides:

- Scripting interface, both a pythonic one and pure APDL tools.
- Plotting of geometry, FEM mesh and results using VTK.
- Access to inputs and results as numpy arrays.

These functionalities tie the well established functionalities and solvers within Mechanical APDL with the vast amount of open source and scientific libraries that are available in Python. This allows different pre-processing pipelines, better handling of the results, the application of a wide variety of readily available optimization algorithms, among many other things.

Another positive point of PyMAPDL is its open-source nature, which allows and encourages collaboration, facilitating rapid development and addition of features when needed by the users themselves. This materializes in a quick update cycle, where some specific issues with the library get fixed within hours of their discovery.

PyMAPDL is based on gRPC or CORBA depending on the version of Ansys it is being used with. These technologies allow the use of the solver as a server, to which the clients send commands, facilitating the use of Mechanical APDL instances running elsewhere.

Despite all these positive points, the use of PyAnsys comes with a few drawbacks, first of which is the lack of a GUI, which makes it so all the work in the FEM stage is code based.

Being a relatively new library, it is very much in development, which means some of its core functionalities are liable to change. Also, the user base is still small, so community support falls upon less people than with other more widely used tools. The documentation is rapidly developing and improving, but it is important to know that the use of PyMAPDL needs some background of pure APDL, of which there are many resources.

## 2.2 Visualization tools

Due to the freedom that the use of PyMAPDL provides, any python visualization tool can be used. For the figures presented in this paper the main 2 libraries used are Holoviews and Pyvista.

The use of Pyvista for the handling of the 3D datasets is natively supported within PyMAPDL, and grants easier and prettier visualizations than the native APDL ones. It also allows easy ways to export results to VTK/VTU, which is easily read with many scientific visualization programs, such as Paraview, to allow further postprocessing

within a GUI interface.

As for Holoviews [3], it is a library that builds on top of other common plotting libraries such as Bokeh, Matplotlib and Plotly. This library is picked mainly for two of its data representations: holomaps and dynamicmaps.

Holomaps are explorable multi-dimensional dictionaries of Holoviews objects. These objects are usually plots, that thanks to the holomap are able to be updated with the use of sliders. This allows for easier exploration of model results, which can be highly dimensional due to the many parameters that can be modified in the mount model.

Dynamicmaps are objects very similar to the Holomaps explained above, but instead of taking a dictionary of plots, it takes a function that returns these plots. This coupled with the ability of wrapping entire models within a single function, provides a tool to interface with the model creation directly, and seeing the output plots as soon as they are ready. This could allow for the creation of future web applications, that interface with a server instance of Mechanical APDL in order to provide a simple way to explore the effect of various parameters without the need for the user to know have any coding skills.

## 3 MOUNT MODEL

The mount FEA model consists mainly of SHELL281 elements that are used to represent the geometry of the mount, having a single MASS21 element representing the OSS. This point mass element is then attached to the rest of the structure through MPC184 elements, which represent a rigid beam. These elements connect to the structure in the trunnion holes.

It is important to note that the elevation axis rigidity is overvalued in this model due to the use of infinitely rigid elements. Later iterations of the telescope models will have to include bearing and motor stiffness in some way. However, for the purposes of this study, which

aims to optimize the LRF, this infinite rigidity is considered adequate.

The boundary condition for the model consists of a circular surface on the bottom plate with  $U_x = U_y = U_z = 0$ . This fixed surface represents the union with the azimuth ring that is below the base. In a similar way to the elevation axis, the behaviour of this surface will be less stiff in the actual telescope, and correctly representing the bearing stiffness is among the future tasks that will be carried out.

The complete mount model, from geometry creation to result extraction has been compiled into a Python function with 40 parameters. These parameters are divided in:

- 1 mechanical APDL instance (mapdl).
- 28 parameters defining the geometry of the mount.
- 8 parameters defining the various steel plate thicknesses
- 1 parameter defining the OSS properties
- 2 parameters that control number of modes to be extracted and element size.

All these parameters have a predefined value (based on the original mount design), except for the mapdl instance. This allows for easy wrapping of the function, in order to work with a lesser number of parameters each time.

The usefulness of having the Mechanical APDL instance as a parameter when encapsulating a model within a function can't be understated: this allows a flexibility in the number of instances running within a single environment and is necessary in order to run large batches of models with a parallel pool of instances.

By running the function with its default values, we get the following mesh (Fig. 2). Running the function solves the model, but the results of this (and other models) will be discussed in the following section.

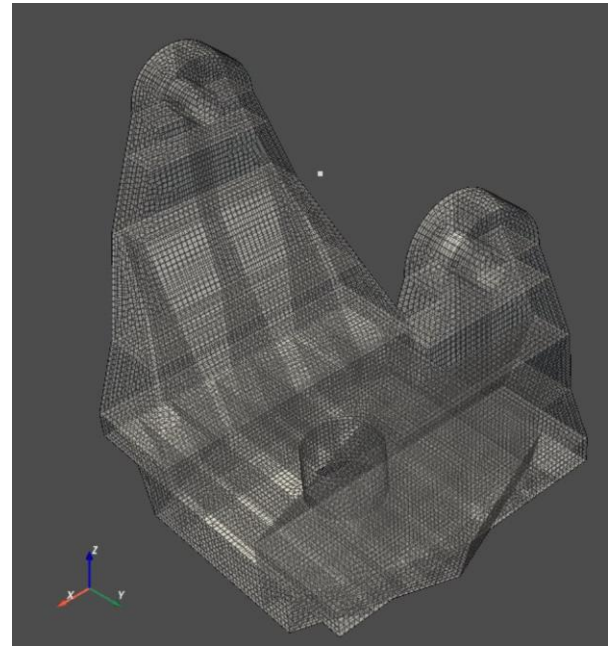


**Figure 2:** FEM mesh. The floating point is attached through MPC elements to the trunnion

## 4 RESULTS

As the design and modelling of the NRT structure is still an ongoing effort, the results presented here are partial and preliminary. Only a few test cases have been run, but in this section we explore the following results:

- Running the function with its default values (that correspond to the preliminary design from [1])
- Simple exploration of the effect overall height has on modal performance.
- Parametric sweep over many combinations of different plate thicknesses

### 4.1 Preliminary design

The preliminary mount design has been previously tested with FEA[1], although due to the nature of design, some of the aspects that were tested have changed. Running a modal analysis for this mount design yields the following mode shapes (Fig. 3 and 4).

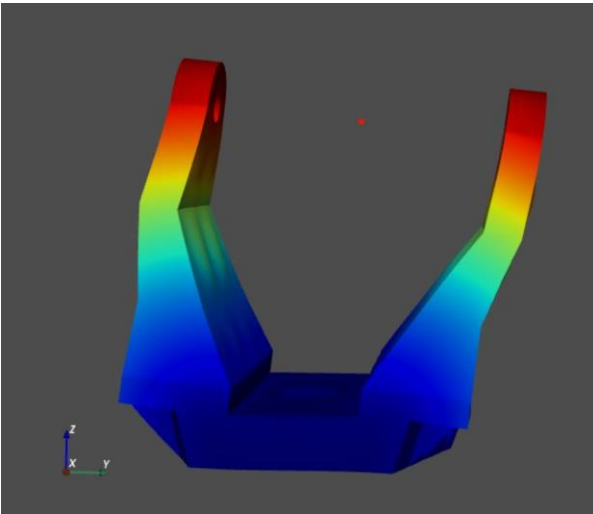


**Figure 3:** First mode shape (16.09 Hz).

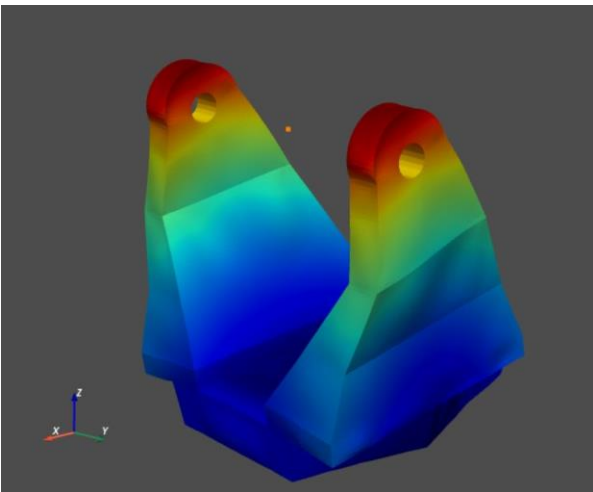


**Figure 4:** Second mode shape (24.33 Hz).

The first mode is found at 16.09 Hz, the second mode at 24.33 Hz and the third one at 37 Hz, for a mount weight of 45 tonnes. Going forward only the first two modes will be considered, as the third mode is composed of local vibrations, that would not affect the whole structure.

It is important to know that these values are overshooting the results a full model of the telescope would give, because of the representation of the OSS as a point mass. Even if its approximate inertia value has been considered, not representing the tube makes the structure stiffer, specially in the second

mode, to which the tube of the telescope would contribute. Thus, even if these values greatly exceed the 10Hz goal that was mentioned in the introduction, the structure would be closer to that performance.

Early testing with a simple tube concept shows both these modes decrease to about 12 and 15 Hz respectively, suggesting that a first mode of 15 Hz could be a good objective for this model.

## 4.2 Effect of overall yoke height

To illustrate and quantify the effect of changing the yoke size, two more models have been run in the same batch as the model from the previous section. In these models the height of each yoke layer height is increased or decreased by 20 %, keeping the proportions the same, but changing the overall height.

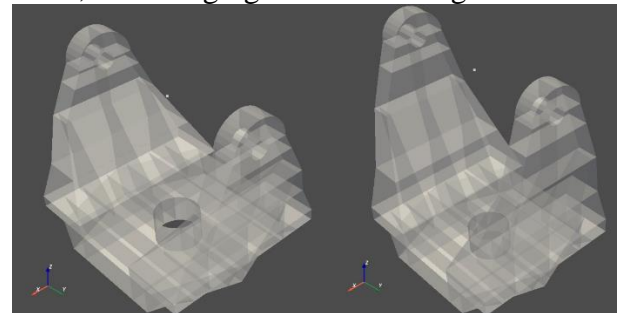


**Figure 5:** 20 % shorter mount (left) and 20% taller mount (right).

After running these models we get the following results (Table 1)

Yoke height	First mode [Hz]	Second mode [Hz]	Mass [t]
Short	21.1	30.9	42.8
Regular	16.1	24.3	45.0
Tall	13.4	21.7	48.3

**Table 1:** Modal performance by yoke length.

As expected, the shorter mount performs better. However, while the increase in modal performance is notable, the change in overall mount mass is only around a 5% in each direction. From this we can see that shortening

the mount would be great for modal performance, while it would have a lesser effect on the azimuth drive.

However, there are important limitations to mount height, because of the space needed between the primary mirror and the base box, to improve image quality. Thus, in order to shorten the mount, the need arises for development of a tube that can be balanced with the primary mirror as close to the elevation axis as possible.

### 4.3 Effect of plate thicknesses

Finally, the effect of changing different plate thicknesses is analysed. The thickness of the following plates has been explored.

- Base box walls
- Base box covers (top and bottom)
- Base box ribs
- Yoke walls
- Yoke horizontal ribs
- Yoke vertical ribs

We have performed a sweep in order to explore all the possible combinations of these parameters. The thicknesses that have been explored are the following:

- 5, 10, 15 and 20 mm for walls
- 2.5, 5, 10 and 15 mm for ribs
- 15, 25 and 35 mm for the base box covers.

The possible combinations of these parameters amount to a total of 3072 models. The exploration of these results involves looking at the first 2 modes and the mount mass, both of which depend on all 6 parameters. This amount of parameters lend themselves to interactive visualization, covered in section 2.2 of this paper, as representing the whole input and output space would be way more complicated otherwise.

For the purposes of this section, a holomap is chosen as the best exploration tool. This requires for all the models to be run beforehand. While it would be possible to run

each parameter combination on demand with the use of a dynamicmap, this would require a coarser mesh in order to feature the same level of interactivity, as every model would have to run in a really short time every time the sliders are moved.

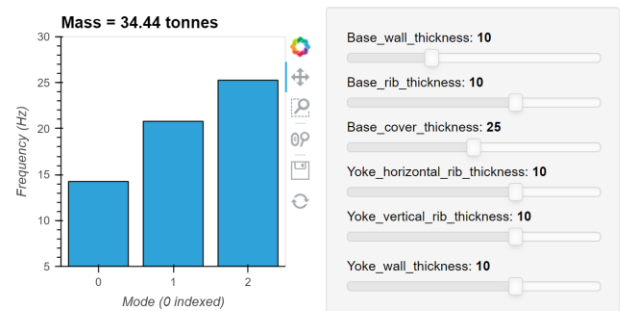


**Figure 6:** Holomap of the thickness exploration results

With this tool it is easy to explore the results of hundreds of models in a quick way. Figure 7 shows a parameter selection that complies with the modal performance requirements, while being approximately 10 tonnes lighter than the preliminary design. It is possible to get closer to these requirements, but further optimization will be done in the future, in models that incorporate the OSS behaviour.

Also, while manually exploring results is important, as it provides the design engineer with deeper understanding of the structure, automatic optimization of some of these parameters could prove a useful tool for the final design.

## 5 CONCLUSIONS AND FUTURE WORK

Although the results and methodology presented in this study are preliminary and part of an ongoing work, there are some key takeaways that can be obtained from it.

- PyMAPDL proves to be a tool that is already suitable for the development of big projects, allowing a modular

and parametric approach to design. It also shows great potential for being used in conjunction with other already established Python libraries.

- Interfacing with highly dimensional parametric models through interactive visualizations can help quick understanding about how each parameter affects modal performance
- The proposed design for the mount works as intended and is suitable for the modal performance needs that are required. However, there are many optimizations that can be made, both to plate thicknesses and to the size of different parts.

Due to the preliminary nature of this study, it opens a lot of avenues for future work and improvements, such as the following:

- Integration of the mount with parametric models of the OSS.
- Representation of the stiffness of motors and bearings.
- Dynamic simulation of the telescope movement and settling time.
- Optimization of the structure with the use of multiparameter optimization techniques, such as genetic algorithms.

## REFERENCES

- [1] Ranjbar, A., Copley, D., Steele, I. A., Harvey, E. J., Torres, M., Oria, A., & Rodríguez, J. G. (2020, December). Conceptual design of a fast-slewing mount for the New Robotic Telescope. In *Ground-based and Airborne Telescopes VIII* (Vol. 11445, p. 1144556). International Society for Optics and Photonics.
- [2] Kaszynski, A. (2020). Pyansys: Python Interface to MAPDL and Associated Binary and ASCII Files. *Zenodo*. DOI: 10.5281/zenodo.4009467
- [3] Philipp Rudiger, Jean-Luc Stevens, James A. Bednar, Bas Nijholt, Jon Mease, Andrew, ... Lukas Barth. (2021). holoviz/holoviews: Version 1.14.4 Zenodo. DOI: 10.5281/zenodo.4775303

## KALMAN-BASED VIRTUAL SENSING FOR STRUCTURAL HEALTH MONITORING

**B. Mora\***, **J. Basurko\*\***, **U. Leturiondo\*\*\*** and **J. Albizuri†**

\* Ikerlan Technology Research Centre, Basque Research and Technology Alliance (BRTA). P<sup>o</sup>. J. M<sup>a</sup>. Arizmendiarieta, 2. 20500 Arrasate/Mondragón.  
e-mail: bmora@ikerlan.es  
ORCID: 0000-0002-2174-5103

\*\*Ikerlan Technology Research Centre, Basque Research and Technology Alliance (BRTA). P<sup>o</sup>. J. M<sup>a</sup>. Arizmendiarieta, 2. 20500 Arrasate/Mondragón.  
e-mail: jbasurko@ikerlan.es  
ORCID: 0000-0003-3982-785X

\*\*\*Ikerlan Technology Research Centre, Basque Research and Technology Alliance (BRTA). P<sup>o</sup>. J. M<sup>a</sup>. Arizmendiarieta, 2. 20500 Arrasate/Mondragón.  
e-mail: uleturiondo@ikerlan.es  
ORCID: 0000-0003-4913-6438

† Escuela de Ingeniería de Bilbao (Universidad del País Vasco). Ingeniero Torres Quevedo Plaza, 1, 48013 Bilbao.  
e-mail: joseba.albizuri@ehu.es  
ORCID: 0000-0002-4516-694X

**Abstract.** Virtual sensing techniques use available data from a limited set of sensors to obtain estimated data at unmeasured points. These techniques are of interest in the field of structural health monitoring, where they allow reducing the number of sensors and obtaining estimated measurements at points of a structure where placing a sensor is not feasible. Several approaches for implementing virtual sensing have been found in the literature, but a lack of consensus has been detected on which techniques are more suitable depending on the circumstances. In this paper, various model-driven algorithms based on the Kalman filter are tested estimating strain and acceleration data using different sensor configurations and different input excitations. Reduced structural models obtained from FE models and acceleration and strain measurements are used by the estimation algorithms. A case study based on a scaled offshore wind turbine tower, that includes nacelle and jacket support structure, is used to apply the proposed methodology and evaluate the results. Two estimation algorithms, the Augmented Kalman filter and the Dual Kalman filter, are compared using different sensor configurations, and then the obtained estimates are validated using reference sensors located at the same point as the virtual sensors, first in a simulated environment and then in a laboratory case study. In the simulated case, it is observed that the Augmented Kalman filter performs better when strain gauges and accelerometers are combined, while the Dual Kalman filter provides better results when using a single class of sensors. In the laboratory environment, despite the increase in error caused due to possible inaccuracies of the model, correct estimates are obtained.

**Key words:** Virtual sensing, Structural health monitoring, Model reduction, Kalman filter.

## 1 INTRODUCTION

Structural health monitoring (SHM) is the field of the engineering that focuses on sensing and monitoring structural facilities, with the aim of detecting possible damage and make predictions of the remaining useful life of the critical components, increasing safety and allowing the optimization of maintenance actions [1]. SHM systems require to know real data through sensors, but not always is possible to place them at points of interest. The technique of obtaining measures from a system not directly with a physical sensor but using data inference from other sensors is known as virtual sensing (VS) [2]. The use of virtual sensors in SHM is of interest to face scenarios such as the need to obtain measurements at points where it is not technically feasible to locate a real sensor [3], or in cases where it is necessary to obtain measurements from a large number of points, requiring a too extensive sensor network [1]. The application of virtual sensors therefore offers both technical and economic advantages. VS techniques can be classified into two main groups: data-driven methods and model-based methods [4]. On the one hand, data-driven techniques use data obtained from real sensors as training data to create numerical relations between the real and virtual sensors, avoiding the need of a physical model of the system [5]. On the other hand, model-based techniques require the definition of a model capable of describing the physical behavior of the system. Model-based techniques can be classified in two main groups: stochastic techniques, where it is assumed that the model and sensor data have certain degree of uncertainty, and deterministic techniques, where uncertainties are not assumed [6].

Data-driven techniques are useful for creating virtual sensors in systems that are very complex to model. Each virtual sensor consists of a unique numerical relation with the real

sensors of the system, obtained by a large quantity of real data used as training. These techniques can be inflexible because if some sensors are relocated or added, or if some parameters of the system change, all virtual sensors must be redefined. Moreover, real data series must be available for training the virtual sensors, which is not always possible [7].

Deterministic model-based techniques are limited by the precision of the model used. Their application in virtual sensing is very limited when the definition of a sufficiently precise model becomes too difficult due to the complexity of the system [8]. Stochastic model-based techniques are therefore considered more suitable due to their ability to reduce the impact of measurement and modeling errors on the estimates [9].

In 1960, Rudolph Kalman raised the today known as Kalman filter (KF), which became the basis of stochastic model-based estimation [10]. In its classical approach, the KF needs the inputs to the system to be known, which is often not possible in SHM applications, so alternative versions of the KF have been proposed over the years. Two main solutions for the mentioned problem have been identified in the bibliography: the two-stage KF implementation (which for every time step estimates the states and the inputs separately) and the combined implementation of the KF with the augmented state-space (which estimates the inputs together with the states of the system).

The use of the two-stage filter architecture started in 1969 when Glover proposed a pioneering KF-based recursive filter capable of estimating both states and inputs [11]. In 1987, P. Kitanidis proposed a recursive algorithm for linear state estimation with unknown inputs, bypassing the estimation of the inputs themselves. His algorithm used a linear unbiased minimum-variance estimation. [12]. Kitanidis' work was later extended by Darouach and Zasadzinski [13]. Gillijns and

De Moor combined the work of Kitanidis and Hsieh obtaining a two-stage KF with a linear unbiased minimum-variance estimation [14]. The obtained algorithm was later applied in combination with reduced-order models to obtain state and input estimates from structures using vibration data from a limited number of accelerometers [15]. Based on the previous work, Papadimitriou et al. proposed in 2015 the Dual Kalman filter (DKF), capable of obtaining state and input estimates from limited acceleration data with the aim of estimating fatigue damage accumulation in structures.

The use of the KF in combination with the augmented state-space also began in 1969 with the work proposed by B. Friedland for state estimation with unknown inputs [16]. In 2010, E. Lourens et al. used the KF with the augmented state-space for dynamic force identification [17], and the following year they consolidated the so-called Augmented Kalman filter (AKF) [8], which has been used in later publications [18].

The contribution of this paper is to exemplify the implementation of a VS system in a real case, comparing the performance of the DKF and the AKF algorithms both in a simulation framework and in a real environment, using different load cases and different sensor combinations.

The paper is organized as follows. In section 2, the theoretical background is presented, covering the modeling process, the model reduction techniques, and the estimation algorithms. In section 3, the abovementioned algorithms are validated through a case study. The obtained results are shown in section 4, and the conclusions of the paper are presented in section 5.

## 2 THEORETICAL BACKGROUND

This section describes the theoretical bases used in this work, referring mainly to modeling methods and estimation algorithms.

### 2.1 System modeling

A model able to describe the dynamical behavior of a structure is typically formulated as a second order differential as shown in equation (1), where  $\mathbf{q}(t)$  is the displacement vector (with  $n \times 1$  dimension),  $\mathbf{M}$ ,  $\mathbf{C}_D$  and  $\mathbf{K}$  being the stiffness, damping and mass matrix respectively (with  $n \times n$  dimension) and  $\mathbf{f}(t)$  being the external forces vector (with  $n \times 1$  dimension), where  $n$  is the number of degrees of freedom (DoFs) of the model. This formulation is hereinafter referred to as MCK modeling.

$$M\ddot{\mathbf{q}}(t) + C_D\dot{\mathbf{q}}(t) + K\mathbf{q}(t) = \mathbf{f}(t) \quad (1)$$

To facilitate the resolution of the equation (1) by numerical solvers, an MCK model can be described as a state-space system as seen in expression (2). A state-space system consists of two equations: the state equation (above) and the output equation (below).  $\mathbf{x}$  is the state vector, with  $2n \times 1$  dimension. As shown in expression (3), the state vector contains the displacements and the velocities of each DoF.  $\mathbf{u}$  is the inputs vector, and with  $n$  dimension, contains the possible external input for each DoF.  $\mathbf{A}$  and  $\mathbf{B}$  are the state and input matrices respectively. As it seen in the expressions (4) and (5), the dimensions of these matrices are  $2n \times 2n$  and  $2n \times n$ . The elements of the output equation: the output vector  $\mathbf{y}$  and the output and feedthrough matrices  $\mathbf{C}$  and  $\mathbf{D}$ , have no fixed dimensions; they change according to the desired output variables.

$$\begin{cases} \dot{\mathbf{x}} = \mathbf{A}\mathbf{x} + \mathbf{B}\mathbf{u} \\ \mathbf{y} = \mathbf{C}\mathbf{x} + \mathbf{D}\mathbf{u} \end{cases} \quad (2)$$

$$x = \begin{pmatrix} q \\ \dot{q} \end{pmatrix} \quad (3)$$

$$A = \begin{bmatrix} 0 & I \\ -M^{-1}K & -M^{-1}C_D \end{bmatrix} \quad (4)$$

$$B = \begin{bmatrix} 0 \\ M^{-1} \end{bmatrix} \quad (5)$$

## 2.2 Model reduction

To simulate the behavior of a structural system, finite elements (FE) models are used, which usually contain a large quantity of DoF. Model reduction methods allow to significantly reduce the number of DoF of a model maintaining a sufficient precision in their behavior. Two model reduction methods are used in this study: Guyan reduction and modal truncation. These methods are chosen due to their simplicity and their convenience with the estimation algorithms used.

### 2.2.1 Guyan reduction

Guyan method was first proposed by Robert Guyan in 1965 [19]. First, a set of master nodes has to be selected, which will be the nodes of the reduced model. If a FE model has  $m$  total nodes and  $p$  selected master nodes, the number of slave nodes (the rest of nodes) is  $m-p=s$ . The Guyan-reduced model is obtained with the equation (6) from the MCK equation (1) assuming there is no damping.  $\mathbf{M}_{p \times p}$  and  $\mathbf{K}_{p \times p}$  are the reduced matrices.  $\mathbf{x}_p$  is the displacement vector of the master nodes.  $\mathbf{M}_{s \times s}$  and  $\mathbf{K}_{s \times s}$  are the matrices corresponding to the slave nodes and  $\mathbf{x}_s$  is the displacement vector of the slave nodes. A proportional damping reduced matrix can be obtained from the reduced stiffness and mass matrices.

$$\begin{bmatrix} M_{pp} & M_{ps} \\ M_{sp} & M_{ss} \end{bmatrix} \begin{pmatrix} \ddot{x}_p \\ \ddot{x}_s \end{pmatrix} + \begin{bmatrix} K_{pp} & K_{ps} \\ K_{sp} & K_{ss} \end{bmatrix} \begin{pmatrix} x_p \\ x_s \end{pmatrix} = \begin{pmatrix} F_p \\ 0 \end{pmatrix} \quad (6)$$

### 2.2.2 Modal truncation

A dynamical model can be described with its mode shapes, through a transformation with the mode shape matrix  $\Phi$ . Each column of  $\Phi$  corresponds to an eigenvector, associated to an eigenvalue ( $\lambda_i$ ). The square root of every eigenvalue corresponds to a natural angular frequency of the system ( $\omega_i$ ). The  $\Phi$ -transformation implies a domain change for the model, from the physical domain (with cartesian base) to the modal domain [20].  $\Phi$  can be obtained solving the equation (7), discarding the trivial solution  $\Phi=0$ .  $\Phi$  is considered mass-normalized when expression (8) is satisfied. A dynamical model can be described with its mode shapes, through a transformation with the mode shape matrix  $\Phi$ . Each column of  $\Phi$  corresponds to an eigenvector, associated to an eigenvalue ( $\lambda_i$ ). The square root of every eigenvalue corresponds to a natural angular frequency of the system ( $\omega_i$ ). The  $\Phi$ -transformation implies a domain change for the model, from the physical domain (with cartesian base) to the modal domain [20].  $\Phi$  can be obtained solving the equation (7), discarding the trivial solution  $\Phi=0$ .  $\Phi$  is considered mass-normalized when expression (8) is satisfied.

$$(K - \lambda M)\Phi = (K - \omega^2 M)\Phi = 0 \quad (7)$$

$$\Phi^T M \Phi = I \quad (8)$$

In its full form,  $\Phi$  contains as many mode shapes as DoF the model has, but it is possible to reduce the model removing the modes out of the frequency range of interest (modal truncation). For a  $k$  number of modes of interest,  $\Phi$  is reduced to  $\Phi_K$  (9), being its dimension reduced to  $n \times k$  [21].

$$\Phi_{(n,k)} = [\Phi_1, \Phi_2 \dots \Phi_k] \quad (9)$$

The MCK equation of the model (1) is

transformed into the generalized MCK equation (10), that can also be expressed as follows (11).  $\mathbf{z}(t)$  is the vector of modal displacements (also known as generalized displacements), obtained with the transformation  $\mathbf{q}(t) = \Phi_K \mathbf{z}(t)$ .

$$\Phi_k^T M \Phi_k \ddot{\mathbf{z}}(t) + \Phi_k^T C_D \Phi_k \dot{\mathbf{z}}(t) + \Phi_k^T K \Phi_k \mathbf{z}(t) = \Phi_k^T \mathbf{f}(t) \quad (10)$$

$$\ddot{\mathbf{z}}(t) + 2\xi\omega\dot{\mathbf{z}}(t) + \omega^2\mathbf{z}(t) = \Phi_k^T \mathbf{f}(t) \quad (11)$$

### 2.3 Measurement

The model receives data from the real system via the sensors. Sensor data is introduced in the model in a discrete-time approach (where subscript  $t$  represents the time index). For that purpose, the state-space model (2) is reformulated as the expression (12), where  $w$  and  $v$  are the uncertainties (represented as zero-mean white noises) associated to the process and the inputs respectively.  $z$  is the measurement vector of size  $r$  (number of sensor channels), whose data are incorporated into the model through the observation matrix  $\mathbf{H}$ . System matrices  $\mathbf{A}$  and  $\mathbf{B}$  must be discretized, as seen in (13) and (14).

$$\begin{cases} x_{t+1} = Ax_t + Bu_t + w_t \\ z_t = Hx_t + v_t \end{cases} \quad (12)$$

$$A_{(disc.)} = e^{A\Delta t} \quad (13)$$

$$B_{(disc.)} = (e^{A\Delta t} - I)A^{-1}B \quad (14)$$

The observation matrix  $\mathbf{H}$  has  $r \times 2n$  dimension, containing a row for each sensor channel. Each row of  $\mathbf{H}$  incorporates the sensor data to the state vector every step of time. The content of  $\mathbf{H}$  depends on the physical quantity measured by each sensor. For SHM approaches, the most used sensors are accelerometers and strain gauges [22] [17]. To incorporate acceleration data to the model, the following row must be incorporated into the

observation matrix (15).

$$H_{ai}: [-M_i^{-1}K_i \quad -M_i^{-1}C_{Di}] \quad (15)$$

Strain measurements are estimated using strain coefficients, which relate strain at a specific point with the DoFs of the model. Strain coefficients can be defined in cartesian basis ( $SC$ ) or modal basis ( $MSC$ ). In each case,  $SCs$  or  $MSCs$  must be incorporated to its corresponding row in the observation matrix (16) (17). It should be highlighted that the coefficients are obtained through the FE model.

$$H_{gi}: [SC_{1i}, SC_{2i}, SC_{3i} \dots 0, 0, 0 \dots] \quad (16)$$

$$H_{gi}: [MSC_{\Phi_{1i}}, MSC_{\Phi_{2i}} \dots 0, 0, \dots] \quad (17)$$

### 2.4 Virtual measurement

As mentioned in section 1, the KF approach is used in this paper for data estimation at unmeasured points. The standard KF works in three phases: for each time step, first a prediction of the model state is made based on known information from the previous state. Then, observation data (measurements from real sensors) is obtained. Finally, the state prediction is corrected using the observation data.

The standard KF can be implemented in five substeps, which are executed recursively every time step. In the first substep, a prediction of the state is made based on the states of the previous time interval and the current inputs (18). In the second substep, a prediction of the estimator covariance ( $\mathbf{P}(t)$ ) is made, starting from the predicted covariance in the previous interval (19). In the third substep, the optimal filter gain is calculated for the present time interval (20). In the fourth substep, the prediction of the state previously made is corrected based on the calculated gain and the observation data (21). In the last substep, the

filter covariance is corrected based on the calculated gain (22).

$$x_t = Ax_{t-1} + Bu_t \quad (18)$$

$$P_t = AP_{t-1}A^T + Q \quad (19)$$

$$K_{GAIN} = P_t H^T (HP_t H^T + R)^{-1} \quad (20)$$

$$x_t^{updated} = x_t + K_{GAIN}(z_t - Hx_t) \quad (21)$$

$$P_t^{updated} = P_t - K_{GAIN}HP_t \quad (22)$$

The uncertainties  $w$  and  $v$  are incorporated into the KF using covariance matrices, which contain in their diagonal the standard deviations ( $\sigma^2$ ) associated with each state and each measurement.  $\mathbf{Q}$  is the covariance matrix associated to the process (23), with  $2n \times 2n$  dimension.  $\mathbf{R}$  is the covariance matrix associated to the measurements (24), with  $r \times r$  dimension.  $\mathbf{P}$  is the covariance matrix of the estimator itself, with  $2n \times 2n$  dimension. Unlike  $\mathbf{Q}$  and  $\mathbf{R}$ , which remain constant during the estimator operation,  $\mathbf{P}$  is updated in every time step. Therefore, only an initial state ( $\mathbf{P}_0$ ) has to be selected (25).

$$Q = \text{diag}(\sigma_{Q11}^2, \sigma_{Q22}^2, \dots, \sigma_{Q2n2n}^2) \quad (23)$$

$$R = \text{diag}(\sigma_{R11}^2, \sigma_{R22}^2, \dots, \sigma_{R2n2n}^2) \quad (24)$$

$$P_0 = \sigma_P^2 I_{2n2n} \quad (25)$$

The standard KF needs the system inputs to be known. The AKF and the DKF, two KF-based algorithms that are able to perform with unknown inputs, are used in this article.

### 2.4.1 Augmented Kalman filter

The AKF is basically a standard KF with a model described in an augmented state space, where the inputs are incorporated into the state vector. The augmented state matrix ( $\mathbf{A}^*$ ), a

modification of the conventional state space matrix, is composed of the  $\mathbf{A}$  and  $\mathbf{B}$  matrices (26), with (27) standing for its discretized version. The augmented state vector ( $\mathbf{x}^*$ ) is made up of the displacements and velocities of each DoF and the input forces (28). Note that the observation matrix is also augmented (29). The unknown input is modeled as a zero mean random walk model (30).

$$A^* = \begin{bmatrix} A & B \\ 0 & I \end{bmatrix} \quad (26)$$

$$A^*_{(disc.)} = \begin{bmatrix} e^{A\Delta t} & (e^{A\Delta t} - I)A^{-1}B \\ 0 & I \end{bmatrix} \quad (27)$$

$$x^* = \begin{pmatrix} q \\ \dot{q} \\ u \end{pmatrix} \quad (28)$$

$$H^* = \begin{bmatrix} SC & 0 & 0 \\ -M^{-1}K & -M^{-1}C_D & M^{-1} \end{bmatrix} \quad (29)$$

$$u_t = 0 + w_{u_t} \quad (30)$$

### 2.4.2 Dual Kalman filter

The DKF is based on a double implementation of the standard Kalman filter. For each time step a prediction-update of the inputs and a prediction-update of the states are performed independently. Unlike the AKF, the DKF does not use a non-augmented state space. Process and filter covariance matrices have to be defined for both the states and the input, being  $\mathbf{Q}$  and  $\mathbf{P}$  the state covariance matrices and  $\mathbf{Q}_U$  and  $\mathbf{P}_U$  the input covariance matrices. Two observation matrices are defined: the state observation matrix  $\mathbf{G}$  (31) and the input observation matrix  $\mathbf{J}$  (32).

$$G = \begin{bmatrix} PF & 0 \\ -M^{-1}K & -M^{-1}C_D \end{bmatrix} \quad (31)$$

$$J = \begin{bmatrix} 0 \\ M^{-1} \end{bmatrix} \quad (32)$$

The implementation of the DKF can be done in ten substeps: five for the inputs estimation and five for the states estimation. Inputs estimation phase (33) (34) (35) (36) (37)

and states estimation phase (38) (39) (40) (41) (42) have the same structure as the conventional KF, with the difference that in the inputs estimation phase, due to the absence of real sensors for inputs measurement, the inputs prediction is improved using an estimated observation created using the previous state estimation and the available sensor data [23].

$$u_t = u_{t-1} \quad (33)$$

$$P_{U_t} = P_{U_{t-1}} + Q_U \quad (34)$$

$$K_{U\_GAIN} = P_{U_t} J^T (J P_{U_t} J^T + R)^{-1} \quad (35)$$

$$u_t^{updated} = u_t + K_{U\_GAIN} (z_t - G x_t - J u_t) \quad (36)$$

$$P_{U_t}^{updated} = P_{U_t} - K_{U\_GAIN} J P_{U_t} \quad (37)$$

$$x_t = A_{(disc.)} x_{t-1} + B_{(disc.)} u_t \quad (38)$$

$$P_t = A_{(disc.)} P_{t-1} A_{(disc.)}^T + Q \quad (39)$$

$$K_{GAIN} = P_t G^T (G P_t G^T + R)^{-1} \quad (40)$$

$$x_t^{updated} = x_t + K_{GAIN} (z_t - G x_t - J u_t) \quad (41)$$

$$P_t^{updated} = P_t - K_{GAIN} G P_t \quad (42)$$

### 3 CASE STUDY

The VS techniques described in this paper are applied to a lab prototype for validation purposes. The process described in Figure 3 has been followed for the implementation of virtual sensors and validation of the obtained results. Once a FE model of the system is created, the model is calibrated first adjusting its mass and later matching its mode shapes and their corresponding frequencies to the ones of the real system. The model is then simplified by applying a reduction method and converted into a set of linear equations. In parallel, the

real system is sensorized with the aim of obtaining real data measurements for the estimator. Once the model and the inputs are defined, an estimation algorithm is implemented to generate virtual sensors, which are validated placing real sensors in their locations, comparing estimated data with real data.

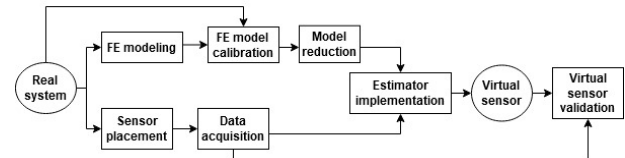


Figure 1: workflow followed for the implementation and validation of virtual sensors.

### 3.1 Prototype

The case study, seen in Figure 2, consists of a scaled offshore wind turbine tower prototype placed on a jacket support structure. An oscillator is installed at one end of the nacelle to apply forces.

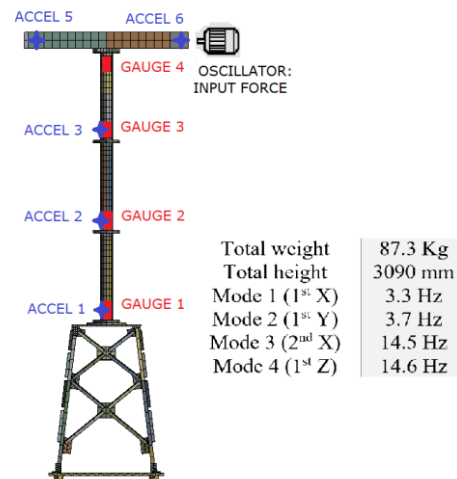


Figure 2: illustration of the prototype, including main features and sensor locations.

### 3.2 Modeling

A FE model of the prototype is implemented in a FE software. The model is

calibrated by adjusting the stiffness of the flexible mounts that connect the jacket to the ground and the Young modulus of the model, searching that the natural frequencies and mode shapes of the model to coincide as much as possible with those of the real system. Once the FE model is adjusted, the reduced model matrices are obtained. Both reduction methods above mentioned are performed: a 7-node model is used as Guyan's reduction example, and a 6-mode model is used as modal truncation example. The response of both reduced models is compared to the response of the full FE model in order to validate the reduced models.

### 3.3 Sensor placement

To decide the location of the sensors, first the lab prototype is divided into 6 sensing points, similarly spaced between them. Points 1, 2, 3 and 4 correspond to the junction points between the tower segments, with point 1 at the joint between the base of the tower and the jacket support, and point 4 at the joint between the top of the tower and the nacelle. Points 5 and 6 correspond to each end of the nacelle, being 6 the point where the external force is applied. Four strain gauges are placed at points 1, 2, 3 and 4 in the axial direction, and four triaxial accelerometers are placed at points 1, 2, 3, 5 and 6. The placement of a large number of sensors allows the subsequent use of different sensor configurations, making it possible to locate the virtual sensors in any of the sensorized points and validate the obtained virtual data with real data. Sensor locations can be seen in Figure 2.

### 3.4 Validation criteria

The estimated measurements by the virtual sensors are compared to the equivalent real measurements to validate the VS techniques. For this purpose, two time series comparison methods are used to evaluate how close the

estimates are to the real measurements: variance ratio and peaks ratio. The variance ratio, shown in expression (43), compares the variance of the estimated data with the variance of the (real) reference data. The closer the var. ratio approaches 1, the more accurate the estimate is.

$$ratio_{var} = \frac{\sigma^2_{est}}{\sigma^2_{real}} \quad (43)$$

The peaks ratio, shown in expression (44), compares the values of the local peaks of the estimation data with the values of the local peaks of the real data. To obtain this coefficient, a peak-finding algorithm is needed. The summation of the absolute value of the detected positive and negative peaks divided by the number of peaks found is obtained both for the estimation and the reference data. The ratio is obtained by dividing the smallest summation by the largest, with the objective of keeping the ratio always below 1.

$$ratio_{peaks} = \frac{\left( \frac{\sum |peaks_{est}|}{num. peaks_{est}} \right)}{\left( \frac{\sum |peaks_{real}|}{num. peaks_{real}} \right)},$$

$$if \frac{\sum |peaks_{est}|}{num. peaks_{est}} < \frac{\sum |peaks_{real}|}{num. peaks_{real}}$$

$$ratio_{peaks} = \frac{\left( \frac{\sum |peaks_{real}|}{num. peaks_{real}} \right)}{\left( \frac{\sum |peaks_{est}|}{num. peaks_{est}} \right)}, \quad (44)$$

$$if \frac{\sum |peaks_{est}|}{num. peaks_{est}} > \frac{\sum |peaks_{real}|}{num. peaks_{real}}$$

In this paper, a mean value of the average of the two described ratios, (43) and (44), is used to simplify the results obtained (45). The closer the averaged ratio (avr) approaches 1, the more accurate the estimate is.

$$ratio_{averaged} = \frac{ratio_{peaks} + ratio_{var}}{2} \quad (45)$$

If the avr is in a range between 0.9 and 1.1, the estimation is evaluated with the mark ✓; if it is outside the above mentioned range but between 0.5 and 1.5, is evaluated with the mark !; and if it is out of these ranges, as ✗. If the estimation diverges, it is indicated with “-”.

### 3.5 External excitations

For the simulation tests, synthetic input excitations are generated and applied at one end of the nacelle (near point 6) in the nacelle axis direction. Four different input excitations are generated: a zero-mean 0-60Hz white noise with a standard deviation of 120N, a 5Hz and a 15Hz zero-mean sinus, both with a 120N amplitude and a 50N impact. For the real tests, four different input excitations, similar to those used in the simulated environment, are applied at one end of the nacelle with the oscillator: a zero-mean 4-25Hz white noise, a 5Hz and a 15Hz zero-mean sinus and an impact. The amplitude of the inputs in the real tests is unknown, due to the lack of a force sensor in the lab prototype. Simulation tests are performed with a sampling rate of 1000Hz, while real tests are performed with a sampling rate of 1652Hz.

## 4 RESULTS

The VS techniques described in this paper are validated through their implementation in the mentioned case study. The validation process is first performed in a simulated environment, where observation data does not come from real sensors but from a transient simulation carried out using the same model as the one implemented in the estimation algorithms. Different sensor configurations are tested. The configurations that work properly in the simulated environment are tested using observation data from real sensors. A virtual

strain gauge and a virtual accelerometer are ubicated at point 1. The data estimated by these virtual sensors are compared with simulated or real data (depending on the case) provided by the sensors located at point 1.

### 4.1 Simulated environment

The two estimation algorithms used in this paper, the AKF and the DKF, are first tested using synthetic observation data, coming from a transient simulation that uses the same model as the one implemented in the algorithms, with the aim of avoiding possible modeling errors. Artificial gaussian zero-mean white noise is added to the synthetic measurements to generate some uncertainty in them. Four sensor configurations (described in Table 2) are tested.

Sensor config.	g2	g3	g4	a2	a3	a5	a6
3-4	x	x	x	x	x	x	x
3-0	x	x	x				
0-4				x	x	x	x
1-1		x					x

**Table 1:** sensors used in each sensor configuration. *g* stands for strain gauge and *a* stands for accelerometer.

Sensor config.	White noise	Sin 5Hz	Sin 15Hz	Impact
3-4 (g)	✓/✓	✓/✓	✓/!	✓/✓
3-4 (a)	✓/✓	✓/!	✓/!	✓/✗
3-0 (g)	-/!	-/!	✗/!	-/!
3-0 (a)	-/-	-/-	✗/✓	-/-
0-4 (g)	!/!	✗/✓	-/!	-/✓
0-4 (a)	✓/✓	✓/!	✓/!	✓/✓
1-1 (g)	✓/!	✓/✗	✓/!	✓/✓
1-1 (a)	✓/✗	✓/-	✓/✗	✓/✓

**Table 2:** results obtained in the simulated environment. AKF results are to the left of the “/” and DKF results are to the right.

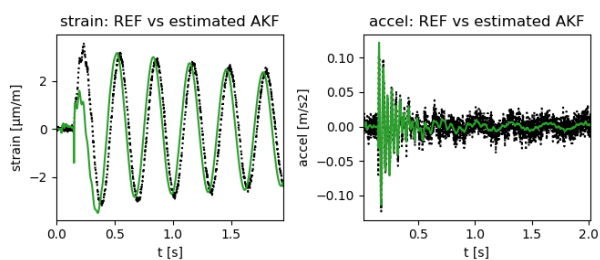


**Figure 3:** example of strain and acceleration estimation in the simulated environment using the AKF and the 3-4 configuration. Black signal corresponds to the reference signal and green signal corresponds to the estimation.

The obtained estimates are shown in tables 3 and 4. (*g*) stands for virtual gauge and (*a*), for virtual accelerometer. The AKF provides highly accurate estimates when using the sensor configurations that combine both types of sensors (3-4 and 1-1). A significant loss of precision is observed when the sensor configurations with only one type of sensor are used: a total malfunction occurs when only strain gauge data is used as input data (config. 3-0), and only the acceleration is correctly estimated when only accelerometer data is used as input data (config. 0-4). The DKF in general shows less precision, but relatively accurate strain estimates are obtained using the sensor configurations with only a type of sensors. The acceleration estimates obtained with the impact excitation (marked with \* in the tables 3 and 4) show less accuracy than those obtained with other excitations, but this is explained by the characteristics of the signal. After the impact, the measured acceleration quickly vanishes, remaining the noise from the sensors. The existing error between this noise and the estimated signals causes the decrease of the accuracy ratios.

#### 4.2 Real environment

After validating the two used estimation algorithms in a simulated environment, the best performing sensor configurations for each

algorithm are tested using real sensor data. Configurations 3-4 and 1-1 are used with the AKF, while configurations 3-4 and 0-4 are used with the DKF.

Sensor config.	White noise	Sin 5Hz	Sin 15Hz	Impact
3-4 (g)	✓	✓	!	!
3-4 (a)	✓	✓	✗	✓
1-1 (g)	✓	✗	✗	✗
1-1 (a)	✓	✓	!	✓

**Table 3:** results obtained in the real environment using the AKF

Sensor config.	White noise	Sin 5Hz	Sin 15Hz	Impact
3-4 (g)	!	!	✗	!
3-4 (a)	✓	!	✗	!
0-4 (g)	✗	✗	✓	✗
0-4 (a)	✓	✓	✗	!

**Table 4:** results obtained in the real environment using the DKF

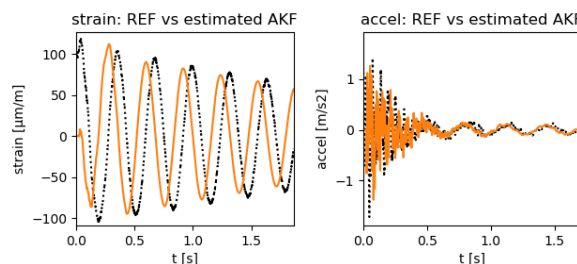


**Figure 4:** example of strain and acceleration estimation in the real environment using the AKF and the 3-4 configuration. Black signal corresponds to the reference signal (obtained with a real sensor) and orange signal corresponds to the estimation.

The obtained estimates are shown in tables 5 and 6. In general, a loss of precision is observed in the estimates respect to tests in a simulated environment. When the 15Hz-sinus input case is tested, both algorithms give imprecise estimates, which can be improved by varying the filter tuning parameters at the cost of losing precision in other input cases.

Leaving aside this specific input case, the AKF using the 3-4 sensor configuration provides correct strain and acceleration estimates. The AKF using the 3-4 config. and the DKF using the 0-4 config. provide correct acceleration estimates but fail estimating strain.

## 5 CONCLUSIONS AND FUTURE WORK

In this paper, a methodology to apply and validate virtual sensors for structural monitoring has been presented. Using model reduction techniques and Kalman-type estimation algorithms, virtual sensors have been implemented to estimate strain and acceleration at unmeasured points. Two different estimation algorithms (the AKF and the DKF) have been tested using different sensor configurations, first in a simulated environment and then on a real lab prototype. In general, the AKF has proven to be a more robust estimation algorithm, being able to provide accurate estimations if a combination of strain gauges and accelerometers is used as input data. The DKF has shown less accuracy, but in the other hand has been able to provide estimations in some cases where the AKF fails, such as using a sensor config. with only accelerometers. The validation tests performed with the real lab prototype have given less accurate results than the simulated ones. This may occur due to inaccuracies in the dynamic behavior of the model used in the estimation algorithms, as well as the lack of precision of the sensors used in a certain frequency range.

As described in section 2.4, the uncertainties are managed by the KF through noise covariance matrices. Despite the uncertainties associated with the measurements (values of  $\mathbf{R}$  matrix) can be estimated doing a previous analysis of the sensor outputs, the uncertainties associated with the process (values of  $\mathbf{Q}$  matrix) are not easily estimable, although they are of

fundamental importance in the correct operation of the algorithm [24]. As of today, in most KF implementations, a manual adjustment of process covariance is used due to the lack of a standardized method to get the optimal  $\mathbf{Q}$  matrix values, although some proposals for specific cases can be found in the bibliography [25]. Further research on the optimal adjustment of the process covariance values, or even on an adaptive approach for the  $\mathbf{Q}$  matrix, is considered of interest.

## 6 ACKNOWLEDGMENTS

Ikerlan's research has been supported by CDTI, depending by Ministerio de Ciencia e Innovación, through the "Ayudas Cervera para centros tecnológicos 2019" program, project MIRAGED with expedient number CER-20190001. This research center is certificated as "Centro de Excelencia Cervera".

## REFERENCES

- [1] D. Hajjalizadeh, E. J. O'Brien, and A. J. O'Connor, "Virtual structural health monitoring and remaining life prediction of steel bridges," *Can. J. Civ. Eng.*, vol. 44, no. 4, pp. 264–273, 2017.
- [2] L. Liu, S. M. Kuo, and M. C. Zhou, "Virtual sensing techniques and their applications," *Proc. 2009 IEEE Int. Conf. Networking, Sens. Control. ICNSC 2009*, pp. 31–36, 2009.
- [3] K. Maes, A. Iliopoulos, W. Weijtjens, C. Devriendt, and G. Lombaert, "Dynamic strain estimation for fatigue assessment of an offshore monopile wind turbine using filtering and modal expansion algorithms," *Mech. Syst. Signal Process.*, vol. 76–77, no. 0, pp. 592–611, 2016.
- [4] E. Bin Ilyas, M. Fischer, T. Iggena, and R. Tonjes, "Virtual Sensor Creation to Replace Faulty Sensors Using Automated Machine Learning Techniques," *GloTS 2020 - Glob. Internet Things Summit, Proc.*, pp. 3–8, 2020.
- [5] J. Kullaa, "Combined empirical and analytical virtual sensing for full-field dynamic response estimation," *8th Eur. Work. Struct. Heal.*

- Monit. EWSHM 2016*, vol. 4, no. July, pp. 2736–2745, 2016.
- [6] T. Woodbury and A. N. Srivastava, “Analysis of virtual sensors for predicting aircraft fuel consumption,” *AIAA Infotech Aerosp. Conf. Exhib. 2012*, pp. 1–15, 2012.
- [7] T. N. J. Geelen, “Time Domain Force Identification for Noise and Vibration Prediction in Vehicles,” TU Delft, 2019.
- [8] H. Li, D. Yu, and J. E. Braun, “A review of virtual sensing technology and application in building systems,” *HVAC R Res.*, vol. 17, no. 5, pp. 619–645, 2011.
- [9] R. Soman, “Semi-automated methodology for damage assessment of a scaled wind turbine tripod using enhanced empirical mode decomposition and statistical analysis,” *Int. J. Fatigue*, vol. 134, no. April 2019, 2020.
- [10] E. Lourens, E. Reynders, G. De Roeck, G. Degrande, and G. Lombaert, “An augmented Kalman filter for force identification in structural dynamics,” *Mech. Syst. Signal Process.*, vol. 27, no. 1, pp. 446–460, 2011.
- [11] R. P. Palanisamy, S. Cho, H. Kim, and S. H. Sim, “Experimental validation of Kalman filter-based strain estimation in structures subjected to non-zero mean input,” *Smart Struct. Syst.*, vol. 15, no. 2, pp. 489–503, 2015.
- [12] R. E. Kalman, “A new approach to linear filtering and prediction problems,” *J. Fluids Eng. Trans. ASME*, vol. 82, no. 1, pp. 35–45, 1960.
- [13] J. Glover, “The Linear Estimation of Completely Unknown Signals,” *IEEE Trans. Automat. Contr.*, no. 1, 1969.
- [14] P. K. Kitanidis, “Unbiased minimum-variance linear state estimation,” *Automatica*, vol. 23, no. 6, pp. 775–778, 1987.
- [15] M. Darouach and M. Zasadzinski, “Unbiased minimum variance estimation for systems with unknown exogenous inputs,” *Automatica*, vol. 33, no. 4, pp. 717–719, 1997.
- [16] C. S. Hsieh, “Robust two-stage Kalman filters for systems with unknown inputs,” *IEEE Trans. Automat. Contr.*, vol. 45, no. 12, pp. 2374–2378, 2000.
- [17] S. Gillijns and B. De Moor, “Unbiased minimum-variance input and state estimation for linear discrete-time systems with direct feedthrough,” *Automatica*, vol. 43, no. 5, pp. 934–937, 2007.
- [18] E. Lourens, C. Papadimitriou, S. Gillijns, E. Reynders, G. De Roeck, and G. Lombaert, “Joint input-response estimation for structural systems based on reduced-order models and vibration data from a limited number of sensors,” *Mech. Syst. Signal Process.*, vol. 29, pp. 310–327, 2012.
- [19] S. Eftekhari Azam, E. Chatzi, and C. Papadimitriou, “A dual Kalman filter approach for state estimation via output-only acceleration measurements,” *Mech. Syst. Signal Process.*, vol. 60, pp. 866–886, 2015.
- [20] B. Friedland, “Treatment of Bias in Recursive Filtering,” *IEEE Trans. Automat. Contr.*, vol. AC-14, no. 4, pp. 359–367, 1969.
- [21] S. H. Park, P. S. Kim, O. K. Kwon, and W. H. Kwon, “Estimation and detection of unknown inputs using optimal FIR filter,” *Automatica*, vol. 36, no. 10, pp. 1481–1488, 2000.
- [22] E. Lourens, E. Reynders, G. Lombaert, G. De Roeck, and G. Degrande, “Dynamic force identification by means of state augmentation: A combined deterministic-stochastic approach,” *Proc. ISMA 2010 - Int. Conf. Noise Vib. Eng. Incl. USD 2010*, pp. 2069–2080, 2010.
- [23] F. Naets, J. Cuadrado, and W. Desmet, “Stable force identification in structural dynamics using Kalman filtering and dummy-measurements,” *Mech. Syst. Signal Process.*, vol. 50–51, pp. 235–248, 2015.
- [24] R. Guyan, “Reduction of stiffness and mass matrices,” *AIAA Journal, Am. Inst. Aeronaut. Astronaut.*, vol. 3, no. 2, p. 380, 1965.
- [25] M. H. Richardson, “Modal mass, stiffness and damping,” no. 6, pp. 1–6, 2000.
- [26] W. Gressick, J. T. Wen, and J. Fish, “Order Reduction for Large-Scale Finite Element Models: A Systems Perspective,” *Int. J. Multiscale Comput. Eng.*, vol. 3, no. 3, pp. 337–362, 2005.
- [27] C. Papadimitriou, C.-P. Fritzen, P. Kraemer, and E. Ntotsios, “Fatigue predictions in entire body of metallic structures from a limited number of vibration sensors using Kalman filtering,” *Struct. Control Heal. Monit.*, 2010.
- [28] F. Elies Henar, “Application of a Kalman filter with augmented measurement model in non-invasive cardiac imaging,” *Kalsruhe Inst. Technol.*, 2011.
- [29] L. Zhang, D. Sidoti, A. Bienkowski, K. R. Pattipati, Y. Bar-Shalom, and D. L. Kleinman, “On the identification of noise covariances and adaptive kalman filtering: A new look at a 50 year-old problem,” *IEEE Access*, vol. 8, no. February, pp. 59362–59388, 2020.

## ANALYSIS AND CORRECTION OF VIBRATIONS GENERATED BY A PLASTIC BAG PRODUCTION MACHINE

A. Kharazian\* and F. López-Almansa†

\*Instituto de Multidisciplinar para el Estudio del Medio Ramon Margalef (IMEM),  
Universidad de Alicante  
e-mail: alireza.kharazian@ua.es  
ORCID: 0000-0003-2691-8875

† Departamento de Tecnología de la Arquitectura,  
Universidad Politécnica de Cataluña, Barcelona  
e-mail: francesc.lopez-almansa@upc.edu  
ORCID: 0000-000-2-7359-110X

**Abstract.** This paper discusses the vibrations engendered on a composite (concrete-steel) building slab by a machine for automated production of plastic bags; the slab is rather flexible, lightweight, lightly damped, and rests on steel columns (RSS). That machine has a number of rotating parts; in one of them (for plastic welding), an impact is generated at each cycle (4.17 Hz). Apparently, that impact causes relevant vibrations; concern arose regarding their effects on people, structure (fatigue) and the machine itself. The overall approach consists of the following rather consecutive stages: (i) identification of the dynamic effect generated the aforementioned impact (excitation), (ii) numerical modelling of the linear static and dynamic behavior of the slab (using a finite element model), (iii) calculation of the dynamic response of the slab, (iv) measuring of the vibrations (in terms of accelerations), (v) comparison between the numerical and experimental results (to calibrate the numerical model), (vi) analysis of the obtained values and comparison with the code thresholds (regarding human, structural and operation effects), (vii) proposal for vertical stiffening (strengthening) of the involved slab, (viii) implementation of the proposed slab stiffening, (ix) calculation of the dynamic response of the stiffened slab, (x) new measuring of the vibrations (in terms of accelerations and displacements), (xi) new comparison between the numerical and experimental results (to further calibrate the numerical model), and (xii) new comparison with the code thresholds. The final comparison shows a satisfactory performance; the acceleration levels for the effects on the workers are not exceeded (although the response acceleration is above the perception level), the fatigue is insignificant, and no influence on the machine operation is to be expected. Noticeably, the vibration is not caused by resonance effects, but by merely impact excitation on a flexible, light and little damped structure; this circumstance impaired the solution of the analyzed problem, given that it could not be based on separating the frequencies of the excitation (input) and of the structure.

**Key words:** Vibrating Machinery, Buildings, Human Effects, Fatigue.

### 1 BACKGROUND

In May 2019, a new automatic plastic bag production machine was installed on the

second floor of an industrial building. Upon starting the machine operation, an apparently excessive level of vibration was detected, and after several attempts and brief tests it was

decided to interrupt the machine operation until the situation was clarified. Noticeable, the company intended to install new machines capable of generating vibrations.

The first attempt to solve the situation consisted in installing vibration isolators; this strategy did not work, even the vibration increased significantly. Then the authors of this study were asked to take care of this issue.

## 2 BUILDING AND MACHINE DESCRIPTION

### 2.1 Building

The building has three stories, the global configuration is prismatic with an irregular trapezoidal base and a flat roof. The structure consists of square steel tube columns and composite concrete-steel slabs. Figure 1 presents an exterior image of the building. The axes ( $x$ ,  $y$ ,  $z$ ) in Figure 1 are consistently maintained throughout the paper.



Figure 1: Analyzed building

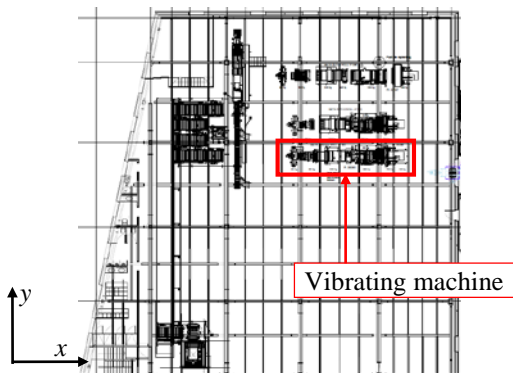


Figure 2: Plan view of the vibrating slab

Figure 2 displays a plan view of the slab that

contains the machine under consideration.

### 2.2 Machine

Figure 3 presents a plan view of the plastic bags production machine that is causing the vibrations. The direction of advance of the plastic roll (right to left) is indicated, as well as the body (welding) that is apparently generating the undesired effects.



Figure 3: Plan view of the vibrating machine

Apparently, the undesired dynamic effects are generated in the welding box; Figure 4 shows that a vertically moving part is impacting regularly against the upper part of the machine.

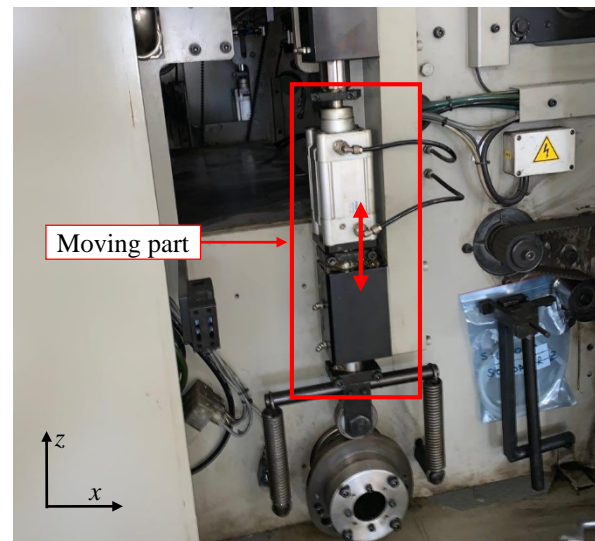


Figure 4: Moving part that is causing impact

The mass of the moving part is 50 kg and its stroke is 10 mm; the frequency is 4.17 Hz (250 hits per minute), thus, the average velocity of the moving part is  $0.02 / 0.24 = 0.833$  m / s. Consequently, the momentum is  $50 \text{ kg} \times 0.833 \text{ m / s} = 4.17 \text{ Ns}$ . Regarding the duration of the generated pulse ( $t_{imp}$ , Figure 5), it has not been possible to obtain any estimation; thus, a sensitivity study is required. Since this

duration is expected to be short (a few milliseconds), it is assumed that the exact shape of the impulse does not have a highly significant influence on the response; conservatively, triangular waves are assumed. Figure 5 displays a sketch of the wave train.  $F_{imp}$  and  $t_{imp}$  represent the maximum force (pulse height) and the pulse duration, respectively.

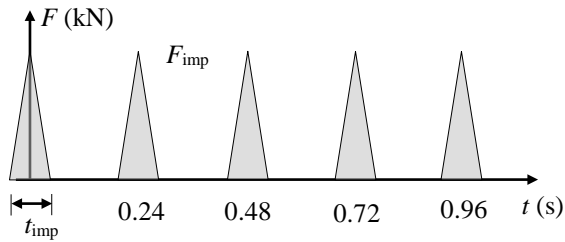


Figure 5: Dynamic loading on the slab

### 3 PREVIOUS EXPERIMENTAL MEASUREMENTS

#### 3.1 Preliminary inspections

On June 2019, the site was visited in order to study, in an unquantified way, the vibrations. Such vibrations were clearly perceived, and it was concluded that there was no resonance; this is because the vibrations were felt just right after the start of the machine, and for the reason that such vibrations were insensitive to any shift of the input frequency. In other words, the perceived vibrations are merely the dynamic response of a flexible, lightweight and lightly damped slab to the excitation depicted by Figure 5. Since there is no resonance, the solution of the problem cannot be based on separating the predominant frequencies of the structure and of the excitation; as discussed next (Section 4), the proposed strategy is to stiffen the supporting slab.

#### 3.2 Measured vibrations

Prior to any intervention, the vertical acceleration was measured in 24 points (A01-A24) located near the machine; the horizontal

components were significantly smaller and were disregarded. Figure 6 displays the location of such measuring points. In Figure 6, the point that exhibited the maximum response (A05) is highlighted; as expected, this point is located under the moving part (Figure 3 and Figure 4).

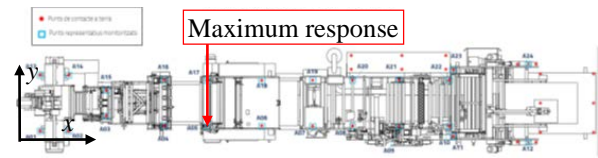


Figure 6: Measuring points

Figure 7 presents the vertical Fourier acceleration spectra in between 1 and 80 Hz (range of interest for human effects, [1]) for all the measuring points; the median spectrum is also plotted (black thick line). The points of the spectrum of the spectra correspond to the thirds of octave in the range 1-80 Hz.

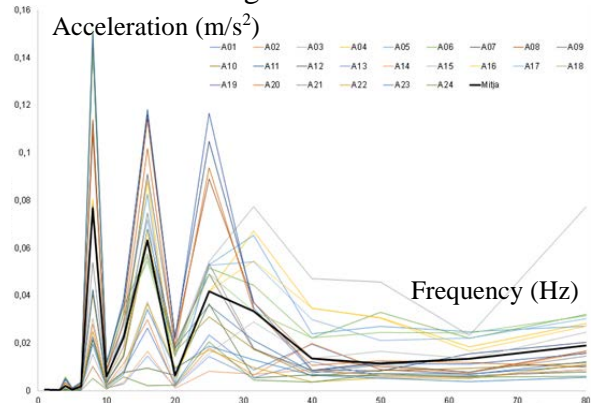


Figure 7: Acceleration spectra in the range 1-80 Hz

Figure 7 shows that the plotted spectra are rather constant; this states that, most likely, the excitation is wide-range, and that most modes respond to the excitation (Figure 5). Peaks are observed near the aforementioned machine operating frequency (4.17 Hz), and all their multiples (higher harmonics, 8.34 Hz, 12.51 Hz, 16.68 Hz, 20.85 Hz, 25.02 Hz, etc.); this confirms that the excitation is not harmonic but can be represented as shown in Figure 5.

After the vertical spectra in Figure 7, the following frequency-weighted quadratic average acceleration [1] is computed:

$$a_w = \sqrt{\sum_{i=1}^n (a_i W_i)^2} \quad (1)$$

In equation (1),  $n$  is the number of considered frequencies (thirds of octave), and  $a_i$  and  $W_i$  are the corresponding root mean square acceleration and weighting factor, respectively. The average acceleration is expressed in decibels [2] as:

$$L_{aw} = 20 \log \frac{a_w}{a_0} \quad (2)$$

In equation (2),  $a_0$  is the reference value ( $a_0 = 10^{-6} \text{ m/s}^2$ ). For the average spectrum in Figure 7,  $L_{aw} = 91.39$ , and for the point of maximum amplitude,  $L_{aw} = 97.44$ . Both levels are clearly above the perception threshold ( $L_{aw} \approx 84$  [1]), but do not even approach the acceptable levels for working environments. [3] states two bounds, the “*daily exposure limit value*”, and the “*daily exposure action value*” (less severe). For continuous exposure to vibration (8 hours per working day), such levels are established as  $L_{aw} = 121$ , and for the point of maximum amplitude,  $L_{aw} = 114$ , respectively. For non-continuous exposure, the following empirical correction expression is proposed [1, 4-5]:

$$A(8) = a_w \sqrt{\frac{T_{exp}}{T_0}} \quad (3)$$

In equation (3),  $A(8)$  is the equivalent level,  $a_w$  is the vertical average acceleration given by equation (1),  $T_{exp}$  is the average daily time exposure, and  $T_0$  is the reference time ( $T_0 = 8$  hours). By assuming that the daily time exposure is 30% of the total working time, the aforementioned thresholds are extended to  $L_{aw} = 129$  and  $L_{aw} = 119$ , respectively.

These considerations show clearly that the measured accelerations do not exceed the accepted levels. However, the company decided to obtain further reduction, in order to avoid any conflict with their employees.

## 4 PROPOSED STRATEGY: SLAB STIFFENING

As the vibrations were not caused by the slab resonance (subsection 3.1), the solution cannot consist in modifying (reducing, in fact) the machine operation frequency; moreover, it would have caused a reduction in its bags production capacity. Apparently, the only feasible strategies are increasing the slab damping or stiffness. Regarding damping, it is well-known that adding significant damping is rather difficult; moreover, its effect on the steady-state response is only moderate, except near the resonance peak. Therefore, the only feasible approach is to increase the slab stiffness in the vicinity of the vibrating machine; given that the slab structural behavior is basically linear, it is expected that the vibration reduction will be proportional to the stiffness increase.

Figure 8 displays the steel profiles that are incorporated to the supporting slab in order to increase its stiffness.



**Figure 8:** Added steel beams (dark red) to strengthen the slab

It is estimated that this slab strengthening is going to increase its stiffness around 4 times.

## 5 SLAB NUMERICAL MODELLING

### 5.1 Model description

The linear static and dynamic 3-D structural

behavior of the building slab (both before and after the stiffening) is modeled with ETABS software (version 17) [6]. The model includes the first floor slab and the corresponding supporting columns (half segments under and above the slab). Such segments are considered to be pin-ended in both directions. Figure 9 display a global view of the structural model.

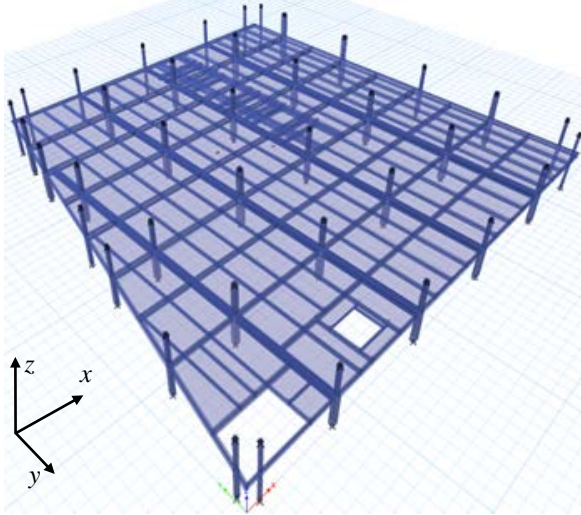


**Figure 9:** 3-D view of the structural model of the strengthened slab

The influence of the non-structural components (cladding, partitioning and stairs) has been conservatively neglected, except for the mass participation the dynamic analyses. The steel modulus of elasticity is 210 GPa for the profiles and the trapezoidal sheet, and 200 GPa for the reinforcement. Regarding the concrete, its modulus of deformation is 27.26 GPa; the cracking has not been accounted, given that most of the concrete is under compression. It is assumed the shear connectors prevent any slippage between the topping concrete, the trapezoidal sheet and the lower steel profiles. For the dynamic analyses, the damping factor is taken as 0.8%.

## 5.2 Static analyses

The static analyses are intended to determine the vertical stiffness in the machine location. Figure 10 displays the deformation

caused by a concentrated load located in the point A05 (Figure 6).

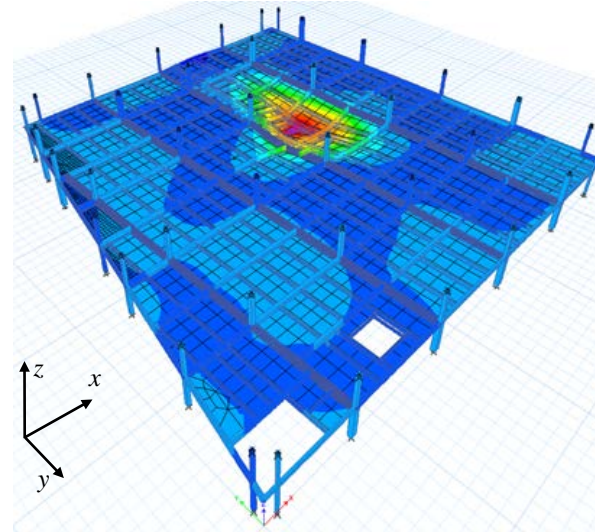


**Figure 10:** Deflection of the stiffened slab caused by a point load

The stiffness of the slab prior and post-stiffening are 14.25 kN/mm and 62.31 kN/mm, respectively. Therefore, a reduction of the vibration of nearly 77% is to be expected; however, this is only approximate, given that the frequency responses are not uniform.

## 5.3 Dynamic analyses

The conducted linear dynamic analyses consist in obtaining the response of the slab to the excitation depicted by Figure 5; the modal formulation is considered. The duration of each analysis is 2.64 s (corresponding to 11 pulses), and the discretization period is 0.0005 s. Noticeably, no static gravity load is considered; obviously, the dynamic mass effect is accounted for.

As previously announced (subsection 2.2), a sensitivity study to the pulse duration ( $t_{imp}$ ) is conducted. In this sense, Table 1 and Table 2 present the variations of the bending moments and the axial stresses in the bottom fibers of the most demanded sections of the steel beams of the strengthened slab; in Table 1 and Table 2  $t_{imp} = 5 \mu\text{s}$  and  $t_{imp} = 5 \text{ms}$ , respectively. In

Table 1 and Table 2,  $M_{\min}$  and  $M_{\max}$ , refer to the minimum and maximum, respectively, moments during the vibration; the positive sign corresponds to tensioned bottom fibers. Also,  $\sigma_{\min}$  and  $\sigma_{\max}$  are the minimum and maximum axial (normal, longitudinal) stresses; the positive sign corresponds to tension.

Beam	$M_{\max}$ (kNm)	$M_{\min}$ (kNm)	$ \sigma_{\max} - \sigma_{\min} $ (MPa)
2 IPE400	0.1589	-0.1650	0.1497
IPE500	0.2816	-0.2392	0.2701
IPE450	0.2950	-0.2824	0.3850
2 IPE450	0.2587	-0.2261	0.1708
HEB300*	0.1263	-0.1083	0.1007
HEB300*	0.1773	-0.1579	0.1439
2 IPE240	0.0183	-0.0169	0.0633
IPE240*	0.0420	-0.0440	0.1062
IPE330	0.0240	-0.0228	0.0656
IPE400	0.1062	-0.1160	0.1922
IPE360	0.1444	-0.2145	0.3971
IPE300	0.0528	-0.0546	0.1928
IPE270	0.0078	-0.0079	0.0366
IPE220*	0.4249	-0.3847	1.1819

Beam	$M_{\max}$ (kNm)	$M_{\min}$ (kNm)	$ \sigma_{\max} - \sigma_{\min} $ (MPa)
2 IPE400	0.1584	-0.1642	0.1491
IPE500	0.2807	-0.2383	0.2692
IPE450	0.2935	-0.2812	0.3832
2 IPE450	0.2579	-0.2601	0.1825
HEB300*	0.1256	-0.1080	0.1003
HEB300*	0.1767	-0.1574	0.1435
2 IPE240	0.0181	-0.0167	0.0626
IPE240*	0.0418	-0.0439	0.1058
IPE330	0.0239	-0.0228	0.0655
IPE400	0.1059	-0.1156	0.1916
IPE360	0.1439	-0.1146	0.2860
IPE300	0.0526	-0.0544	0.1921
IPE270	0.0078	-0.0079	0.0366
IPE220*	0.4332	-0.3834	1.1921

\* These beams involve the topping concrete layer

Comparison between the results in Table 1 and Table 2 shows that they are very similar; it

shows that the influence of  $t_{\text{imp}}$  is only moderate. On the other hand, the oscillations of the normal stress are extremely small; therefore, there is absolutely not any risk of fatigue in the structure.

For further information, Table 3 displays the variations of vertical displacements (deflections) in characteristic sections of the beams of the strengthened slab (same sections than in Table 1 and Table 2).

Beam	$w_{\max}$ (mm)	$w_{\min}$ (mm)	$ w_{\max} - w_{\min} $ (mm)
2 IPE400	0.006	-0.006	0.012
IPE500	0.005	-0.002	0.007
IPE450	0.007	-0.007	0.014
2 IPE450	0.006	-0.006	0.012
HEB300*	0.002	-0.001	0.003
HEB300*	0.002	-0.002	0.004
2 IPE240	0.001	-0.001	0.002
IPE240*	0.001	-0.001	0.002
IPE330	0.003	-0.003	0.006
IPE400	0.002	-0.002	0.004
IPE360	0.007	-0.007	0.014
IPE300	0.003	-0.003	0.006
IPE270	0.001	-0.001	0.002
IPE220*	0.032	-0.026	0.058

\* These beams involve the topping concrete layer

Table 3 shows that the variations of deflections are negligible, thus confirming the absence of fatigue.

Regarding the response accelerations (relevant to the human effects), the computed accelerations at a given point before and after the intervention are compared. Before the slab strengthening, the Fourier amplitudes for the 16.67 Hz frequency before and after the intervention are 0.052  $\text{m/s}^2$  (maximum spectral amplitude) and 0.00336  $\text{m/s}^2$ , respectively. Despite this huge reduction, a deeper examination shows that the maximum spectral amplitude of the strengthened slab is 0.032  $\text{m/s}^2$  for the frequency 29.17 Hz. This shows that the peak spectral accelerations do not

correspond to the same frequencies, and the full range needs to be examined; such operation is performed after the acceleration measurements in the reinforced slab (subsection 6.1).

In order in to compare with the aforementioned new acceleration experiments (subsection 6.1), it is observed that in the point A17 (Figure 6), the Fourier amplitude for the 16 Hz frequency is 0.00538 m/s<sup>2</sup>; this result matches the experimental one.

## 6 AFTER-STIFFENING EXPERIMENTAL MEASUREMENTS

### 6.1 Accelerations

These tests recorded the acceleration levels at the supports of the welding body (Figure 3) of the machine (points A05, A06, A17 and A18, Figure 6), at the center of the machine, and at an intermediate point between the main machine and the adjoining one. These recordings were performed under three conditions: operation of the main machine, operation of both machines, and cultural noise (no machine operation). For each of these 18 cases (6 points times 3 conditions), two tests (named 1 and 2) were performed to obtain more reliable results; each of these tests lasted only a few minutes (between slightly more than 2 and up to 6). The results are analyzed at intervals of 1 s and 1/8 s; the 1 s time window is chosen because has better time uniformity (stationarity). For each interval and frequency (between 1 and 80 Hz in thirds of octave), the quadratic average and its decibel value ( $L_{aw}$ , equation (2)) are provided;  $L_{aw}$  is also obtained globally (for all the frequencies). Table 4 summarizes the most relevant results of the two tests.

Point	Main machine	Both machines	Noise
A05	83.29 / 83.25	85.59 / 85.67	55.24 / 54.81
A06	84.60 / 84.57	87.16 / 87.25	56.01 / 55.97
A17	83.28 / 83.25	85.01 / 85.08	54.78 / 54.69
A18	85.06 / 85.03	87.02 / 87.09	56.00 / 55.92
Centre	84.77 / 84.78	86.99 / 87.13	57.91 / 57.94
Between machines	84.86 / 84.83	85.86 / 85.90	55.68 / 54.95

Table 4 shows quite clear trends: (1) the amplitudes at the six points are almost alike, (2) the results from tests 1 and 2 are very similar, (3) the influence of the additional machine is moderate, and (4) the vibrations generated by the cultural noise are clearly small, but not irrelevant. The comparison between the values shown in Table 5 and the result for the previous (non-stiffened) slab presented in subsection 3.2 (97.44) indicates a clear reduction.

As a complement to the results in Table 4, Figure 11 displays the Fourier acceleration spectral amplitudes at point A05 (Figure 6) before and after the slab strengthening.

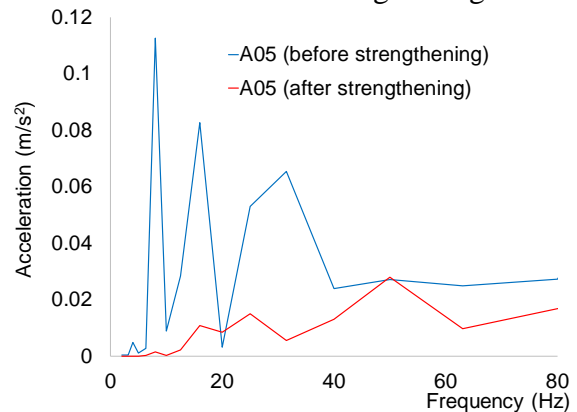


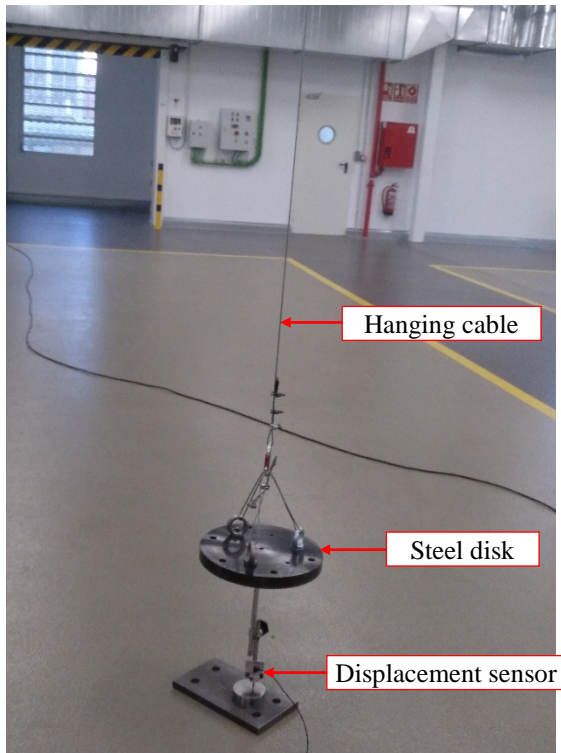
Figure 11: Acceleration amplitudes at point A05 for the previous and the stiffened slab

Figure 11 confirms that the proposed intervention has generated a relevant reduction

of the acceleration for nearly all the frequencies; this decrease is coherent with the computed stiffness increase (subsection 5.2).

## 6.2 Displacements

In order to obtain further information, the slab deflections were measured using an inductive displacement transducer (LVDT); its maximum stroke is 2 mm. Figure 12 presents an image of the testing setup. The measuring point is located near the maximum deflection point of the bay (span, rectangular space bounded by four columns) that is aside the vibrating machine.



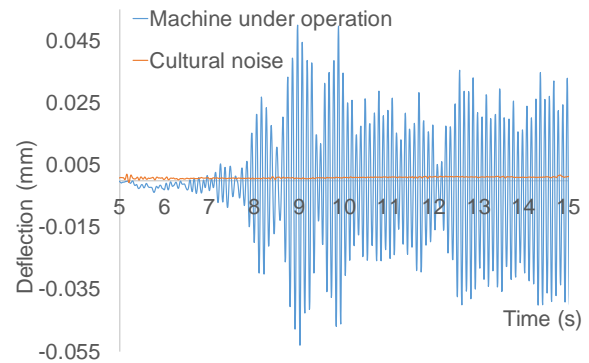
**Figure 12:** Displacement measurement arrangement

Figure 12 shows that the displacement sensor is connected to a massive steel disk that is suspended from a cable connected to the above slab. The objective of the disk is to stabilize the sensor position and to maintain the cable strained (tense), as to ensure that the distance between the sensor and the top slab holds reasonably constant. Then, by assuming

that the deflections of such roof slab can be neglected (any operation was prevented during the test), the transducer measures the deflections of the floor slab.

Three types of experiments were performed: operation of the machine, excitation by cultural noise only (preventing any operation in this slab and in the above one), and vibration caused by a heel impact (an adult weighting 80 kg). Each type of test was conducted three times; the durations were approximately one minute each.

Figure 13 displays the time histories of the displacement in the first test under two conditions: operation of the machine and excitation by the cultural noise only. Figure 13 shows that the deflection generated by the cultural noise is significantly smaller. Most probably, if the operation had not been totally restricted the difference would not have been so large (Table 4).



**Figure 13:** Measured displacement time histories for the strengthened slab in the 1<sup>st</sup> test

Comparison between the plots in Figure 13 and the values in Table 3 shows a rather reasonable agreement, given the numerous uncertainties involved in the numerical simulation (Table 3) and the experiments (Figure 13). As a matter of fact, the measured displacements tend to be higher than the computed ones; this difference can be partially explained by the location of the measuring point (Figure 12) near the span maximum deflection point. This similarity further

confirms the irrelevance of the fatigue effects.

## 7 CONCLUSIONS

This paper describes the analysis and reduction of vibrations of a building slab generated by a plastic bag production machine. The vibrations are caused by the impact of a 50 kg moving part; its stroke is 10 mm and the operation frequency is 4.17 Hz. The vibrations proved not to correspond to resonance; thus, the proposed strategy is to strengthen the slab area located near the machine. The analysis is supported by experiments and by numerical simulations; both types of studies are performed for the previous and final situations (before and after the slab strengthening, respectively).

The vibration intensity is quantified in terms of the  $L_{aw}$  coefficient, which corresponds to the weighted quadratic acceleration average expressed in decibels. Before and after the intervention,  $L_{aw}$  was 97 and 83, respectively. This shows that the vibration reduction is relevant, and that both levels are clearly above the perception threshold ( $L_{aw} \approx 84$ ), but do not even approach the acceptable level for working environments (it ranges in between and 119 and 129). In other words, the slab strengthening was unnecessary, but has provided a significant vibration reduction.

## REFERENCES

- [1] ISO 2631. *Mechanical vibration and shock. Evaluation of human exposure to whole-body vibration*. (1997 Part 1; 2003 Part 2).
- [2] *Legislative compilation for the management and evaluation of acoustics*. Generalitat de Catalunya. 2010.
- [3] Directive 2002/44/EC of the European Parliament and of the Council of 25 June 2002. *Minimum health and safety requirements regarding the exposure of workers to the risks arising from physical agents (vibration)*.
- [4] *Guide to good practice on Whole-Body Vibration*. European Commission Directorate General Employment, Social Affairs and Equal Opportunities. (2006).
- [5] EN 14253. *Mechanical vibration. Measurement and calculation of occupational exposure to whole-body vibration with reference to health - Practical guidance*. European Committee for Standardization. (2007).
- [6] ETABS. *Integrated Building Design Software*. Version 17. CSI (Computers and Structures Inc.). 2019.

# OPERATIONAL MODAL ANALYSIS FOR BUILDINGS EFFICIENT SEISMIC DAMAGE IDENTIFICATION

J.P. Reyes\*, M. Mansilla†, G. Valdebenito†, D. Alvarado†, and F. López-Almansa††

\* Instituto de Obras Civiles,  
Universidad Austral de Chile  
Valdivia, Chile  
e-mail: jpreyes@uach.cl  
ORCID: 0000-000-1-6870-706X

† Núcleo de Investigación RiNA, Instituto de Obras Civiles,  
Universidad Austral de Chile  
Valdivia, Chile  
e-mail: gvaldebe@uach.cl  
ORCID: 0000-000-3-1872-9484

†† Núcleo de Investigación RiNA, Departamento de Tecnología de la Arquitectura,  
Universidad Austral de Chile, Universidad Politécnica de Cataluña  
Valdivia, Chile, Barcelona  
e-mail: francesc.lopez-almansa@upc.edu  
ORCID: 0000-000-2-7359-110X

**Abstract.** This paper presents an Operational Modal Analysis (OMA) of a 3-storey RC building located in Valdivia, Chile; it is the Informatics Institute of the Austral University of Chile. The analyzed building is roughly shaped as a parallelepiped, being founded on a soft soil. The building structure consists basically of shear walls and solid slabs, but the first floor has an open side atrium that is only supported by rather flexible columns; this asymmetry presumes an important eccentricity between the first floor centers of gravity and stiffness. The building was inaugurated in 2010, having not been damaged by any earthquake; the objective of the carried out OMA is to calibrate the analysis model and, in particular, to detect the presence of torsional modes (being strongly detrimental to the earthquake resistance). Results confirm this trend and highlight the relevant influence of the soil flexibility.

**Key words:** Operational Modal Analysis, Buildings, Model Calibration, Torsional Modes Detection.

## 1 INTRODUCTION

EMA (Experimental Modal Analysis) [1-3] consists in identifying the structural parameters of a given construction (mainly civil engineering structures, as buildings or bridges) by measuring its response to a known dynamic excitation (usually, ad hoc-generated). That response allows estimating the modal parameters (natural frequencies,

modal shapes and damping ratios); then their stiffness and damping can be calculated, thus obtaining information about the structural state (structural health) through proper DI (Damage Identification) approaches [4-5].

OMA (Operational Modal Analysis, also known as output-only modal analysis) [6-8] is a highly promising technique that is similar to EMA. The only difference is that the structural response is not generated by any purposed

known dynamic excitation, but merely by the random effects of the construction operation (functioning). Such input is commonly known as cultural noise (or ambient vibration); it can be generated either inside or outside the construction and corresponds to wind, traffic (road and railway), human activities, building machines, etc. Therefore, is characterized by being rather weak (small) and highly irregular. Regarding the first feature (weakness), nowadays sensors are extremely sensitive, being able to measure almost insignificant levels of velocity and acceleration (clearly under any human perception threshold). Concerning the second issue (irregularity), the input is considered to be unknown, and is commonly modelled as random (usually, as a wide-band white noise). As its name states, the output of Operational Modal Analyses are the modal parameters of the construction under consideration, mainly natural periods and mode configurations (modal vectors); damping ratios are harder to estimate, given the small vibrations involved.

Broad comparison between EMA and OMA, states the information obtained from OMA is less reliable, but this analysis is more feasible, given that no intended excitation has to be generated. On the other hand, in OMA, given the high uncertainty of the involved parameters and the performed operations, the identification algorithms are rather complex, and a stochastic (random) framework is considered; the parameters identification can be performed either in the time or frequency domains. Noticeably, both techniques are inherently non-destructive.

Noticeably, OMA and SHM (Structural Health Monitoring) [9-10] are highly similar and highly related issues. Perhaps the main difference lies in the fact that OMA focusses on civil engineering constructions, while SHM rather refers to aerospace structures (typically, composite materials).

This paper presents an Operational Modal

Analysis of a 3-storey RC building located in Valdivia, Chile; it is the Informatics Institute of the Austral University of Chile [11]. The building was inaugurated in 2010, having not been damaged by any earthquake; the objective of the carried out OMA is to calibrate the analysis model and, in particular, to detect the presence of torsional modes (being strongly detrimental to the earthquake resistance).

## 2 BUILDING DESCRIPTION

Figure 1 displays two general views (front and rear, (Figure 1(a) and Figure 1(b), respectively) of the aforementioned 3-story RC building under consideration. The global coordinates ( $x, y, z$ ) are maintained along this paper for easy reference;  $x$  and  $y$  correspond approximately to NS and EW directions, respectively.



(a) Front view



(b) Rear view

**Figure 1:** Analyzed building

Figure 1 shows that the building global configuration is rather regular, with rectangular layout and overall geometric uniformity along height. The building height is 11.60 m and the plan size is 25.1 m × 15.65 m (on the ground); the constructed area is approximately 1080 m<sup>2</sup>. There are no basements.

The building structure is made of reinforced concrete. Most of the supporting elements are shear walls, although there are also some columns (Figure 1(a), respectively). The wall thickness ranges between 15 and 35 cm; the slabs are solid with 20 cm thickness.

The characteristic value of the concrete compressive strength is  $f_c' = 200 \text{ kgf/cm}^2$ , the concrete deformation modulus is  $E_c = 15100 \times (f_c')^{1/2} = 213550 \text{ kgf/cm}^2$  [12], the concrete Poisson ratio is  $\nu_c = 0.18$ , and the reinforcement steel is A630-420H (its ultimate stress are  $f_u = 630 \text{ MPa}$  and yield point  $f_y = 420 \text{ MPa}$ , respectively [13]).

For further clarity, Figure 2 displays the structural layouts of the three building stories.

In Figure 2, points labelled 1-9 correspond to the sensors locations; noticeably, points 1, 4 and 7 are vertically aligned (as well, 2, 5 and 8, on one side, and 3, 6 and 9, on the other side). This layout is aimed to provide smooth and reliable measurement. On the other hand, the high separation between pairs 2-3, 5-6 and 8-9 is intentional in order to provide clear and reliable information on the torsional motion (section 1).

Figure 1 and Figure 2 show that the supporting elements are not uniformly distributed along the building height, as the first story front has only bare columns, while that façade is quite rigid in the second and third stories. In other words, Figure 2.a seems to indicate that a relevant eccentricity between the centers of mass and of stiffness is to be expected; therefore, the first mode might be predominantly torsional, this being detrimental regarding the building seismic performance.

As discussed in the Introduction, one of the major objectives of this paper is to clarify this highly relevant issue (regarding the building earthquake-resistant capacity).

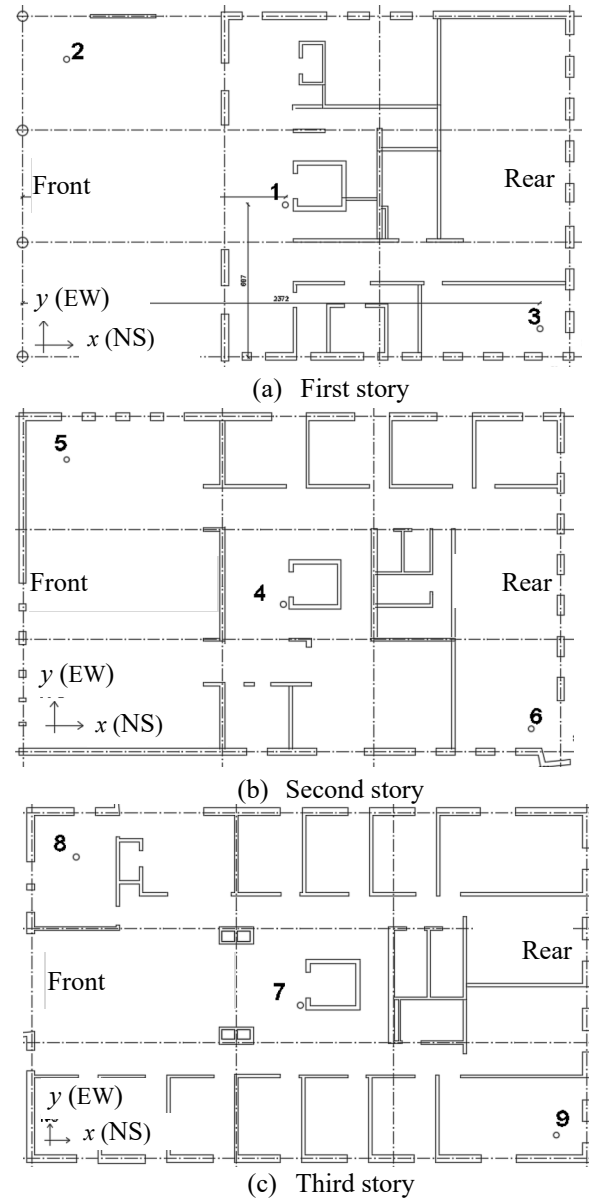


**Figure 2:** Structural story layouts of the analyzed building

### 3 STRUCTURAL MODEL

This section depicts the numerical modelling of the building under consideration.

### 3.1 General Description

The building had been designed by using the SAP2000 program [14]; given that the original code was not available, another model implemented in the same program was developed specifically for this study. However, the first three natural periods from the original code were retained for comparison purposes, such values are:  $T_1 = 0.224$  s,  $T_2 = 0.175$  s and  $T_3 = 0.141$  s.

The aforementioned developed model was created by using the data available in the project (section 2); therefore, this model is not calibrated with any experimental result.

Figure 3 displays two global sketches of the developed structural model.

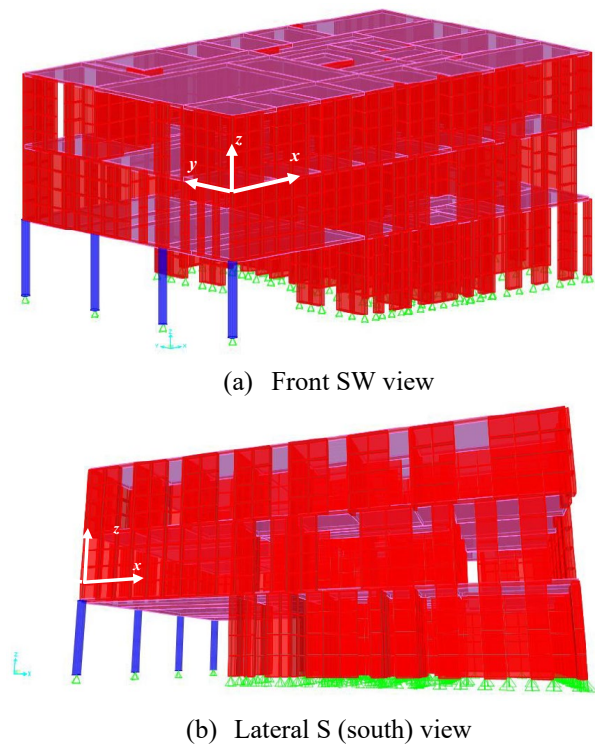


**Figure 3:** Structural model of the analyzed building

Figure 3 shows that only the major structural elements are modeled (i.e. walls, slabs and columns); additionally, it is imposed that the three slabs constitute rigid diaphragms (in their own planes). Columns and walls are considered embedded (clamped) in the

foundation; additionally, the rotations of the columns top sections with respect to  $x$  and  $y$  axes are also restrained.

### 3.2 Initial Numerical Modal Analysis

The structural model described in the previous subsection has been utilized to perform a numerical modal analysis of the building under consideration.

Major characteristics of this analysis are discussed in this paragraph. Given that the building is not damaged, the stiffness of the structural elements is not reduced due to cracking of the tensioned concrete. The mass corresponds to permanent loads; this is because the measurements were made when the building was empty (i.e. during the holiday period). Then, the building seismic weight is 16660 kN.

Table 1 displays the most representative results of the first five modes computed with the developed model.

Mode	Period (s)	$U_x$	$U_y$	$U_z$	$R_x$	$R_y$	$R_z$
1	0.0641	0	0.41	0	0	0	0.56
2	0.0454	0.87	0	0	0	0	0
3	0.0412	0	0.47	0	0	0	0.4
4	0.0310	0	0	0.66	0	0.23	0
5	0.0217	0	0	0	0.36	0	0

In Table 1,  $U_x$ ,  $U_y$ ,  $U_z$ ,  $R_x$ ,  $R_y$  and  $R_z$  refer to the percentages of equivalent modal masses in the corresponding displacement ( $U$ ) and rotation ( $R$ ) directions, respectively. Then, Table 1 shows that the rotational component of the first mode is high, thus indicating a certain lack of torsional stiffness (Figure 2); noticeably, this remark is corroborated by the fact that the third mode has a similar configuration. Conversely, the second mode is purely translational in the  $y$  direction, thus showing that the apparent eccentricity between the aforementioned centers of mass and stiffness occurs only in the  $x$  direction (Figure 1.a and Figure 3).

Table 1 also shows that the computed

periods are extraordinarily short, thus corresponding to a highly rigid building; this is coherent with the rather high wall densities in both directions (Figure 2 and Figure 3), and with the assumption that the walls and columns are clamped to the foundation, it being modelled as infinitely rigid (together with the surrounding soil, then). Noticeably, the empirical expressions proposed in the Chilean seismic design code [15] predict a fundamental period of 0.47 s (more than seven times longer than the computed one, Table 1); this discrepancy indicates that the soil flexibility (through the soil-structure interaction) might play a highly relevant role. On the other hand, comparison between the original (subsection 3.1) and the new (subsection 3.2) computed periods, shows a huge discrepancy (e.g. 0.224 s vs. 0.0641 s for the first mode), as the original ones are significantly longer and closer to those foreseen by the said Chilean regulation [15].

Finally, Table 1 reveals also that the configurations of the fourth and fifth modes are rather weird, with important vertical displacements (local slab deflections), and global rotations with respect to the  $x$  and  $y$  horizontal axes. These circumstances highlight the high lateral stiffness of the building, as these unusual modal deformations ordinarily would correspond to higher modes.

#### 4 OMA OF THE BUILDING

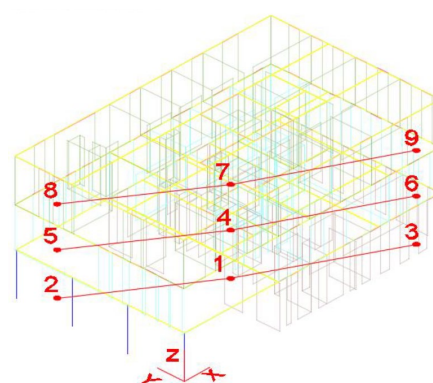
This section describes broadly the performed Operational Modal Analysis of the building under consideration. The description covers the sensors, their measured results, and the Operational Modal Analysis itself.

##### 4.1 Sensing System

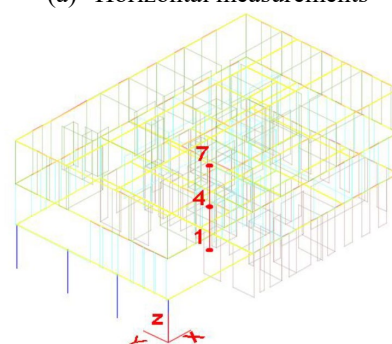
In the Operational Modal Analysis of the building, two types of sensors were utilized: 25 geophones (Soilspy) and velocity and acceleration sensors Tromino. Both devices were installed in the points labelled 1 through

9 in Figure 2; as described in section 2, those points belong to the same vertical.

For further clarity, Figure 4 displays 3-D views of the locations of the aforementioned measuring points; the horizontal measurements were taken in all the points (Figure 4.a), while the vertical ones were only taken in the centrally located points (i.e. 1, 4 and 7, see Figure 4.b).



(a) Horizontal measurements



(b) Vertical measurements

Figure 4: Measuring points

##### 4.2 Geophones

The main characteristics of the Soilspy geophones are:

- Dynamic range: 142 dB (from  $\pm 3.2$  mV to  $\pm 665$  mV, 8 options).
- Resolution: from  $0.1 \mu\text{V}/\text{digit}$  to  $20 \mu\text{V}/\text{digit}$  (8 options).
- Sampling frequency: 89 kHz per channel in continuous mode.

- Data output: 256 Hz, 512 Hz, 1 kHz for each channel.
- Operating environmental condition: temperature 0-50 °C, humidity 0-100%.
- Waterproofing: IP Protection Index = 65 (dust and splash proof).

Figure 5 displays two geophones installed in the vertical (Figure 5.a) and horizontal (Figure 5.b) directions.

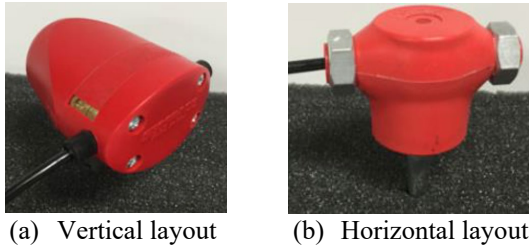


Figure 5: Geophones

### 4.3 Velocity and Acceleration Sensors

The main characteristics of the Tromino velocity and acceleration sensors are:

- Number of channels is 9: 3 speedometers, 3 accelerometers, 1 analog channel, 1 radio channel and 1 GPS.
- Dynamic range: 142 dB, from  $\pm 3.2$  mV to  $\pm 665$  mV (8 options).
- Resolution: from  $0.1 \mu\text{V}/\text{digit}$  to  $20 \mu\text{V}/\text{digit}$  (8 options)
- Sampling frequency: 64 kHz per channel in continuous mode.
- Data output: 124 Hz, 256 Hz, 512 Hz, 1024 Hz, 2048 Hz.
- Maximum analog input: Full Scale 51 mV and High Gain channels:  $\pm 25.6$  mV (781 nV/digit). Low Gain Channels:  $\pm 1$  V.
- Data recording: standard 4 Gb internal memory.
- Operating environmental condition: temperature  $-10$  °C to  $+70$  °C, humidity 0-90% non-condensing.
- Waterproofing: IP Protection Index = 65 (dust and splash proof).

Figure 6 displays a velocity and acceleration sensor (Figure 6.a) and its

installation (Figure 6.b).

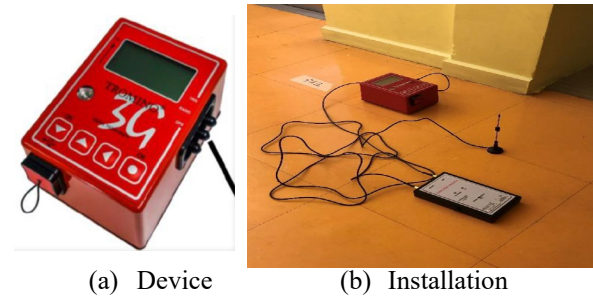


Figure 6: Velocity and Acceleration Sensors

### 4.4 Results of the Geophones

Measurement batches (of nine points) of 10 minutes each were taken (60 minutes horizontally and 40 minutes vertically). Data was sampled at a frequency of 256 Hz, and the data format is 16 bytes.

For further clarification, Figure 7 displays a set of three geophones installed in vertical and horizontal directions.

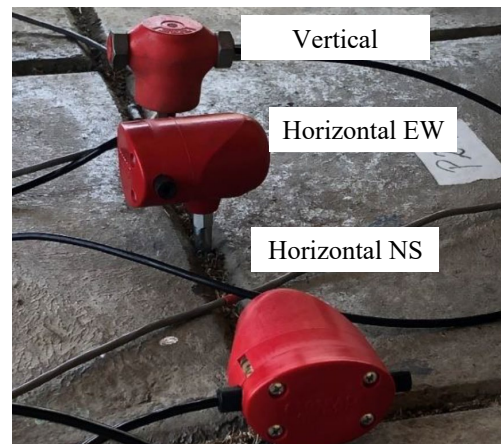
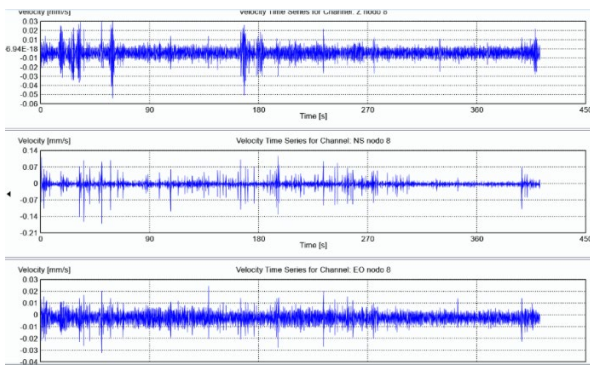


Figure 7: Geophones in point 1

Figure 8 displays a representative example of 3-D velocity (mm/s) measurements taken by a geophone in point 8 (third floor, Figure 4.a).

In Figure 8, the top time-history plot corresponds to the vertical direction, and the two other ones refer to NS (middle plot) and EW (bottom plot) horizontal directions. The velocity in the (Figure 1 and Figure 2) NS direction is clearly predominant.



**Figure 8:** Velocity measurements of point 8 (Figure 2 and Figure 4) from a geophone

Broadly speaking, the velocity measurements with the geophones were considered highly reliable and uniform.

#### 4.5 Results of the Velocity and Acceleration Sensors

Two measurement batches (of three points) of 10 minutes each were taken (80 minutes). Data was sampled at a frequency of 256 Hz, and the data format is 16 bytes. For further clarification, Figure 9 displays an example of 3-D acceleration measurements taken by a sensor at point 7 (Figure 2 and Figure 4).

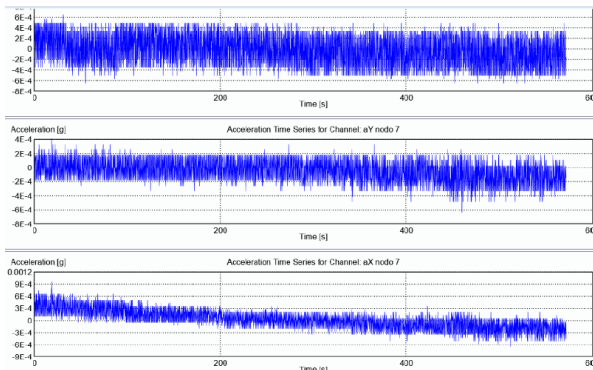


**Figure 9:** Acceleration measurements from a Tromino sensor

Figure 9 shows that the plotted signals are rather inadequate, with rather flat spectra (i.e. similar to white noise), and deviation from the base line (mainly the third plot). For that reason, the acceleration measurements were disregarded, and only the velocity ones were

taken into consideration. In this sense, Figure 10 displays an example of high gain 3-D velocity measurements taken by a sensor at point 2 (Figure 2 and Figure 4).

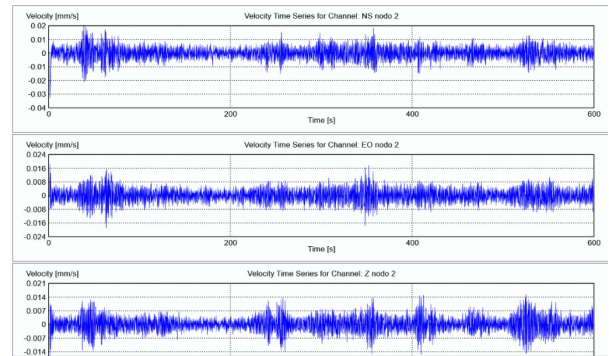
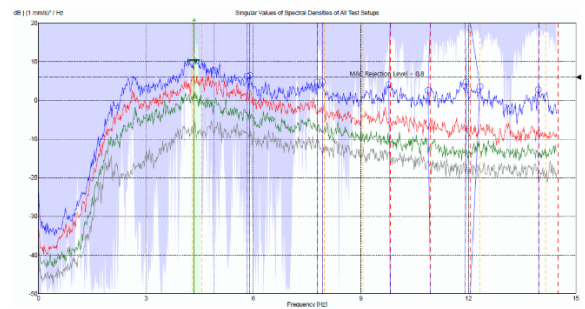


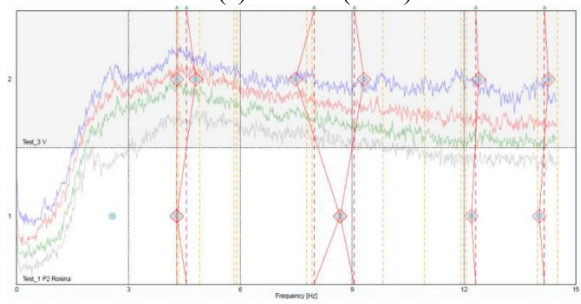
**Figure 10:** High gain velocity measurements of point 2 from a Tromino sensor

In general, the high gain velocity measurements were preferred to the low gain ones because of the small level of ambient vibration.

#### 4.6 Operational Modal Analysis



(a) EFDD (SVD)

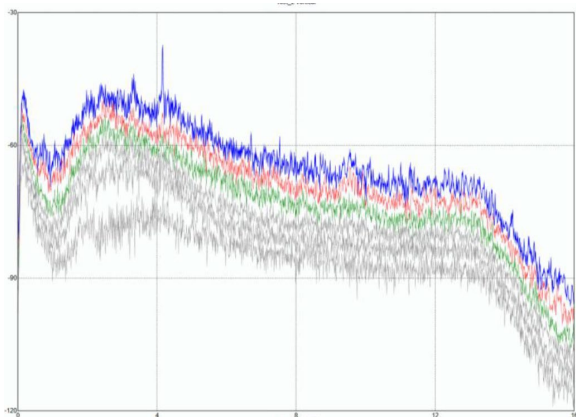


(b) SSI

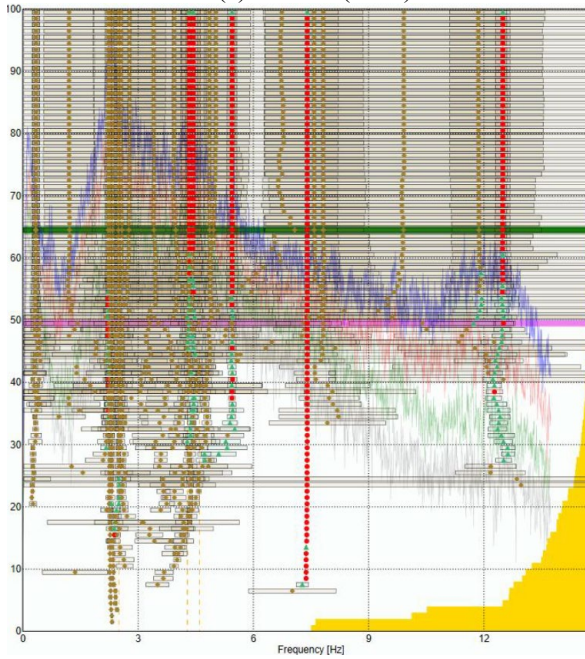
**Figure 11:** Power spectral density function from the Geophones

The Operational Modal Analysis of the

measured signals was carried out with the ARTeMIS program [16] by using formulations in the time and frequency domains: SSI (Stochastic Subspace Identification) and EFDD (Enhanced Frequency Domain Decomposition), respectively. Point 1 (Figure 2 and Figure 4) was utilized as reference node.



(a) EFDD (SVD)



(b) SSI

**Figure 12:** Power spectral density function from the Tromino sensors

Figure 11 and Figure 12 display examples of PSDFs (Power Spectral Density Functions) from the Geophones and the Tromino sensors, respectively. Figure 11.a and Figure 12.a

present results of SVD (Singular Values Decomposition), Figure 11.b and Figure 12.b refer to SSI.

Table 2 presents the average values of the first five modes natural periods obtained from the EFDD and SSI approaches. In Table 2, both the velocity records by the Tromino sensors (high gain, Figure 11) and the geophones (Figure 12) were utilized.

Table 2. Natural periods (s) from the Operational Modal Analysis of the building under consideration				
Mode	EFDD		SSI	
	High gain sensor	Geophone	High gain sensor	Geophone
1	0.239	0.235	0.234	0.232
2	0.192	0.204	0.198	0.203
3	0.133	0.130	0.136	0.134
4	0.106	0.104	0.105	0.111
5	–	0.082	0.080	0.810

Table 2 shows a highly satisfactory agreement between the periods estimated after the two different approaches (EFDD and SSI) and devices (Tromino sensors and geophones). Regarding the dispersion, it is rather low, with coefficients of variation ranging between approximately 0.013 and 0.075.

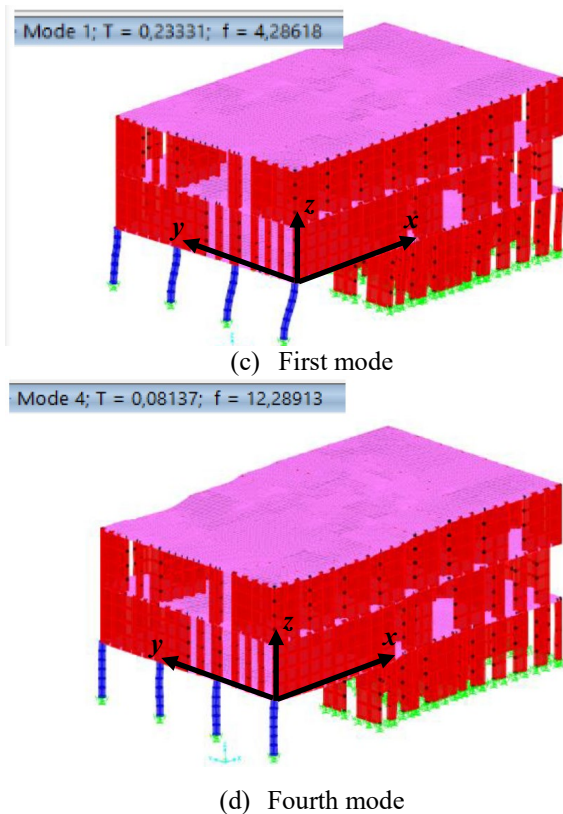
Concerning damping, EFDD provided rather reasonable values, while those of SSI were highly inconsistent. Table 3 contains the identified modal damping ratios.

Table 3. Damping ratios (%) from the Operational Modal Analysis of the building under consideration				
Mode	EFDD		SSI	
	High gain sensor	Geophone	High gain sensor	Geophone
1	0.172	0.495	–	–
2	0.342	0.178	–	–
3	0.060	0.273	–	–
4	0.255	0.207	–	–
5	–	0.575	–	–

Table 3 exhibits rather reasonable results, given the inherent difficulty of estimating the damping from extremely small vibrations.

## 5 FINAL NUMERICAL MODAL ANALYSIS

The OMA results obtained were used to calibrate the numerical model (section 3). In order to perform this operation, given the observed discrepancies between the computed periods (Table 1) and the expected longer values, the column clamping to the foundation was replaced with flexible connections using 3-D elastic springs; their stiffness (soil ballast coefficient) were varied until the building frequencies fit roughly those provided by the Operational Modal Analysis (Table 2). For the walls, the vertical and horizontal stiffness was 80 and 20 kN/mm, respectively; for the columns, such values were 630 and 40.



**Figure 13:** First and fourth modes from the final numerical analyses

The first 4 modes were analyzed; Figure 13 displays the computed first (Figure 13.a) and fourth modes (Figure 13.b) configurations.

Figure 13 shows that the first mode involves torsion and translation (in the  $y$  direction, see Figure 13.a) while the fourth one corresponds basically to vertical displacement (deflection) of the front part of the slab. For further clarity, Table 4 displays, analogously to Table 1, the computed natural periods and the translational and rotation modal ratios.

Mode	Period (s)	$U_x$	$U_y$	$U_z$	$R_x$	$R_y$	$R_z$
1	0.233	0	0.27	0	0	0	0.72
2	0.198	0.97	0	0	0	0	0
3	0.134	0	0.73	0	0	0	0.27
4	0.081	0	0	0.59	0	0.3	0

## 6 DISCUSSION ON RESULTS

Comparison between Table 2 and Table 4 shows that the periods that have been identified from OMA (Table 2) are highly similar to those from the final numerical calculation (Table 4); this indicates that the selection of the soil stiffness has been adequate.

On the other hand, comparison between Table 1 and Table 4 shows that the natural periods are significantly longer once the soil flexibility is accounted for. Conversely, the mode configurations are rather similar in both initial and final numerical modal analyses; this seems to point to a rather correct description of the structural behavior. As a matter of fact, the first mode identified from the final numerical modal analysis has even more torsional equivalent mass ratio; this trend corroborates the important detrimental effect of the first floor asymmetry (Figure 1.a, Figure 2.a, Figure 3, Figure 13.a).

## 7 CONCLUSIONS

This paper describes the numerical and Operational Modal Analyses of an undamaged 3-story RC building located in Valdivia (Chile), built in 2010, and founded on soft soil.

The building is basically supported by walls, but the first floor has an open front entrance atrium with flexible columns (Figure 1.a); this irregularity ventures a relevant eccentricity between the centers of mass and stiffness. OMA is carried out by using horizontal and vertical arrays of geophones and velocity and acceleration sensors. Two types of numerical simulations are performed: by neglecting the soil flexibility (initial) and by identifying such parameter from the OMA results (final).

This study provides two major outputs:

- The natural periods identified after the Operational Modal Analysis are significantly longer than the computed ones. This difference is apparently due to the relevant influence of the soil flexibility.
- Both the initial and final numerical simulations and the identification with OMA confirm that the first mode is predominantly torsional. In other words, this building configuration can be qualified as seismically irregular.

## REFERENCES

- [1] Ewins DJ. *Modal testing, theory, practice and application*. Research Studies Press Ltd. 2000.
- [2] He J. Fu ZF. *Modal Analysis*. Butterworth-Heinemann. 2001.
- [3] Heylen W, Lammens S. Sas P. *Modal analysis theory and testing*. Department of Mechanical Engineering, Katholieke Universiteit Leuven. 2007.
- [4] Fan W, Qiao P. *Vibration-based Damage Identification Methods: A Review and Comparative Study*. Structural Health Monitoring. 2010.
- [5] Doebling SW, Farrar CR, Prime MB, Shevitz DW. *Damage identification and health monitoring of structural and mechanical systems from changes in their vibration characteristics: A literature review*. USDOE (USA). 1996.
- [6] Au SK. *Operational Modal Analysis. Modeling, Bayesian Inference, Uncertainty Laws*. Springer. 2017.
- [7] Brincker R, Ventura CE. *Introduction to Operational Modal Analysis*. Wiley. 2015.
- [8] Rainieri C, Fabbrocino G. *Operational Modal Analysis of Civil Engineering Structures*. Springer. 2014.
- [9] Chang FK. *Structural Health Monitoring*. CRC Press. 2000.
- [10] Ren H, Chen X, Chen Y. *Reliability Based Aircraft Maintenance Optimization and Applications*. Aerospace Engineering. 2017.
- [11] Mansilla MN, Valdebenito G, Alvarado D, Reyes JP. *Análisis Modal Operacional de Edificio Utilizando Arreglos de Geófonos Horizontales*. Universidad Austral de Chile, Valdivia. 2020.
- [12] *SAP2000. Structural Analysis Procedure. Version 20.2.0*. CSI (Computers and Structures Inc.). 2019.
- [13] NCh 170. *Hormigón Requisitos Generales*. Instituto nacional de normalización (Chile). 2016.
- [14] NCh 204. *Barras laminadas en caliente para hormigón armado*. Instituto nacional de normalización (Chile). 2020.
- [15] NCh 433. *Diseño sísmico de edificios*. Instituto nacional de normalización (Chile). 2009.
- [16] *ARTEMIS Modal Pro v6.0*. Structural Vibrations Solutions. 2021.

## TOWARDS AUTONOMOUS VEHICLE COMFORT MODELLING FOR REAL WORLD ROAD VEHICLE SIMULATION

Verónica Santos Arconada<sup>\*</sup>, Jon García-Barruetabeña<sup>†</sup>, Fernando Cortés<sup>†</sup>, María  
Jesús Elejabarrieta<sup>†</sup>, Pelayo Fernández<sup>†</sup>

<sup>\*</sup> Technical Unit, AIC-Automotive Intelligence Center, Boroa Business Park, P2-A4, 48340  
Amorebieta-Etxano, Bizkaia, Spain, Phone: (+34) 946569400. Fax: (+34) 946569399. e-mail:  
v.santos@aicenter.eu

ORCID: <https://orcid.org/0000-0003-3684-0733>

<sup>†</sup> Dep. of Mechanical Engineering, Deusto University, Unibertsitate Etorb. 24, 48007 Bilbo, Bizkaia,  
Spain, Phone: (+34) 944139000. Fax: (+34) 944456817. e-mails: jgarcia.barruetabena@deusto.es,  
fernando.cortes@deusto.es, maria.elejabarrieta@deusto.es

**Abstract.** The autonomous car will completely change the current concept of road travel. Vehicle users are no longer looking exclusively for a safe car, but for a space that offers an environment with a high degree of comfort. Thus, vehicle simulators present a multitude of advantages as a tool for ride and comfort analysis in the preliminary stages of the dynamic development of a car. This paper studies the feasibility of a Stewart Platform for comfort studies by correlating the measured vibrations in the passenger car of a Toyota Prius with pressurized twin-tube hydraulic shock absorbers in the 1-10 Hz frequency range.

**Key words:** Comfort study - Damper model - Driving simulator – Vehicle dynamics.

### 1 INTRODUCTION

Driving simulators play an important role in research concerning vehicle dynamics, human comfort factors and the development of new advanced driver assistance systems [1].

These platforms enable testing to take place much earlier in the development process at lower cost, meaning the vehicle is closer to production when the physical prototypes are produced. The simulator then becomes an integral part of the vehicle development cycle as it provides a natural link between the phases of car design, from computer modelling to laboratory testing and, finally, to the test track [2].

Ride comfort is a critical factor to evaluate the automobile performance and has been an interesting topic for researchers for many years, being vibration transmission to passengers one of the most influent aspects on

comfort, performance, and health [3]. Transmission associated with the dynamic system depends on the frequency and direction of the input motion and the characteristics of the seat from which the vibration exposure is received. Vibrations up to 12 Hz affect all of the human organs [4], being the human body most sensitive to vertical vibrations in the 4-8 Hz frequency range [5]. Vibrations beyond 12 Hz have local effects [4].

In consequence, automobile designers give great attention to the isolation of vibrations in the car in order to provide a comfortable ride for the passengers.

Vehicle's suspension is an important component to ensure ride comfort, since its performance directly affects the vehicle's ride comfort and handling stability. The design of the vehicle's suspension system must fulfil the demand of ride comfort and handling stability. The shock absorber spring assembly is a funda-

mental element of the suspension system [6]. While the spring has a linear dynamic behavior depending on the displacement, the shock absorber presents a nonlinear behavior that requires more complex mathematical models for its dynamic characterization [7].

Since the human body is a very sensitive system, driving simulator experiences must be as close as possible to reality in order to conduct simulated experiments that generate accurate results, so they can be extrapolated to real driving situations. In consequence, developing reliable vehicle models is essential to make simulators a useful tool for dynamic and comfort applications.

Consequently, this paper study the feasibility of a Stewart Platform for com-fort studies by correlating the measured vibrations for Z-direction excitations in the passenger car of a Toyota Prius with pressurized twin-tube hydraulic shock absorbers.

The paper is structured as follows: in section 2, the technical characteristics of the Stewart platform used for this study are presented. In section 3, the development and validation of a simplified non-linear dynamic model of a passive twin-tube hydraulic shock absorber mounted on the Toyota Prius is explained. In section 4, the validation of the driving simulator for ride and comfort applications is exposed. Finally, in section 5, the main conclusions of the study are summarized.

## 2 THE DRIVING SIMULATOR

Hydraulic motion-control systems have been used in the flight and automotive industry for more than 40 years for meeting the required performance specifications. Nevertheless, the nowadays electric systems are presented as a better solution since these platforms are more efficient and offer higher uptime for lower maintenance and less-costly infrastructure [8]. That is why electric servo drive systems are

chosen as the driving mechanism for small-scale Stewart platform application, such as research in vehicle dynamics [9].

A Stewart platform is a parallel manipulator consisting of a fix base, a mobile platform and six linear actuators that join both parts. The actuators give the plat-form six degrees-of-freedom positioning capabilities: three translational (sway, surge and heave) and three rotational (roll, pitch, yaw) (see Figure 1).



Figure 1. Electric Stewart Platform.

The driving simulator from Figure 1 is an inverse electric Stewart platform (eMove eM6-640-1000 Cruden model) where the input signals are referenced to the moving platform centroid (MPC) through a soft-real time communication system. The mobile platform is based on a 1000-kg-playload mockup including the seat, the dashboard, three-42''-screens and the audio system. Table 1 shows the application range at a gross moving load of 1000 kg of the 640-motion base for 1-10 Hz frequency range.

DOF	Position	Velocity
Sway	-480 / 600 [mm]	800 [mm/s]
Surge	-500 / 500 [mm]	800 [mm/s]
Heave	-413 / 418 [mm]	600 [mm/s]
Roll	-23.8 / 23.8 [°]	35 [°/s]
Pitch	-23.7 / 26.1 [°]	35 [°/s]

Table 1. Technical specifications of the 640-motion base at a gross moving load of 1000 kg.

From Table 1 is deduced that this platform is suitable for working in vehicle dynamics applications, where the maximum accelerations are framed within the range of  $\pm 2 \text{ ms}^{-2}$  [10]. On the other hand, the platform working frequency range (1-10 Hz) allows to address comfort studies in the field of handling, body motion and primary and secondary ride [11].

The actuators are linked to the base with a universal joint and to the moving platform with a spherical joint, while the torque-force of the actuator is transmitted from a synchronous belt and snail system. Each actuator is moved by a permanent magnet synchronous motor (PMSM).

### 3 THE DAMPER MODEL

In this section, the non-linear dynamic mathematical model of the passive twin-tube hydraulic shock absorber is presented.

#### 3.1 Dynamic model

The dynamic model of a shock absorber is derived from a force balance in the piston valve. Figure 2 shows the free body diagram of the shock absorber in its vertical position.

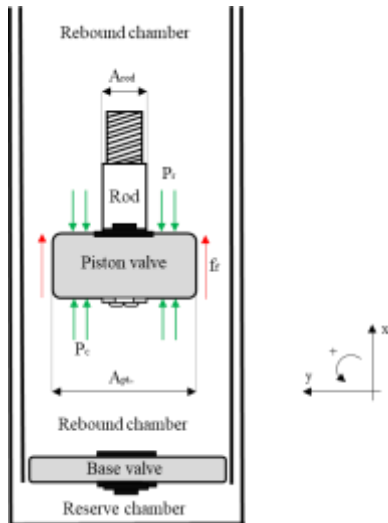


Figure 2. Shock-absorber free body diagram.

From Figure 2, the balance of forces ( $f_{damper}$ ) on the piston valve results in [12]

$$f_{damper} = P_c A_{P_t} - P_r (A_{P_t} - A_{Rod}) \pm f_f. \quad (1.1)$$

where  $P_c$  is the pressure in the compression chamber,  $P_r$  is the pressure in the rebound chamber,  $A_{P_t}$  is the area of the piston,  $A_{Rod}$  is the area of the rod and  $f_f$  is the friction force generated during the dynamic performance of the damper.

Eq. (1) leads to a system of differential equations that calculates the pressure inside the inner tube of the shock absorber. The pressure in the compression chamber is obtained as [13]

$$\dot{P}_c(x_d(t), \dot{x}_d(t)) = \frac{(\dot{x}_d A_{P_t} + Q_{pv} + Q_{bv})(1 - \alpha P_c)}{\left[ x_0 + \left( \frac{\Delta}{2} + x_d \right) \right] A_{P_t} \alpha}. \quad (1)$$

The pressure in the rebound chamber is obtained as [13]

$$\dot{P}_r(x_d(t), \dot{x}_d(t)) = \frac{(-\dot{x}_d (A_{P_t} - A_{Rod}) + Q_{pv})(1 - \alpha P_r)}{\left[ L_{P_t} - x_0 - \left( \frac{\Delta}{2} - x_d \right) \right] (A_{P_t} - A_{Rod}) \alpha}. \quad (2)$$

From Eqs. (2) and (3), it is seen that the geometrical change of the volume of the compression chamber is balanced by the sum of both flow rates, the flow through the piston valve ( $Q_{pv}$ ) and the flow through the base valve ( $Q_{bv}$ ), and the oil compressibility factor ( $\alpha$ ). Besides,  $L_{P_t}$  represents the length of the piston tube,  $x_d$  the damper displacement and  $\dot{x}_d$  the damper velocity.

Regarding the friction force,  $f_f$ , (see Eq. (1)), it has been determined from the experimental results for each velocity value.

discrete values have been adjusted to a DPPR friction model [14] according to

$$f_f = f_{f_1} \cdot \text{sign}(\dot{x}_d) + (f_{f_0} - f_{f_1}) e^{-\left(\frac{\dot{x}_d}{f_{f_2}}\right)^2} + f_{f_3} \cdot \text{sign}(\dot{x}_d) \quad (3)$$

where  $f_{f_1}$ ,  $f_{f_0}$ ,  $f_{f_2}$ ,  $f_{f_3}$  are the fitted parameters.

### 3.2 Model validation

The numerical-experimental correlation of the developed dynamic model is performed on force-movement dynamic behavior. For that, A MTS-850.67 test bench has been used to obtain the experimental dynamic response of a Vogtland 967003. The damper has been subjected to a constant amplitude sinusoidal displacement ( $v_i = 100$  mm) at different velocities ( $\Delta$ ): 0.052 m/s, 0.131 m/s, 0.261 m/s, 0.393 m/s, 0.524 m/s, 0.785 m/s, 1.047 m/s and 1.571 m/s.

Table 2 shows the coefficient of determination ( $R^2$ ) between the experimental results and the model results.

Speed (m/s)	$R^2$ rebound	$R^2$ compression
0.052	0.84	0.82
0.131	0.97	0.96
0.261	0.99	0.92
0.393	0.96	0.91
0.524	0.96	0.89

**Table 2.** Coefficient of determination of the dynamic damper model.

As can be seen from Table 2, all the results have a coefficient of determination greater than 0.8, so the model can be validated.

## 4 COMFORT VALIDATION

Once the non-linear dynamic model of the damper has been validated, it has been integrated into the complete vehicle model of a Toyota Prius that governs the driving platform from Figure 1 in order to validate the simulator for ride and comfort applications in the 1-10 Hz frequency range.

### 4.1 Experimental tests

The driving simulator validation has been based on the correlation of accelerations measured on the seat of the platform and the seat of a Toyota Prius III Generation for acceleration tests at 10 and 50 km/h, where the chassis is subjected to vertical forces imposed by the road profile.

**Toyota Prius III Generation.** The vehicle model that governs the dynamics of the driving simulator from Figure 1 is a Toyota Prius III Generation. In consequence, the experimental measurements have been carried out in this vehicle to have comparable results in the physical and in the virtual testing scenarios. Thus, the vibrations measured on the seat of the simulator and on the seat of the physical car respond to the same dynamic behavior.

The seat accelerations have been measured with a Brüel & Kjaer 4515 triaxial seat accelerometer. This sensor is specially designed for full body vibration. It consists of an accelerometer housed by a semi-rigid nitrile rubber disc and complies with ISO 7096, ISO 2631 and ISO 10326-1.

**Driving simulator.** Acceleration tests at 10 and 50 km/h have been replicated on the Stewart Platform with the complete vehicle model of a Toyota Prius and with the developed damper model explained in section 3. As with the physical car, accelerations on the seat have been measured. The platform seat has been re-placed with the physical seat

installed in the Toyota to ensure the same vibration transmissibility considered in both testing scenarios.

## 4.2 Results

After performing the tests on the physical platform and on the virtual platform, the applicability of a Stewart Platform for ride and comfort applications in the 1-10 Hz frequency range has been validated by frequency correlation of the measured seat vibrations for each of the test speeds.

Figure 3 and Figure 4 show a study of the linear accelerations measured on the seat for the tests carried out with the physical car and the linear accelerations measured on the seat for the tests carried out on the platform (for 10 and 50 km/h).

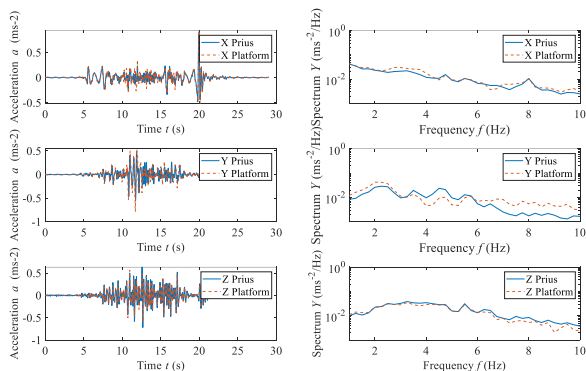


Figure 3. Temporal and frequency analysis of the seat vibrations at 10 kmh.

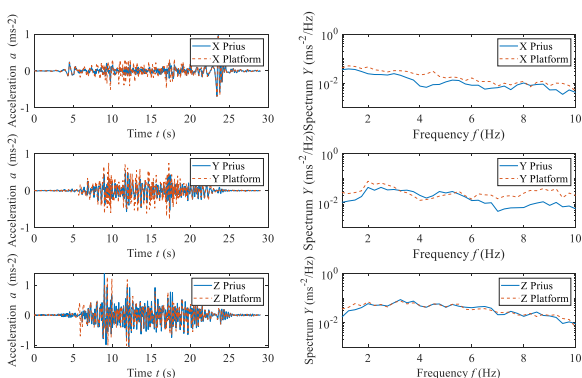


Figure 4. Temporal and frequency analysis of the seat vibrations at 50 kmh.

According to Figure 3 and Figure 4, there is a good correlation of results for all speeds, especially for the X and Z axes for the low and medium frequency ranges, which are the axis that most affect comfort. However, higher deviations are observed in the Y-axis, which may be due to a different mass distribution in the simulator and in the real car.

## 5 CONCLUSIONS

This paper studies the feasibility of a Stewart Platform for comfort studies by correlating the measured vibrations in the passenger car of a Toyota Prius with pressurized twin-tube hydraulic shock absorbers. Then, it is concluded that a driving hexapod is a useful tool for comfort applications in the 1-10 Hz range if a high-level dynamic damper model is considered.

## REFERENCES

- [1] Fernandez JG. A vehicle Dynamics Model for Driving Simulators 2016.
- [2] Static W. Advanced Vehicle Driving Simulators n.d.
- [3] Patil SA, More ID. On-Road Ride Comfort Test and Simulation Analysis of Passenger Cars with Emphasis on Indian Suburban and Rural Road Conditions. SAE Tech Pap 2016. <https://doi.org/10.4271/2016-01-1680>.
- [4] Nahvi H, Fouladi MH, Nor MJM. Evaluation of whole - Body vibration and ride comfort in a passenger car. 16th Int Congr Sound Vib 2009, ICSV 2009 2009;1:473–80. <https://doi.org/10.20855/ijav.2009.14.3.245>.
- [5] Rahman MS, Kibria KMG. Investigation of vibration and ride characteristics of a five degrees of freedom vehicle suspension system. Procedia Eng 2014;90:96–102. <https://doi.org/10.1016/j.proeng.2014.1>

- 1.820.
- [6] Mihon L, Lontış N, Deac S. The behaviour of a vehicle's suspension system on dynamic testing conditions. IOP Conf Ser Mater Sci Eng 2018;294. <https://doi.org/10.1088/1757-899X/294/1/012083>.
- [7] Elliott SJ, Tehrani MG, Langley RS. Nonlinear damping and quasi-linear modelling Subject Areas : 2015.
- [8] Murthy S (Moog IG. Electrifying the feel of flight. Mach Des 2009;4.
- [9] Lou JH, Tseng SP. Developing a real-time serial servo motion control system for electric stewart platform. 2014 Int Conf Adv Robot Intell Syst ARIS 2014 2014:66–71. <https://doi.org/10.1109/ARIS.2014.6871494>.
- [10] Dixon JC. The Shock Absorber Handbook: Second Edition. 2007. <https://doi.org/10.1002/9780470516430>.
- [11] Arvidsson K, Runolfsson RM. Development of methods for objectively quantifying performance of active suspension systems 2019:58.
- [12] Jugulkar L, Singh S, Sawant S. Mathematical modelling and experimental validation of mono-tube shock absorber. World J Eng 2016;13:294–9. <https://doi.org/10.1108/WJE-08-2016-040>.
- [13] Taylor P. Vehicle System Dynamics : International Journal of Vehicle Mechanics and Mobility Simulation Tools , Modelling and Identification , for an Automotive Shock Absorber in the Context of Vehicle Dynamics Simulation Tools , Modelling and Identification , for a 2010;3114:37–41.
- [14] Na J, Chen Q and Ren X: Emerging Methodologies and Applications in Modelling, Adaptive Identification and Control of Uncertain Systems with Non-smooth Dynamics. 2018. Academic Press. *Chapter 6 - Adaptive Control for Manipulation Systems With Discontinuous Piecewise Parametric Friction Model.*

## **Section 6: Bridge dynamics**

---

## NUMERICAL MODELLING AND MODAL ANALYSIS OF THE PEDESTRIAN FOOTBRIDGE AT THE MILAN'S CAMPUS

**Natalia García-Fernández\*, M. Rocío Quintana Camporro\*, F. Pelayo\* and Manuel  
Aenlle-López\***

\* Department of Construction and Manufacturing Engineering, EPI Gijón  
Universidad de Oviedo  
33206 Gijón, Spain  
e-mail: garciafernatalia.uo@uniovi.es  
ORCID: 0000-0003-4870-7710

**Abstract.** Monitoring and vibration serviceability of structures is commonly addressed analyzing their dynamical behavior. Both calibrated numerical models and experimental results such as modal parameters (natural frequencies and mode shapes) obtained by modal analysis can be used.

The footbridge located at the Milan's campus (Oviedo) is a peculiar lattice structure, since it is placed on top of the buildings at the main entrance to the Milan's Campus. The structure has a complete glass enclosure, which favors the influence of the wind on the structure, and therefore, it can be subjected to greater dynamic loads than those foreseen in the design phase.

In this work, a study of the dynamic behavior of the pedestrian footbridge is presented. Firstly, a finite element model (FEM) of the structure was assembled in ABAQUS. On the other hand, the experimental modal parameters were identified by operational modal analysis (OMA). Finally, the experimental results were used to update the finite element model and to analyze the dynamic behavior of the structure.

**Key words:** Footbridge, Modal Analysis, OMA, Numerical analysis.

### 1 INTRODUCTION

Structural health monitoring (SHM) techniques are increasingly used, allowing to obtain accurate information about changes in the structures and their dynamic behavior, especially, when they are combined with numerical models. In order to perform an precise analysis, the FE model of the structure has to be as similar to reality as possible, for this purpose Model Updating is needed [1].

In this work, the first stage of the structural health monitoring process was performed in a pedestrian footbridge. This stage includes FE model of the footbridge, Operational Modal Analysis (OMA) and Model Updating of the FEM. Finally, the dynamic behavior of the structure was analyzed.

### 2 THE FOOTBRIDGE STRUCTURE

The pedestrian footbridge was built between the late 80s and early 90s and it is located in Asturias (Spain) belonging to the Milan's Campus of the University of Oviedo (see Fig. 1). The footbridge is a steel structure formed by two Pratt truss joined in the top part by a gable roof which allows the enclosure of the footbridge by a glass cover. Both lateral sides are also closed by glass enclosures. The deck consists of concrete T beams connected to the two trusses. The main structure was built in factory and then was placed on the buildings by a crane, being located finally at an approximate height of 12 meters from the base of the building.



**Figure 1:** Pedestrian Footbridge at the Milan's campus

The pedestrian footbridge has a span of 34 meters, a width of 4.35 meters and a height of 3.4 meters, being in contact with each building for a length of 5 meters (see Fig. 2). Information about how the structure was fixed to the buildings is not available.

The main structure is made of steel S275. The superior and inferior chords of the trusses are equal, formed by two box-welded UNP280 profiles. The rest of the bars are box-welded UNP140 profiles.

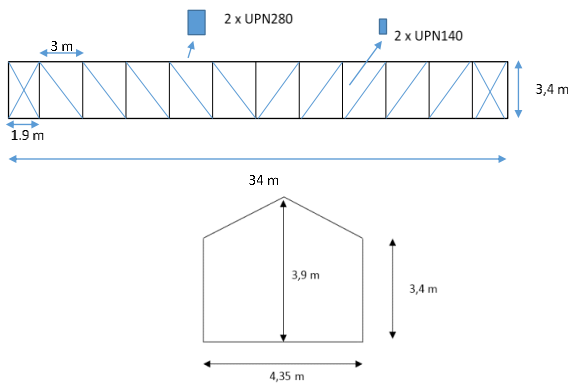


**Figure 2:** General dimensions of the pedestrian footbridge

## 2.1 Numerical model

The finite element model of the pedestrian footbridge was modeled in ABAQUS CAE. The model was assembled using 1-D beams elements (B3D3) for all the structural elements (see Fig. 3). The footbridge enclosure (glass + aluminum frames) was modeled as point-

masses on the structure, therefore, the possible effect on the stiffness of the structure was neglected.

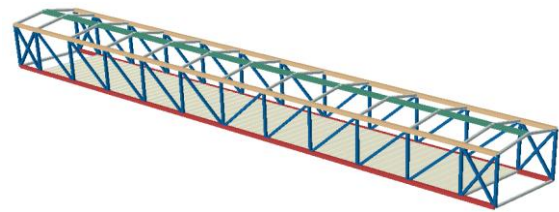


**Figure 3:** Finite element model of the structure (each color represents a section/material)

As it was previously mentioned, boundary conditions are unknown in detail. Due to that, pin conditions over the 5 meters that support the structure were created (see Fig. 4a). The numerical natural frequencies corresponding to the first five modes are presented in Table 1.

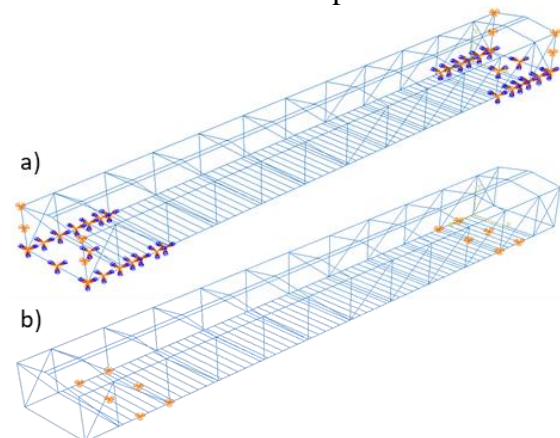


**Figure 4:** Boundary conditions used in the FE Model.

## 2.2 Modal analysis

In order to obtain the experimental modal parameters of the structure (natural frequencies, mode shapes and damping ratios), an Operational Modal Analysis (OMA) test was carried out.

Taking into account the numerical mode shapes defined previously, the number of sensors locations and their position was decided (see Fig. 5). Additionally, as the real support conditions in both ends of the footbridge are unknown, it was also considered to measure the vertical displacements along the sides of the 5 meters support (see Fig. 5). To complete the 14 locations of Figure 5, 3 data sets were performed using 6 accelerometers

(PCB 393B31) with a sensitivity of 10 V/g of sensitivity. The responses were acquired with a TEAX-LX 120 acquisition system. The sampling frequency was 100 Hz and each data set was about 20 minutes long. Artificial excitation was applied during testing by 3 people walking and jumping randomly over the structure.

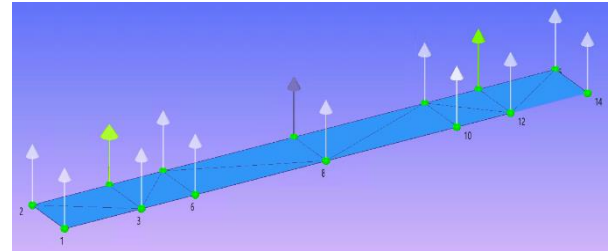


Figure 5: Measured points used for vertical direction.

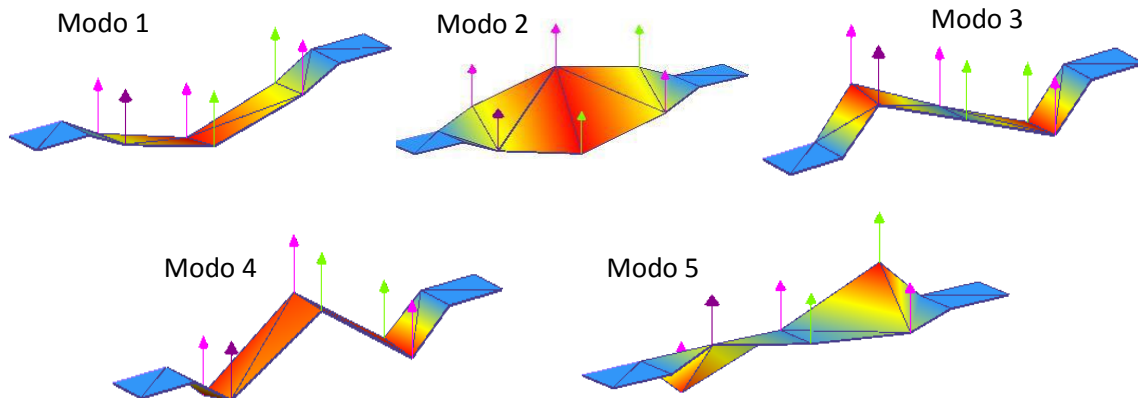


Figure 6: Experimental mode shapes

Modal identification was performed using the software Artemis Modal with the CFDD (Curve-fit frequency domain decomposition) and SSI (subspace stochastic identification) techniques [2]. The singular value decomposition for the CFDD technique and the SSI stabilization diagram are presented in figure 7. For the first modal analysis identification, only the six sensors located in the middle of the deck were used (see Fig. 6). The experimental natural frequencies for the first vertical mode shapes obtained with the CFDD technique are presented in Table 1

whereas the mode shapes are presented in figure 6. Similar results were obtained with the SSI identification technique.

Mode	Exp. Freq. [Hz]	Numerical Freq. [Hz]	Error [%]
1 (bending)	7.56	7.43	1.67
2 (torsion)	11.05	11.11	0.52
3 (bending)	15.87	14.67	9.19
4 (bending)	21.79	19.17	12.02
5 (torsion)	24.32	23.46	3.52

Table 1: Natural frequencies of the numerical and experimental models

The errors between the experimental and numerical frequencies are also presented in Table 1. From the results, it can be inferred that a good correlation is obtained for modes 1, 2 and 5, whereas modes 3 and 4, both bending modes, present higher errors.

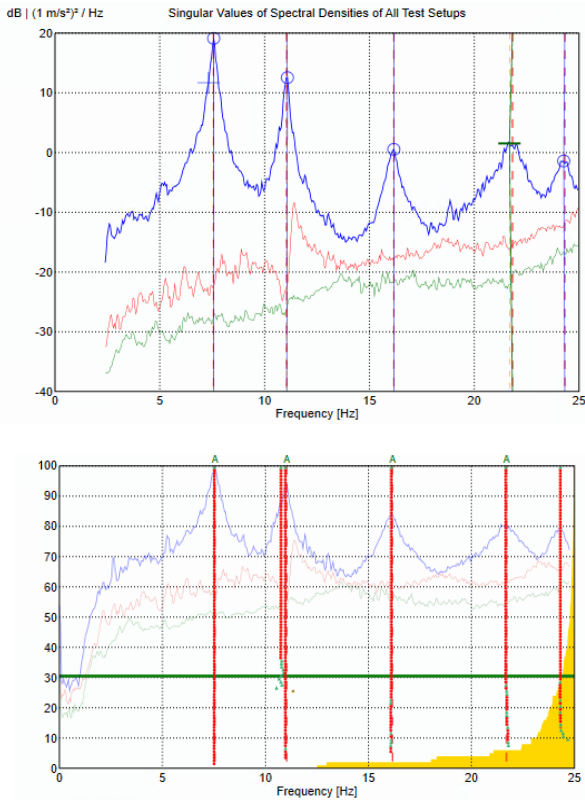


**Figure 7:** SVD of Spectral densities for the CFDD technique and the SSI Stabilization diagram for the SSI technique.

### 3 MODEL UPDATING

In order to improve the numerical model, a model updating [3] was performed using the experimental modal parameters. The main

difficulty of Model Updating process is that there is not one single solution, and so there are several combinations of parameters which minimize the error.

Moreover, any change in the structural parameters must be done considering physical limitations, i.e., introducing reasonable changes. Taking into account all these considerations, as well as the relation between the natural frequencies and the mass and stiffness of the structure, the structural parameters to modify have to be decided.

According to Table 1, the numerical natural frequencies were, in general, lower than the experimental natural frequencies. Moreover, the maximum errors were found in the bending modes 3 and 4.

As it was previously mentioned, there were uncertainties about the real support conditions of the structure and, therefore, how to modelling that boundary conditions. The first step was to analyze in detail the mode shapes in those areas. For this purpose, a second modal analysis was performed using the 14 acceleration channels shown in Figure 5. Vertical displacement at both ends of the structure were observed being the corresponding first two modes presented in Figure 8. From these results, it was inferred that the structure was not completely connected to the buildings along the 5 meters supporting area.

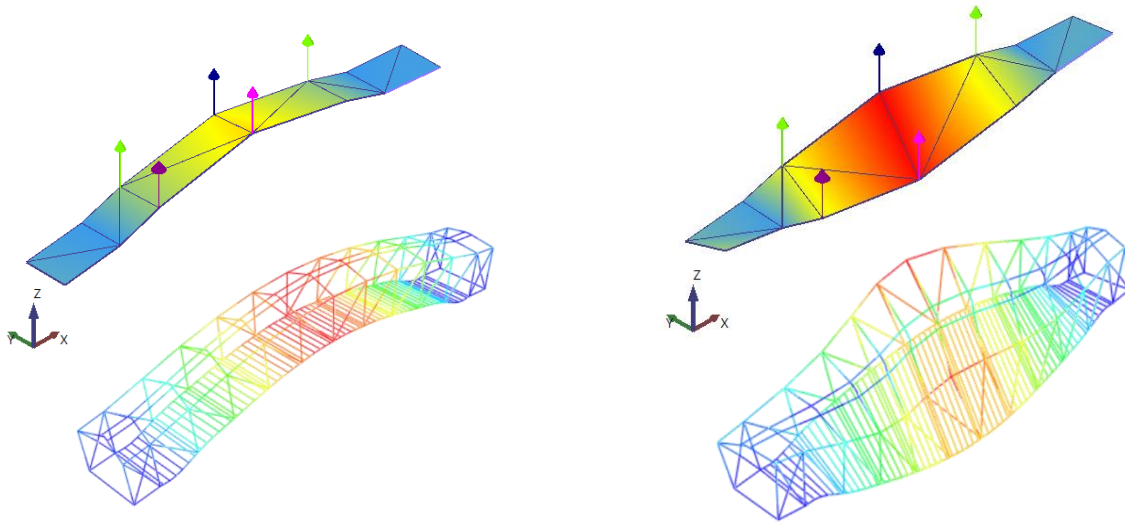


**Figure 8:** Modes shapes 1 and 2 model and experimental model

Finally, after some iterations, a good correlation for all modes was obtained when only the area close to the end of both spans was only restricted (see Fig. 4b). This fact would indicate that the structure is not fully connected to the buildings.

Moreover, this is in good agreement with the experimental mode shapes that presents almost no motion in these areas (see Figure 8).

The results obtained after performing the model updating are shown in Table 2.

Mode	Exp. Freq. [Hz]	Numerical Freq. [Hz]	Error [%]
1	7.56	7.5	0.81
2	11.05	11.21	1.46
3	15.87	15.06	5.10
4	21.79	21.50	1.32
5	24.32	24.11	0.86

**Table 2:** Natural frequencies of the updated numerical

The maximum error obtained after the updating is approximately 5% (mode 3) which means that the modal correlation between the numerical and experimental model can be considered accurate.

## 5 CONCLUSIONS

- The dynamic behavior of the pedestrian footbridge of Milan's campus is presented in this work through a numerical model and modal analysis.
- The numerical model was updated using the experimental modal parameters obtained with operational modal analysis (OMA).
- The structural parameters modified during the updating process were mainly the boundary conditions. After analyzing the experimental mode shapes and the final boundary conditions of the FEM, it can be concluded that the structure is not completely connected to the buildings.
- The monitoring of the structure could be addressed in the future based on the numerical model and the experimental results.

- Further studies must be carried out in order to identify the lateral behaviour of the structure. If the structure is not completely fixed in the vertical direction, it could also be partially free in the lateral direction, which could explain some vertical cracks that exist in the supporting area.

## ACKNOWLEDGES

The economic support given by the Spanish Ministry of Education through the project MCI-20-PID2019-105593GB-I00/AEI/10.13039/501100011033 are gratefully appreciated.

## REFERENCES

- [1] H.-P. Chen, Y.-Q. Ni, Structural Health Monitoring of Large Civil Engineering Structures, Wiley-Blac, John Wiley & Sons, Ltd, Chichester, UK, 2018.  
<https://doi.org/10.1002/9781119166641>.
- [2] R. Brincker, C.E. Ventura, Introduction to Operational Modal Analysis, John Wiley & Sons, Ltd, Chichester, UK, 2015.  
<https://doi.org/10.1002/9781118535141>.
- [3] M.I. Friswell, J.E. Mottershead, Finite Element Model Updating in Structural Dynamics, Springer Netherlands, Dordrecht, 1995.  
<https://doi.org/10.1007/978-94-015-8508-8>.

# INFLUENCE OF PASSIVE AND ACTIVE PEDESTRIANS ON THE DYNAMIC PARAMETERS OF A LIGHTWEIGHT FRP FOOTBRIDGE

Christian Gallegos-Calderón\*, Carlos M. C. Renedo\*, José M. Goicolea\*, Jaime H. García-Palacios\* and Iván M. Díaz\*

\*ETS Ingenieros de Caminos, Canales y Puertos  
Universidad Politécnica de Madrid  
28040 Madrid, Spain  
e-mail: christian.gallegos@upm.es  
ORCID: 0000-000-2-0358-8810

**Abstract.** Since high strength-to-weight ratio is a relevant characteristic of composite materials, dynamic parameters of FRP structures may vary significantly due to occupants. This paper presents an experimental study of a simply supported FRP footbridge considering passive and active pedestrians. The 10 m long laboratory facility is formed by pultruded elements and presents a linear mass density around 80 kg/m. Using data from 18 high sensitivity accelerometers placed on the bridge deck, an Operational Modal Analysis (OMA) was initially carried out to determine the vibration modes of the structure. Then, controlled forced vibration tests were conducted considering 2, 4, 6 and 10 pedestrians standing on the bridge deck. Employing the data recorded from the force applied by an electrodynamic shaker and the response measured by 9 accelerometers attached to the bottom of the stringers, an Experimental Modal Analysis (EMA) was performed for each test. Finally, an OMA in presence of exogenous inputs (OMAX) was carried out accounting for people walking in a closed-loop path over the bridge. In the cases of humans standing, the fundamental frequency of the footbridge decreased drastically from 7.85 Hz (empty) to 4.54 Hz (10 people). Whilst the first natural frequency of the FRP structure slightly changed when people walked. As expected, passive and active pedestrians contributed to increase the damping ratio of the vibrating system.

**Key words:** FRP footbridge, pedestrians standing, pedestrians walking, OMA, EMA, OMAX.

## 1 INTRODUCTION

Excessive human-induced vibrations in pedestrian structures have been the subject of several studies over last years given the adoption of novel materials and new construction process [1, 2]. In this field, an important aspect that remains to be fully comprehended is the influence of humans on the dynamic behaviour of lightweight and slender footbridges, in which human-structure interaction phenomenon may play an important role.

Human presence, either passive or active, on structures has proved to modify the natural

frequencies [3] and increase the damping potential [4] of vibration systems. In fibre reinforced polymer (FRP) or composite footbridges, which are usually lightweight [5], excessive human-induced vibrations may drive the structural design. Hence, the second mentioned effect may contribute to mitigate the vibration response.

In addition to the increment of the intrinsic damping of the structural system, the ratio between the live load (pedestrians) and the dead load (self-weight) may be high in FRP footbridges. Thus, significant changes in the dynamic parameters (modal masses, natural

frequencies, and damping ratios) of composite structures may be also expected.

This paper presents an experimental dynamic study of an FRP footbridge, built at the laboratory of the School of Civil Engineering - UPM. The aim of the work is to characterize the influence of passive and active pedestrians on the dynamic properties of the pedestrian facility by carrying out OMA, EMA, and OMAX based on ambient vibration and forced vibrations tests, respectively.

## 2 BARE STRUCTURE

### 2.1 FRP Footbridge

The structure studied hereby is 10 m long and 1.5 m wide (Figure 1). CFRP strips and GFRP stringers, crossbeams, handrail poles, and deck panels form the footbridge. These pultruded elements were manufactured by Fiberline Composites A/S [6]. To assemble the structure, stainless-steel bolts were used, and an epoxy adhesive was employed to join the stringers and strips. Concrete blocks at the ends of the bridge eased the installation of the pinned and roller supports. The linear mass density of the structure is around 80 kg/m, without accounting for the weight of the end-side concrete elements.



Figure 1: FRP Footbridge.

### 2.2 OMA

Prior the experimental campaign with

pedestrians, the vibration modes of the bare structure were identified by performing an OMA. Data recorded with 18 high sensitivity accelerometers placed vertically on the bridge deck (Figure 2(a)) was employed for the analysis. First, an ambient vibration test (Test 1) was carried out. As ambient loads inside the laboratory were almost inexistent, another experiment (Test 2) was performed exciting the structure slightly with a hammer. In both tests, the sampling frequency was 5120 Hz, and the duration was 10 minutes.

The first three vibration modes of the footbridge were identified using MACEC [7] software. A low-pass filter with a cut-off frequency at 80 Hz was used, and a factor of 64 was applied to decimate the raw data. The data-driven Stochastic Subspace Identification (SSI-data) method was employed. Figure 2(b)-(c) displays the stabilization diagrams for the Test 1 and Test 2 with a model order of 160 and the power spectral density of all the signals superimposed. The stable poles selected as solution were around the modal order of 70.

The vibration modes of the structure, shown in Figure 2(d), are: 1<sup>st</sup> vertical bending mode (Mode 1), 1<sup>st</sup> lateral-torsional mode (Mode 2), and the 2<sup>nd</sup> lateral-torsional mode (Mode 3). Although Modes 2 and 3 seem to be similar, the former is mainly controlled by the lateral movement of the stringers. Whilst the latter involves an action of the stringer-deck system. This difference can be seen in a FE model that is not described in this work. Table 1 presents the natural frequencies ( $f_s$ ) and damping ratios ( $\zeta_s$ ) of the vibration modes computed for each test.

Mode	Test 1		Test 2	
	$f_s$ [Hz]	$\zeta_s$ [%]	$f_s$ [Hz]	$\zeta_s$ [%]
1	9.13	0.6	7.66	1.4
2	11.43	0.6	10.96	1.3
3	16.23	0.6	15.01	1.0

Table 1: Modes of vibration of the FRP footbridge.

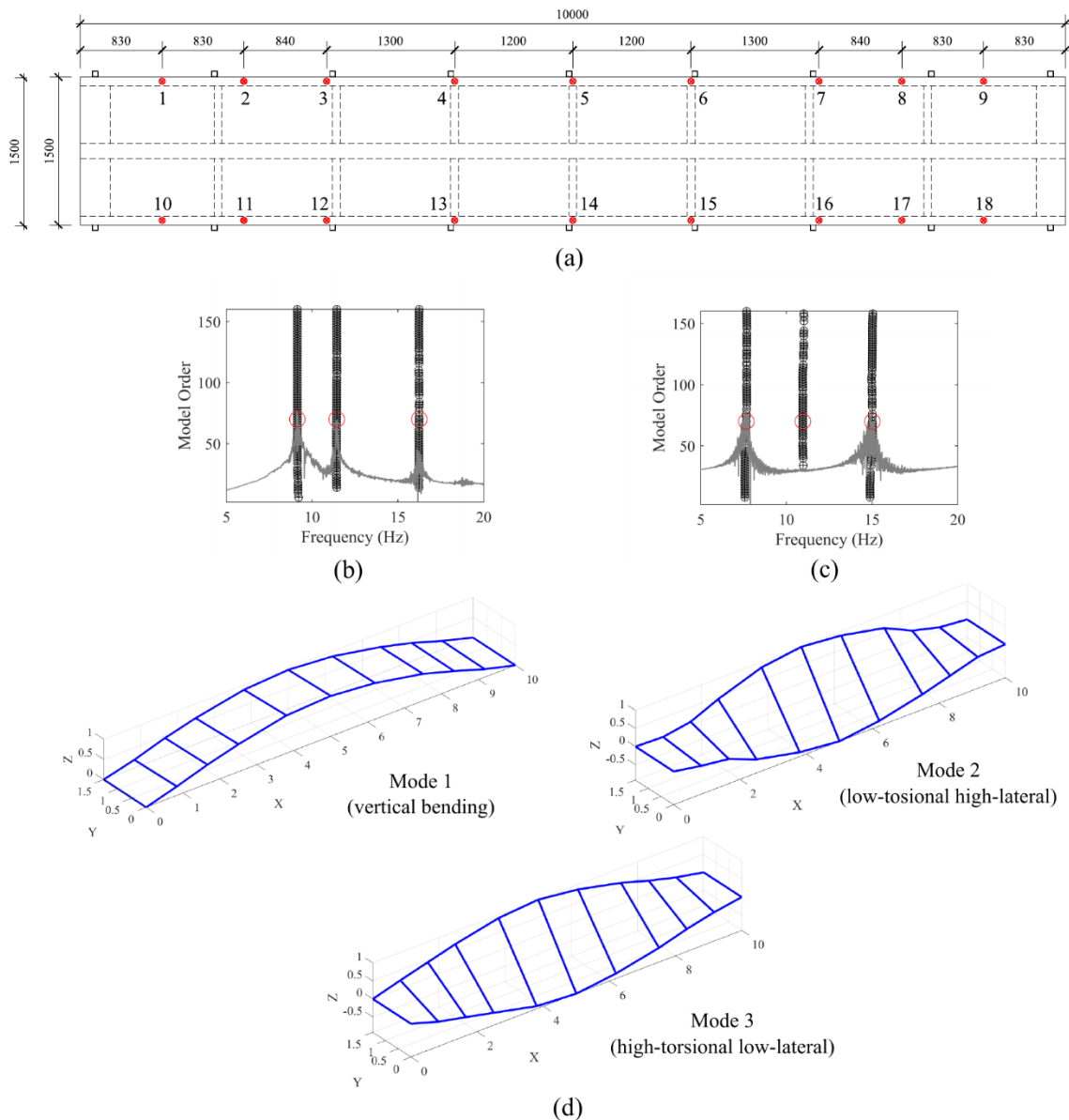


**Figure 2.** OMA of the bare FRP footbridge: (a) Location of 18 accelerometers, (b) Stabilization diagram of Test 1, Stabilization diagram of Test 2, and (d) First three modes of vibration.

The difference between the natural frequencies computed in Tests 1 and 2 might be explained by the activation, or not, of the roller support. The FRP footbridge appears to be much stiffer when negligible excitation is applied. Regarding the damping ratios, the values calculated for Test 2 are higher than the ones obtained in Test 1 given this parameter is dependent on the amplitude achieved by the structure when it is excited.

### 3 PASSIVE PEDESTRIANS

#### 3.1 Humans standing

To study the influence of passive pedestrians on the structural dynamic properties of the FRP structure, four experiments were performed considering the following number of humans standing on the

bridge deck: 2 (Test A), 4 (Test B), 6 (Test C) and 10 (Test D). Also, a test with the bare structure was carried out for comparison.

The position of the pedestrians during the experiments is shown in Figure 3(a), where the symbols and numbers refer to the location of a person in a test. For example, a triangle and number 2 correspond to the location of a human in Test A. This experiment is shown in Figure 3(b).

The total mass of the people involved in each experiment is presented in Table 2. Besides, the ratio between the mass of the pedestrians and the mass associated to the first flexural mode of vibration of the FRP structure is stated. The mass of the first mode ( $m_{s1}$ ) was assumed to be 400 kg. Given the inherent lightweight property of FRPs, the ratio easily surpassed the value of 0.3 for all tests.

Test	Number of pedestrians	Total mass [kg]	Mass ratio
A	2	142.9	0.36
B	4	286.9	0.72
C	6	420.1	1.05
D	10	728.1	1.82

**Table 2:** Mass of pedestrians.

### 3.2 EMA

To carry out the EMA of the FRP structure with people standing, an APS 400 electrodynamic shaker [8], placed under the footbridge, was employed. To excite the flexural and lateral-torsional modes of the structure, the device was attached to a crossbeam near the edge of the mid-span cross-section by means of a stainless-steel rod, as shown in Figure 3(c). Also, nine PCB accelerometers, model 393B12, were attached to the bottom of the stringers (Figure 3(d)).

As the shaker was setup in a fixed body mode, the force generated by the device was obtained by monitoring its instantaneous current during the tests. In each experiment, the bridge was excited by a white noise signal,

with a frequency content between 1 and 100 Hz, for 5 minutes. Additionally, the sampling frequency was 1000 Hz.

The collected data from the accelerometers and the measured shaker force were processed applying a low-pass filter at 40 Hz and a decimation factor of 25. The peak picking method, available in MACEC [7] software, was used to find the first three natural frequencies of the bridge. Table 3 presents the obtained results.

Test	$f_{s1}$ [Hz]	$f_{s2}$ [Hz]	$f_{s3}$ [Hz]
Empty	7.85	11.02	15.11
A	7.42	10.97	15.09
B	5.88	8.21	10.78
C	4.96	7.27	9.36
D	4.54	6.34	8.51

**Table 3:** Natural frequencies of vibration of the FRP footbridge with passive pedestrians.

## 4 ACTIVE PEDESTRIANS

### 4.1 Humans walking

The dynamic parameters of the FRP footbridge with active pedestrians was assessed by performing four tests. The people involved in the experiments explained in Section 3.1 were asked to walk in a closed-loop path over the bridge deck for 5 minutes.

The following experiments were carried out accounting for 2 (Test I), 4 (Test II), 6 (Test III), and 10 (Test IV) humans. Thus, the crowd density went from 0.13 to 0.67 pedestrians/m<sup>2</sup> in the tests. Figure 4 shows the first performed test, where 2 people walked constantly over the structure.

### 4.2 OMAX

Employing the shaker explained in Section 3.2 and the nine high-sensitive accelerometers shown in Figure 3(d), an OMAX was carried out for every test with humans walking. A white noise signal with a frequency content between 1 and 100 Hz was applied to the

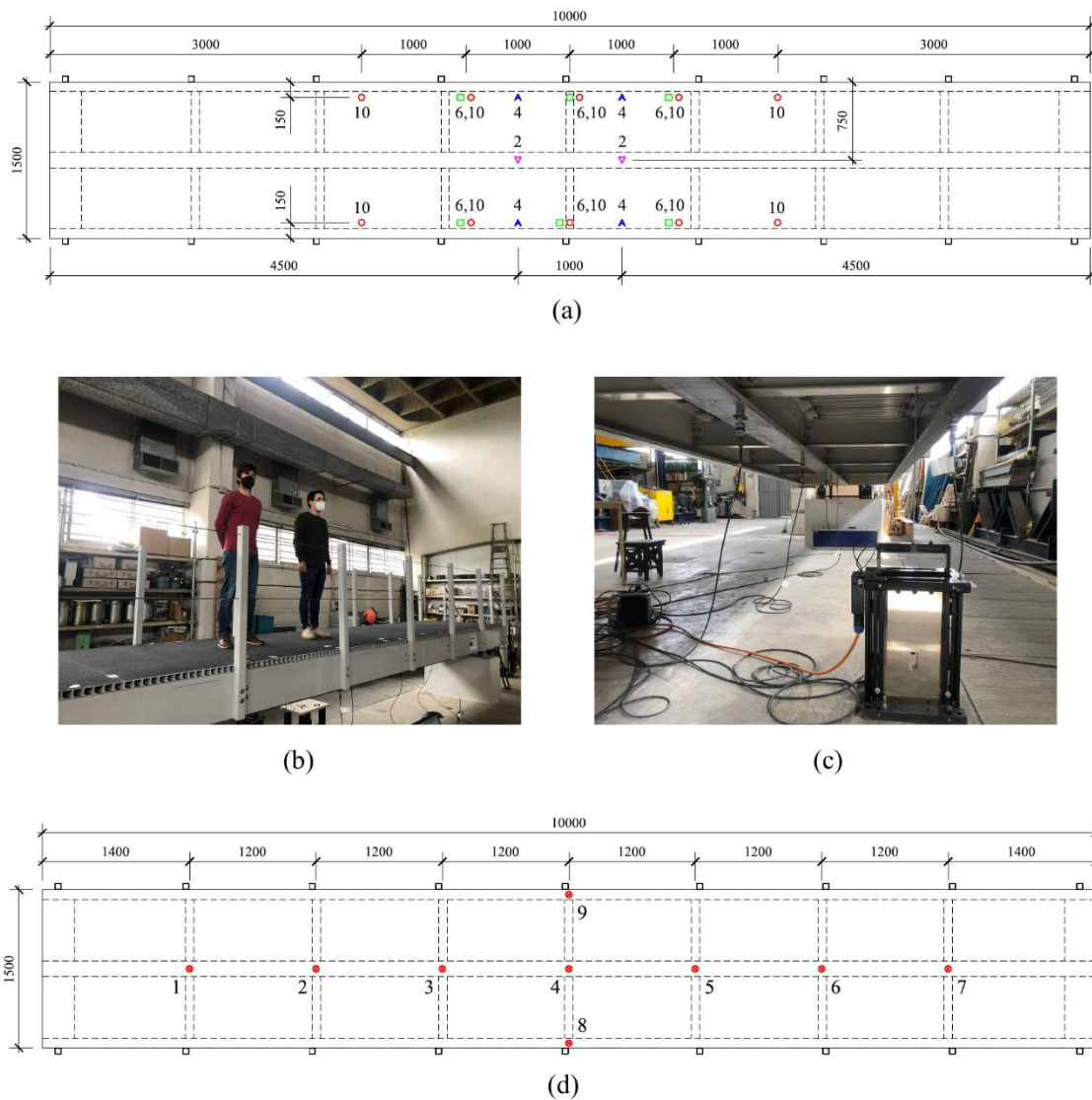


**Figure 3.** Forced vibration tests: (a) Position of passive pedestrians, (b) Test A, (c) Shaker setup, and (d) Location of 9 accelerometers attached at the bottom flange of the stringers.

structure for 5 minutes, and the sampling frequency of the recorded data was 1000 Hz.

A low-pass filter with a cut-off frequency at 40 Hz and a decimation factor of 25 were used to process the signals. For the analysis, the reference-based combined deterministic-stochastic subspace system identification algorithm [9], implemented in MACEC [7] software, was employed. Also, the signal from accelerometer No. 9 (Figure 3(d)) was used as the reference output. Table 4 presents the

results computed for the Modes 1 and 3 of the FRP footbridge with active pedestrians.

Test	OMAX	
	$f_{s1}$ [Hz]	$f_{s3}$ [Hz]
I	7.57	15.45
II	7.67	15.51
III	7.72	15.59
IV	7.98	15.65

**Table 4:** Natural frequencies of vibration of the FRP footbridge with active pedestrians.

As Mode 2 is controlled by the lateral movement of the stringers and the load due to walking is in the vertical direction, the natural frequency  $f_2$  could not be obtained. The natural frequencies of the Modes 1 and 3 of the structure slightly vary due to the active pedestrians, in comparison with the bare structure (empty).



Figure 4. Test I.

## 5 COMPARISON

In this section, results obtained for the vertical bending vibration mode (Mode 1) of the composite footbridge with passive and active pedestrians are compared.

First, using the information collected in Section 3.2, the frequency response functions (FRFs) of the vibrating systems were found for the footbridge with passive pedestrians. Data from the accelerometer No. 9 (Figure 3(d)) and the measured shaker force were considered. The  $H_I$  estimator [10], available in MATLAB [11] through the function TFESTIMATE, was employed to determine the FRFs.

The transfer function in each test was calculated as the average of 30 FRFs, obtained from 30-time windows with a duration of 10 s. The overlap between windows was 50%, so the window of each FRF was 20 s. Analytical transfer functions were computed by a trial-and-error procedure, aiming to reduce the root mean square error between the experimental

and numerical results. For the calculation, the total mass of each system was assumed to be the sum of  $m_{sl}$  and the mass of the pedestrians involved in the test (Table 2). Additionally, the natural frequencies of the systems were selected according to the values presented in Table 3. Figure 5 shows the FRF calculated based on the outcome of Test A (Figure 3(b)).

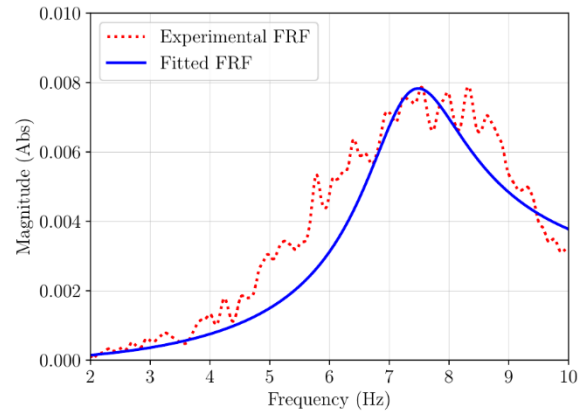


Figure 5. FRFs of the structure with 2 passive pedestrians.

Table 5 presents the results obtained for the analytical models according to the mass ratios explained in Section 3.1. The natural frequencies and damping ratios computed from the OMAX, carried out in Section 4.2, are included (active humans) in this table. In addition, outcomes of the empty structure (mass ratio of 0) are presented after performing the respective analyses.

Mass ratio	Passive Pedestrians		Active Pedestrians	
	$f_{sl}$ [Hz]	$\zeta_{sl}$ [%]	$f_{sl}$ [Hz]	$\zeta_{sl}$ [%]
0	7.85	1.6	7.85	1.3
0.36	7.42	11.8	7.57	4.1
0.72	5.88	17.1	7.67	5.3
1.05	4.96	11.8	7.72	6.8
1.82	4.54	13.5	7.98	7.7

Table 5. Results comparison for the fundamental vibration mode of the FRP footbridge.

Figure 6 depicts the analytical FRFs and the corresponding phase angles for all the

performed tests with humans standing.

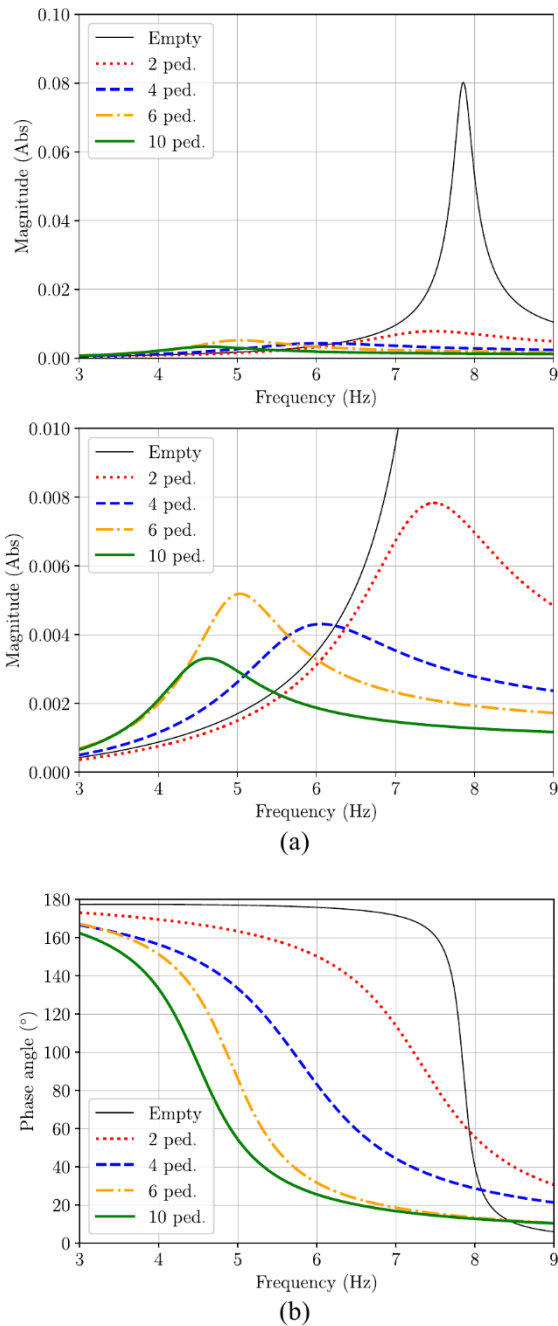


**Figure 6.** Footbridge with passive pedestrians: (a) FRFs, and (b) Phase angles.

The variation of the fundamental frequency and damping ratio of the structure due to passive and active humans are shown in Figures 7 and 8, respectively.

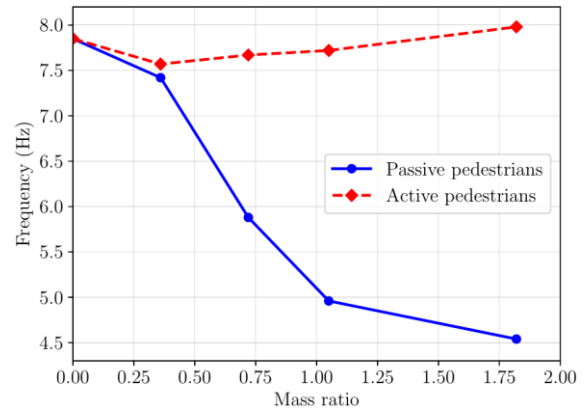


**Figure 7.** Variation of the fundamental frequency of the structure due to pedestrians

Although the systems compounded of the structure and passive pedestrians may not be comparable due to their different mass, it is seen that the fundamental frequency decreased, and the damping ratio increased with the addition of humans. The peak for the experiment with mass ratio of 0.72 may be explained by the position of the standing people respect to the mid-span (Figure 3(a)) and the selected accelerometer for the computation.

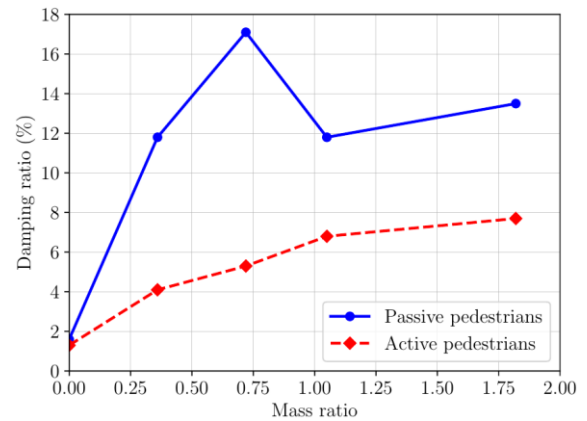


**Figure 8.** Variation of the damping ratio of the structure due to pedestrians

For the footbridge with active people,  $f_{sI}$  slightly varied ( $\pm 4\%$  the value of the bare structure). Whereas  $\zeta_{sI}$  increased significantly, almost 6 times higher than the initial value.

## 6 CONCLUSIONS

An experimental study has been carried out to assess the impact of passive and active pedestrians on the structural dynamic properties of an FRP footbridge, which linear mass density is only 80 kg/m. OMA, EMA and OMAX were performed using high-sensitivity accelerometers and an electrodynamic shaker, depending on the analysis.

The natural frequency and damping ratio of the vertical bending vibration mode of the structure were assessed accounting for humans standing and walking. As expected, the impact of passive pedestrians on the dynamic properties of the structure was more evident than the influence due to active humans.

In general, the damping of the vibrating system increased due to the presence of the pedestrians. Therefore, considering this effect at the design stage of composite footbridges may be beneficial to meet vibration serviceability requirements.

## ACKNOWLEDGEMENTS

The authors acknowledge the financial support provided by the Ministry of Science, Innovation and Universities of Spain through the project SEED-SD RTI2018-099639-B-I00. Christian Gallegos-Calderón thanks the Secretariat of Higher Education, Science, Technology and Innovation of Ecuador (SENESCYT) for the PhD scholarship CZ02-000167-2018. Carlos M. C. Renedo thanks UPM for the financial support through a PhD research grant.

## REFERENCES

- [1] Boniface V, Bui V, Bressolette P, et al. *Footbridges: Assessment of vibrational behaviour of footbridges under pedestrian loading*. Paris: Service d'Études Techniques des Routes et Autoroutes, 2006.
- [2] Heinemeyer C, Butz C, Keil A, et al. *Design of Lightweight Footbridges for Human Induced Vibrations*. European Commission, 2009.
- [3] Naranjo-Pérez J, González-Gómez N, Jiménez-Alonso J, et al. Experimental analysis of the effect of rhythmic dynamic crowd loads on stadium grandstands. In: *1st Conference on Structural Dynamics DinEst*. Madrid, pp. 46–49.
- [4] Živanović S, Díaz IM, Pavić A. Influence of walking and standing crowds on structural dynamic properties. In: *IMAC XXVII Conference & Exposition on Structural Dynamics*. Orlando, FL: The Society for Experimental Mechanics, Inc., 2009.
- [5] Wei X, Russell J, Živanović S, et al. Measured dynamic properties for FRP footbridges and their critical comparison against structures made of conventional construction materials. *Compos Struct* 2019; 223: 110956.
- [6] Fiberline Composites A/S. *General Design Certification*. Middelfart, Denmark: Fiberline Composites A/S, 2018.
- [7] Reynders E, Schevenels M, De Roeck G. *MACEC 3.3: a MATLAB toolbox for experimental and operational modal analysis*. Leuven, 2014.
- [8] APS. *APS 400 ELECTRO-SEIS® - Long Stroke Shaker with Linear Ball Bearings*. APS Dynamics Inc., 2013.
- [9] Reynders E, Roeck G De. Reference-based combined deterministic-stochastic subspace identification for experimental and operational modal analysis. *Mech Syst Signal Process* 2008; 22: 617–637.
- [10] Vold H, Crowley J, Rocklin GT. New ways of estimating frequency response functions. *Sound Vib* 1984; 18: 34–38.
- [11] Mathworks. *MATLAB - Getting Started Guide*. Matick, 2019.

# DINEST 2021

2<sup>nd</sup> Conference on Structural Dynamics 2021

Gijón (Spain), 22 -23 July

Xixón

Turismo

